UNIVERSITEIT VAN PRETORIA
UNIVERSITY OF PRETORIA
YUNIBESITHI YA PRETORIA

THE DEVELOPMENT OF ANALYTICAL METHODS FOR PBMR TRISO SIC CHARACTERIZATION

by

Noko Nepo Ngoepe

Submitted in partial fulfillment for the degree

Master of Engineering (Metallurgical Engineering)

In the Faculty of Engineering, the Built Environment and Information Technology**,**

University of Pretoria

2 June 2009

© University of Pretoria

ACKNOWLEDGEMENTS

- My Lord and Saviour, Jesus Christ for the purpose, abilities, prospects and life He has given me.

- My father, mother, sister and the rest of the extended family for your prayers, advice, support and encouragement.

- My supervisor Prof. Johan de Villiers for his guidance, encouragement, patience and tirelessness.

- Mr Dave Liles, Mr Werner Barnard and Dr Linda Prinsloo of the Department of Chemistry, University of Pretoria for assistance and inputs with the qualitative Raman spectroscopy work.

- Dr Bruce Anderson, Dr Jonathan Chetty and Dr Llewelyn Damoense of SASOL Technology (Pty) Limited, Research and Development in Sasolburg for availing and assisting with their Raman spectrometer for quantitative work.

- Mr Mpho Lekgoathi from TUT for availing the Department of Chemistry Raman spectrometer for quantitative work.

- Prof Sylvia Paul of the Department of Chemistry at UNISA for inputs regarding the quantitative Raman spectroscopy.

- Dr Sabine Verryn from the Department of Geology for assistance with analysis and interpretation of X-ray diffraction, including high temperature work.

- Mrs Alison Tuling of IMMRI (facilitated at the department of Materials Science and Metallurgical Engineering) for operation and inputs related to the TEM work.

- Dr Nic van der Berg of the department of Physics for issuing and preparing various samples and for inputs regarding the SEM.

- Mr Marko Claassen of the Department of Geology for sample preparation

- Mr Carel Coetzee and Mr Andre Botha of IMMRI and the Microscopy Unit respectively for assistance with the SEM and the high resolution SEM analyses.

- PBMR, NECSA and SANHARP for financial assistance and technical inputs

- The Department of Materials Science and Metallurgical Engineering, University of Pretoria whose staff and laboratory facilities made it possible to complete this study.

UNIVERSITEIT VAN PRETORIA
UNIVERSITY OF PRETORIA
YUNIBESITHI YA PRETORIA

THE DEVELOPMENT OF ANALYTICAL METHODS FOR PBMR TRISO SIC CHARACTERIZATION

Candidate: Noko Ngoepe

Supervisor: Professor Johan P. R. de Villiers

Department: Materials Science and Metallurgical Engineering, University of Pretoria

Degree: Master of Engineering (Metallurgy)

ABSTRACT

This experimental work aims to characterize the SiC layer of various Tri-Structural Isotropic (TRISO) coated fuel particles. In the first part of the work, Raman spectroscopy is used to qualitatively characterize the SiC TRISO layer and to identify the presence of silicon from peak positions. Free silicon poses a significant threat to the integrity of the SiC layer because it melts at 1414°C, significantly lower than the maximum operating temperature of 1550°C. Crystalline silicon is characterized with qualitative Raman spectroscopy by a 520 cm^{-1} peak. Silicon is found to be preferentially concentrated along the SiC layer close to the inner pyrolytic carbon (IPyC) layer. Samples that were only mounted and polished are compared with those that have in addition also been etched. Disordering of the crystals and peak splitting necessitated the use of peak de-convolution. The 3C, 6H and 15R polytypes of SiC were identified.

The second part of the Raman spectroscopy work involves the development of calibration curves using peak areas from known binary mixtures (5%, 25%, 50% and 75% Si) to quantify the amount of silicon found relative to SiC. Initially the SiC polytypes used in these mixtures are 3C, 4H and 6H. Reasonably good logarithmic calibration fits were obtained with R^2 values of 0.996, 0.966 and 0.988 respectively. However some error accompanied the calibration values and an average of ten analyses yielded a more reliable

average. The calibration curve results made it possible to estimate the silicon content throughout the SiC layer for each sample, when combining the results of the qualitative and quantitative Raman spectroscopic study. Samples PO6 and PO8 revealed high peaks of crystalline silicon. When peak areas were quantified and related to the 3C calibration curve, as much as 60% silicon was calculated for both samples. Etching was found to slightly lower the silicon to SiC ratio. The calibration accuracy for the binary mixtures was checked by plotting calculated values against weighed-off values, yielding 3C, 4H and 6H straight-line fits with R^2 values of 0.983, 0.941 and 0.981 respectively. These binary mixtures were analyzed with the SEM, which revealed variable particle size and segregation of silicon and SiC. Quantitative Raman spectroscopy is however known to be affected by a significant number of variables that are difficult to control. Attempts were made to decrease the scatter of the results from the calibration curve to yield more precise results. Two pure samples of silicon and SiC were studied separately, in attempts to better understand particle size and distortion effects. Distortion was found to have a greater impact on the scatter of peak area values than particle size. The scatter associated with pure sample peak areas casts doubt on the accuracy of the binary calibration curves.

Rietveld analysis using X-ray powder diffraction is used to further support the Raman spectroscopy work by qualitatively and quantitatively characterizing the phases involved in each TRISO particle, to a greater degree of accuracy than the Raman spectroscopy. Refinement components include 2H graphite, quartz, SiC (3C, 6H, 8H and 15R), silicon and tetragonal ZrO_2. Oxidized samples were compared with unoxidized samples. The outer pyrolytic carbon (OPyC) layer was oxidized (to improve the accuracy of quantitative measurements). Graphite percentages dominated the refinements with values ranging from 57% to 90% for unoxidized samples and 28% to 83% for oxidized samples. The 3C SiC polytype is the most abundant polytype and constitutes 78% to 83% of the SiC (unoxidized samples) and 82% to 90% (oxidized samples). Trace percentages of silicon were detected for PO6 (0.4%), PO8 (0.6%) and PO10 (0.1%) Quantitative XRD results are known to be accurate to around 1% at the 3σ level. Calibration curves were also subsequently constructed from the same samples as those used for quantitative Raman spectroscopy by comparing the weighed-off values to the measured ones. The 3C,

4H and 6H R^2-fits are 0.991, 0.978 and 0.984 respectively. All the milled samples contained significant α-Fe which contaminated the samples from the grinding process. After dissolving the α-Fe in HCl a sample was tested to check the effect of the α-Fe specifically on microabsorption. Microabsorption was found to be an insignificant effect.

The second part of the XRD work focused on the high-temperature stability of SiC up to 1400°C. Al_2O_3 was used as the standard and the instrument was calibrated using its two independent lattice parameter values along the a-axis and c-axis to make temperature corrections. Temperature corrected curves (of SiC and graphite) were constructed, which superimposed the theoretical Al_2O_3 curve along the a-axis and c-axis. The linear thermal expansion coefficients of SiC and graphite could then be determined from corrected lattice parameter values. The thermal expansion coefficients of G102 SiC had similar values to the literature values up to 800°C. Thereafter the experimental values had significantly higher thermal expansivity when compared to literature values. PO4 and PO9 thermal expansion coefficient values were higher below 500°C, but much closer as temperatures approached 1400°C. There was little correlation between G102, PO4 and PO9 graphite c-axis thermal expansion coefficient curves and literature values.

The third section of the work involves the characterization of the SiC layers of three of the samples by transmission electron microscopy using their selected area electron diffraction patterns. This facilitates the unequivocal characterization of the SiC polytypes. The 3C and 6H polytypes were identified. There is substantial disorder in the crystals. Planar defects of differing periodicity are seen along the [111] direction of the 3C polytype.

Keywords: SiC, silicon, characterization, Raman spectroscopy, X-ray powder diffraction, electron diffraction

DECLARATION

I hereby declare that this thesis is my own work and that I have not incorporated the work forming its basis in any thesis submitted for another degree.

____

Noko N Ngoepe

02 June 2009

TABLE OF CONTENTS

1. INTRODUCTION **15**

2. LITERATURE REVIEW **17**

2.1. TRISO PARTICLE PROPERTIES 17
2.2. SILICON CARBIDE – BASIC BACKGROUND 18
2.3. POLYTYPISM OF SIC 20
2.3.1. Cubic 3C/(∞), β-SiC polytype *22*
2.3.2. Hexagonal 2H/(11), α-SiC polytype *23*
2.3.3. Higher order α -SiC polytypes (unit cells larger than 3C) *23*
2.3.4. Factors influencing polytypism *23*
2.4. RAMAN THEORY 24
2.4.1. The Raman effect *24*
2.4.2. Theoretical overview *26*
2.4.3. Raman Spectroscopy of condensed phases *32*
2.4.4. Quantitative Raman spectroscopy *35*
2.4.5. Raman properties of SiC *38*
2.5. X-RAY POWDER DIFFRACTION 42
2.5.1. General background *42*
2.5.2. Rietveld method *45*
2.5.3. Characterization of SiC by XRD *47*
2.6. HIGH TEMPERATURE XRD - THERMAL EXPANSION 48
2.6.1. Factors influencing cell parameters *48*
2.6.2. Thermal expansion properties of Al_2O_3 ..... *48*
2.6.3. Thermal expansion properties SiC polytypes *49*
2.6.4. The thermal expansion of graphite *53*
2.7. TRANSMISSION ELECTRON MICROSCOPY 56
2.7.1. Conventional transmission electron microscopes *56*
2.7.2. Limitations of the TEM *59*
2.7.3. Electron Diffraction *61*
2.7.4. The reciprocal lattice *62*

3. OBJECTIVES AND HYPOTHESIS **65**

3.1. OBJECTIVES AND OUTCOMES 65
3.2. HYPOTHESIS 65

4. EXPERIMENTAL PROCEDURE **66**

4.1. RAMAN SPECTROSCOPY 66
4.1.1. Samples and labeling *66*
4.1.2. Calibration *66*
4.1.3. Qualitative analysis *69*
4.1.4. Quantitative analysis (calibration curve) *72*
4.1.5. Improved calibration curve *74*
4.2. X-RAY DIFFRACTION 75
4.2.1. Analysis of experimental samples from PBMR *75*
4.2.2. Quantitative analysis (calibration curve) *76*
4.2.3. XRD analysis of sample with removed α-Fe *77*
4.2.4. High temperature XRD *78*
4.3. TEM EXPERIMENTAL PROCEDURE 79

5. RESULTS AND DISCUSSION **80**

5.1. QUALITATIVE RAMAN SPECTROSCOPY 80

5.1.1. Characterization of PO samples ... 80
5.1.2. Silicon to Silicon Carbide ratios of PO samples ... 93
5.1.3. Silicon Carbide Peak Width Half Maximum measurements ... 94
5.1.4. The Silicon to Silicon carbide ratio along the SiC layer cross-section ... 96
5.2. QUANTITATIVE RAMAN SPECTROSCOPY ... 98
5.2.1. Calibration curves ... 98
5.2.2. Quantitative silicon distribution ... 105
5.2.3. Error Analysis ... 106
5.2.4. Scanning electron microscopy analysis ... 106
5.2.5. Particle size and distortion effects ... 108
5.2.6. Quantitative Raman Spectroscopy discussion ... 120
5.3. QUANTITATIVE X-RAY DIFFRACTION CHARACTERIZATION ... 122
5.3.1. As-received (normal) samples ... 122
5.3.2. Oxidized samples ... 124
5.3.3. Calibration curve ... 127
5.4. HIGH TEMPERATURE XRD THERMAL EXPANSION OF SIC AND GRAPHITE ... 128
5.4.1. Experimental results ... 129
5.4.2. Corrected Curves ... 132
5.4.3. Thermal expansion coefficients of SiC ... 140
5.5. TRANSMISSION ELECTRON MICROSCOPY ... 143
5.5.1. Polytype characterization ... 143
5.5.2. Disorder and twinning ... 151

6. CONCLUSIONS & RECOMMENDATIONS ... 154

6.1. RAMAN SPECTROSCOPY ... 154
6.1.1. Qualitative Raman spectroscopy ... 154
6.1.2. Quantitative Raman spectroscopy ... 155
6.2. X-RAY POWDER DIFFRACTION ... 157
6.2.1. Analysis of PO samples ... 157
6.2.2. High temperature XRD ... 157
6.3. TRANSMISSION ELECTRON MICROSCOPY ... 158

7. REFERENCES ... 160

LIST OF FIGURES

FIGURE 2.1 – SCHEMATIC DIAGRAM OF TRISO PARTICLES AND THE RESPECTIVE LAYER THICKNESSES. 17
FIGURE 2.2 – THE SI-C BINARY PHASE DIAGRAM SYSTEM AT P ≤ 1 BAR. THE DOTTED LINE, SQUARE AND DIAMOND SCATTER POINTS ALL SHOW DATA AVAILABLE FROM LITERATURE. 18
FIGURE 2.3 – SILICON CARBIDE POLYTYPE STRUCTURES. POLYTYPES OF SIC ARE FORMED BY PERIODIC STACKING SEQUENCES OF BILAYERS THAT PRODUCE TETRAHEDRAL SHEETS. ATOMIC MODELS OF THE SIX UNIQUE (FUNDAMENTAL) BILAYERS (*BA, CA, AB, CB, AC*, AND *BC)* OF SIC (TOP LEFT) BASED ON THREE PRINCIPAL CLOSE PACKED PLANES (*A, B,* AND *C*) (LOWER LEFT) ARE SHOWN. BLUE ATOMS REPRESENT C AND ORANGE ATOMS REPRESENT SI. THE TWO BASIC STACKING ARRANGEMENTS, *A-B* AND *A-C* THAT FORM PLANES OF VERTEX-SHARING PARALLEL AND ANTIPARALLEL TETRAHEDRA, RESPECTIVELY, ARE SHOWN (LOWER LEFT). ATOMIC MODELS OF THE FOUR SIMPLEST, 3C/(∞), 2H/(11), 4H/(22), AND 6H/(33), POLYTYPES ARE SHOWN SUPERIMPOSED ON CALCULATED HR-TEM LATTICE IMAGES PRODUCED USING DEFOCUS CONDITIONS THAT REPRODUCE THE SYMMETRY OF THE PROJECTED LATTICE (CENTER COLUMN). SCHEMATIC ILLUSTRATIONS OF DIFFRACTION PATTERNS (INCLUDING FORBIDDEN REFLECTIONS IN SOME CASES) ARE ALSO SHOWN (RIGHT COLUMN). 21
FIGURE 2.4 – ENERGY LEVEL DIAGRAM, ILLUSTRATING THE FUNDAMENTAL PROCESSES OF RAMAN SCATTERING, ADAPTED FROM GRASSELLI ET AL, (1981) 25
FIGURE 2.5 – POLARIZATION (P) INDUCED IN A MOLECULE'S ELECTRON CLOUD INDUCED BY AN OPTIC ELECTRIC FIELD E, SHOWN FOR 90° AND 180° GEOMETRY. 28
FIGURE 2.6 – THE PRINCIPAL AXIAL COEFFICIENTS OF THERMAL EXPANSION FOR THE 3C, 4H AND 6H SIC POLYTYPES. 50
FIGURE 2.7 – LINEAR THERMAL EXPANSION VERSUS TEMPERATURE RELATION FOR Β-SIC 53
FIGURE 2.8 – THE COEFFICIENT OF THERMAL EXPANSION IN THE A-DIRECTION RESULTS AGAINST TEMPERATURE. 55
FIGURE 2.9 – THE COEFFICIENT OF THERMAL EXPANSION IN THE C-DIRECTION RESULTS AGAINST TEMPERATURE. 56
FIGURE 2.10 – SCHEMATIC RAY PATH FOR A TRANSMISSION ELECTRON MICROSCOPE EQUIPPED FOR ADDITIONAL X-RAY AND ELECTRON ENERGY-LOSS SPECTROSCOPY.. 57
FIGURE 2.11 – RAY DIAGRAM FOR A TRANSMISSION ELECTRON MICROSCOPE IN (A) THE BRIGHT FIELD IMAGING MODE AND (B) THE SELECTED-AREA ELECTRON DIFFRACTION MODE. 59
FIGURE 2.12 – THE GEOMETRIC RELATIONSHIPS BETWEEN THE GEOMETRIC LATTICE VECTORS $\mathbf{a}^*, \mathbf{b}^*$ AND $\mathbf{c}^*$ AND THE REAL LATTICE VECTORS A, B, C. 63
FIGURE 2.13 – THE GEOMETRICAL RELATIONSHIP BETWEEN THE PLANE NORMAL AND G............................. 64
FIGURE 4.1 – INSTRUMENTAL ERROR ANALYSIS OF THE 4H SINGLE CRYSTAL WAFER (COHERENT INNOVA MACHINE). 67
FIGURE 4.2 – SAMPLE ERRORS ANALYSIS OF THE 4H SINGLE CRYSTAL WAFER (COHERENT INNOVA MACHINE). 68
FIGURE 4.3 – SAMPLE HOLDER DESIGN (SIDE VIEW). UNITS ARE IN MILLIMETERS. 70
FIGURE 4.4 – SAMPLE HOLDER DESIGN (TOP VIEW) 70
FIGURE 4.5 – LABELING SYSTEM USED FOR QUALITATIVE MICRO RAMAN SPECTROSCOPY ANALYSES. 71
FIGURE 4.6 – SAMPLE HOLDER DESIGN. MANUFACTURING MATERIAL IS BRASS. UNITS ARE IN MILLIMETERS. 73
FIGURE 4.7 – SAMPLE ARRANGEMENT UPON ANALYSIS WITH THE TEM FOR SAMPLE PO 9. 79
FIGURE 5.1 – OPTICAL MICROSCOPE IMAGES OF PO3 POLISHED COATED PARTICLES. 82
FIGURE 5.2 – RAMAN SPECTRA OF THE SIC LAYER OF A PO3 POLISHED AND ETCHED COATED PARTICLE. A IS THE INNERMOST AND H IS THE OUTERMOST SPOT ALONG THE SIC CROSS-SECTION. THERE SEEMS TO BE A MIXTURE OF AMORPHOUS AND CRYSTALLINE SILICON THROUGHOUT THE ANALYSES. THE MOST INTENSE CRYSTALLINE SILICON PEAKS OCCUR IN THE MIDDLE OF THE SIC LAYER (ANALYSIS C TO E) PEAK SPLITTING IS CLEARLY EVIDENT, INDICATING THAT THE 3C POLYTYPE IS NOT THE ONLY ONE THAT IS PRESENT. 82

FIGURE 5.3 – RAMAN SPECTRA OF THE TO SIC PEAKS AFTER DECONVOLUTION FOR ANALYSIS 3A (ETCHED). IT WAS ASSUMED THAT THERE WERE THREE COMPONENTS MAKING UP THE MAIN PEAK. THE PEAKS INDICATE THE PRESENCE OF THE 3C, 6H AND 15R POLYTYPES. 83
FIGURE 5.4 – RAMAN SPECTRA OF THE SIC COATING OF PO3 POLISHED (UNETCHED) COATED PARTICLE. A IS THE INNERMOST AND K IS THE OUTERMOST SPOT ALONG THE SIC CROSS-SECTION. THERE SEEMS TO BE PREDOMINANTLY AMORPHOUS SILICON, WITH SMALL CRYSTALLINE SILICON PEAKS EVIDENT FOR SOME ANALYSES. PEAK SPLITTING IS CLEARLY EVIDENT, INDICATING THAT THE 3C POLYTYPE IS NOT THE ONLY ONE THAT IS STABLE. THERE IS NO EVIDENCE OF GRAPHITE. 84
FIGURE 5.5 – RAMAN SPECTRA OF THE TO SIC PEAKS AFTER DECONVOLUTION FOR ANALYSIS 3A (POLISHED). IT WAS ASSUMED THAT THERE WERE THREE COMPONENTS MAKING UP THE MAIN PEAK. THE PEAKS INDICATE THE PRESENCE OF THE 3C AND 6H POLYTYPES. 85
FIGURE 5.6 – OPTICAL MICROSCOPE IMAGES OF PO5 POLISHED COATED PARTICLES. 86
FIGURE 5.7 – RAMAN SPECTRA OF THE SIC COATING OF PO5 ETCHED AND POLISHED COATED PARTICLE. A IS THE INNERMOST AND K IS THE OUTERMOST SPOT ALONG THE SIC CROSS-SECTION. NEITHER THE AMORPHOUS NOR CRYSTALLINE SILICON IS SEEN THROUGHOUT THE SIC LAYER. THE SIC PEAKS DO NOT SPLIT, HOWEVER PEAK DECONVOLUTION INDICATES THE PRESENCE OF A RELATIVELY SMALL 6H PEAK. 86
FIGURE 5.8 – RAMAN SPECTRA OF THE TO SIC PEAKS AFTER DECONVOLUTION FOR ANALYSIS 5A (ETCHED). IT WAS ASSUMED THAT THERE WERE TWO COMPONENTS MAKING UP THE MAIN PEAK. THE PEAKS INDICATE THE PRESENCE OF THE 3C AND 6H POLYTYPES. 87
FIGURE 5.9 – RAMAN SPECTRA OF THE SIC COATING OF PO5 POLISHED (UNETCHED) COATED PARTICLE. A IS THE INNERMOST AND I IS THE OUTERMOST SPOT ALONG THE SIC CROSS-SECTION. NEITHER THE AMORPHOUS NOR CRYSTALLINE SILICON IS SEEN THROUGHOUT THE SIC LAYER. THE SIC PEAKS DO NOT SPLIT, HOWEVER PEAK DECONVOLUTION INDICATES THE PRESENCE OF A RELATIVELY SMALL 6H PEAK. GRAPHITE IS ONLY SEEN AT ANALYSIS I AT 1360 CM^{-1}. 88
FIGURE 5.10 – RAMAN SPECTRA OF THE TO SIC PEAKS AFTER DECONVOLUTION FOR ANALYSIS 5A (POLISHED). IT WAS ASSUMED THAT THERE WERE TWO COMPONENTS MAKING UP THE MAIN PEAK. THE PEAKS INDICATE THE PRESENCE OF THE 3C AND 6H POLYTYPES. 89
FIGURE 5.11 – OPTICAL MICROSCOPE IMAGES OF PO6 POLISHED COATED PARTICLES. 90
FIGURE 5.12 – RAMAN SPECTRA OF THE SIC COATING OF PO6 POLISHED AND ETCHED COATED PARTICLE. A IS THE INNERMOST AND H IS THE OUTERMOST SPOT ALONG THE SIC CROSS-SECTION. THE CRYSTALLINE SILICON PROGRESSIVELY INCREASES FROM ANALYSIS A TO C BEFORE DECLINING AGAIN. THE SILICON TO SIC RATIO OF PEAKS IS PARTICULARLY HIGH RELATIVE TO THAT OF OTHER SAMPLES. CONSEQUENTLY, THERE IS VERY LITTLE THAT CAN BE SAID ABOUT THE SIC PEAKS. THERE IS A HINT OF GRAPHITE DETECTED FROM THE SLIGHT CHANGE OF SLOPE FROM ANALYSIS B. 90
FIGURE 5.13 – RAMAN SPECTRA OF THE TO SIC PEAKS AFTER DECONVOLUTION FOR ANALYSIS 6A (ETCHED). IT WAS ASSUMED THAT THERE WERE TWO COMPONENTS MAKING UP THE MAIN PEAK. THE PEAKS INDICATE THE PRESENCE OF THE 3C AND 6H POLYTYPES. 91
FIGURE 5.14 – RAMAN SPECTRA OF THE SIC COATING OF PO6 POLISHED COATED PARTICLE. A IS THE INNERMOST AND I IS THE OUTERMOST SPOT ALONG THE SIC CROSS-SECTION. THE CRYSTALLINE SILICON INCREASES FROM ANALYSIS A TO B BEFORE PROGRESSIVELY DECLINING UP TO ANALYSIS I. THE SILICON TO SIC RATIO OF SOME PEAKS IS PARTICULARLY HIGH RELATIVE TO THAT OF OTHER SAMPLES. THERE IS NO EVIDENCE OF GRAPHITE. 92
FIGURE 5.15 – RAMAN SPECTRA OF THE TO SIC PEAKS AFTER DECONVOLUTION FOR ANALYSIS 6A (POLISHED). IT WAS ASSUMED THAT THERE WERE TWO COMPONENTS MAKING UP THE MAIN PEAK. THE PEAKS INDICATE THE PRESENCE OF THE 3C AND 6H POLYTYPES. 93
FIGURE 5.16 – MEAN VALUES OF THE RATIO OF THE CRYSTALLINE SILICON PEAK TO THE DOMINANT TRANSVERSE OPTIC MODE SIC PEAK FOR BOTH ETCHED AND UNETCHED SAMPLES. SAMPLES PO6 AND PO8 CLEARLY HAVE HIGH FREE SILICON CONTENTS IN THE SIC LAYER. 94
FIGURE 5.17 – MEAN VALUES OF THE PEAK WIDTH HALF MAXIMUM OF THE TRANSVERSE OPTIC MODE SIC PEAK. THERE IS SIGNIFICANT DIFFERENCE IN THE PEAK WIDTH VALUES, WITH THE BIGGEST BEING SAMPLE PO3 AND PO5. 95
FIGURE 5.18 – STANDARD DEVIATION VALUES OF THE PEAK WIDTH HALF MAXIMUM OF THE TRANSVERSE OPTIC MODE SIC PEAK 95
FIGURE 5.19 – THE SILICON TO SIC RATIO ALONG THE CROSS-SECTION OF THE ETCHED TO SIC LAYER, WHERE A DENOTES THE INNERMOST PART OF THE SIC AND J THE OUTERMOST. SAMPLES PO6 AND PO8

POSSIBLY HAVE UNACCEPTABLY HIGH FREE SILICON CONTENTS IN THE SIC LAYER. THE GENERAL TREND IS THAT THE SILICON IS MAINLY CONCENTRATED ALONG THE INNER PARTS OF THE SIC LAYERS. 96
FIGURE 5.20 – THE SILICON TO SIC RATIO ALONG THE CROSS-SECTION OF THE (UNETCHED) POLISHED TO SIC LAYER, WHERE A DENOTES THE INNERMOST PART OF THE SIC AND K THE OUTERMOST. ONCE MORE, SAMPLES PO6 AND PO8 HAVE UNACCEPTABLY HIGH FREE SILICON CONTENTS IN THE SIC LAYER. THE GENERAL TREND IS THAT THE SILICON IS MAINLY CONCENTRATED ALONG THE INNER PARTS OF THE SIC LAYERS. 97
FIGURE 5.21 – RAMAN CALIBRATION CURVE OF THE 3C POLYTYPE 99
FIGURE 5.22 – CALIBRATION CHECK OF THE 3C POLYTYPE 100
FIGURE 5.23 – RAMAN CALIBRATION CURVE OF THE 4H POLYTYPE 101
FIGURE 5.24 – CALIBRATION CHECK OF THE 4H POLYTYPE 102
FIGURE 5.25 – RAMAN CALIBRATION CURVE OF THE 6H POLYTYPE 103
FIGURE 5.26 – CALIBRATION CHECK OF THE 6H POLYTYPE 104
FIGURE 5.27 – PLOT OF THE INDIVIDUAL POINTS OF THE CALIBRATION CURVE, ILLUSTRATING THE SCATTER. 104
FIGURE 5.28 – QUANTITATIVE LINE PROFILE OF THE FRACTION OF SILICON ALONG THE SIC CROSS-SECTION 105
FIGURE 5.29 – PLOT OF RELATIVE RAMAN SPECTROSCOPY INTENSITIES FROM THE FIVE 50%SI-50%3C SIC MIXTURES. 106
FIGURE 5.30 – BACKSCATTERED SEM IMAGES OF MIXTURE OF TWO RAMAN SPECTROSCOPY QUANTITATIVE SAMPLES. THE SAMPLE ON THE LEFT (3C SIC- 50% SILICON) CONTAINS A-FE AFTER GRINDING, WHILE THE A-FE OF THE SAMPLE ON THE RIGHT HAS BEEN DISSOLVED (4H SIC- 50% SILICON). 107
FIGURE 5.31 – BACKSCATTERED SEM IMAGE OF THE SIC LAYER OF SAMPLE PO10 108
FIGURE 5.32 – THE PARTICLE SIZE DISTRIBUTION CURVE OF AMERICAN ELEMENT' SILICON POWDER 109
FIGURE 5.33 – THE PARTICLE SIZE DISTRIBUTION BY SIZE FRACTION BINS, OF AMERICAN ELEMENTS' SILICON POWDER. 110
FIGURE 5.34 – THE PARTICLE SIZE DISTRIBUTION CURVE OF AMERICAN ELEMENT' SIC POWDER 110
FIGURE 5.35 – THE PARTICLE SIZE DISTRIBUTION BY SIZE FRACTION BINS, OF AMERICAN ELEMENTS' SIC POWDER. 111
FIGURE 5.36 – RAMAN SPECTROSCOPY ANALYSIS OF SILICON PARTICLES SIZES: (A) >38 MICRONS, (B) 10-38 MICRONS AND (C) <10 MICRONS. THE Y-AXIS IS THE INTENSITY IN ARBITRARY UNITS, WHILE THE X-AXIS IS THE WAVENUMBER IN CM^{-1}. 113
FIGURE 5.37 – RAMAN SPECTROSCOPY ANALYSIS OF SIC PARTICLES SIZES: (A) >38 MICRONS, (B) 10-38 MICRONS AND (C) <10 MICRONS. THE Y-AXIS IS THE INTENSITY IN ARBITRARY UNITS, WHILE THE X-AXIS IS THE WAVENUMBER IN CM^{-1}. 115
FIGURE 5.38 – RAMAN SPECTROSCOPY ANALYSIS OF SILICON PARTICLES ANNEALED FOR: (A) 2 HOURS, (B) 4 HOURS AND (C) 8 HOURS. THE Y-AXIS IS THE INTENSITY IN ARBITRARY UNITS, WHILE THE X-AXIS IS THE WAVENUMBER IN CM^{-1}. 117
FIGURE 5.39 – RAMAN SPECTROSCOPY ANALYSIS OF SIC PARTICLES ANNEALED FOR: (A) 2 HOURS (B) 4 HOURS AND (C) 8 HOURS. THE Y-AXIS IS THE INTENSITY IN ARBITRARY UNITS, WHILE THE X-AXIS IS THE WAVENUMBER IN CM^{-1}. 119
FIGURE 5.40 – QUANTITATIVE ANALYSIS OF PO SAMPLES BY X-RAY DIFFRACTION WITH ALL LAYERS INTACT. GRAPHITE IS BY FAR THE MOST ABUNDANT PHASE. 123
FIGURE 5.41 – QUANTITATIVE ANALYSIS OF PO SAMPLES IN THE NORMAL (AS RECEIVED) CONDITION CONSIDERING ONLY THE SIC POLYTYPES, NORMALIZED TO 100%. THE 3C POLYTYPE IS BY FAR THE MOST ABUNDANT RANGING FROM 78% TO 83%. 124
FIGURE 5.42 – QUANTITATIVE ANALYSIS OF PO SAMPLES BY X-RAY DIFFRACTION, WITH THE SAMPLES OXIDIZED AT $850^{o}C$. EVEN AFTER OXIDIZING THE OPYC LAYER, GRAPHITE IS STILL THE MOST ABUNDANT PHASE. 125
FIGURE 5.43 – QUANTITATIVE ANALYSIS OF PO SAMPLES IN THE OXIDIZED CONDITION CONSIDERING ONLY THE SIC POLYTYPES, NORMALIZED TO 100%. THE 3C POLYTYPE IS BY FAR THE MOST ABUNDANT RANGING FROM 82% TO 90% 126
FIGURE 5.44 – THE XRD CALIBRATION CURVE RELATING THE MASS FRACTION OF SILICON DETERMINED BY AUTOQUAN VERSUS THE WEIGHED OFF MASS FRACTION OF SILICON. THE BINARY MIXTURES ARE OF SILICON AND THE 3C, 4H AND 6H POLYTYPES OF SIC. 128

FIGURE 5.45 – PLOTS OF THE UNCORRECTED EXPERIMENTAL A-AXES LATTICE PARAMETERS VERSUS TEMPERATURE OF AL_2O_3 FOR G102, PO4 AND PO9, COMPARED WITH THE THEORETICAL AL_2O_3 A-AXIS LATTICE PARAMETER. A MOLYBDENUM HEATING STRIP WAS USED FOR G102 WHEREAS PO4 AND PO9 WERE ANALYZED USING A GRAPHITE HEATING STRIP. 129
FIGURE 5.46 – PLOTS OF THE EXPERIMENTAL A-AXES LATTICE PARAMETERS VERSUS TEMPERATURE OF AL_2O_3 FOR G102, PO4 AND PO9, COMPARED WITH THE THEORETICAL AL_2O_3 C-AXIS LATTICE PARAMETER. A MOLYBDENUM HEATING STRIP WAS USED FOR G102 AND A GRAPHITE STRIP FOR PO4 AND PO9........ 131
FIGURE 5.47 – PLOT OF EXPERIMENTAL THE A-AXIS LATTICE PARAMETER FOR SIC........ 132
FIGURE 5.48 – PLOT OF THE EXPERIMENTAL A-AXIS LATTICE PARAMETER AT CORRECTED TEMPERATURES FOR AL_2O_3, SUPERIMPOSED ON THE THEORETICAL CURVE. 133
FIGURE 5.49 – PLOT OF THE CORRECTED C-AXIS LATTICE PARAMETER AT CORRECTED TEMPERATURES FOR AL_2O_3. 134
FIGURE 5.50 – PLOT OF EXPERIMENTAL THE A-AXIS LATTICE PARAMETER FOR G102, PO4 AND PO9 SIC, UPON HEATING UP AND COOLING DOWN (THE CORRECTION IS BASED ON A-AXIS VALUES OF AL_2O_3). THERE IS VERY GOOD CORRESPONDENCE WITH THE DATA BY LI ET AL. [72]. 135
FIGURE 5.51 – PLOT OF EXPERIMENTAL THE A-AXIS LATTICE PARAMETER FOR G102, PO4 AND PO9 SIC, UPON HEATING UP AND COOLING DOWN (THE CORRECTION IS BASED ON C-AXIS VALUES OF AL_2O_3). 136
FIGURE 5.52 – THE BEST FIT A-AXIS SIC LATTICE PARAMETER FITS FOR G102, PO4 AND PO9 BASED ON THE A-AXIS AND C-AXIS TEMPERATURE CORRECTED VALUES. THERE IS GENERALLY A GOOD CORRELATION BETWEEN THE A-AXIS AND C-AXIS BASED CORRECTION DATA. 137
FIGURE 5.53 – PLOT OF EXPERIMENTAL THE C-AXIS LATTICE PARAMETER FOR G102, PO4 AND PO9 GRAPHITE UPON HEATING UP AND COOLING DOWN (THE CORRECTION IS BASED ON A-AXIS VALUES OF AL_2O_3). 138
FIGURE 5.54 – PLOT OF EXPERIMENTAL THE C-AXIS LATTICE PARAMETER FOR G102, PO4 AND PO9 GRAPHITE UPON HEATING UP AND COOLING DOWN (THE CORRECTION IS BASED ON C-AXIS VALUES OF AL_2O_3). 140
FIGURE 5.55 – PLOT OF THE A-AXIS SIC THERMAL EXPANSION COEFFICIENTS OF THE TRISO SAMPLES. 141
FIGURE 5.56 – BEST FIT PLOT OF THE A-AXIS SIC THERMAL EXPANSION COEFFICIENTS OF THE TRISO SAMPLES. 142
FIGURE 5.57 – BRIGHT FIELD IMAGE OF PO5 IMAGE 5 (FROM THE APPENDIX C), ALONG WITH ITS DIFFRACTION PATTERNS. THE TWO ORDERED DIFFRACTION PATTERNS REPRESENT THE 3C [100] AND 3C [111] ZONE AXES OF THE SAME TWINNED CRYSTAL. THE CENTRAL DIRECT BEAM DIFFRACTION SPOT IS BLANKED OUT ON THE EXPERIMENTAL DIFFRACTION PATTERNS. 144
FIGURE 5.58 – BRIGHT FIELD IMAGE OF PO5 IMAGE 4 (FROM THE APPENDIX C) ALONG WITH ITS DIFFRACTION PATTERN. THE DIFFRACTION PATTERN REPRESENTS THE 3C [111] ZONE AXIS. THE CENTRAL DIRECT BEAM DIFFRACTION SPOT IS BLANKED OUT ON THE EXPERIMENTAL DIFFRACTION PATTERN........ 145
FIGURE 5.59 – BRIGHT FIELD IMAGE OF PO6 IMAGE 7 (FROM THE APPENDIX C) ALONG WITH ITS DIFFRACTION PATTERN. THE DISORDERED DIFFRACTION PATTERNS REPRESENTS THE 3C [111] ZONE AXIS. THE CENTRAL DIRECT BEAM DIFFRACTION SPOT IS BLANKED OUT ON THE EXPERIMENTAL DIFFRACTION PATTERNS. 146
FIGURE 5.60 – BRIGHT FIELD IMAGE OF PO6 IMAGE 8 (FROM THE APPENDIX C) ALONG WITH ITS DIFFRACTION PATTERN. THE TWO ORDERED DIFFRACTION PATTERNS REPRESENT THE 3C [211] AND 3C [110] ZONE AXES OF THE SAME CRYSTAL. THE CENTRAL DIRECT BEAM DIFFRACTION SPOT IS BLANKED OUT ON THE EXPERIMENTAL DIFFRACTION PATTERNS. 147
FIGURE 5.61 – BRIGHT FIELD IMAGE OF PO 9 CRYSTAL 16 (FROM THE APPENDIX C) ALONG WITH ITS DIFFRACTION PATTERN. THE DIFFRACTION PATTERN REPRESENTS THE 3C [100] ZONE AXIS. THE CENTRAL DIRECT BEAM DIFFRACTION SPOT IS BLANKED OUT ON THE EXPERIMENTAL DIFFRACTION PATTERN. 149
FIGURE 5.62 – BRIGHT FIELD IMAGE OF PO 9 IMAGE 15 (FROM THE APPENDIX C) ALONG WITH ITS DIFFRACTION PATTERN. THE DIFFRACTION PATTERN REPRESENTS THE 6H [100] OR [110] ZONE AXIS. THE MAGNIFIED IMAGE SHOWS THE VARYING PERIODICITY OF THE STACKING DISORDER. THE CENTRAL DIRECT BEAM DIFFRACTION SPOT IS BLANKED OUT ON THE EXPERIMENTAL DIFFRACTION PATTERN. THE SCALE BAR OF THE LOWER IMAGE IS 20 NM LONG. 150

FIGURE 5.63 – A MAGNIFIED IMAGE OF THE DIFFRACTION PATTERN OF FIGURE 5.59, DEPICTING STREAKING DUE TO STACKING DISORDER EVIDENT BETWEEN THE DIFFRACTION SPOTS. OVERLAPPING CRYSTALS YIELD ADDITIONAL, WEAKER DIFFRACTION SPOTS. 152

LIST OF TABLES

TABLE 2.1 – RAMAN FREQUENCIES OF FUNDAMENTAL SIC POLYTYPES. THE ASTERISK DENOTES THE FOURIER TRANSVERSE ACOUSTIC (FTA) AND FOURIER TRANSVERSE OPTIC (FTO) MODES WITH THE MAXIMUM INTENSITY IN EACH PHONON BRANCH. FLA AND FLO ARE ABBREVIATIONS FOR THE FOURIER LONGITUDINAL ACOUSTIC AND FOURIER LONGITUDINAL OPTIC MODES. Q/Q_B IS THE REDUCED WAVE VECTOR OF THE CORRESPONDING PHONON MODE IN 3C SIC. 39
TABLE 2.2 – THE COEFFICIENTS DESCRIBING THE TEMPERATURE DEPENDENCE OF THE CELL PARAMETER OF AL_2O_3 USING EQUATION 2.24. UNITS ARE IN Å. 49
TABLE 2.3 – THERMAL EXPANSION DATA OF SIC AND PYC. 52
TABLE 2.4 – VARIOUS COEFFICIENTS IN THE EXPRESSION OF α_a 54
TABLE 2.5 – VARIOUS COEFFICIENTS IN THE EXPRESSION OF α_c 56
TABLE 4.1 – SAMPLE LAYER THICKNESSES IN MICRONS. SAMPLE PO7 CONTAINS NO SIC LAYER AND THE SAMPLE WITH THICKEST SIC LAYER IS PO9. 66
TABLE 4.2 – 4H SINGLE CRYSTAL SIC STATISTICAL DATA OF THE INSTRUMENTAL ANALYSIS MEASURED AREA VALUES (COHERENT INNOVA MACHINE), USED FOR QUALITATIVE RAMAN SPECTROSCOPY RESULTS. . 67
TABLE 4.3 – 4H SINGLE CRYSTAL SIC STATISTICAL DATA OF THE MEASURED AREA VALUES OF THE INSTRUMENTAL ANALYSIS (RENISHAW RM 2000 INVIA), USED FOR QUANTITATIVE RAMAN SPECTROSCOPY RESULTS 68
TABLE 4.4 – STATISTICAL DATA OF THE MEASURED AREA VALUES OF THE SAMPLE ANALYSIS (COHERENT INNOVA MACHINE) 69
TABLE 5.1 – SUMMARY OF PEAK POSITIONS IDENTIFIED WITH QUALITATIVE RAMAN SPECTROSCOPY (UNITS ARE IN WAVENUMBERS; CM^{-1}). *, ** AND *** DENOTE A LOW, HIGH AND VERY HIGH CRYSTALLINE SILICON PEAK. X INDICATES THE ABSENCE OF A PEAK. 81
TABLE 5.2 – SETTLING RATES OF SILICON AND SIC PARTICLES ACCORDING TO STOKES' LAW FOR 38, 10 AND 1 MICRON PARTICLE SIZES 112
TABLE 5.3 – THE INDIVIDUAL PEAK AREA VALUES SHOWING VARIATIONS FOR >38 MICRONS, 10-38 MICRONS AND <10 MICRONS SILICON PARTICLE SIZES. 112
TABLE 5.4 – THE INDIVIDUAL PEAK AREA VALUES SHOWING VARIATIONS FOR >38 MICRONS, 10-38 MICRONS AND <10 MICRONS SIC PARTICLE SIZES. 114
TABLE 5.5 – THE INDIVIDUAL PEAK AREA VALUES SHOWING VARIATIONS FOR 2 HOURS, 4 HOURS AND 8 HOURS ANNEALING OF SILICON. 116
TABLE 5.6 – THE INDIVIDUAL PEAK AREA VALUES SHOWING VARIATIONS FOR 2 HOURS, 4 HOURS AND 8 HOURS ANNEALING OF SILICON. 118
TABLE 5.7 – A SUMMARY OF THE AUTOQUAN REFINEMENTS, COMPARING THE ORIGINAL AND OXIDIZED SAMPLES. THE 3C POLYTYPE IS THE SIGNIFICANTLY THE MOST ABUNDANT SIC POLYTYPE. SAMPLE PO7 CONTAINS NO SIC LAYER AND HAS FOR THIS REASON BEEN EXCLUDED. 127
TABLE 5.8 – SUMMARY OF THE INTERPRETED DIFFRACTION PATTERNS OF PO5 INCLUDED IN THE APPENDIX SECTION, SHOWING THAT THE 3C POLYTYPE IS THE MOST COMMONLY OCCURRING. 143
TABLE 5.9 – SUMMARY OF THE INTERPRETED DIFFRACTION PATTERNS OF PO6 INCLUDED IN THE APPENDIX SECTION. THE 3C POLYTYPE IS THE MOST COMMONLY OCCURRING POLYTYPE OF SIC. 146
TABLE 5.10 – SUMMARY OF THE INTERPRETED DIFFRACTION PATTERNS OF PO9 INCLUDED IN THE APPENDIX SECTION. THE 3C POLYTYPE IS ONCE MORE DOMINANT, AND 6H IS THE ONLY OTHER POLYTYPE THAT WAS DETECTED. 148

1. INTRODUCTION

The Pebble bed modular reactor (PBMR) is a helium-cooled, graphite-moderated high temperature reactor (HTR). The PBMR will consist of a vertical steel reactor pressure vessel with a 6.2 m inner diameter and about 27 m high. To remove the heat generated by the nuclear reaction, helium coolant enters the reactor vessel at a temperature of about 500°C and at a pressure of 9 MPa. It then flows down between the hot fuel spheres, after which it leaves the bottom of the vessel, having been heated to a temperature of about 900 °C. The heated gas directly drives a power -turbine-compressor mounted on a single shaft. This shaft is coupled to a generator through a speed reduction gearbox. The coolant exits the power turbine at about 500°C and at a pressure of about 3 MPa. It then passes through a high efficiency recuperator. After the recuperator the gas is cooled and recompressed in two stages after which it returns to the reactor core after being reheated to 500°C in the secondary side of the recuperator[1].

PBMR fuel is based on a proven, high-quality German fuel design consisting of low enriched uranium triple-coated isotropic (LEU -TRISO) particles contained in a moulded graphite sphere[1]. A coated particle comprises of a kernel of uranium dioxide surrounded by four coating layers: the porous carbon layer, inner pyrolytic carbon layer, silicon carbide layer and the outer pyrolytic carbon layer (which form the so-called tri-structural isotropic particle (TRISO))[2]. In the coated particle fabrication process, a solution of uranyl nitrate is sprayed to form micro-spheres, which are then gelled and calcined to produce uranium dioxide fuel "kernels". The kernels are then run through a chemical vapour deposition (CVD) furnace (typically using a gaseous environment at a temperature of 1 000 ºC) in which layers of specific composition can be added with extreme precision[3].

This study aims to compare experimental SiC TRISO particles from different batches that were produced under various conditions in the CVD coater. This serves the purpose of comparing the experimental PBMR particles with others known to have superior properties. All batches were produced by PBMR. The kernels used are ZrO_2 and not

radioactive UO_2. This comparison is done by making use of different analytical methods, each with its own strengths and limitations.

The SiC layer plays a key role in the TRISO particle coating layer because it provides mechanical strength for the particle and acts as a barrier to diffusion of metallic and gaseous fission products. Since there are in excess of 200 SiC polytypes to date[4], the characterization of SiC polytypes is particularly challenging. However it has been shown that the most commonly occurring polytypes of SiC (namely 3C, 2H, 4H, 6H, 8H and 15R) can be characterized by Raman spectroscopy[5] and the Rietveld method of X-ray diffraction[6]. The most definitive means of SiC polytype characterization however is with transmission electron microscopy and selected area electron diffraction. There are however few studies that focus specifically on the SiC layer of TRISO particles.

From communication with PBMR, it has been established that the SiC prepared by chemical vapour deposition has the following general properties[7]:

- As the main retention layer the SiC is rather brittle in tension but strong in compression
- Methyl trichlorosilane (MTS) is used in coating SiC, where Si and C combine in a 1:1 ratio at an optimum temperature of about 1550°C. A lower temperature leads to a greater proportion of free silicon, while a higher temperature leads to a greater proportion of free carbon
- The size of SiC crystals may play a significant role in the effectiveness of the layer as a barrier

2. LITERATURE REVIEW

2.1. TRISO particle properties

The Tri-structural isotropic (TRISO) coated fuel particles consist of a micro-spherical kernel of uranium oxide or oxycarbide fuel and coating layers. These consist of a porous pyrolytic carbon (PyC) layer, the inner PyC (IPyC) layer, the silicon carbide (SiC) layer, and outer PyC (OPyC) layer. Figure 2.1 illustrates these layers schematically. The function of the coating layers is to retain fission products within the particle[8]. The TRISO layer also functions to withstand the thermo-mechanical stresses generated during burnup[9].

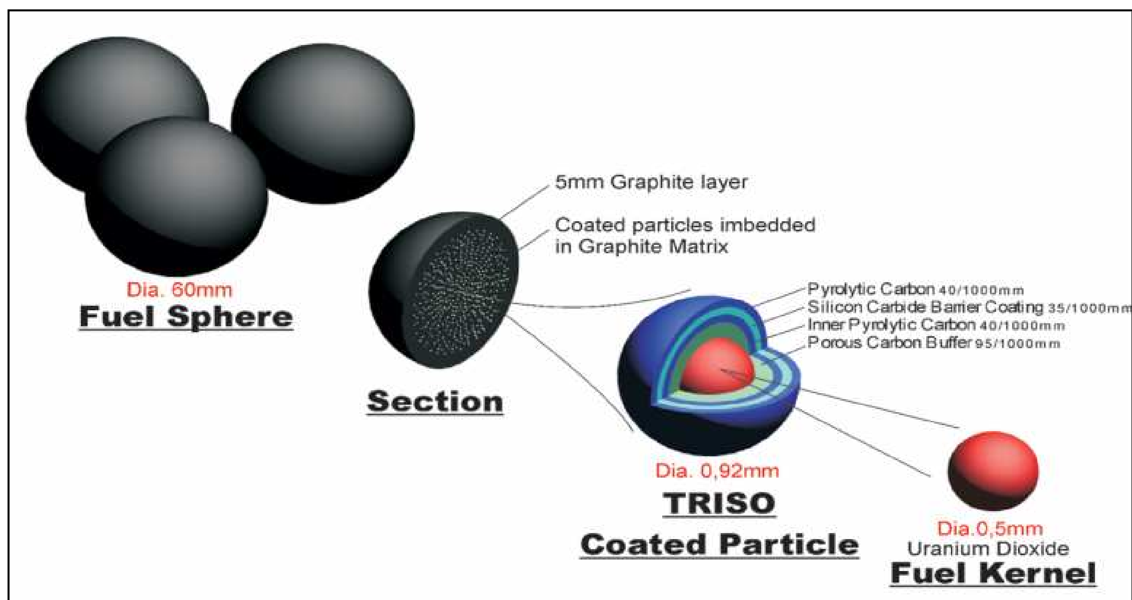

Figure 2.1 – Schematic diagram of TRISO particles and the respective layer thicknesses[10].

The low density porous PyC coating layer is called the buffer layer (about 50% void) and attenuates fission recoils and provides void volume for gaseous fission products including carbon monoxide. It also accommodates kernel swelling without transmitting forces to the outer coatings. The high density, isotropic IPyC coating layer contains the fission

products and carbon monoxide during irradiation, protects the kernel from reactions with chlorine during SiC deposition and provides structural support for the SiC layer. The SiC coating layer provides the mechanical strength to withstand stresses developed due to irradiation-induced dimensional changes in the pyrolytic carbon layer. Secondly, it acts as a barrier to high pressure diffusion of gaseous and metallic fission products generated in the kernel/buffer region, which diffuse easily through the IPyC layer. The function of the high density OPyC layer is to protect the SiC during the remainder of the fabrication process and to provide structural stability to the SiC coating during irradiation[8,11].

The coating layers should ideally be intact before and during irradiation. It is the case in practice that a small fraction of the particles with defective coatings are present in the fabrication batch. A defective SiC layer carries the greatest risk from the point of view of fission product retention. The burn leach test is used to detect defective SiC layers. In this test, particles are heated to 800 to 900°C in air in order to oxidize the OPyC layers. Acid leaching of the exposed uranium follows. The defective SiC layer of coating will then expose uranium upon burning[12].

2.2. Silicon carbide – basic background

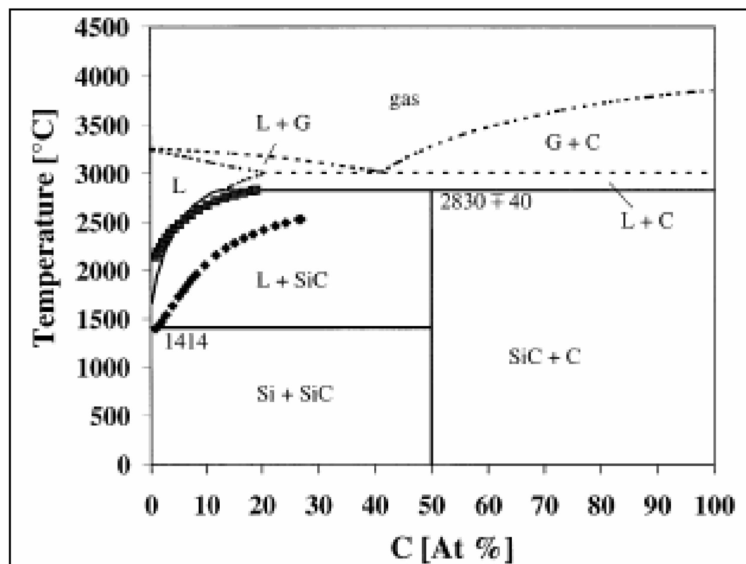

Figure 2.2 – The Si-C binary phase diagram system at p ≤ 1 bar[13]. The dotted line[14], square[15] and diamond[16] scatter points all show data available from literature.

Silicon carbide is the only solid phase binary compound of silicon and carbon under standard conditions. This is confirmed by figure 2.2, which is a binary phase diagram of silicon and carbon. It is evident that the solubility (*X*) of C in liquid Si is low, reaching a maximum value of *X* ~15 mol% (at 2830°C). The solubility ranges from 0.5 to 7 mol% between 1800 and 2300°C [13].

SiC has a very high thermal stability. It is not possible to melt it at atmospheric pressure as it sublimes and dissociates into C and Si-rich vapour. Dissociation and sublimation are appreciable above 2000°C[14]. From pressure experiments the peritectic reaction occurs at 2830 (±40°C)[15]. Under such the solid decomposes into a Si-rich liquid in graphite. As a result silicon carbide has no congruent melting point[17].

It has been reported that the coating temperature is the main variable affecting the content of free silicon and density. At temperature below 1400°C - 1500°C, the free silicon was found to increase with decreasing coating temperature. The density was found to decrease with increasing free silicon content[18].

Silicon carbide is one of the hardest materials, with a Moh's scale hardness of 9 (between diamond (10) and topaz (8)). It also has a high resistance to wear with a value of 9.15 when compared with diamond at 10.00 and corundum at 9.00[19]. The SiC prepared by chemical vapour deposition (CVD) has good mechanical properties and good stability against oxidation[18] . CVD SiC is synthesized using MTS (Methyl Tri-Chlorosilane) according to equation 2.1:

$$CH_3SiCl_3 \rightarrow SiC + 3HCl \qquad (2.1)$$

2.3. Polytypism of SiC

The ability of compounds and elements to occur in more than one crystal structure is termed polymorphism. The one-dimensional variation of this is polytypism. Polytypes differ by the stacking sequence along one direction[17]. Polytypism refers to the occurrence of different stacking sequences in the same material and can reflect a change of physical properties with a change in crystal structure[4]. The physical properties that are observed are strongly dependent on the amounts of the various polytypes[20].

There are in excess of 200 SiC polytypes (one cubic (C), and numerous hexagonal (H) and rhombohedral (R) ones). Of these the most common polytypes are 3C, 4H, 6H and 15R[11]. Silicon carbide exhibits an extensive range of well ordered structures[4,21]. The rhombohedral and hexagonal classes of SiC polytypes are collectively called α-SiC and the cubic class (consisting of one member) is called β-SiC[22].

Polytypes of SiC arise from different periodic stacking sequences of bilayers[23]. This is seen from figure 2.3. There are six different bilayers each consisting of two close packed planes of polytypes described by different stacking sequences of Si-C double layers, perpendicular to the close-packed plane; i.e. [111] for cubic and [0001] for hexagonal[4]. The stacking sequences of the atomic double atomic planes Si-C along the c-direction are different and the polytypes are regarded as natural superlattices[5]. Bilayers stack to form vertex-sharing tetrahedral cages of Si_4C (or SiC_4) with a C (or Si) atom at the center of each cage. The stacking sequence does not significantly alter bond lengths or affect bulk density (3.2 g/cm^3) [24]. With a Si-C bond distance $\delta = 1.89$ Å, bilayers are spaced $4/3\ \delta \approx 2.52$ Å apart. If the number of bilayers in the unit cell is even, the symmetry must be hexagonal; otherwise it is cubic or rhombohedral[4].

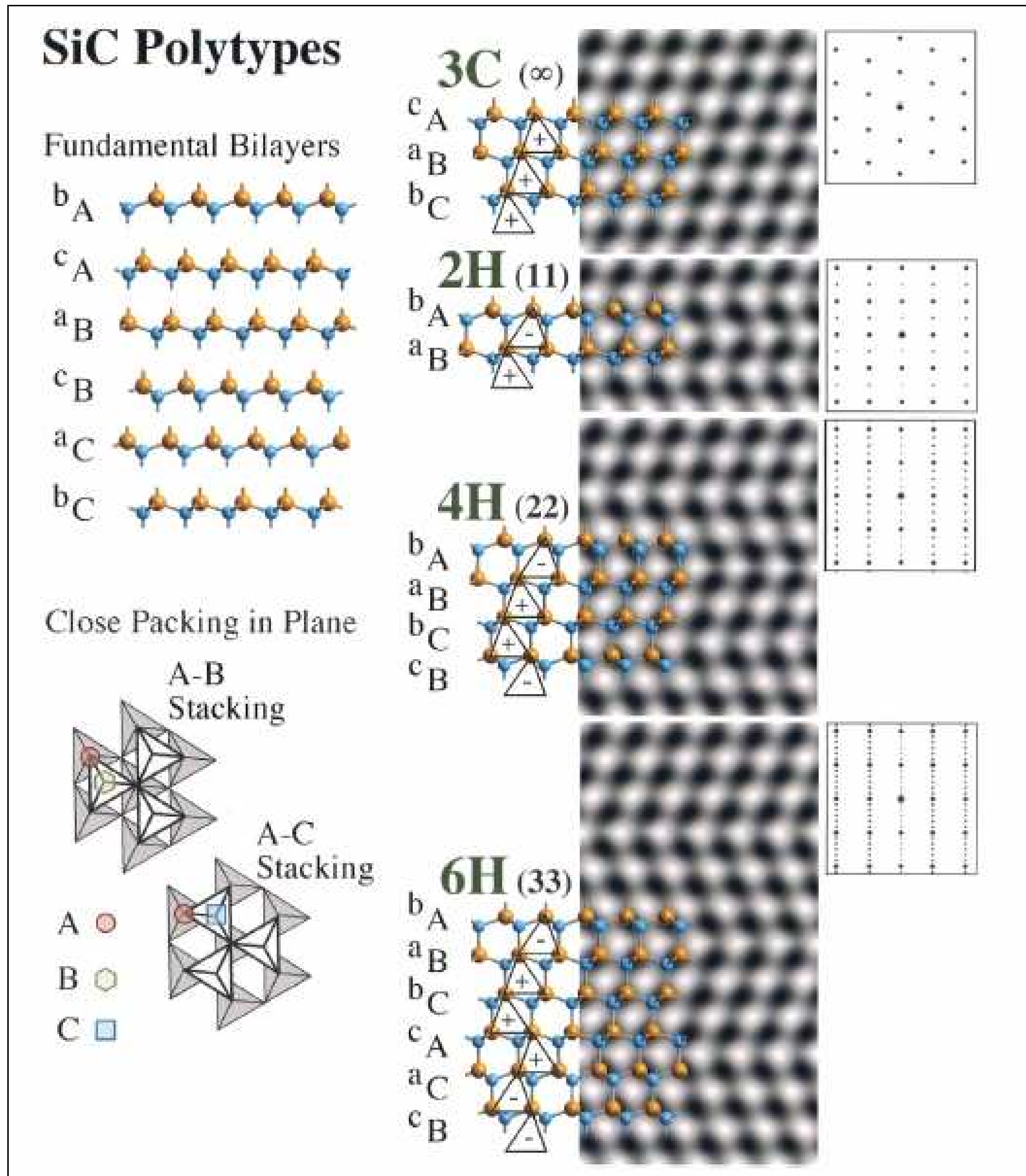

Figure 2.3 – Silicon carbide polytype structures[23]. Polytypes of SiC are formed by periodic stacking sequences of bilayers that produce tetrahedral sheets. Atomic models of the six unique (fundamental) bilayers (*bA, cA, aB, cB, aC*, and *bC)* of SiC (top left) based on three principal close packed planes (*A, B,* and *C*) (lower left) are shown. Blue atoms represent C and orange atoms represent Si. The two basic stacking arrangements, *A-B* and *A-C* that form planes of vertex-sharing parallel and antiparallel tetrahedra, respectively, are shown (lower left). Atomic models of the four simplest, 3C/(∞), 2H/(11), 4H/(22), and 6H/(33), polytypes are shown superimposed on calculated HR-TEM lattice images produced using defocus conditions that reproduce the symmetry of the projected lattice

(center column). Schematic illustrations of diffraction patterns (including forbidden reflections in some cases) are also shown (right column).

A number of notation schemes are used to describe SiC polytypes. The Ramsdell[25] notation is such that a polytype is denoted by the number of bilayers in the unit cell followed by C, H, or R, denoting the crystal symmetry (i.e., cubic, hexagonal, or rhombohedral). The fundamental bilayers are denoted *bA, cA, aB, cB, aC,* and *bC*. In the earlier Zhdanov[26] notation, sheet tetrahedra are assigned a positive or negative sense defined by a relative rotation of radians about the stacking direction (as is shown in figure 2.3). The successive number of tetrahedral layers, having tetrahedra with a common positive or negative sense, is counted in each subseries present. For example, the polytype denoted 6H (i.e. {. . .*AaBbCcAaCcBb*. . .}) in the Ramsdell notation (figure 2.3) has two subseries each consisting of three tetrahedral layers of the same sense, {. . . +++ ---. . .}, and in the Zhdanov notation is denoted (33). The polytype denoted 3C (i.e., {. . .*AaBbCc*. . .}) in the Ramsdell notation has an infinite number of tetrahedral layers of the same sense in one subseries, {. . .+. . .}, and is denoted (∞) (figure 2.3)[23].

2.3.1. Cubic 3C/(∞), β-SiC polytype

The cubic SiC polytype has the second smallest unit cell, with a $F\bar{4}3m$ space group (unit cell length a = 4.36 Å). This structure is formed by the stacking sequence {. . .*AaBbCc*. . .} of three bilayers, and is denoted 3C in the Ramsdell notation and (∞) in the Zhdanov notation. Cubic 3C-SiC is iso-structural to cubic 3C diamond and consists of two interpenetrating face-centered cubic (FCC) sublattices, one lattice entirely Si and one entirely C, which are separated by the displacement vector a/4 [111]. Tetrahedra lie in (111) planes and the 3C stacking sequence of tetrahedral planes is best viewed along the [011] zone axis[23].

2.3.2. Hexagonal 2H/(11), α-SiC polytype

This polytype has the smallest unit cell (lowest order) and is hexagonal (space group *P*63*mc*, unit cell lengths a = 3.08 Å, c = 5.03 Å). This structure is formed by the stacking sequence {. . .*AaBb*. . .}, and is denoted 2H in the Ramsdell notation and (11) in the Zhdanov notation. Hexagonal 2H α-SiC is iso-structural to hexagonal 2H diamond (lonsdaleite). It is the only polytype with a 1 in its Zhdanov symbol; meaning that no other polytype contains subsequences of 2H order. Tetrahedra lie in {0001} planes and the 2H stacking sequence of tetrahedral planes is best viewed along the $[11\bar{2}0]$ zone axes[23].

2.3.3. Higher order α -SiC polytypes (unit cells larger than 3C)

Lattice images of α-SiC along zone axes perpendicular to the tetrahedral stacking direction and analogous to 3C $[01\bar{1}]$ and 2H $[11\bar{2}0]$ display a characteristic zigzag contrast pattern reflecting their Zhdanov symbol, under defocus conditions where the symmetry of the open channels in the structure is reproduced. Furthermore, the different polytypes can be readily identified by their electron diffraction patterns and HR-TEM images[23].

2.3.4. Factors influencing polytypism

Polytypic structure is influenced by dopants. By increasing the partial pressure of nitrogen (n-type dopant), the formation or growth of 3C-SiC is promoted. Aluminium (p-type dopant) increases the probability if 6H or 4H formation. In the case of 3C-SiC, SiC growth occurs at temperatures of up to 2475K, in the presence of supersaturated Si vapour. This sometimes leads to the formation of a silicon liquid phase. Solid-state phase transformation between SiC polytypes has been illustrated in the literature as a function of temperature and applied stress[4]. If a solid phase has several modifications, one is usually the thermodynamically stable one while the others are metastable. Formation of

one or more metastable phases is often observed. Most theories that explain the formation of certain polytypes are usually based on the following[4]:

- Impurities
- Si/C ratio
- Temperature
- Presence of dislocations
- Presence of vacancies ordered in superlattices
- Stacking fault energy
- Formation of polymers within the gas phase
- Non-equilibrium conditions within the vapour phases
- Surface vibrational entropy contribution to free energy
- Native defects
- Surface superstructures

2.4. Raman theory

2.4.1. The Raman effect

Raman scattering or the Raman effect is the inelastic scattering of a photon. When light is scattered from an atom or molecule, most photons are elastically scattered (Rayleigh scattering). The scattered photons have the same energy (frequency) and wavelength as the incident photons. However, a small fraction of the scattered light (approximately 1 in 1 million photons) is scattered by an excitation, with the scattered photons having a frequency different from, and usually lower than, the frequency of the incident photons[27].

Scattering is defined as light deflected from the original direction of propagation of the incident light. From spectral analysis of the light scattered there exist discrete components of altered wavenumbers in addition to Rayleigh scattering (scattering of light without change in the wavenumber of the incident light). There are in general, pairs of

new lines appearing in the spectrum at wavenumbers positioned symmetrically relative to the Rayleigh line[28,29,30]. Figure 2.4 shows the possibilities that occur when radiation is scattered. Molecules in the ground state give rise to Raman scattering with energy $h(\nu_0 - \nu_1)$. Molecules in a vibrationally excited state scatter inelastically back to the ground state, giving the Raman-effect with an energy of $h(\nu_0 + \nu_1)$.

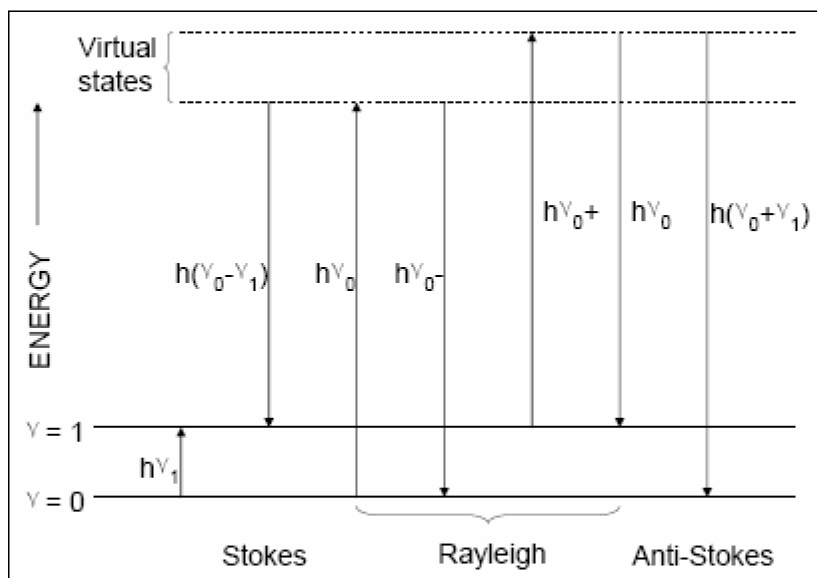

Figure 2.4 – Energy level diagram, illustrating the fundamental processes of Raman scattering, adapted from Grasselli et al, (1981) [28]

The appearance of altered frequencies (wavenumbers) in scattered light is called the Raman effect or Raman scattering. The Rayleigh scattering that accompanies Raman scattering is usually 3-5 orders of magnitude greater, rendering the latter a feeble effect. The Rayleigh scattering itself is 3-4 orders of magnitude lower than the intensity of the incident exciting radiation. The new components that appear in the spectrum of the scattered radiation at shifted wavenumbers are called Raman lines or Raman bands and collectively they are referred to as the Raman spectrum. The Raman bands at wavenumbers less than the exciting wavenumber $(\nu_0 - \nu_1)$ are the Stokes lines, while those that appear at higher wavenumbers are anti-Stokes lines $(\nu_0 + \nu_1)$. Generally, the anti-Stokes lines are considerably weaker and quickly diminishing in intensity with increasing ν_1 relative to the Stokes lines[31]. Frequency shifts of Stokes and anti-Stokes Raman

spectra correspond to the frequency of the normal modes of molecular vibrations. The shift values are therefore more valuable for characterizing band position, rather than the absolute wavenumbers. Most Raman applications use the more observable Stokes side of the Raman spectrum and the plot is on a relative scale ($\nu_0 - \nu = \nu_1$)[28].

Dispersive Raman spectroscopy uses a visible laser for excitation, a dispersive spectrometer and a charge coupled device (CCD) for detection. The main disadvantage of using visible excitation is common to all visible spectrometer systems and this is fluorescence. Since Raman scattering is a weak effect, a powerful excitation source is chosen to provide a high power density at the sample. The implication is that fluorescence can not only occur from the sample under investigation, but also from any contaminant which is fluorescent. Fluorescence will not occur at energies below that of excitation and it can therefore be intense in the energy region covered by Stokes Raman scattering. As a result, interference often occurs and accounts for why Raman scattering is not more widely used[29].

2.4.2. Theoretical overview

The classical description of Raman scattering is of a polarization induced in the molecule by the oscillating electric field of the incoming light. The induced dipole then radiates scattered light with or without exchanging energy with vibrations in the molecule. The effect is described by the equation 2.2 below and describes the case for both classical and quantum mechanical treatments of Raman scattering[30]:

$$P = \alpha E \qquad (2.2)$$

Where: P is the strength of the induced dipole
α refers to the molecular polarizability
E is the incident electric field

The classical treatment of Raman scattering is based on the effects of molecular vibrations on the polarizability α. The electric field resulting from the incident radiation is a time-varying function as is shown by equation 2.3.

$$E = E_0 \cos 2\pi v_0 t \qquad (2.3)$$

Where: v_0 is the frequency of the laser light

The molecular vibrations are usually composed of normal modes, Q_j, where there are 3N-6 (and 3N-5 for a linear molecule) modes for a molecule of N atoms.

$$Q_j = Q_j^o \cos(2\pi\ v_j\ t) \qquad (2.4)$$

Where: v_j is the characteristic harmonic frequency of the j-th normal mode.

Q_j is the j-th normal coordinate of the vibration

When a molecule vibrates, the polarizability is also a time-varying term which depends on the vibrational frequency of the molecule.

$$\alpha = \alpha_0 + \left(\frac{\delta\alpha}{\delta\, Q}\right) Q_j + \ldots \qquad (2.5)$$

The polarizability of electrons in the molecule is modulated by the molecular vibration as is shown in figure 2.5. A combination of equations 2.2, 2.3 and 2.5 yields equation 2.6; assuming that the higher order terms of equation 2.5 are ignored. Raman scattering

occurs because a molecule can change the polarizability. The change is described by the polarizability derivative $\frac{\delta\alpha}{\delta Q_j}$.

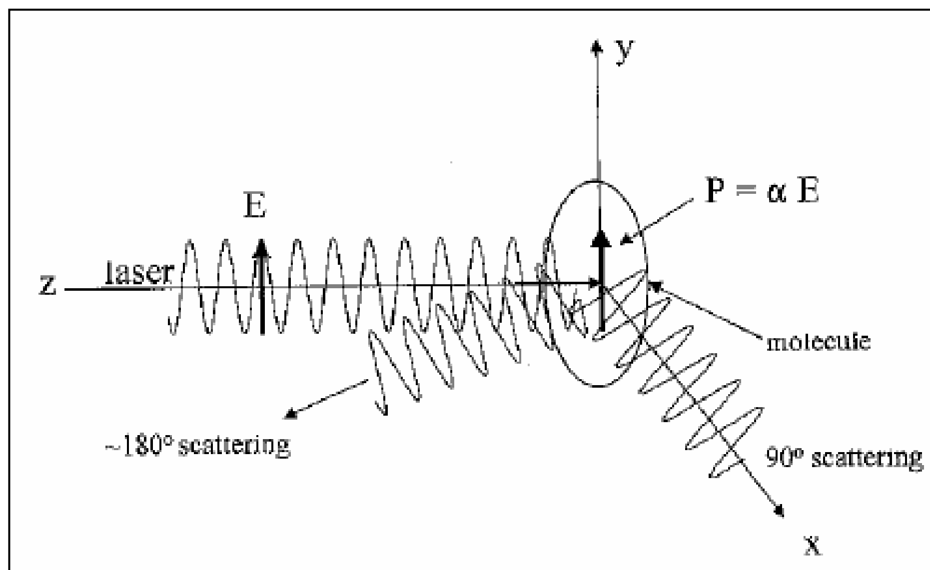

Figure 2.5 – Polarization (P) induced in a molecule's electron cloud induced by an optic electric field E, shown for 90° and 180° geometry[30].

$$P = \alpha_0 E_0 \cos(2\pi\ v_j\ t) + E_0 Q_j^o \left(\frac{\delta\alpha}{\delta\ Q}\right) \frac{\cos 2\pi(v_0 + v_j)t + \cos 2\pi(v_0 - v_j)t}{2} \tag{2.6}$$

When polarized electrons radiate light at the frequency of their oscillations, scattering occurs at three frequencies, as is confirmed by equation 2.6. The first term denotes Rayleigh scattering, which is the same frequency as the laser. Its magnitude is proportional to α_0 which is the inherent polarizability of the molecule. The second term is the anti-Stokes Raman scattering and occurs at $(v_0 + v_j)$. The third term is the Stokes Raman scattering at $(v_0 - v_j)$.

Equation 2.6 is derived classically and is incomplete, with the following implications[30]:

- Polarization and scattering (Raman and Rayleigh) intensities are linear with the laser intensity. Even though non-linear Raman scattering can occur at high E_0 values, this is not an issue in analytical applications.
- Only vibrations that change the polarizability (hence the $\delta\alpha/\delta Q \neq 0$) yield Raman scattering. This governs the primary selection rule for Raman scattering.
- Raman shifts may be both positive and negative. The Raman anti-Stokes intensity depends on the population of the first vibrationally excited state, its intensity is related to temperature by the Boltzmann distribution, which is given by equation 2.7, for the case of non-degenerate vibration.
- $\delta\alpha/\delta Q_j$ may vary greatly for different molecules and different modes within a molecule, leading to a wide variation in Raman scattering intensity
- $\delta\alpha/\delta Q_j$ is generally much smaller than α_0 and Raman scattering is much weaker than Rayleigh scattering, even though this is not apparent from equation 2.6.

The observed intensity of Raman scattering is proportional to the cross-section σ_j (square centimeters per molecule). The magnitude of σ_j is related to $\delta\alpha/\delta Q_j$. The effect of this relationship is shown in equation 2.7, where the Raman intensity is shown to vary with frequency.

$$\frac{I_R(v_0 + v_j)}{I_R(v_0 - v_j)} = \frac{(v_0 + v_j)^4}{(v_0 - v_j)^4} \exp\left(\frac{-hv_j}{kT}\right) \tag{2.7}$$

From equation 2.8, it is evident that the Raman intensity varies with the fourth power of the observed frequency for normal Raman scattering, which depends on the laser frequency. The v^4 factor gets derived from the classical treatment of scattering from an oscillating induced dipole. The scattered light occurs at an absolute frequency of $\bar{v}_0 \pm \bar{v}_j$.

$$I_R = \mu'(\bar{v}_0 \pm \bar{v}_j)^4 \alpha_j^2 Q_j^2 \tag{2.8}$$

Where : I_R is the Raman intensity

μ' is a constant

$\bar{v}_j$ is the Raman shift (in reciprocal centimeters)

Raman Cross section

In addition to the factors affecting the Raman intensity, such as the laser wavelength and polarizability, the empirically determined cross-section is equally important for analytical applications. This is especially true in cases involving weak or characteristic scattering from several components. The polarization, laser wavelength and observation geometry are often invariant, being determined by the instrument. This makes it sufficient to use the empirical cross section for a given Raman band in that geometry to estimate the signal strength. The cross section, denoted as σ_j (centimeters squared per molecule) is proportional to the probability of an incident photon being scattered as a Raman-shifted photon with a particular Raman shift[30].

For the classic approach the Raman scattering (watts) is related to the cross-section and laser intensity (I_0 in watts) by equation 2.9.

$$I_R = I_0 \sigma_j D dz \qquad (2.9)$$

Where : D is the number density of scatters (molecules per cubic centimeter)

dz is the path length of the laser in the sample

For a scatter that is not resonant or pre-resonant (which follows the classical $\bar{v}^{-4}$ dependence) a frequency independent cross-section σ_j^o (centimeters to the sixth power per molecule) may be defined by equation 2.10.

$$\sigma_j^o = \frac{\sigma_j}{(\bar{v}_0 - \bar{v}_j)^4} \qquad (2.10)$$

Where: $\bar{v}_j$ is the vibrational frequency of the Raman mode (in cm^{-1})

$\bar{v}_0 - \bar{v}_j$ is the absolute frequency of scattered light (in cm^{-1})

$\bar{v}_0$ and $\bar{v}_j$ are expressed in wavenumbers (in cm^{-1})

The introduction of photon counting detectors into Raman instrumentation has meant that current spectrometers count photons as opposed to measuring watts, with the two differing by a factor of hv. Photons counting derivations are more consistent with a quantum mechanical treatment whereas the classical derivation is based on induced dipoles. Equation 2.11 is the result of equation 2.9 rewritten for photon counting systems.

$$P_R = P_0 \sigma_j^{'} Ddz \qquad (2.11)$$

P_R and P_0 have units of photons per second, while $\sigma_j^{'}$ has a different frequency dependence than for equation 2.10. The substituting of σ_j from this equation into equations 2.9 and 2.11 yields equation 2.12.

$$I_R = I_0 \sigma_R^o (\bar{v}_0 - \bar{v}_j)^4 Ddz \qquad (2.12)$$

Since $I_R = P_R hc(\bar{v}_0 - \bar{v}_j)$ and $I_0 = P_0 hc\bar{v}_0$ equation 2.12 can be rewritten as:

$$P_R = P_0 \sigma_j^o \bar{v}_0 (\bar{v}_0 - \bar{v}_j)^3 Ddz \qquad (2.13)$$

and

$$\sigma_j^{'} = \sigma_j^o \bar{v}_0 (\bar{v}_0 - \bar{v}_j)^3 \qquad (2.14)$$

Hence whenever P_R is measured in photons per second, the Raman intensity scales with $\bar{v}_0(\bar{v}_0 - \bar{v}_j)^3$ as opposed to $(\bar{v}_0 - \bar{v}_j)^4$.

The differential Raman cross-section is defined as $d\sigma_j / d\Omega$ where Ω represents the solid angle of collection (equation 2.15).

$$\beta(cm^2 molecule^{-1} sr^{-1}) = \frac{d\sigma_j}{d\Omega} \tag{2.15}$$

Equation 2.15 can be summarized as $\frac{d\sigma_j}{d\Omega} = \frac{\text{scattered flux / unit of solid angle}}{\text{incident flux / unit of surface}}$, where the units are $cm^2 molecule^{-1} sr^{-1}$. The sr^{-1} term refers to the reciprocal of the steradian (the SI unit of solid angle). The symbol β is used to differentiate from the integrated σ_j and from the cross section differentiated with respect to the observation angle and with respect to the wavelength $\beta^{'}$ (equation 2.16). $\beta^{'}$ depends both on observation direction and the Raman shift.

$$\beta^{'}(cm^2 molecule^{-1} sr^{-1} wavenumber^{-1}) = \frac{\delta^2 \sigma_j}{\delta\Omega \delta(\Delta \bar{v})} \tag{2.16}$$

2.4.3. Raman Spectroscopy of condensed phases

The analysis of solids with Raman spectroscopy is significantly more complex than is the case with liquids and gases since atoms, ions or molecules may be distributed with either no long-range order (amorphous), perfect order in one, two or three dimensions (crystalline) or a mixed state (semi-crystalline). As is the case with infra-red spectroscopy, Raman spectroscopy is highly sensitive to the state of order in solids[32].

In a crystal, the vibration selection rules depend upon the symmetry and the occupancy of the unit cell and the molecular symmetry (molecules are classified according to symmetry

elements or operations that leave at least one common point unchanged). Generally, when a molecule is placed at a lattice site of lower symmetry than its point group, the molecule is perturbed and more bands can appear due to removal of vibrational degeneracy (band splitting)[32]

Disordered solids

In extreme cases of disordered material such as inorganic glass or an amorphous polymer, translational periodicity is very low and a wide range of local molecular environments exist. This gives rise to very broad features in place of sharp bands observed from crystals[32].

Influence of sample form

The sample form can have a significantly large influence on Raman band intensities, shapes and positions. These factors are particularly significant when interpreting spectra to draw quantitative conclusions[32].

Size effects in polycrystalline particles – diffuse reflection

The overall scattering intensity can be strongly dependent on the particle size and particle packing. This happens because both the laser beam and the Raman radiation will suffer multiple elastic scattering events in a polycrystalline powder. The observed Raman intensity will then depend on the diffuse reflectivity of the sample. The effect of forward and backscattered Raman intensities have been related to the incident laser power, sample thickness, sample absorption, elastic scattering coefficient and the Raman scattering coefficient by means of the Kubelka-Munk theory[33]. The basic results are that[32]:

- The Raman intensity decreases as the particles get smaller
- For samples with a low absorption coefficient, the Raman/Rayleigh ratio is maximized by using coarse powders in a forward scattering arrangement

- For strong absorbers it is better to use coarse powders and backscattering geometry

Absolute Raman intensities from powders are of limited use because they will be influenced by particle size. The use of a powder standard as an intensity standard is therefore not recommended. Quantitative measurements of heterogeneous powders should be made using band ratio methods. This will necessitate the measuring of two or more compounds by ratioing discrete Raman bands that arise from each of the compounds. This approach could be invalid if the particle sizes of the components vary from sample to sample. The particle sizes in a calibration need to be similar to those of the sample; otherwise the intrinsic Raman intensity of each component will not be constant. As the particle size drops significantly below 1 µm it is generally observed that the intrinsic scattering efficiency falls dramatically for non-surface modes. For instance, a 10 µm particle will have a much stronger intrinsic Raman spectrum than 0.01 µm particles of the same material[32].

The following artefacts can arise when dealing with condensed phases[32]:

<u>Self absorption (colour)</u>

If the sample possesses strong absorption bands in the absolute wavelength region of the Raman scatterer, the Raman scattered radiation will be attenuated. In some cases, the effect is obvious and expected – as such strongly coloured samples are likely to absorb Raman scatter excited by a visible laser. The absorption band of coloured samples is generally broad leaving a large region of the Raman spectrum suppressed. It has been shown through studies how attenuation can be quantified as a function of absorber concentration and optical properties[34]. The same study also showed that for a sample that absorbs both laser and Raman wavelengths, 180° backscattering is greatly preferred if the absorber molecule is also the Raman scatterer of interest. If 90° scattering is employed, it becomes necessary to carefully optimize the absorber concentration thereby maximizing its Raman signal, whereas 180° scattering efficiency reaches a plateau once the absorber

reaches a sufficient concentration. In this case, the laser beam will penetrate deeply into the sample, yielding an analysis specific to the sample surface. In this case, it is best to use the widest aperture collection lens available in order to obtain the highest Raman signal.

Heating, degradation and fluorescence

Condensed samples are prone to heating in the laser beam, even if they are slightly coloured. This leads to subtle phase changes such as crystal form or conformational modifications. In addition the laser-induced heating can induce subtle, reversible effects such as band broadening and shifting as is the case with carbon[35]. These changes can be hard to avoid because the intensity at the laser focus can be very high, especially in Raman microscopy measurements. Therefore, even with a solid that does not visibly melt, burn or otherwise indicate damage, it is not safe to assume that the laser has not modified the sample. Where possible, spectra should be recorded using different laser powers to check for changes.

If the laser light is absorbed by the sample, this often leads to relatively intense fluorescence, which can severely degrade the signal-to-noise ratio of the Raman spectrum. Fluorescence can be minimized using a number of techniques to either clean up the sample chemically (removing the fluorescor) or to suppress the fluorescence signal by distinguishing Raman and fluorescence signals. However, the most effective universal approach is to shift the excitation laser to a longer wavelength (about 785 nm or 1064 nm) to avoid exciting electronic transitions.

2.4.4. Quantitative Raman spectroscopy

Both currently and historically, the majority of applications of Raman spectroscopy have been qualitative, with the objective being to determine the peak frequencies and comparing vibrational features to spectra from different laboratories, or those predicted theoretically. The vast majority of reported Raman spectra are not corrected for variation

of instrumental sensitivity across the spectrum, with the intensity scale often being arbitrary. Unlike ultra violet visible and infrared absorption spectroscopy, Raman scattering is viewed as a single beam mode, without a reference channel to compensate for instrumental sensitivity variation with time or wavelength[36,37]. Consequently, it is generally difficult to compare relative or absolute Raman intensities from different instruments, and calibration transfer based on intensities is exceedingly difficult. The problem is further compounded by the dependence of observed Raman intensity on focusing and alignment, so that a given sample may yield a significant variation of intensities from day to day, even on a particular instrument and under apparently identical conditions. The main drawback with the use of the Raman spectroscopy as a quantitative technique has been the difficulty in the reliable determination of relative and absolute intensities[36].

Basic theory of peak intensities

The factors that influence the observed Raman intensities can be divided into two categories: sample and laser variables as well as collection and detection variables. Most of these variables are kept constant by using the same spectrometer and laser in addition to checking the Raman signal with a silicon standard.

$$S(e^-) = LA_D\Omega_D TQt \quad (2.17)$$

$$S(e^-) = (P_D \beta DK)(A_D\Omega_D TQt) \quad (2.18)$$

$S(e^-)$ = Observed signal (in photoelectrons), L = Specific intensity, P_D = Laser power density (in photons s^{-1} cm^{-2}), β = Differential Raman cross-section (in cm^2 $molecule^{-1}$ sr^{-1}), D = Number density of scatters (in molecules cm^{-3}), K = Path length (in cm), t = Observation time (in seconds), A_D = Sample area monitored by spectrometer (in cm^2), Ω_D = Collection solid angle of the spectrometer at the sample (in sr), T = Transmission of the

spectrometer and collection optics (unitless), Q = Quantum efficiency of the detector (in e^- per photon).

When considering the photometric accuracy in Raman spectroscopy, the most basic issue is the relationship between the observed signal and the sample variables, such as the cross-section and concentration. This basic objective is difficult to achieve because it depends on a large number of variables as shown by equations 2.17 and 2.18. This issue is illustrated by comparing Raman scattering with absorption techniques. For instance the Fourier Transform Infrared spectroscopy (FT-IR), has a reference spectrum that effectively calibrates most of the instrumental variables. Variables such as the detector response, source intensity and optical losses are all relevant to an absorption experiment; however their effects are removed from the final spectrum by calculating a ratio of reference and sample spectra. In Raman spectroscopy however, one usually measures only the scattered intensity with no reference beam. As such the variations in the collection function with time or with wavelength are not compensated for by a reference spectrum[36]. Any such fluctuations are checked for by daily calibration with a silicon standard.

There are three steps that need to be followed to achieve a corrected Raman spectrum that accurately represents the scattering intensity of a given sample as a function of Raman shift[36]:

1. Reproducibility of the observed scattering intensity
2. Correction for variation of instrument response across a Raman spectrum
3. Determination of absolute scattering intensity and absolute Raman cross-sections

The first two objectives can be achieved by more straightforward calibration than the third step, which is more involved. The great majority of applications however, do not require the assessment of absolute intensity, with its accompanying experimental difficulties. Measurements of the cross-section are generally left to the specialists. Reproducible Raman intensities may be achieved with sensible design of sampling optics

and reasonable experimental care. Response function correction is not yet routine but it can be applied. The result of the first two steps is a Raman spectrum that accurately reflects relative Raman scattering intensities and is useful for library searching, quantitative analysis and comparison of spectra between libraries[36].

2.4.5. Raman properties of SiC

The salient features of the spectra of Raman SiC polytypes are the appearance of many weaker lines due to the increased number of molecules per unit cell and the decreased symmetry of the crystal forms. There is a splitting of the TO vibration near 794 cm^{-1} into two components TO_1 with a constant frequency and TO_2, which varies with polytype and drops as low as 782 cm^{-1}. The 3C-SiC unit cell has a T_d symmetry yielding one triply degenerate Raman active phonon (T_{2x}, T_{2y}, T_{2z}). This mode is polar and leads to two longitudinal optic (LO) and transverse optic (TO) components. In 3C-SiC, two Raman peaks are therefore observed corresponding to the TO and LO modes at 796 cm^{-1} and 972 cm^{-1}, respectively. The point group for the hexagonal polytypes is C_{6v}. It gives rise to the Raman active A_1, E_1 and E_2 modes. Both E_1 and E_2 are doubly degenerate (E_{1x}, E_{1y} and E_{21}, E_{22}) and only A_1 and E_1 are polar and split in TO and LO phonons[38]. As the unit cell increases, additional phonons with different energies may appear. These new Raman bands are called folded modes, as they correspond to phonon modes located within or at the edge of the Brillouin zone[39].

The intensities of the Raman phonons vary with the orientation of the crystal about the laboratory axes (XYZ). The scattering efficiency (I) is related to the polarization of the incident (e_i) and scattered (e_s) light and is given by $I=C\Sigma_j \cdot |e_i \cdot R(j) \cdot \xi_j \cdot e_s|^2$, where C is a constant, R_j is the Raman tensor and ξ_j is the polarization of the phonon j [40]. The T_2, A_1 and E_1 modes are polar. The intensities of the LO and TO vibrations therefore vary with the propagation directions in the crystal. The intensities of the LO and TO vibrations therefore vary with the propagation directions in the crystal. In the backscattering configuration, the wave vector of the phonon q is parallel to the light propagation. The consequence is straightforward for both the A_1 and E_1 modes: A_1(LO) is active when q is

along the c axis of the crystal, whereas the A_1(TO) and E_1(TO) modes are active when q is perpendicular to c. For the cubic zinc-blend crystal, the assessment of the TO and LO peak intensities is more complex. It can be shown, for instance, that the TO mode is strictly forbidden for the (100) crystal orientation, whereas the LO mode is forbidden for the (110) orientation[41].

		Frequency (cm^{-1})			
Polytype	**x = q/q$_B$**	Planar acoustic FTA (E)	Planar optic FTO (E)	Axial acoustic FLA (A_1)	Axial optic FLO (A_1)
3C	0	–	796*	–	972
2H	0	–	799	–	968
	1	264*	764*	–	–
4H	0	–	796	–	964
	2/4	196, 204*	776*	–	–
	4/4	266		610	835
6H	0	–	797	–	965
	2/6	145, 150*	789*	–	–
	4/6	236, 241		504, 514	889
	6/6	266	767	–	–
15R	0	–	797	–	965
	2/5	167, 173*	785*	331, 337	932, 938
	4/5	255, 256	769	569, 577	860
21R	0	–	797	–	967
	2/7	126, 131*	791*	241, 250	
	4/7	217, 220	780	450, 458	905, 908
	6/7	261	767	590, 594	

Table 2.1 – Raman frequencies of fundamental SiC polytypes. The asterisk denotes the Fourier Transverse Acoustic (FTA) and Fourier Transverse Optic (FTO) modes with the maximum intensity in each phonon branch. FLA and FLO are abbreviations for the

Fourier Longitudinal Acoustic and Fourier Longitudinal Optic modes. q/q_B is the reduced wave vector of the corresponding phonon mode SiC[5].

A detailed study of these aspects is made possible by polarization of the Raman scattered light. This property can be measured using (plane) polarized laser excitation and a polarization analyzer. Spectra acquired with the analyzer set at both perpendicular and parallel to the excitation plane can be used to calculate the depolarization ratio. This technique is useful in analyzing the connections between group theory, symmetry, Raman activity and peaks in the corresponding Raman spectra. The spectral information arising from this analysis gives insight into molecular orientation and vibrational symmetry, allowing the user to obtain valuable information relating to the molecular shape. It is often used to understand macromolecular orientation in crystal lattices, liquid crystals or polymer samples[42].

The various Raman frequencies of 3C, 2H, 4H, 6H, 15R and 21R SiC polytypes are given in table 2.1:

From the literature it has been shown that the 973 cm^{-1} photons of the 3C polytype can shift to around 964 cm^{-1}. This effect is attributed to be independent of the excitation radiation, but is more likely due to small crystallites found in the samples. The position, relative intensity and bandwidth of the Raman bands are closely related to the degree of order in the structure and the stress in the material[43].

The Raman bands in SiC crystals containing stacking disorder exhibit broadening and distortion at frequencies corresponding to the basic polytypes (e.g. 4H, 6H, 15R etc.) [44]. For heavily disordered crystals, a broad background is sometimes observed and corresponds to the so-called ‘density of state’ (DOS) contribution, which superimposes between 700 and 1000 cm^{-1}. This phenomenon is as a result of random faulting in the stacking sequence[45]. In disordered SiC, long-range order in the stacking of the atomic layers is lost. The short-range order remains however, comprised of small domains, each consisting of a basic polytype structure. Consequently, the Raman spectra of the

disordered structures reflect the structures of the domains[46]. SiC rarely has uniform distribution of the stacking order across the entire crystal. A common feature is that in disordered SiC, disordered zones are sandwiched in between the same or different polytype layers, or are located near the surface region[47,48].

Raman shifts toward high wavenumbers are attributed to macroscopic strain induced during the deposition process and the width is also governed by the lattice imperfection and grain boundaries. Increasing the deposition temperature increases the intensity and lowers the wavenumber. A higher intensity indicates a more perfect crystallinity. A change in the wavenumber is a reflection of the degree of distortion of the crystal lattice and therefore of the residual strain. A lower wavenumber indicates a lower strain[49]. It has also been suggested that a high wavenumber region means that crystals are under external pressure[50].

The FTO to FLO SiC line intensity ratio is thought to be a function of the microscopic composition or the structure of the SiC layer. The variation in the SiC line intensities may be caused by changes in the long-range order of the SiC microstructure. Analysis by the scanning electron microscope has revealed a difference in the surface morphology of the coating with and without a strong LO line. A strong LO line is an indication of large, interlocked grains. If no LO is seen, then a ‘cauliflower’ structure with undefined grains is expected. Furthermore, high deposition temperatures lead to SiC grain size increase, but grain boundary gaps also develop. The structural changes as a result of changes in the coating rate depend on the deposition temperature and the coater size [51].

Silicon and carbon

The amount of silicon which forms in TRISO-coated nuclear particles increases with an increase in the coating rate and a decrease in the deposition temperature. The amount of excess carbon increases with an increase in the deposition temperature and a decrease of the coating rate[51].

Single crystal and polycrystalline silicon are characterized by a sharp Raman line centered at 520 cm^{-1} to amorphous silicon with a broad band extending from 415 to 540 cm^{-1} and centered near 480 cm^{-1} [52].

Diamond gives a strong sharp Raman line at 1330 cm^{-1} [53]. Single crystalline and highly oriented pyrolytic graphite materials show a sharp line at 1580 cm^{-1} [54,55]. The more poorly oriented graphitic materials, e.g. activated carbon or glassy carbon show two broader lines at 1335 to 1340 cm^{-1} and at 1580 to 1590 cm^{-1} [56]. Amorphous carbon yields a broad skewed band extending from 1000 to 1700 cm^{-1} centered near 1500 cm^{-1} [51].

2.5. X-ray powder diffraction

2.5.1. General background

X-Ray Diffraction is a powerful non-destructive technique for the structural analysis of crystalline and polycrystalline phases[57]. It is based on the diffraction of a collimated beam of X-rays by the crystalline planes of a solid phase. X-ray powder diffraction can be applied to determine the SiC polytype distributions. A considerable overlap of individual peaks of the x-ray powder diffraction pattern occurs for the SiC polytypes. The reason for this effect is that polytypes are derived from the same parent structures, but contain different stacking vectors to each other. As a result it is difficult to obtain accurate results from a distribution of the polytypes in a mixture. However, the Rietveld method has been found to be a highly effective approach to solving this problem[58].

X-ray wavelengths are typically in the range of 0.7-2 Å. The XRD spectrum is usually obtained by measuring the diffracted intensity as a function of the diffraction angle 2θ, which is the angle between the incident and diffracted beams and the orientation of the specimen. Different maxima, corresponding to the contribution of the different crystalline planes in the crystal, are obtained when constructive interference of diffracted X- rays occurs according to the Braggs law, $\lambda = 2d\sin\theta$, where λ is the wavelength of the x-rays

and d is the inter-atomic planar spacing in the crystal. The technique is extremely sensitive to variations of the inter-atomic planar spacing. In general XRD does not provide spatial resolution, being the measured area of several mm^2. For special applications, spatial resolution approximately 10 µm can be achieved with a microfocus source for films thick enough (1 µm). The penetration depth of the X rays is determined by the absorption length. These characteristics give a strong incentive to also use XRD for the non-destructive analysis of epitaxial films and heterostructures[57].

XRD is also a very useful technique for the analysis of polycrystalline samples. Data related to texture and preferred crystalline orientations, strain, grain size, and crystalline quality of the sample can be obtained from the XRD spectra. For a given orientation of the sample, diffraction will occur from any crystallite with the proper orientation satisfying diffraction conditions. If the crystals are randomly oriented, peaks corresponding to the different planes will appear in the XRD spectrum, and the relative intensity of the different peaks is characteristic of each phase in the material. The amount of preferred orientation can be estimated by comparing the integrated intensities of the different peaks from the calibrated data, once geometrical factors have been corrected. The peak width is also affected by crystalline size and the presence of extended defects in the crystals as dislocations and stacking faults[57]. Determination of accurate compositions in SiC is made difficult because if the significant overlapping of the Bragg reflections from the numerous polytypes as well as texture effects. Results obtained by the traditional quantitative XRD methods are generally unsatisfactory[58].

The diffraction pattern is recorded in digitized form (as a numerical intensity value, y_i) at each of several thousands equal increments, i, in the pattern. The Rietveld method is the same no matter what powder diffraction data are used. The differences among data sources affect the data preparation that is required, whether the steps are in angle or energy, and the instrumental parameters that are refined but not in the method itself. In all cases, the best-fit sought is the best least-squares fit to all of the thousands of y_i ‘s

simultaneously. The quantity minimized in the least-squares refinement is the residual, S_y, while the sum is overall data points[59].

$$S_y = \sum_i w_i (y_i - y_{ci})^2 \tag{2.19}$$

Where: $w_i = 1/y_i$; y_i = observed (gross) intensity at the i-th step; y_{ci} = calculated intensity of the i-th step.

There are typically many Bragg reflections contributing to the intensity y_i, observed at any arbitrarily chosen point, i, in the pattern. The calculated intensities y_{ci} are determined from the $|F_K|^2$ values calculated from the structural model by summing the calculated contributions from neighbouring Bragg reflections including the background[59]:

$$y_{ci} = s \sum_K L_K |F_K|^2 \phi(2\theta_i - 2\theta_K) P_K A + y_{bi} \tag{2.20}$$

Where: s = scale factor; K = Miller indices, $h\ k\ l$, for a Bragg reflection; L_K = Lorentz, polarization and multiplicity factors; ϕ = reflection profile function; P_K = preferred orientation function; A = absorption factor; F_K = structure factor for the K-th Bragg reflection and y_{bi} = background intensity of the i-th step.

The least squares minimization procedures result in a set of normal equations that involve derivatives of all the calculated intensities, y_{ci}, with respect to each adjustable parameter. These are soluble by inversion of the normal matrix with elements M_{jk} given by[59]:

$$M_{jk} = -\sum_i 2w_i \left[(y_i - y_{ci}) \frac{\partial^2 y_{ci}}{\partial x_j \partial x_k} - \left(\frac{\partial y_{ci}}{\partial x_j} \right) \left(\frac{\partial y_{ci}}{\partial x_k} \right) \right] \tag{2.21}$$

Where: x_j, x_k = same set of adjustable parameters

This has to do with the creation and inversion of an *m* by *m* matrix, where *m* is the number of parameters being refined. Since the residual function is non-linear, the solution must be found with an iterative procedure in which the shifts, Δx_k, are:

$$\Delta x_k = \sum M_{jk}^{-1} \frac{\partial S_y}{\partial x_k} \tag{2.22}$$

2.5.2. Rietveld method

The presence of multiple phases in powder diffraction patterns leads to degradation of the resolution of the data. For the same counting time, there is a decrease in the intensities of the patterns from the individual components. It has however become evident that with the Rietveld analysis it is possible to obtain accurate estimates of the relative abundances of the component phases[60,61,62,63,64]

Equation 2.23 is the formula for quantitative analysis with the Rietveld method. This method is then similar to the traditional integrated-intensity techniques for phase analysis. The difference is that the advantages obtained from considering the full pattern are retained.

$$W_p = S_p(ZMV)_p \Big/ \sum_{i=1}^{n} S_i(ZMV)_i \tag{2.23}$$

Where: *W* = relative weight fraction of phase *p* in a mixture of *n* phases, S = Rietveld scale factor, Z = number of formula units per unit cell, M = the mass of the formula unit (in atomic mass units), V = the unit cell volume (in $Å^3$).

The X-ray powder diffraction full-pattern fitting Rietveld method has several advantages[58]:

- It makes use of the full diffraction profile correction factors and hence reduces system effects of preferred orientation, extinction, absorption and instrumental configuration.
- There is more efficient treatment of overlapping peaks resulting in consideration of patterns of great complexity and broader peaks.
- There is correct error propagation for quantitative analysis results, by making use of the standard deviation of the scale factor for each phase (estimation by least squares refinement)
- The sample preparation is relatively easy
- It refines crystal structures and peak profile parameters for individual phases in a mixture, providing interactive adjustments of their properties during the analysis.

Peak intensities

For crystal structures solution and refinement the measured peak intensities must represent a known mapping of the intensity distributions of all the *hkl* reflections onto the 2θ dimension of the powder pattern. The assumptions made during such mapping are that[59]:

I. The sample is composed of randomly oriented crystallites (i.e. no preferential orientation)
II. The crystallites are sufficiently numerous to present just about all possible orientations to the incident beam (i.e. a powder average)

For the *in situ* analysis of intact TRISO coated particles criterion I. is not met because they consist of concentric layers of different phases around a central core. The inner layers are therefore shielded by the outer layers, affecting their diffracted intensities. Since we are however interested in the phases in the SiC layer, we are normalizing to a total phase composition comprising only SiC and Si. This ensures a reliable estimation of the phase ratios in the SiC layer. There are a variety of methods that have been proposed to make sure that such requirements are met, including randomizing sample movements, homogenization with amorphous diluents and crystal size reduction[65].

Micro-absorption

It is required that information about the particle and domain size distribution of each of the phases in the sample be obtained[66,67]. For this reason and because micro-absorption has a small dependence on 2θ, correction for this effect has not yet been implemented in Rietveld analysis. It is possible however to take account of the effects of micro-absorption (and other uncorrected systematic terms) by experimental determination of the constants in the equation 2.23 using a calibration mixture composed of standard materials[64,68,69].

2.5.3. Characterization of SiC by XRD

It has been stated by Ortiz et al,[70] (2001) that quantitative x-ray diffraction is the most suitable method for making accurate measurements of the relative abundance of the SiC polytypes, in order to better understand their processing, microstructural development, mechanical, electrical, electronic and optical properties. Ortiz et al, (2001) used two methods to analyse the 3C, 4H, 6H and 15R polytypes: polymorphic methods and whole pattern methods. The Rietveld method on the other hand is based on analysis of the whole pattern, which is fitted by means of a non-linear least-squares regression. The polymorphic method was found to be easier to operate compared to the Rietveld methods. However it is known that Rietveld methods are more accurate. As was expected, it was found that the Rietveld method gave more accurate results in terms of the quantitative polytype composition analysis of SiC.

Hongchao et al,[58] (1997) studied the quantitative XRD analysis, by the Rietveld method of the 3C, 4H, 6H and 15R polytypes. The detection limit of each polytype was based on the standard deviation. An accurate account of the distribution of the SiC polytypes was obtained. The largest relative error was found to be 13% (for the 4H polytype). However the absolute error was less than 2σ which is why the results were regarded as accurate. When the lower detection limit was 2σ (since the quantitative analysis method can give a

more accurate result in this case), the lower detection limit for the above four polytypes, 6H, 4H, 3C and 15R were 1.26, 0.76, 0.78 and 0.82%. Minor high order polytypes were not detectable with the experimental statistics used. Higher order structures tended to form as a result of stacking faults that were introduced into parent structures resulting in main reflections overlapping with those of the parent polytypes.

2.6. High temperature XRD - thermal expansion

2.6.1. Factors influencing cell parameters

There are a number of factors that influence the peak 2θ position as well as the cell parameters. These are[65,71,72]:

- The sample height
- Experimental temperature
- Sample absorption
- Instrumental calibration
- The peak shape model used

2.6.2. Thermal expansion properties of Al_2O_3

The Al_2O_3 thermal expansion data have been determined in the literature by Touloukian et al.[73] and by Taylor[74].

$$c(T) = c_0(1 + c_1 T + c_2 T^2) \tag{2.24}$$

Equation 2.24 is Taylor's expression and was used in conjunction with table 2.2.

	a	c
c_0	4.75814	12.99113
c_1	6.55E-06	6.54E-06
c_2	1.82E-09	2.60E-09

Table 2.2 – The coefficients describing the temperature dependence of the cell parameter of Al_2O_3 using equation 2.24[75]. Units are in Å.

2.6.3. Thermal expansion properties SiC polytypes

The three principal axis coefficients of thermal expansion of 3C, 4H and 6H SiC polytypes are expressed by equations 2.25-2.29 as second-order polynomials along the a-axes and along the c-axes[76,77,78]. It is not reported what fabrication method was used to manufacture the SiC samples but x-ray diffraction was used to collect data.

$$\alpha(3C) = 3.19\times10^{-6} + 3.60\times10^{-9}T - 1.68\times10^{-12}T^2 \quad (2.25)$$

$$\alpha_{11}(4H) = 3.21\times10^{-6} + 3.56\times10^{-9}T - 1.62\times10^{-12}T^2 \quad (2.26)$$

$$\alpha_{11}(6H) = 3.27\times10^{-6} + 3.25\times10^{-9}T - 1.36\times10^{-12}T^2 \quad (2.27)$$

$$\alpha_{33}(4H) = 3.09\times10^{-6} + 2.63\times10^{-9}T - 1.08\times10^{-12}T^2 \quad (2.28)$$

$$\alpha_{33}(6H) = 3.18\times10^{-6} + 2.48\times10^{-9}T - 8.51\times10^{-13}T^2 \quad (2.29)$$

The numerous SiC structural polytypes can be considered to consist of two different types of layer plane stacking sequences, which correspond to the cubic and hexagonal types. The 4H and 6H are structurally similar within their layers (i.e. along the a-axes of those polytypes), and also to within the layer structure of the cubic SiC polytype. It is therefore not surprising that the principal axial thermal coefficients $\alpha(3C)$, $\alpha_{11}(4H)$ and $\alpha_{11}(6H)$ are similar[79]

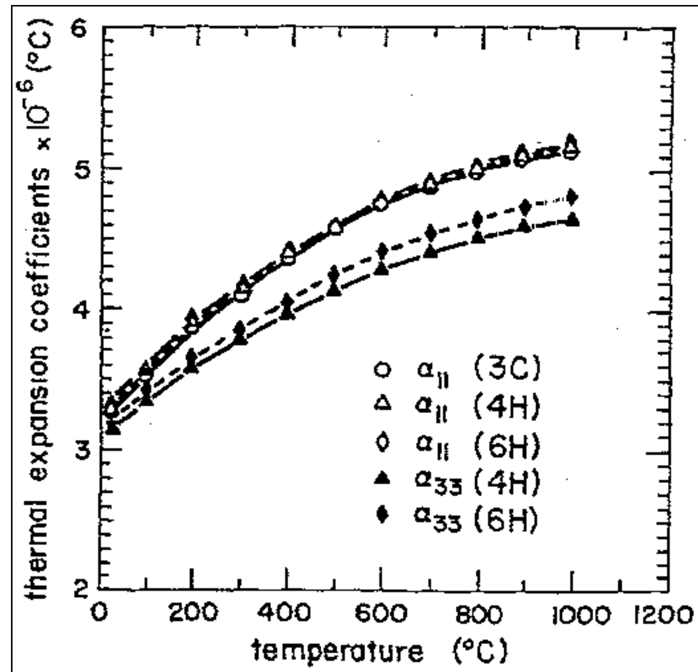

Figure 2.6 – The principal axial coefficients of thermal expansion for the 3C, 4H and 6H SiC polytypes[79].

From figure 2.6 it is evident that the principal axial coefficients of thermal expansion perpendicular to the stacking layers for the 6H and 4H structures are lower than those parallel to, or within the layers. The averages for the three principal axial coefficients of thermal expansion from 20°C to 1000°C can be calculated from the polynomials of equations 2.25-2.27 (along the a-axis) as $\overline{\alpha} = \int \alpha dT / \int dT$, yielding $4.45 \times 10^{-6} /^{o} C$ for $\overline{\alpha}(3C)$, $4.47 \times 10^{-6} /^{o} C$ for $\overline{\alpha}_{11}(4H)$ and $4.46 \times 10^{-6} /^{o} C$ for $\overline{\alpha}_{11}(6H)$. When considering the statistical significance of these averages, the three values are very similar[79].

The averages for the axial coefficients of thermal expansion from 20°C to 1000°C along the c-axis can be calculated from equations 2.28-2.29 to yield values of $4.06 \times 10^{-6} /^{o} C$ for $\overline{\alpha}_{33}(4H)$ and $4.16 \times 10^{-6} /^{o} C$ for $\overline{\alpha}_{33}(6H)$. This confirms that the $\overline{\alpha}_{33}$ values for the 4H and 6H structures are significantly lower than the $\overline{\alpha}_{11}$ values and that the natural

decreasing order is $\overline{\alpha}(3C)$, $\overline{\alpha}_{33}(6H)$ then $\overline{\alpha}_{33}(4H)$. This order is the same as that of the density of the H-stacking layers along the c-axes, indicating that the lower thermal expansion coefficients in the <0001> directions for the 4H and 6H polytypes are a direct consequence of the non-cubic stacking layer sequence. Furthermore, it can be deduced that the magnitude of the thermal expansion anisotropy is directly related to the fraction of the H stacking layer sequence in the non-cubic SiC polytypes[79].

The thermal expansion and the thermal expansion anisotropy of crystals depend on two structural factors[80]:

- The strength of the bonds within the structural polyhedra, which directly relate to the nearest-neighbour effects
- The angular changes between the polyhedra or the structural tiltings that relate to the second, third,…,etc., nearest-neighbour effects.

The thermal expansion coefficients of all crystal structures are determined by a combination of these two factors.

The equation for the thermal expansion of polyhedra is derived on a basis related to the strengths of the individual bonds within the crystal polyhedra[81]. This equation expresses the mean linear thermal expansion coefficient between room temperature and 1000°C.

$$\alpha_{1000^o C} = 4.0(4)\frac{N}{S^2 Z_a Z_c} \times 10^{-6} /^o C \tag{2.30}$$

$\alpha_{1000^o C}$ = mean linear thermal expansion coefficient between room temperature and 1000°C; N = coordination number of the structure; Z_a and Z_c are the cation and anion valencies; S^2 is a factor that is 0.20 for carbides and nitrides.

For SiC the N, Z_a and Z_c are 4. When these values are substituted into equation 2.30, $\alpha_{1000^o C}$ is about $5 \times 10^{-6} /^o C$, which is close to the values given by equations 2.25-2.29.

The theoretical coefficient of thermal expansion is only related to the nearest-neighbour atoms and is slightly larger than the reported values. The difference suggests that it is the presence of bond tilting contributions or further removed bonding effects that reduces the overall thermal expansion within the polytypes. The differences from the theoretically calculated coefficient obtained from equation 2.29 are not the same for the a-axis and the c-axis either. It can therefore be concluded that it is the different atom positions in the C and H stacking layer sequences which directly determine the thermal expansion anisotropies of the SiC polytype[79]. There have been other 3C SiC thermal expansion coefficient data reported in the literature. CVD SiC has been analyzed with x-ray diffraction[11] yielding equation 2.31 (units in 10^{-6}/K).

$$\alpha = -1.8276 + 0.0178T - 1.5544E-05*T^2 + 4.5246E-09*T^3 \quad (2.31)$$

T(K)	α_L - 3C SiC ($10^{-6}K^{-1}$)	α_L - Graphite ($10^{-6}K^{-1}$)
320	2.93	4.62
340	3.08	4.71
360	3.22	4.80
380	3.36	4.88
400	3.49	4.96
420	3.61	5.03
440	3.72	5.10
460	3.83	5.17
480	3.92	5.23
500	4.01	5.28
520	4.08	5.34
540	4.15	5.38
560	4.21	5.43
580	4.27	5.47
600	4.31	5.50
620	4.34	5.53
640	4.37	5.56
660	4.39	5.58
680	4.40	5.59
700	4.40	5.61
720	4.39	5.61
740	4.39	5.62
760	4.38	5.62
780	4.38	5.61

Table 2.3 – Thermal expansion data of SiC and PyC[82].

Table 2.3 is a set of interferometer-collected data from 3C SiC and PyC of a TRISO particle[82]. The TRISO samples were hollow hemispherical SiC shells, prepared by the fluidized bed method, across a temperature range of 300 K to 800 K.

From a dilatometric study, it has been reported that there exists an inflection point in the 1350°C-1450°C temperature range and hysteresis after a SiC sample has been cycled down through this temperature range when plotting the linear expansion versus temperature as is seen in figure 2.7[83]. The cooling curve does not retrace the heating curve below 1450°C, indicating a change that is not completely reversible. The difference is explained by the slight contraction that free silicon impurity (~1%) experiences when going from the solid to the liquid phase

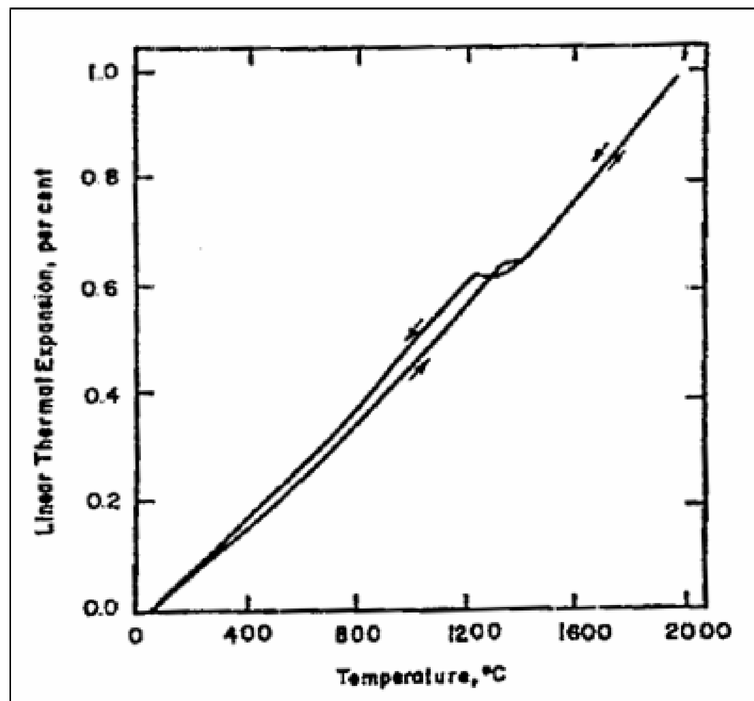

Figure 2.7 – Linear thermal expansion versus temperature relation for β-SiC[83]

2.6.4. The thermal expansion of graphite

It has been shown that the crystal lattice coefficients of thermal expansion parallel and perpendicular to the basal planes may be expressed in the form[84] :

$$\alpha_a = AC_{V_a} + BC_{V_c} + CT$$
$$\alpha_c = LC_{V_a} + MC_{V_c} + NT \tag{2.32}$$

The two components C_{V_a} and C_{V_c} refer to lattice vibrations parallel and perpendicular to the basal planes respectively.

$$C_{V_a} = 3RD\left(\frac{\Theta_a}{T}\right)$$
$$C_{V_c} = 3RD\left(\frac{\Theta_c}{T}\right) \tag{2.33}$$

Where, Θ_a and Θ_c = Debye temperatures associated with the lattice vibrations, T = absolute temperature and R = ideal gas constant.

These are expressible by the Debye function:

$$D(x) = \frac{3}{x^3}\int_0^x \frac{z^4 e^z}{(e^z - 1)^2}\,dz \tag{2.34}$$

Thermal expansion coefficients of graphite have been estimated in the literature. Riley[84], Morgan[85], Kellet and Richards[86] have estimated the coefficients for α_a, as is shown in Table 2.4. These values are compared to those that were experimentally determined by Steward et al.[87].

	$\Theta_a(K)$	$\Theta_c(K)$	A (J/mol)	B (J/mol)	C (deg^{-2})
Morgan	2300	800	1.677E-7	-1.036E-7	-8.30E-11
Kellet and Richards	2280	760	1.777E-7	-1.065E-7	0
Riley	2280	760	1.620E-7	-1.013E-7	0

Table 2.4 – Various coefficients in the expression of α_a[88].

Figure 2.8 shows the plot the α_a curves plotted from table 2.4's coefficients compared with the experimental results of Steward et al.[87]. The non-zero coefficient of the temperature term by Morgan gives a closer solution to the experimental data at high temperatures. Also $\alpha_a = 0$ is predicted to be attained at 393.60°C, which compares well with the 400°C that is found experimentally[88].

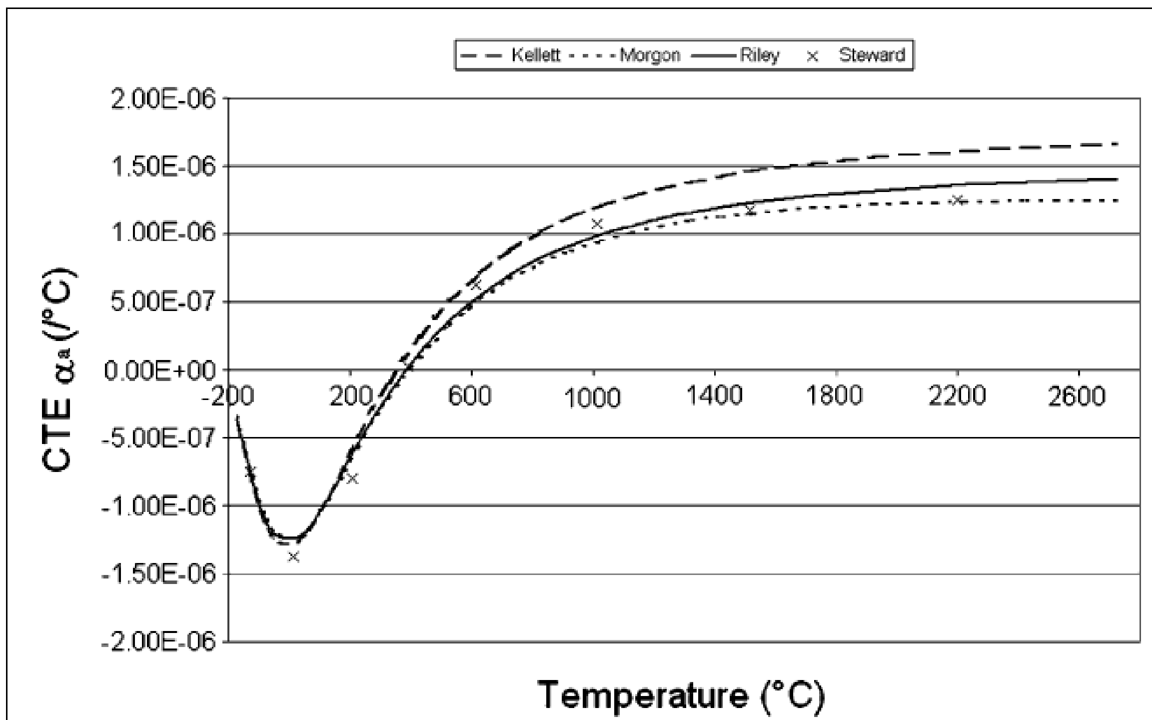

Figure 2.8 – The coefficient of thermal expansion in the a-direction results against temperature[88].

Riley[84] and Morgan[85] have also published their coefficients for the prediction of α_c, with the results shown in table 2.5. The results of Tswang et al.[88], have also been included and better correspond to the experimental values shown in figure 2.9, determined by Steward et al.[87], Nelson and Riley[89], Yates et al.[90] and Harrison[91]. Riley's[84] coefficients give reasonable values at high temperatures but overestimate the α_c at low temperatures.

	$\Theta_a(K)$	$\Theta_c(K)$	L (J/mol)	M (J/mol)	N (deg^{-2})
Morgan	2300	800	-7.93E-7	1.56E-6	7.19E-9
Riley	2280	760	-7.70E-7	1.38E-6	1.08E-8
Tsang et al.	2300	800	-5.05E-7	1.40E-6	5.15E-9

Table 2.5 – Various coefficients in the expression of α_c.

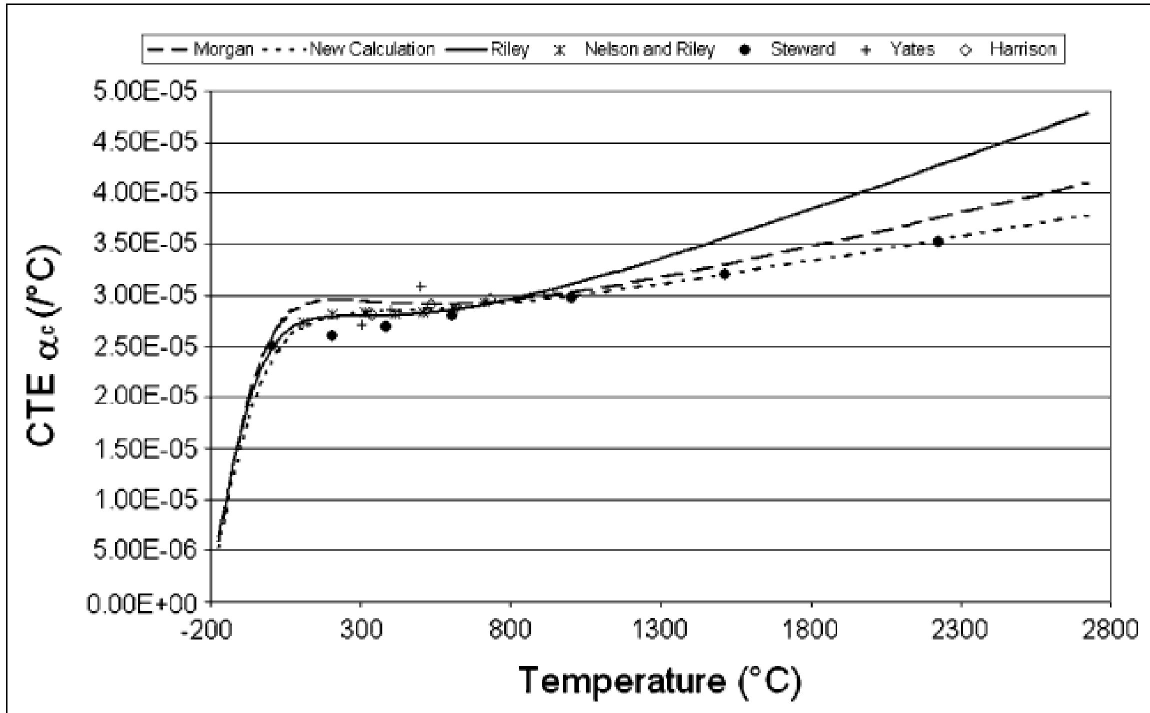

Figure 2.9 – The coefficient of thermal expansion in the c-direction results against temperature[88].

2.7. Transmission electron microscopy

2.7.1. Conventional transmission electron microscopes

In the TEM, a thin specimen is irradiated with an electron beam of uniform current density; the electron energy is in the range 60-150 keV (usually around 100 keV) or 200 keV-3 MeV in the cases of intermediate and high-voltage electron microscopes. Electrons

are emitted in the electron gun by thermionic emission from tungsten hairpin cathodes or LaB_6 rods or by field emission from tungsten filaments (used when high gun brightness is needed). The two stage condenser-lens system permits variation of the illumination aperture and the area of the specimen illuminated. A three or four stage lens system images the electron-intensity distribution behind the specimen onto the fluorescent screen. The image is then recorded by direct exposure of a photographic emulsion inside the vacuum or digitally by CCD or TV cameras[92]. The ray diagrams of the TEM are shown in figures 2.10 and 2.11.

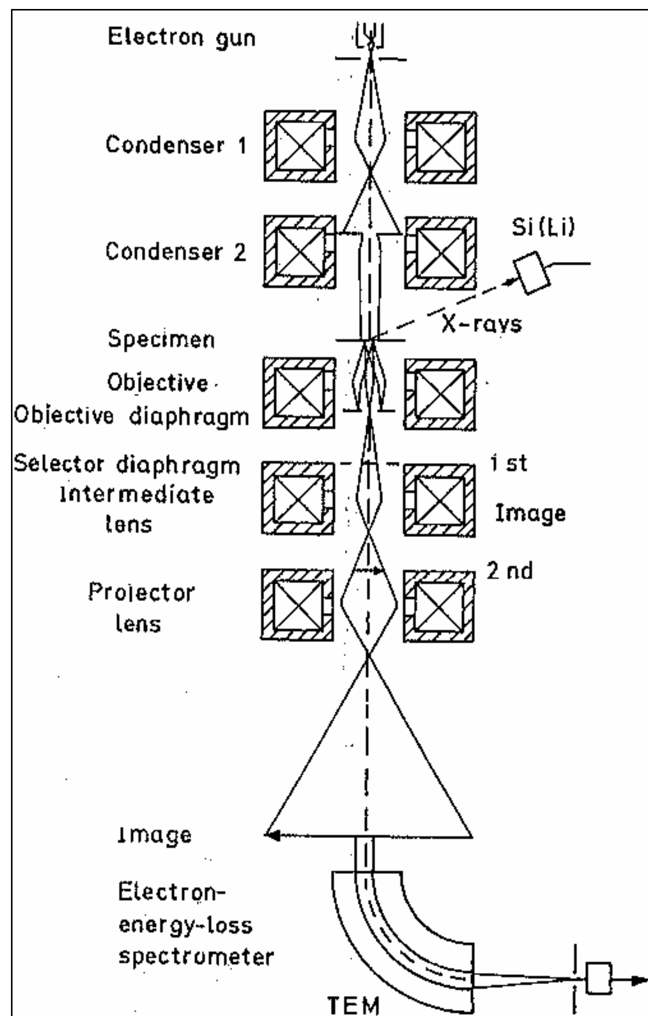

Figure 2.10 – Schematic ray path for a transmission electron microscope equipped for additional x-ray and electron energy-loss spectroscopy[92].

The lens aberrations of the objective lens necessitate the use of very small objective apertures (in the order of 10-25 mrad, to achieve a resolution of 0.2-0.5 nm). The bright field contrast mode is produced by absorption of the electrons scattered through angles larger than the objective aperture (i.e. the scattering contrast) or by interference between the scattered wave and the incident wave at the image point (phase contrast). The phase of the electron waves behind the specimen is modified by wave aberration of the objective lens. The aberration and the energy spread of the electron gun (1-2 eV); limit the contrast transfer of high spatial frequencies. Electrons interact strongly with atoms by elastic and inelastic scattering. This necessitates the use of thin samples of the order 5 nm to 0.5 µm for 100 keV electrons, depending on the density and elemental composition of the object and the resolution desired. Special preparation techniques are used, for instance electropolishing of metal foils. Thicker specimens are investigated with a high-voltage electron microscope. TEM is able to provide high resolution because elastic scattering in an interaction process that is highly localized to the region occupied by the screened coulomb potential of an atomic nucleus. Inelastic scattering is more diffuse and spreads out over about a nanometer[92].

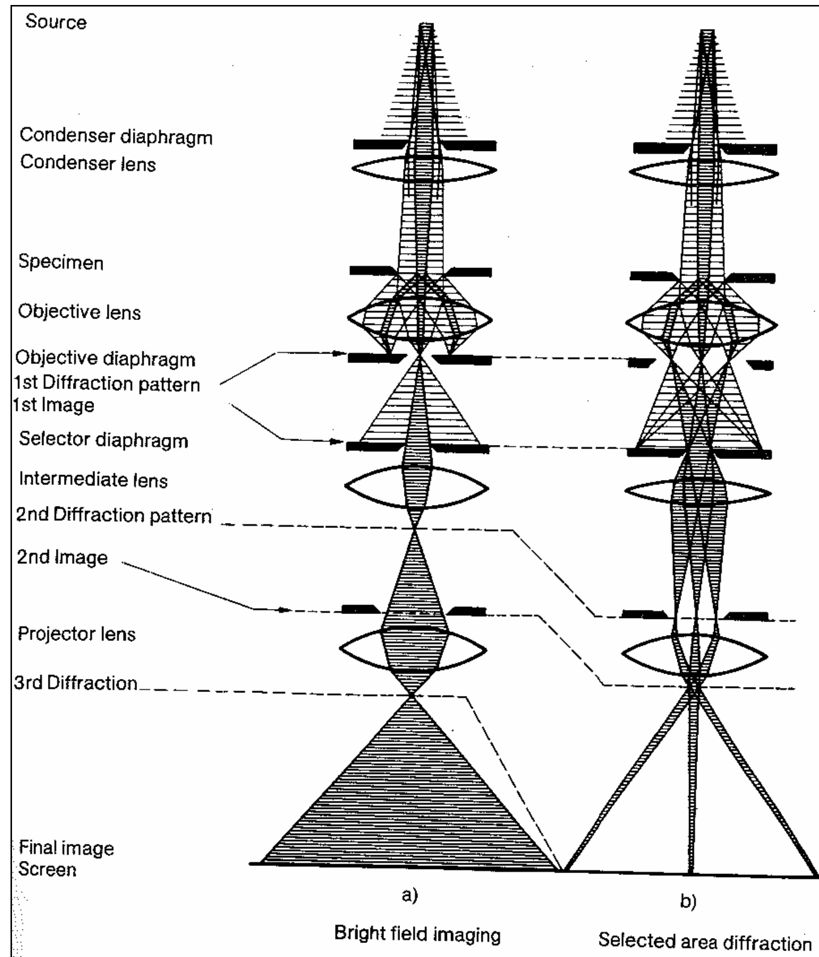

Figure 2.11 – Ray diagram for a transmission electron microscope in (a) the bright field imaging mode and (b) the selected-area electron diffraction mode[92].

2.7.2. Limitations of the TEM

<u>Sampling</u>

As with any high resolution imaging technique, the main limitation is that only a small area can be looked at for any one time. A higher resolution therefore implies worse sampling abilities of the instrument. It is necessary to examine samples with techniques of poorer resolution but better sampling abilities (such as the eye, visible-light microscope and the scanning electron microscope) before utilizing the TEM[93].

Interpreting transmission images

One of the challenges that are associated with the TEM is that it presents us with 2D images of 3D specimens that are viewed in transmission. As a result there are certain artifacts that abound in TEM images. One of the aspects of this drawback is that many of the TEM information such as imaging, diffraction patterns and spectra, is averaged through the thickness of the specimen. Therefore a single TEM image has no depth sensitivity. A full characterization of the specimen would require the assistance of surface sensitive or depth-sensitive techniques[93].

Specimen preparation

It is necessary to have thin samples to get any information from the transmitted electrons of the TEM. A sample is considered thin if it is electron transparent. A prerequisite for a specimen to be transparent to electrons is that it must be thin enough to transmit sufficient electrons such that there is enough intensity falling on the screen or photographic film. This is generally a function of the electron energy and the average atomic number of the specimen. The thinning process does affect the structure and the chemistry of the specimen thereby introducing artifacts[93].

Electron beam damage and safety

Ionizing radiation can damage the specimen particularly in materials such as polymers and some ceramics. The combination of high-kV beams with the intense electron sources that are available means that almost every sample can be destroyed. There is also a danger that is posed to the operator by the ionizing radiation[93].

2.7.3. Electron Diffraction

In the periodic potential of a crystal lattice, the electron waves propagate as a Bloch-wave field, exhibiting the same periodicity as the lattice. The interaction may be characterized by the Bragg condition:

$$\lambda = 2d \sin \theta_B \tag{2.35}$$

This relates the angle 2 θ_B between a Bragg-diffraction spot and the primary beam to the lattice-plane spacing d and the wavelength λ. The kinematical theory of electron diffraction assumes that the amplitude of a Bragg diffracted wave is small compared to that of the primary wave. This is applicable only in for very thin foils which are less than a few nanometers thick. The dynamical theory, which is based on the Schrödinger equation, also describes wave propagation in thick crystals resulting in a 'pendellösung'. This means that the amplitude of the Bragg-diffracted and primary waves oscillate in antiphase as a function of depth and depend sensitively on the tilt of the specimen. The primary beam may show anomalous transmission. A two-beam approximation is often used to discuss the main effects of dynamical electron diffraction on the beam intensity and image contrast in crystals. However, a many-beam theory with 20-100 or more diffracted beams has to be used if the observed phenomena are to be explained in detail. The pendellösung effect causes typical diffraction effects in crystal foils, that can be seen as edge or bend contours. The image intensity depends very sensitively on the strain field of any lattice defects, meaning that a large variety of defects can be imaged and analyzed without resolving the lattice structure. A resolution of the order of 1 nm is attained, if the weak beam technique (in which a dark-field image is formed with a weakly excited Bragg reflection) is used[92].

In the case where the objective aperture is so large that the primary beam and one or more Bragg reflections can pass through the diaphragm, the waves interfere in the image plane forming an interference pattern. This can furnish an image of the crystal structure and its faults, if the specimen is thin enough (≤10nm). The image contrast is often

affected by the dynamical diffraction and the phase shift of the electron lens, so that a high resolution image of lattice structures has to be analyzed with care. It is usually necessary to compare the results with computer simulations in which the crystal orientation and thickness and the phase shift caused by the spherical aberration and defocus of the electron lens are considered[92].

2.7.4. The reciprocal lattice

The reciprocal-lattice concept is important for the understanding and interpretation of electron-diffraction patterns[92]. The Laue conditions that govern the occurrence of strong diffraction to occur and are equivalent to the Bragg law are given by equation 2.44[94]:

$$\mathbf{P}\,.\,\mathbf{a} = \mathrm{h}\lambda \\ \mathbf{P}\,.\,\mathbf{b} = \mathrm{k}\lambda \\ \mathbf{P}\,.\,\mathbf{c} = \mathrm{l}\lambda \qquad (2.36)$$

The reciprocal lattice (equation 2.45) is derived directly from equations 2.44.

$$\mathbf{P} = h\mathbf{a}^* + k\mathbf{b}^* + l\mathbf{c}^* \qquad (2.37)$$

Where, $\mathbf{b}^*$ and $\mathbf{c}^*$ are vectors defined such that $\mathbf{a.a^*} = \mathbf{b.b^*} = \mathbf{c.c^*} = \mathbf{1}$ and $\mathbf{a}^*.\mathbf{b} = \mathbf{b}^*.\mathbf{a}$, etc. = 0. The relations are derived from the fact that $\mathbf{a}^*$ is perpendicular to $\mathbf{b}$ and $\mathbf{c}$ etc. Equation 2.45 is a solution of equations 2.44, since forming the scalar product of equation 2.45 with $\mathbf{a}$ leading to $\mathbf{P}\,.\,\mathbf{a} = \mathrm{h}\lambda$, the first Laue condition. The conditions that $\mathbf{a.a^*} = 1$ and $\mathbf{a.b^*} = 0$ for instance can be explained by the fact that $\mathbf{a}^*$ is perpendicular to $\mathbf{b}$ and $\mathbf{c}$, as is shown in figure 2.12, for non-orthogonal axes.

UNIVERSITEIT VAN PRETORIA
UNIVERSITY OF PRETORIA
YUNIBESITHI YA PRETORIA

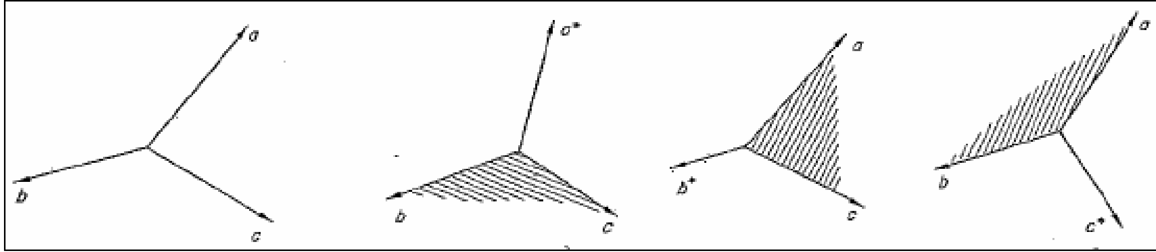

Figure 2.12 – The geometric relationships between the geometric lattice vectors $\mathbf{a}^*, \mathbf{b}^*$ and $\mathbf{c}^*$ and the real lattice vectors a, b, c.

For crystal structures with orthogonal axes (i.e. cubic, tetragonal and orthorhombic), the axes of the reciprocal lattice coincide with those of the crystal lattice[94].

The reciprocal lattice is characterized by two properties:

- The vector $\mathbf{g}_{(hkl)}$ to the point (hkl) of the reciprocal lattice is normal to the plane (hkl) of the crystal lattice
- The magnitude of $\mathbf{g}_{(hkl)}$ is $1/d_{(hkl)}$, where $d_{(hkl)}$ is the interplanar spacing of the family of (hkl) planes

The reciprocal lattice is therefore defined as an array of points, with each of the points corresponding to a particular (hkl) plane as is defined by the two properties above. In figure 2.13, the relationship between planes in the real lattice and point in the reciprocal lattice for a cubic crystal structure is shown[94].

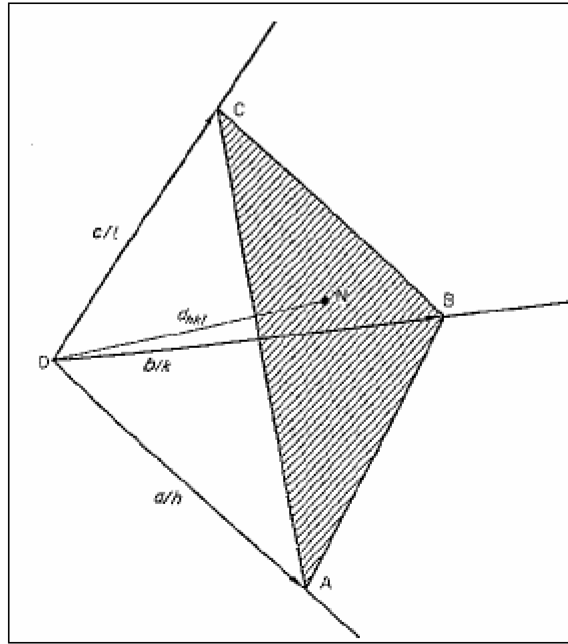

Figure 2.13 – The geometrical relationship between the plane normal and g

3. OBJECTIVES AND HYPOTHESIS

3.1. Objectives and outcomes

The composition and structural integrity of TRISO SiC are important factors in understanding its effectiveness as a barrier to diffusion products. The presence of silicon which melts at 1414°C is particularly detrimental. The transformation of SiC from one polytype to another is known to slightly alter some of the physical and thermal properties. To better understand selected properties of TRISO SiC the following objectives were pursued:

- Phase characterization by means of Raman spectroscopy, XRD and TEM. In addition to the SiC polytypes, the silicon and graphite characterization are critical

- Phase quantification by means of Raman Spectroscopy and XRD

- High temperature stability of SiC up to 1400°C by HT-XRD analysis to provide data for thermal expansion modelling. Of importance is possible phase transformation and volumetric changes

Each experimental technique aids in a unique aspect of characterizing the SiC TRISO layer.

3.2. Hypothesis

The CVD SiC layer properties of the PBMR TRISO coated particle can be characterized in terms of polytypes qualitatively and quantitatively by micro Raman spectroscopy and XRD (Rietveld method). The microstructure can be characterized by TEM.

4. EXPERIMENTAL PROCEDURE

4.1. Raman Spectroscopy

4.1.1. Samples and labeling

Ten different types of samples labeled from PO 1 to PO 10 (supplied by PBMR) were examined in this study. Only the thicknesses of the TRISO layers and the densities are known as is shown in table 4.1. The deposition temperate, rate, gas pressures and impurities are all unknown to the author. All samples used had a TRISO ZrO_2 core instead of the UO_2 used under actual irradiation conditions.

Sample	Thickness (microns)					Densities (g/cm^3)			
	Core	Buffer	IPyC	SiC	OPyC	Buffer	IPyC	SiC	OPyC
PO 1	408	67	35	5	29	1.52		3.03	1.99
PO 2	502	124	14	31	10	1.60		3.13	
PO 3	516	84	10	30	9	1.57		3.09	
PO 4	490	71	20	25	29	1.22		3.17	1.97
PO 5	483	90	13	30	32	1.62		3.13	1.98
PO 6	494	81	8	25	5	1.65		3.10	
PO 7	490	87	20	-	-	1.31		-	
PO 8	496	84	14	31	13	1.20		3.10	
PO 9	481	60	15	51	45	1.75		3.16	1.97
PO 10	520	53	50	27	20	1.00	1.43	<2.87	

Table 4.1 – Sample layer thicknesses in microns. Sample PO7 contains no SiC layer and the sample with thickest SiC layer is PO9.

4.1.2. Calibration

In order to check the instrumental error and sample error, a single crystal 4H (602069 03AA) SiC wafer from 'Intrinsic semiconductor (CREE)' was used. The instrumental error has to be significantly smaller than the sample error in order to attain reliable results.

Instrumental error

The test for the instrumental error was done by simply analyzing the same spot on the single crystal seven times. The variability in the analyses then gave the error. The selected region is in from 100 to 1600 cm^{-1} (wavenumbers). Each time, the area underneath the curve was measured by Sigma plot as a check for statistical variation. The intensities have been offset by a value of 10 000 arbitrary units, for clearer comparison as is seen in figure 4.1.

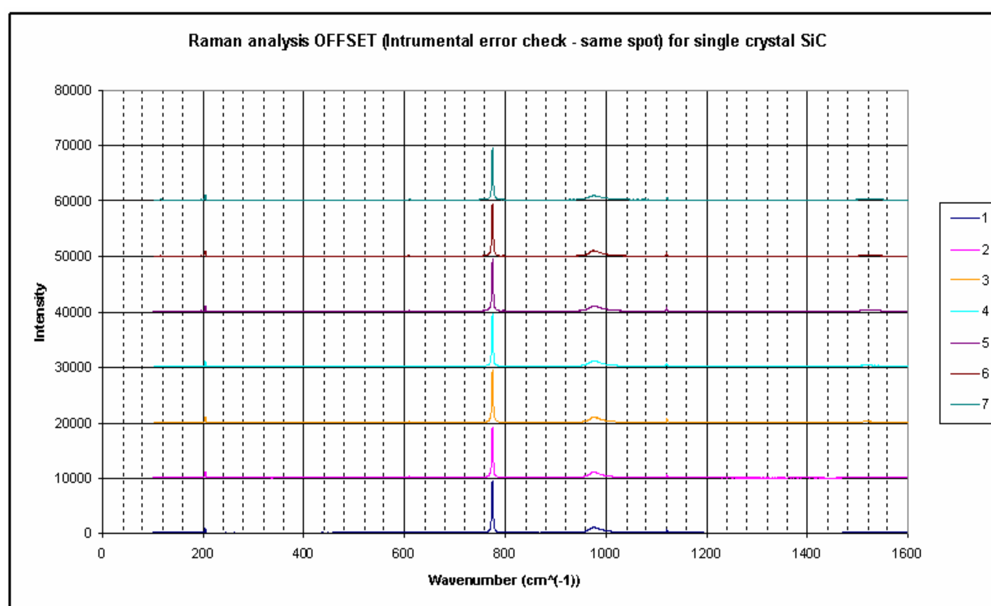

Figure 4.1 – Instrumental error analysis of the 4H single crystal wafer (Coherent Innova machine).

Instrumental Analysis						
Analysis	**Area**	**Mean**	**Std. dev.**	**Max**	**Min**	**Range**
1	259805.7	266212.7	5258.069	274693.4	259805.7	14887.68
2	260471.6					
3	263620.5					
4	268443.5					
5	274693.4					
6	268491.2					
7	267963.2	ERROR (%) = 1.98				

Table 4.2 – 4H single crystal SiC statistical data of the instrumental analysis measured area values (Coherent Innova machine), used for qualitative Raman spectroscopy results.

The measured area values are given by table 4.2. The error is calculated as the percentage of the standard deviation relative to the mean. Table 4.3 shows the error for the dispersive Raman spectroscopy machine used for constructing the calibration curve. The sample analyzed was the 4H single crystal SiC.

Instrumental Analysis						
Analysis	**Area**	**Mean**	**Std. dev.**	**Max**	**Min**	**Range**
1	5719318.5	5831516.1	81111.237	5965571.5	5719318.5	246253
2	5788042					
3	5781072					
4	5817125					
5	5858365.5					
6	5965571.5					
7	5891118.5	ERROR (%) = 1.39				

Table 4.3 – 4H single crystal SiC statistical data of the measured area values of the instrumental analysis (Renishaw RM 2000 inVia), used for quantitative Raman spectroscopy results

Sample error

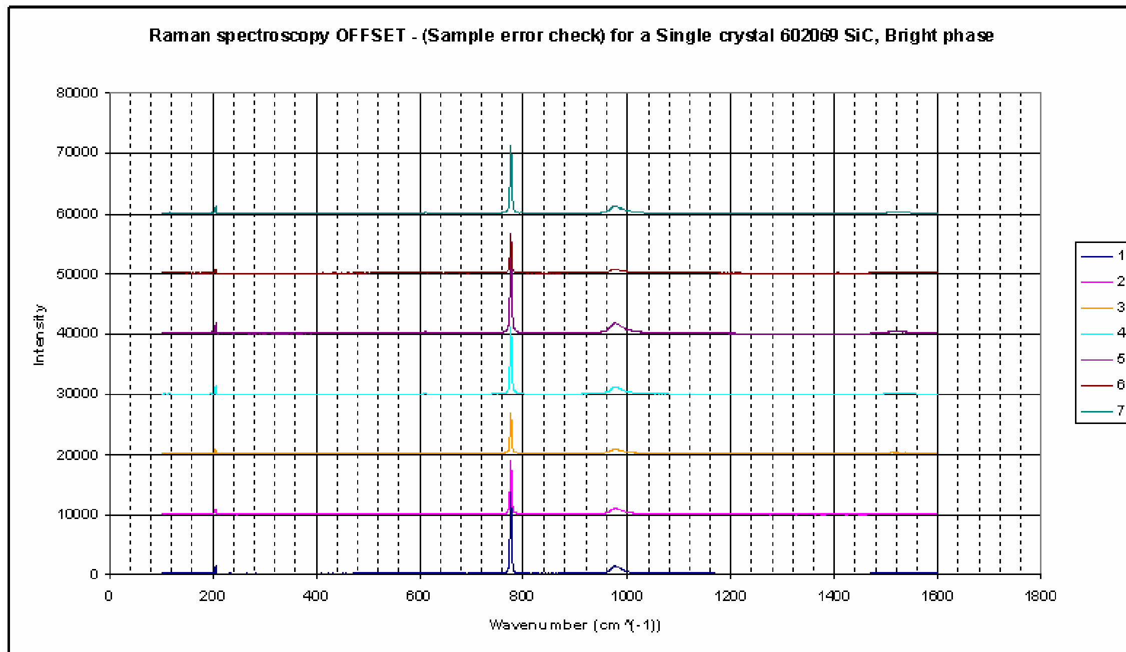

Figure 4.2 – Sample errors analysis of the 4H single crystal wafer (Coherent Innova machine).

The test for the sample error was done by varying the laser beam across the surface of the single crystal wafer for a total of seven analyses. The chosen wavenumber region is again 100 to 1600 cm^{-1} and intensities are offset by a value of 10 000 arbitrary units as is shown in figure 4.2. The measured area values are given by table 4.4.

Sample Analysis						
Analysis	**Area**	**Mean**	**Std. dev.**	**Max**	**Min**	**Range**
1	303280.7	249815	67655.5	356114.7	147675.5	208439.2
2	214283.4					
3	356114.7					
4	226916.9					
5	226916.9					
6	147675.5	ERROR (%) = 27.1				
7	273516.9					

Table 4.4 – Statistical data of the measured area values of the sample analysis (Coherent Innova machine)

The sample error of the Renishaw RM 2000 inVia machine is further discussed in the section 5.2.3.

4.1.3. Qualitative analysis

<u>Sample preparation</u>

The samples, in the as-received condition were fully spherical TRISO particles. The samples were mounted in resin inside sample holders with a design that is shown in figures 4.3 and 4.4. The material used is 1 inch diameter brass. The 0.52mm depth of the cylindrical cutaway was determined by taking half of the average diameter value of 25 TRISO particles analyzed by optical microscopy. Samples were then mounted in resin and polished.

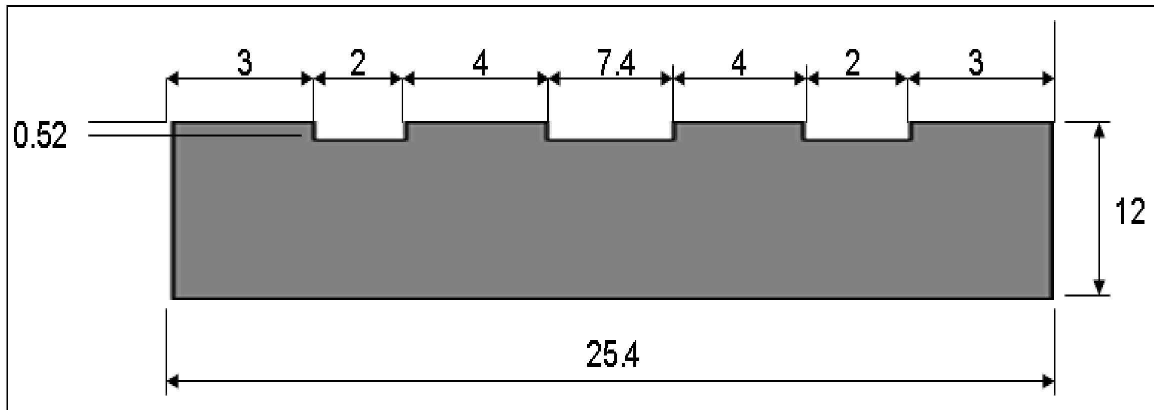

Figure 4.3 – Sample holder design (side view). Units are in millimeters.

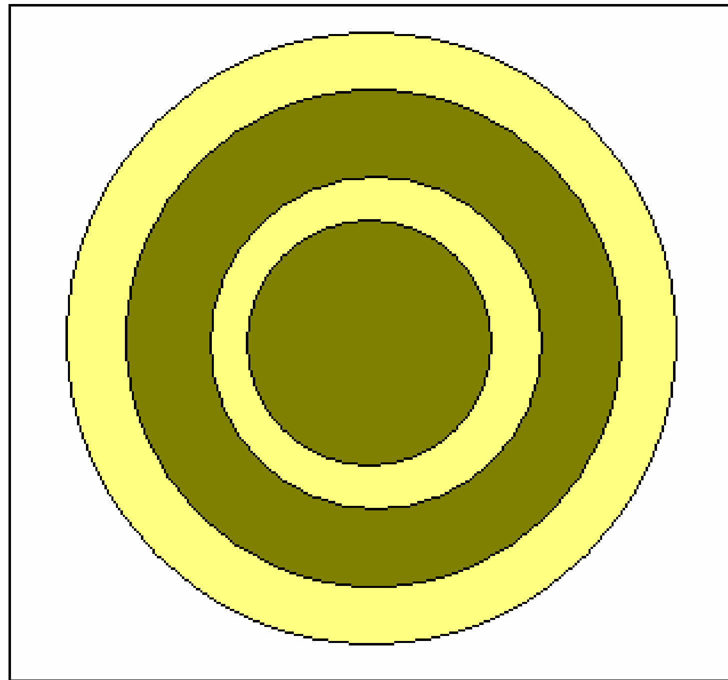

Figure 4.4 – Sample holder design (top view)

It was decided to compare TRISO coated particles that were polished only and particles that were polished and etched (with a mixture of NaOH, $K_3Fe(CN)_6$ and H_2O). Sample PO7 was found to contain no SiC layer and hence no analysis is available.

Analysis of samples

The qualitative analyses were done using the dispersive Raman spectroscopy Coherent Innova machine fitted with the Olympus BH2 microscope. Most of the samples were analyzed with the Coherent Innova 300 Ar^+-ion laser using a 514.5 nm excitation line, with a spectral resolution of 2.2 cm^{-1} and a microscope spatial resolution of < 2μm. In other cases the Stabilite 2017 Kr^+-ion laser with an excitation line of the 647.1 nm was used. The light intensities were between 0.1W and 0.2W. The laser beam was formed to a spot diameter of ~6μm, with an objective lens of 50X magnification.

It was decided to compare TRISO coated particles that were polished only and particles that were polished and etched The Murakami etching[9] procedure was followed, (with a mixture of NaOH, $K_3Fe(CN)_6$ and H_2O).

The SiC layer was in each case characterized by analyzing several spots in a straight line along the cross-section (i.e. A to H). Samples were analyzed from the innermost part of the SiC (closest to the ZrO_2 core) to the outermost part. For instance if the analysis is from point A to H, then A represents the point closest to the centre of the particle (innermost) and H represents the point furthest to the centre of the particle (outermost). This labeling system is illustrated in figure 4.5. The numbers of analyses vary because the SiC layer thicknesses also vary.

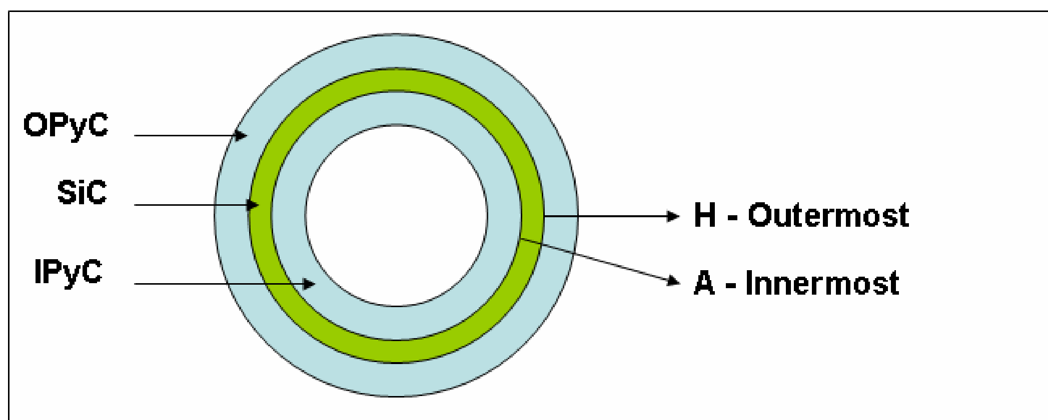

Figure 4.5 – Labeling system used for qualitative micro Raman spectroscopy analyses.

Peak de-convolution procedure

Peak de-convolution was done using LABSPEC 404[95] in an attempt to identify peak positioning and hence the polytypes that are present in the sample. The following procedure was followed:

- The region which was extracted is across wavenumbers 700-1000 cm^{-1}.
- Three bins were used for filtration as a moving average. There is a tradeoff between the level of detail and filtering the noise.
- Removal of the background followed the shape of the spectra; therefore both linear and polynomial profiles were used.
- Peaks were identified and the Lorentzian distribution was chosen as opposed to the Gaussian distribution.
- The peaks were approximated and then de-convoluted.

4.1.4. Quantitative analysis (calibration curve)

Experimental setup

Analytic grade silicon (99.99%) was mixed with monocrystalline SiC wafers supplied by Cree (formerly Intrinsic Semiconductor). The polytypes used are 4H (602069 03AA) and 6H (503030 04AA). In addition a 3C sample was prepared by the Nuclear Energy Corporation of South Africa (NECSA); the details are contained in the appendix B section. This sample underwent a heat treatment of 750°C for 24 hours in order to oxidize the outer graphite layer formed during manufacturing. Each of these polytypes was used to construct a calibration curve. The following procedure was used:

- Mixtures - the proportions used are 5%, 25%, 50% and 75% silicon by mass. The total mass of each mixture is approximately 0.045g (<1% error)
- A Retsch MM 301 mixer mill with a steel ball and lining was used to ensure homogeneity and a fine grind of ~ 5µm. Fine grinding was wet in ethanol. The

capacity of the mill is 35ml and the ethanol used filled about 30% of the container. The mixture was vibrated at a frequency $15s^{-1}$ for 30 minutes.

- Samples were pressed under a uniaxial load of 10 tons for 10 minutes. No binder was used. The sample holder design is shown in figure 4.6.

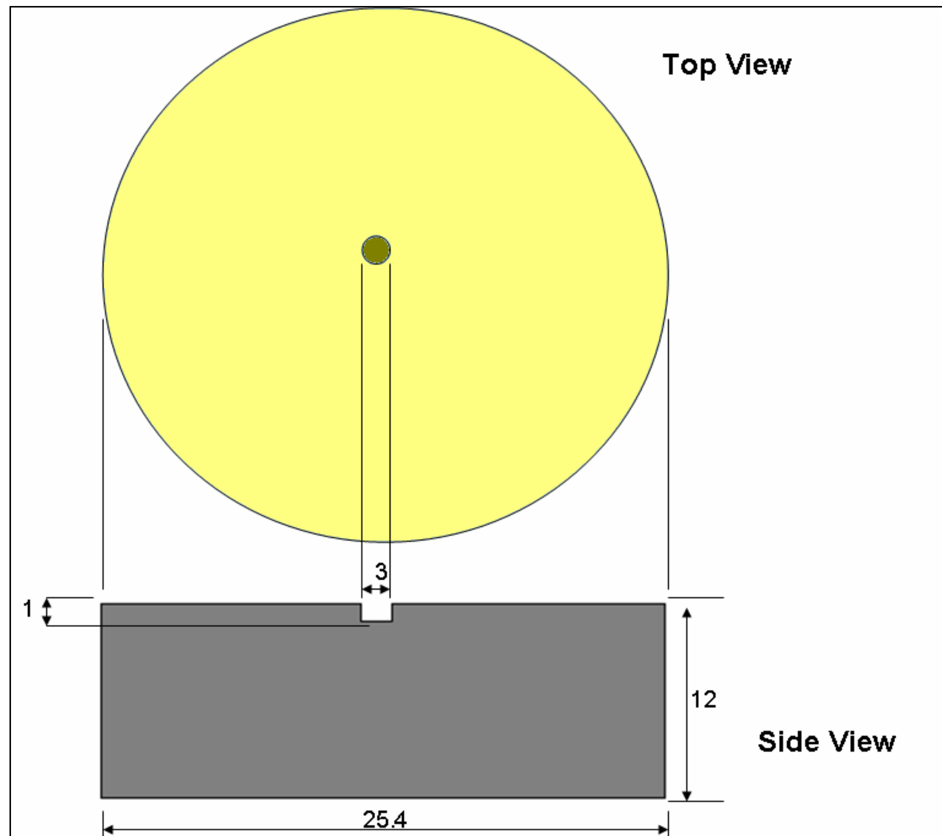

Figure 4.6 – Sample holder design. Manufacturing material is brass. Units are in millimeters.

The measurements were done using the Renishaw RM 2000 inVia Raman spectroscopy microscope using the 514.5 nm excitation line of the Ar^+-ion laser with a spectral resolution of approximately $1cm^{-1}$ and a microscope spatial resolution of $< 1\mu m$. The power of the laser was 0.1W at 8 amps. The quantitative analysis was done at 5x magnification and for each mixture, 10 analyses were taken. Two repetitions were done for each analysis for 20 seconds each. The laser beam was defocused by 25% in order to spread the laser beam and quantitatively analyze a larger area.

Error analysis

The 50% silicon – 50% 3C SiC batch mixture was subdivided into 5 sub-samples in an attempt to calculate the errors within each sample and the scatter across similar samples. Each of samples was analyzed 10 times, using the Renishaw RM 2000 inVia Raman microscope using the 514.5 nm excitation line of the Ar^{+}-ion laser.

4.1.5. Improved calibration curve

Particle size distribution measurements

The particle size distributions of silicon and SiC were measured using the Malvern Analyzer MU 2000. Analyses were done with the minerals in slurry form. The amount of each of the chemicals was determined by the extent of the laser obscuration, which had to be between 10 and 20%. The pumping rate was 2050 rpm. An ultrasonic displacement of 5.5 µm, applied for 10 seconds was used for improved particle dispersion. The analyses spanned 60 seconds and an average from two runs was used as the final result. The refractive indices of silicon and SiC were chosen as 3.5 and 1.5 respectively.

Separation by particle sizes

The +38 µm particles were separated as the oversize by means of a 38 micron sieve. The particles were in slurry form and were thoroughly dispersed and flushed under running water, until only the oversize was left. The undersize was collected in a pan. All particle sizes were dried in pans with an oven operating at 70°C.

The -38 µm particles (in slurry form) were poured into a measuring cylinder, with a volumetric scale that corresponded to the length in centimeters. Water was then added to fill the cylinder such that the slurry reached a height of 20 cm. The settling rate per particle size was determined by Stokes' law.

After the +10 -38 μm particles had settled, the -10 μm slurry was removed with a 30 ml pipette. While the -10 μm was allowed to settle, the +10 -38 μm particles were dried in the oven.

Annealed SiC and Si powders

Silicon and SiC powders obtained from American Elements were annealed at 1000 and 1100°C respectively, by means of a horizontal tube furnace in an inert atmosphere. The powders were placed inside flat-bottomed, boat-shaped sample holders. The furnace was heated up from room temperature to 1000°C in 2 hours and allowed to stabilize for a further 90 minutes. A similar heating rate was used for heating up to 1100°C. It took a total of 4 hours before the reading from the thermocouple stabilized at 1100°C. This is because the furnace was approaching its maximum operating temperature. The hot-zone in the furnace was detected and measured by means of a k-type thermocouple. Argon gas was used at a flowrate of 1-2 L/min. The annealing times for both the silicon and SiC are 2, 4 and 8 hours. The samples were cooled within a few minutes in air.

4.2. X-ray Diffraction

The XRD patterns of all samples were obtained using a PANalytical X'Pert Pro powder diffractometer with CoKα radiation (λ = 1.78901Å). No monochromator was used. The generator settings used are 35 kV and 50 mA. Collection of the powder patterns used for Rietveld analysis is discussed below.

4.2.1. Analysis of experimental samples from PBMR

The 10 samples issued by PBMR (i.e. PO1 to PO 10) were analyzed in two conditions:

- Firstly, in the as-received condition with all the layers intact
- Secondly samples were analyzed with the outermost PyC layer removed via oxidation at 850°C

The unbroken TRISO particles were loaded to fill the 10mm diameter of the sample holder and therefore to give average measurements across many particles. The analysis was performed across an angular range (2θ) of 5° to 120° using a step width of 0.008^o and a counting time of 15.4 seconds per/step with a rotating sample holder. Programmable divergence slits are used in addition to an X'Celerator scanning detector.

The analyses were refined using the BGMN Rietveld analysis program, AUTOQUAN [96]version 2.7.0.0. The polytypes of SiC which were considered in the refinements are the 3C, 2H, 4H, 6H, 8H and 15R. In addition to these the following were also included in the refinements:

- Graphite (from the buffer, IPyC and OPyC)
- Tetragonal ZrO_2 (from the core)
- Silicon (free silicon)
- Quartz (impurity)

In cases where phases were almost absent no refinements of such phases was possible and these were not considered in the calculations. The key parameters are the crystallite size, the particle size, the microstrain and preferred orientation.

4.2.2. Quantitative analysis (calibration curve)

The same samples used for the calibration curve by Raman spectroscopy were analyzed by quantitative x-ray diffraction. The samples were removed from the 1-inch diameter sample holder and placed on a zero background sample holder with the surface of the powder as flat as possible.

The analysis was performed across an angular range (2θ) of 5° to 90° using a step width of 0.017^o and a counting time of 3.0 seconds/step with a rotating sample holder. In addition programmable divergence slits are used along with an X'Celerator detector.

The analyses were also refined using the Rietveld analysis program AUTOQUAN version 2.7.0.0. The following were included in the refinement:

- The relevant SiC polytype phase (main polytype, i.e. 3C, 4H or 6H)
- Silicon (other main constituent)
- Other SiC polytypes (impurities). Only 3C, 2H, 4H, 6H, 8H and 15R are considered
- Graphite (impurity)
- Quartz (impurity)
- α-Fe (contaminant from grinding)

The criteria used for refinement are identical to those used for analyzing the TRISO particles from PBMR.

4.2.3. XRD analysis of sample with removed α-Fe

In order to investigate whether microabsorption plays a significant role in the quantitative XRD investigation, a separate sample was prepared by mixing 50% 4H-SiC with 50% silicon. The same preparation procedure which includes weighing-off, fine-grinding and mixing was followed. The method followed for the removal of α-Fe is as followed:

- The binary mixture is placed inside a 20 ml vial.
- HCl (32% concentrated) is added to fill the vial in order to dissolve the α-Fe.
- After the particles have settled, the HCl is removed with a pipette attached to a rubber stopper. Only the HCl directly in contact with the mixture is left.
- The HCl is diluted with distilled water in order to wash the mixture from the acid. After settling the now dilute acid mixture is removed by the pipette and more distilled water is added.
- This procedure is repeated a total of 5 times (until thorough washing of the sample had taken place).

- The wet mixture inside the vial is placed on a hot stove at 150°C inside a fume cupboard for 15 minutes.
- The dry binary mixture was removed from the vial and placed in a sample holder before being uni-axially pressed together before analysis with XRD and refinement with AUTOQUAN.

4.2.4. High temperature XRD

The TRISO particles are fixed to a heating strip by alumina cement, which is also the standard used for calibrating the SiC. One of the analyses (G102) was done using a molybdenum heating strip with helium as the inert gas, while the other two (PO4 and PO9) made use of a graphite heating strip under ultra high purity nitrogen. The Anton Paar TCU 2000 temperature control unit was used to heat up samples up to 1400°C, by following the following steps:

- Starting from room temperature (25°C), heating up was in increments of 100°C from 100°C to 1100°C
- From 1100°C to 1400°C increments of 25°C are used heating up
- Cooling down from 1400°C to 1100°C, increments of 50°C are used
- Cooling from 1100°C to 26°C was done in a single step

It took a total of 5 hours to heat up and cool down the samples. The Rietveld method using the TOPAS[97] software package was used to refine the lattice parameters by updating each next step with the data for that specific temperature. The analysis was performed across an angular range (2θ) of 5° to 120°, using a step width of 0.033^{o} and a counting time of 11.9 seconds/step. A single simultaneous refinement was performed on all data from the same run or sample. The zero point and crystallite sizes of the phases were refined collectively for all runs, whilst the sample displacement and lattice parameters were individually refined for each run at a different temperature.

4.3. TEM experimental procedure

Thin slices cut from TRISO coated particles were ground to a thickness of approximately 30 microns and polished to further reduce the thickness. The resulting disks were mounted on molybdenum rings with holes that were punched in the centre. Two argon guns operating at 1 kV and 24 (for the left), 29 mA (right) under an angle of 8° were used for the etching of the samples. Sample PO 6 had to in addition be etched from both sides, with the second side etched at 4°. The arrangement of the experimental setup used for analyzing sample PO 9 is shown in figure 4.7. The other two samples had only one disk mounted on the molybdenum ring. The thin area had to be <125 nm for analysis to be possible.

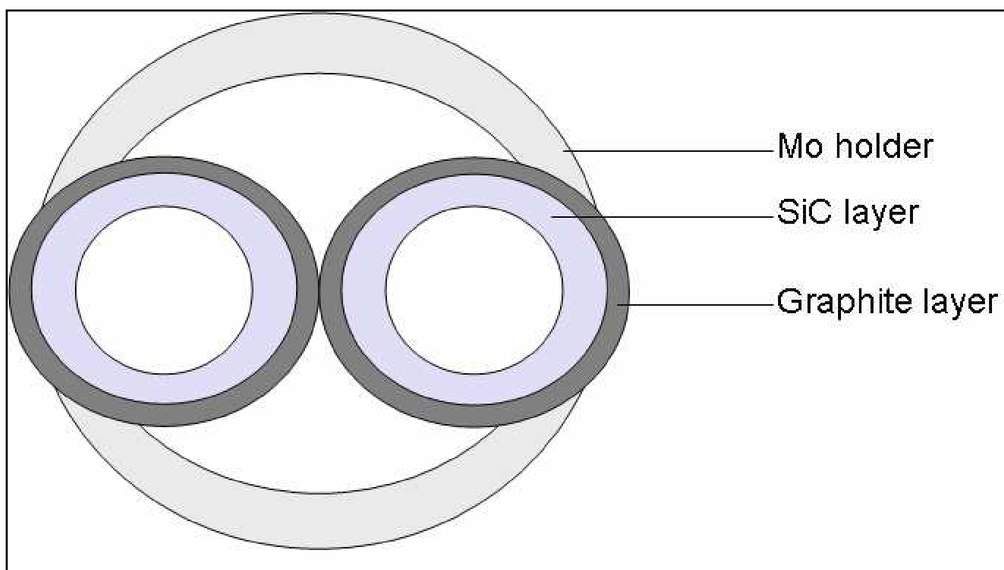

Figure 4.7 – Sample arrangement upon analysis with the TEM for sample PO 9.

The TEM studies were done using a Philips CM 200 electron microscope operating at 160 kV, with a point to point resolution of 0.24 nm and a line resolution of 0.204 nm. The images were collected and analyzed using the Gatan DigitalMicrograph version 3.11.2 for GMS 16.2 software package. The calculated diffraction patterns were generated using the JEMS software package[98].

5. RESULTS AND DISCUSSION

5.1. Qualitative Raman Spectroscopy

The characterization of components such as silicon, SiC polytypes and graphite are key to understand the integrity of the TRISO particles. Using peak positioning, it is possible to characterize each of these components. SiC polytype characterization however required peak deconvolution to result in more meaningful analyses. The Lorentzian peak shape is chosen because it was a closer match to the peaks than the Gaussian profile. The detailed procedure is in section 4.1.3 of the experimental procedure. Peak deconvolution was confined only to the TO SiC peaks and of particular significance is the main peak, where the 3C and 6H SiC main peak coincide. The deconvolutions shown are for the innermost analysis (analysis A in each case is the point closest to the IPyC layer).

5.1.1. Characterization of PO samples

Table 5.1 is a summary of peak positions of the etched and unetched samples (PO1-6 and 8-10). Sample PO7 is not included because it contained no SiC layer. The 3C and 6H polytypes are both identified in all the samples. There is evidence of the 15R polytype in some of the samples. Either some crystalline or amorphous silicon (or a combination of the two) is identified in all the samples, with the exception of PO5 (where there is no evidence of silicon). Samples PO6 and PO8 had exceptionally high 520 cm^{-1} peaks of crystalline silicon (relative to the highest SiC peak). Samples PO2, PO4 and PO10 had high crystalline silicon peaks, while PO3 and PO9 had low silicon peaks. Sample PO1 was the only sample to have had significant evidence of graphite throughout the cross-section. The reason why the 1360cm^{-1} peak is sometimes seen in other analyses is because each analysis is starts or ends close to a PyC interface. Some of the FLO peaks tend to shift significantly (from the peak positions of table 2.1) and even in literature, their behaviour is not well-understood[51].

Sample	Silicon		Silicon Carbide							Carbon
	Crystalline	Amorphous	3C	3C (FLO)	6H (2/6)	6H (6/6)	6H (FLO)	15R (4/5)	15R (FLO)	
PO1 etched	X	420-540	795	969	790	765	X	X	X	1360
PO1 unetched	X	420-540	796	969	791	766	X	X	X	1360
PO2 etched	520**	420-540	796	964	790	768	X	X	X	X
PO2 unetched	520**	420-540	794	964	788	760	X	X	941	X
PO3 etched	520*	420-540	794	965	789	763	960	785	X	X
PO3 unetched	520*	420-540	794	X	788	761	961	X	X	X
PO4 etched	520**	420-540	795	969	792	770	X	X	X	X
PO4 unetched	520**	420-540	794	967	790	765	X	X	940	X
PO5 etched	X	X	795	971	792	764	X	X	X	X
PO5 unetched	X	X	794	971	791	763	X	X	X	X
PO6 etched	520***	X	794	967	788	763	X	X	943	X
PO6 unetched	520***	X	794	965	787	771	X	X	939	X
PO8 etched	520***	X	794	965	788	766	X	X	X	X
PO8 unetched	520***	X	793	964	788	759	X	X	937	X
PO9 etched	520*	420-540	797	967	790	766	X	X	X	X
PO9 unetched	520*	420-540	795	967	787	764	X	X	X	X
PO10 etched	520**	X	796	971	791	766	X	X	X	X
PO10 unetched	520**	X	794	968	790	763	X	X	X	X

Table 5.1 – Summary of peak positions identified with qualitative Raman spectroscopy (units are in wavenumbers; cm^{-1}). *, ** and *** denote a low, high and very high crystalline silicon peak. X indicates the absence of a peak.

Samples PO3, PO5 and PO6 were chosen to illustrate how the results of table 5.1 were derived. The rest of the PO samples' graphs are included in Appendix A.

Sample PO3

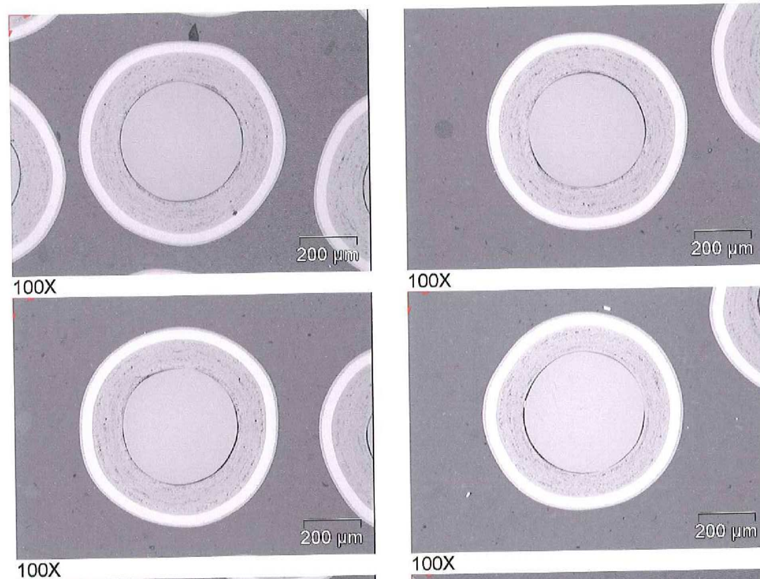

Figure 5.1 – Optical microscope images of PO3 polished coated particles.

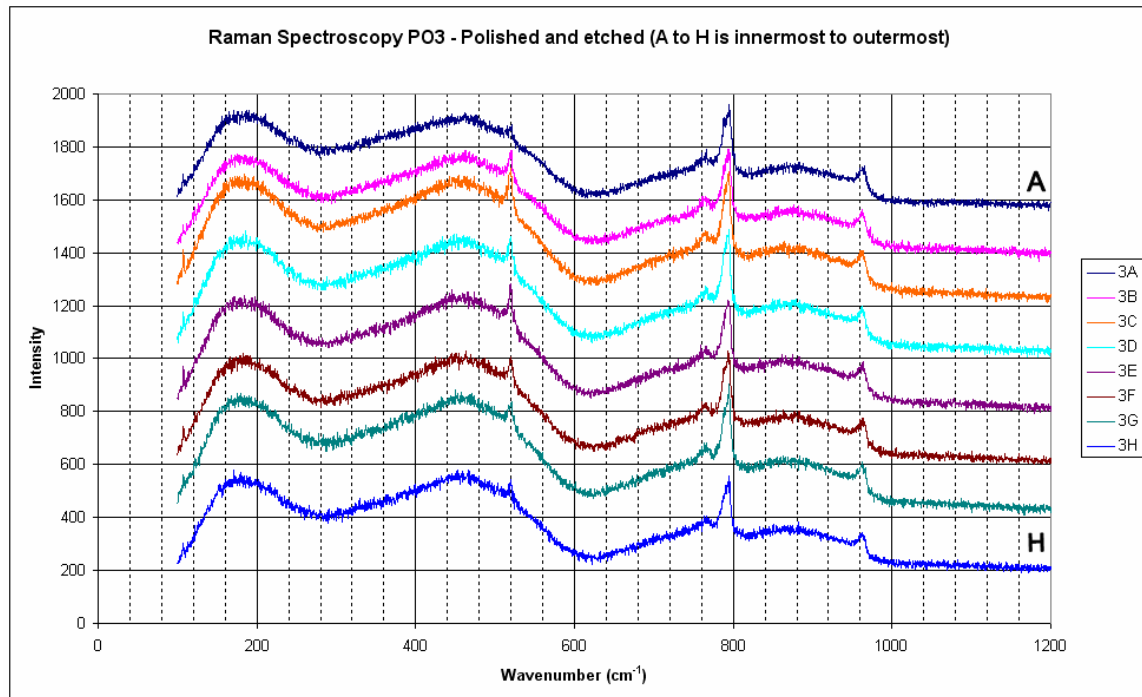

Figure 5.2 – Raman spectra of the SiC layer of a PO3 polished and etched coated particle. A is the innermost and H is the outermost spot along the SiC cross-section. There seems to be a mixture of amorphous and crystalline silicon throughout the analyses. The most intense crystalline silicon peaks occur in the middle of the SiC layer (analysis C to E)

Peak splitting is clearly evident, indicating that the 3C polytype is not the only one that is present.

Once again, there seems to be a mixture of amorphous and crystalline silicon present. In the case of the etched sample (figures 5.1 & 5.2), the crystalline silicon (occurring at 520cm^{-1}) and the amorphous (420-540 cm^{-1}) silicon both seem to be present throughout the whole cross-section. The 3C SiC is characterized by the peak of 794 cm^{-1} as is seen in figure 5.3. The presence of the 2/6 6H peak is confirmed by the peak at 790 cm^{-1}, while the 2/5 15R peak is confirmed by the 786 cm^{-1} peak. The broad peak at 963 cm^{-1} represents the 6/6 6H and 3C polytype. This is further confirmed by the LO peaks at 960 and 965 cm^{-1}. The relative broadness of the peak is an indication of disordered SiC.

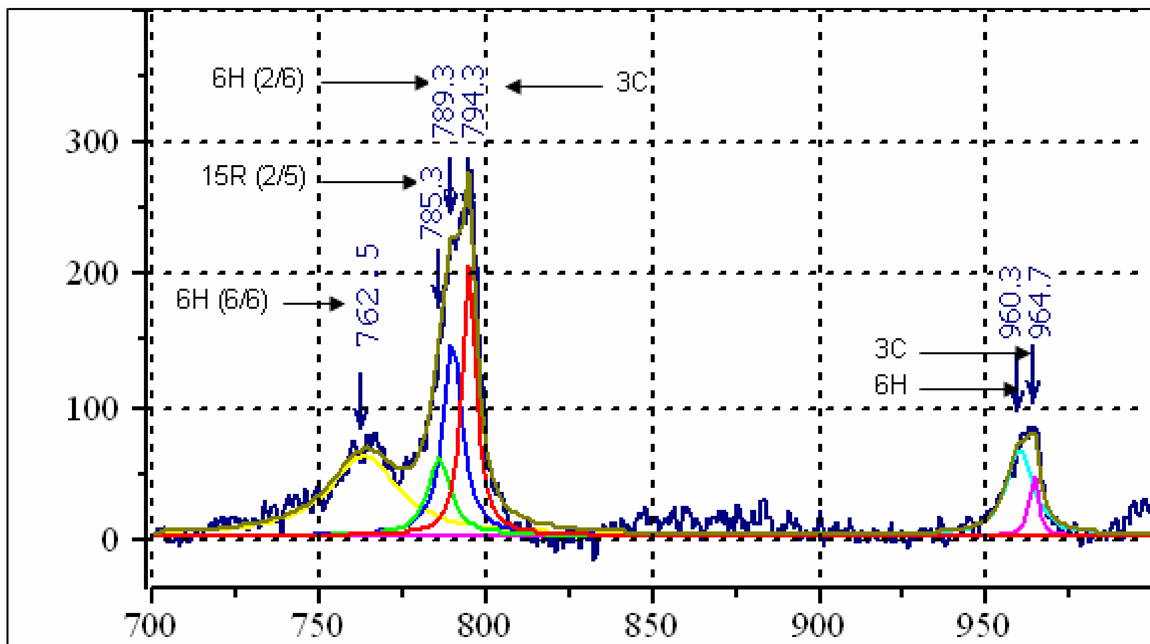

Figure 5.3 – Raman spectra of the TO SiC peaks after deconvolution for analysis 3A (etched). It was assumed that there were three components making up the main peak. The peaks indicate the presence of the 3C, 6H and 15R polytypes.

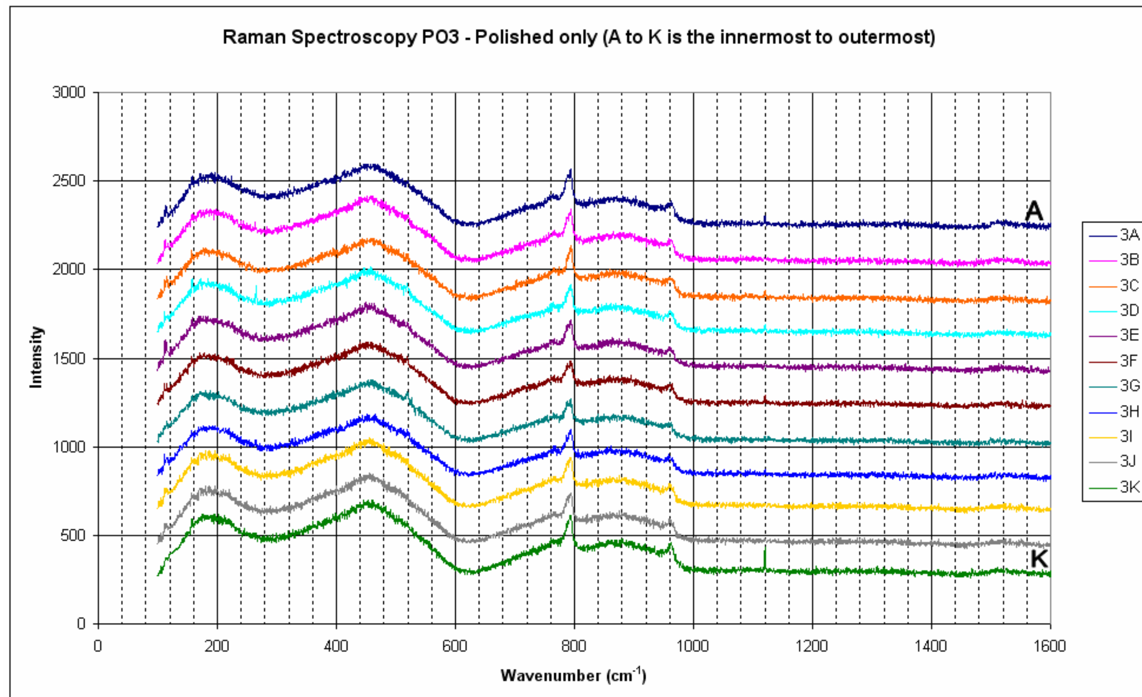

Figure 5.4 – Raman spectra of the SiC coating of PO3 polished (unetched) coated particle. A is the innermost and K is the outermost spot along the SiC cross-section. There seems to be predominantly amorphous silicon, with small crystalline silicon peaks evident for some analyses. Peak splitting is clearly evident, indicating that the 3C polytype is not the only one that is stable. There is no evidence of graphite.

With regards to the polished unetched sample (figure 5.4), amorphous silicon seems to be predominantly present in the region 420-540 cm^{-1}, with trace amounts of crystalline silicon at 520 cm^{-1}. Unlike with the etched sample, the crystalline silicon is almost non-existent. According to figure 5.5, the presence of the 3C polytype is confirmed by the 794 cm^{-1}. The presence of the 2/6 6H polytype is confirmed by the 788 cm^{-1} peak. This is further confirmed by the broad peak, which is at wavenumber 963 cm^{-1}. There is reasonable similarity between the two samples, with the exception that the 15R polytype is detected only in the etched sample.

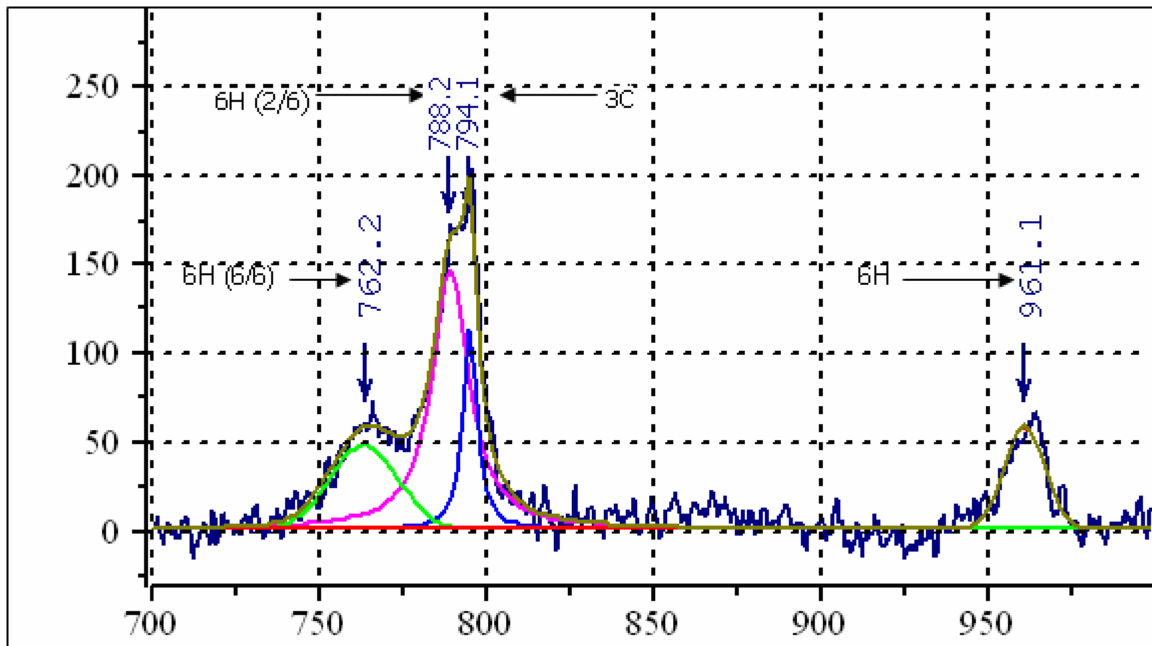

Figure 5.5 – Raman spectra of the TO SiC peaks after deconvolution for analysis 3A (polished). It was assumed that there were three components making up the main peak. The peaks indicate the presence of the 3C and 6H polytypes.

Sample PO5

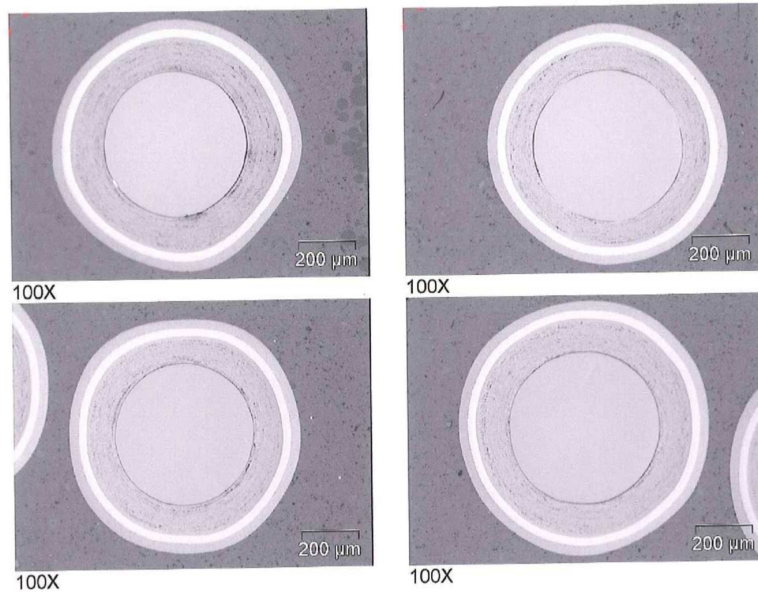

Figure 5.6 – Optical microscope images of PO5 polished coated particles.

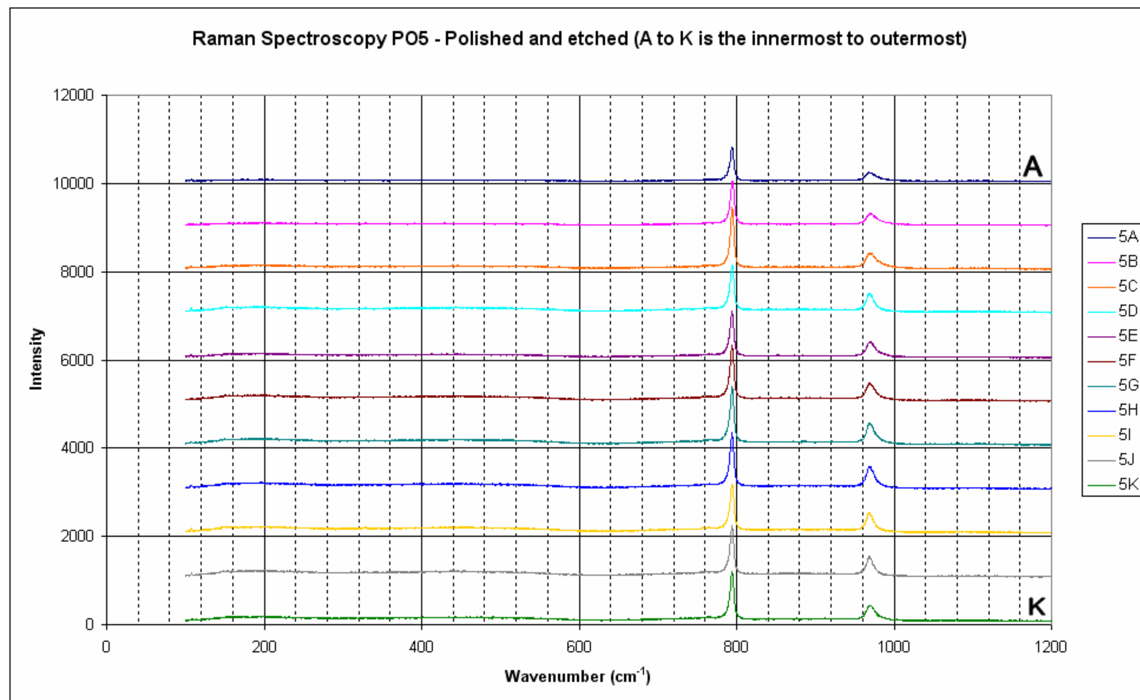

Figure 5.7 – Raman spectra of the SiC coating of PO5 etched and polished coated particle. A is the innermost and K is the outermost spot along the SiC cross-section. Neither the amorphous nor crystalline silicon is seen throughout the SiC layer. The SiC peaks do not split, however peak deconvolution indicates the presence of a relatively small 6H peak.

In the case of the etched sample, (figures 5.6 & 5.7) neither the amorphous nor crystalline silicon is seen throughout the SiC layer. The 3C SiC polytype is characterized by the TO and LO peaks at 795 cm^{-1} and 971 cm^{-1}, as is seen in figure 5.8. The presence of minor 6H polytype is confirmed by the 2/6 and 6/6 6H peaks evident at wavenumbers 792 and 764 cm^{-1} respectively. There is a low background (for both the etched and unetched samples) which is usually an indication of low fluorescence associated with PO5[99].

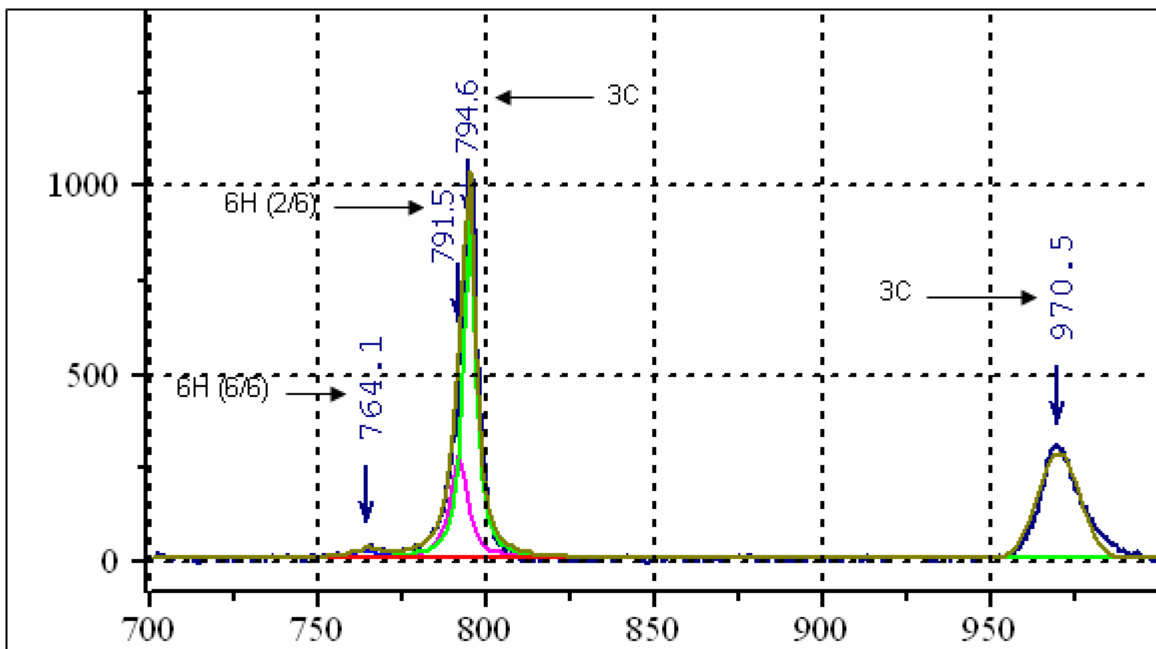

Figure 5.8 – Raman spectra of the TO SiC peaks after deconvolution for analysis 5A (etched). It was assumed that there were two components making up the main peak. The peaks indicate the presence of the 3C and 6H polytypes.

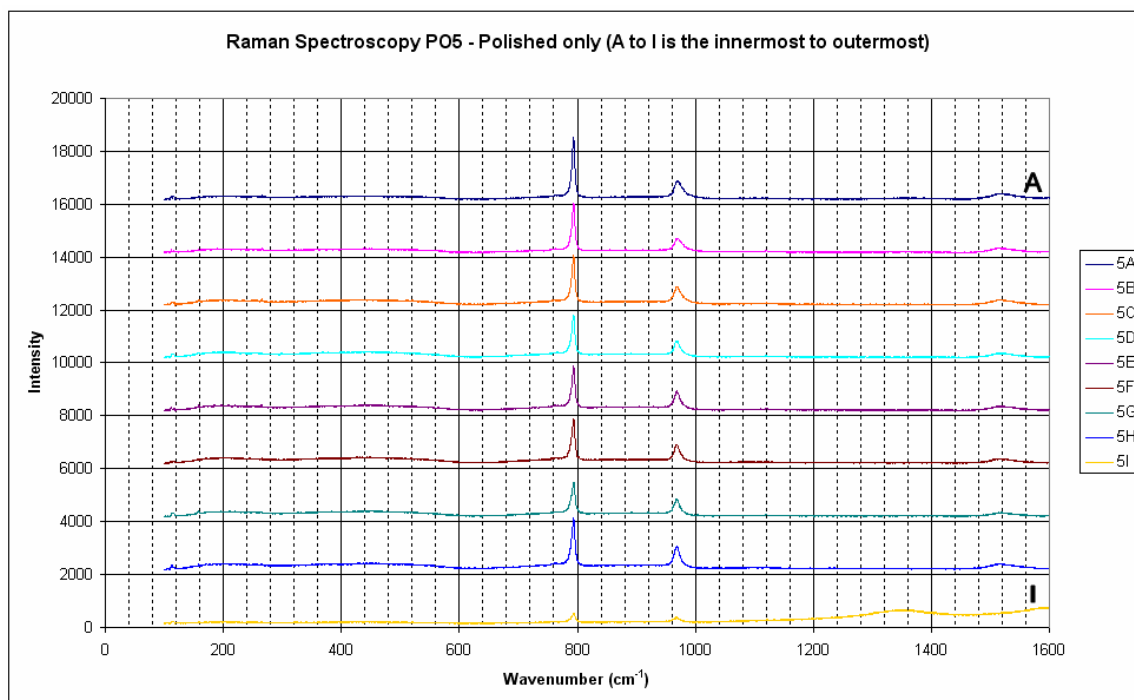

Figure 5.9 – Raman spectra of the SiC coating of PO5 polished (unetched) coated particle. A is the innermost and I is the outermost spot along the SiC cross-section. Neither the amorphous nor crystalline silicon is seen throughout the SiC layer. The SiC peaks do not split, however peak deconvolution indicates the presence of a relatively small 6H peak. Graphite is only seen at analysis I at 1360 cm^{-1}.

In the case of the polished unetched sample, (figure 5.9) the positioning of the peaks seems to be very similar to those of etched samples. No silicon is seen throughout the SiC layer. The 3C SiC polytype is characterized by the TO and LO peaks at 794 cm^{-1} and 971 cm^{-1}, as is seen in figure 5.10. The presence of the 6H polytype is confirmed by the 2/6 and 6/6 6H peaks evident at wavenumbers 791 and 763 cm^{-1} respectively. Of all the samples analyzed, PO5 seems to be the purest in terms of stoichiometry (since no excess silicon or graphite is present in the SiC layer). Analysis I is probably an analysis of the SiC-OPyC interface thereby resulting in significantly smaller SiC peaks and graphite. Also, the 3C polytype seems to be most abundant in this sample.

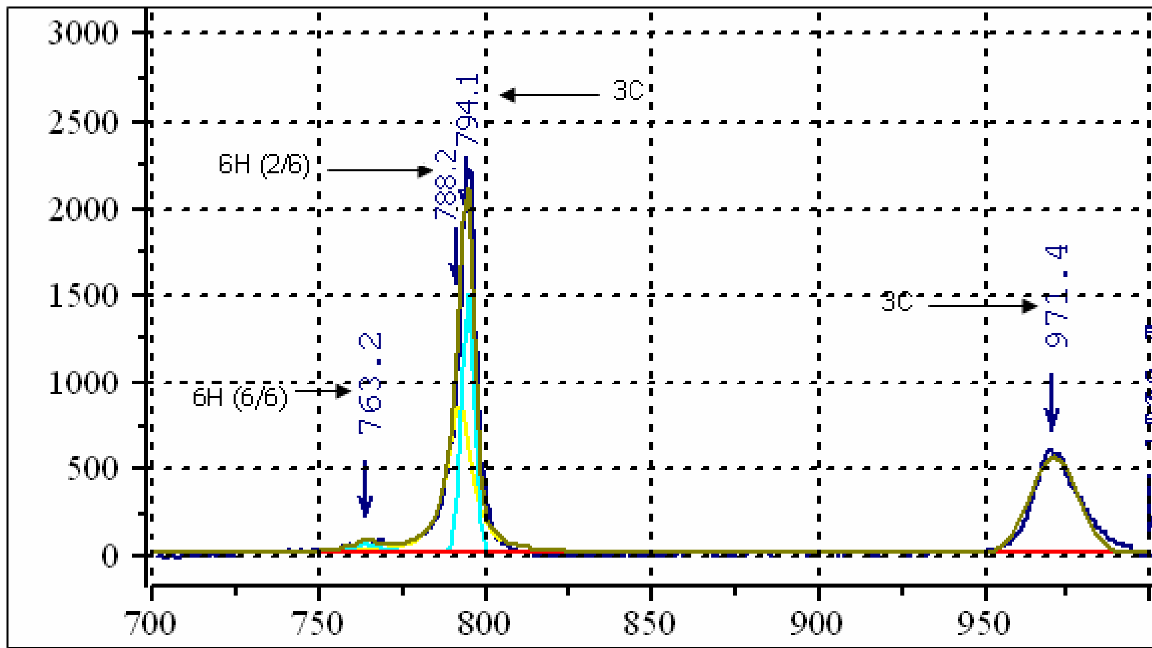

Figure 5.10 – Raman spectra of the TO SiC peaks after deconvolution for analysis 5A (polished). It was assumed that there were two components making up the main peak. The peaks indicate the presence of the 3C and 6H polytypes.

Sample PO6

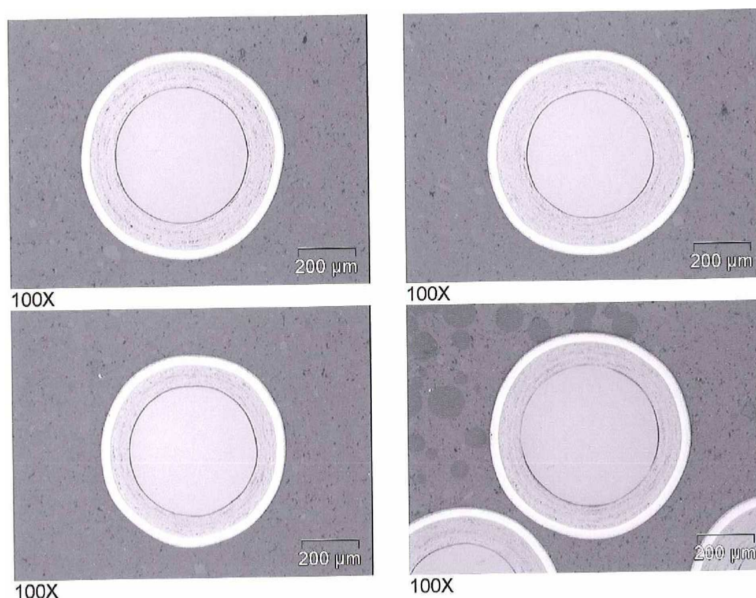

Figure 5.11 – Optical microscope images of PO6 polished coated particles.

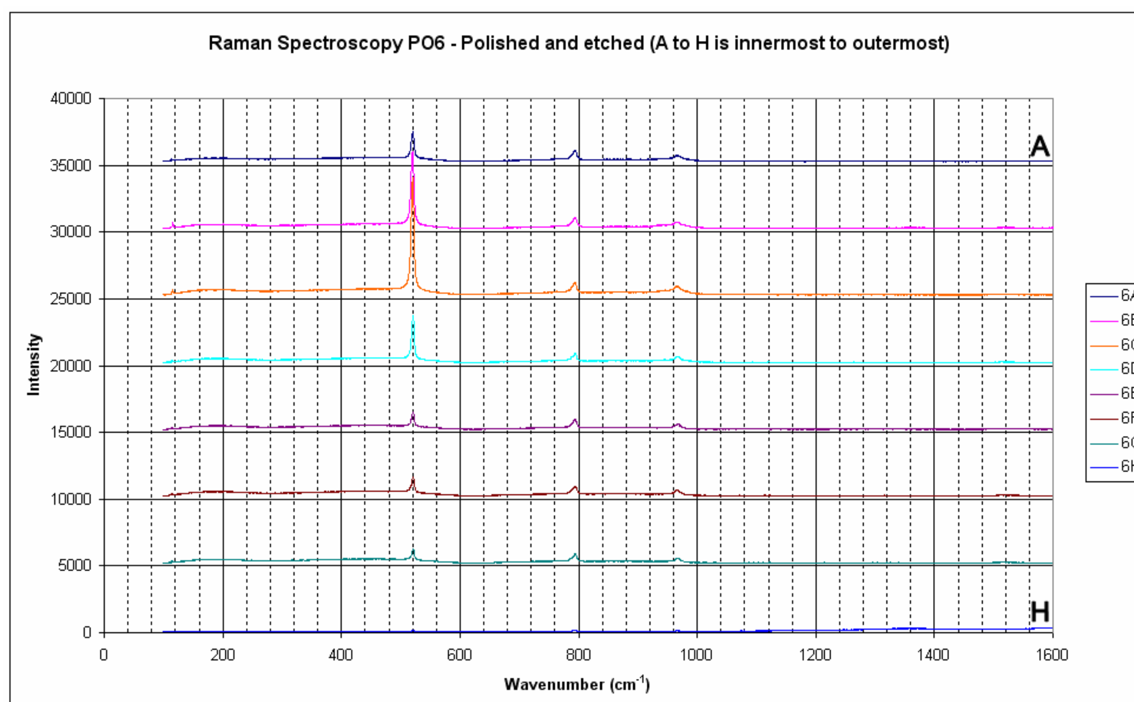

Figure 5.12 – Raman spectra of the SiC coating of PO6 polished and etched coated particle. A is the innermost and H is the outermost spot along the SiC cross-section. The crystalline silicon progressively increases from analysis A to C before declining again. The silicon to SiC ratio of peaks is particularly high relative to that of other samples.

Consequently, there is very little that can be said about the SiC peaks. There is a hint of graphite detected from the slight change of slope from analysis B.

With regards to the etched sample, (figures 5.12 and 5.13) the crystalline silicon occurring at 520cm^{-1}, seems to be more abundant from the innermost part of the SiC (analysis A-D). Hence the Si:SiC ratio increases upon moving closer to the centre (core) of the SiC layer. Unlike with previous samples, the crystalline silicon peak is significantly higher than that of the SiC (with a maximum at analyses B and C). The 3C SiC is characterized by the peaks at 795 and 965 cm^{-1}, as seen in figure 5.13. The peaks occurring at 790 and 763 cm^{-1} confirm the presence of the 2/6 and 6/6 6H peaks. The split of the LO peak resulting in the peak occurring at 943 cm^{-1} is thought to be due to the 2/5 15R polytype. Excess graphite is seen at 1360cm^{-1} at analysis B.

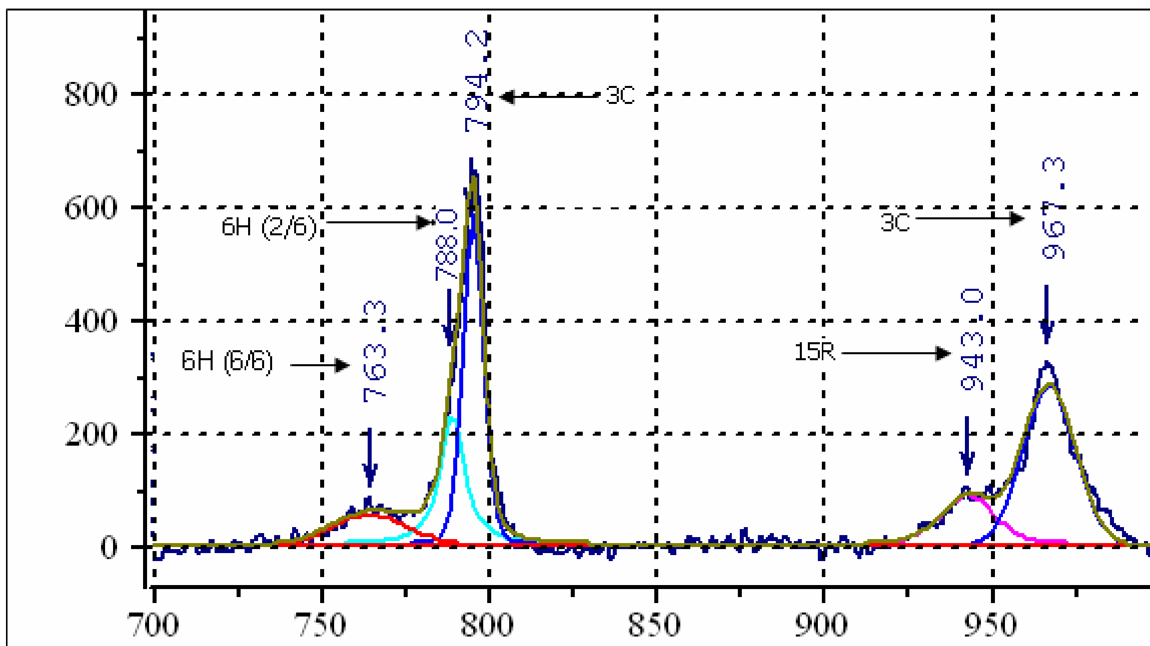

Figure 5.13 – Raman spectra of the TO SiC peaks after deconvolution for analysis 6A (etched). It was assumed that there were two components making up the main peak. The peaks indicate the presence of the 3C and 6H polytypes.

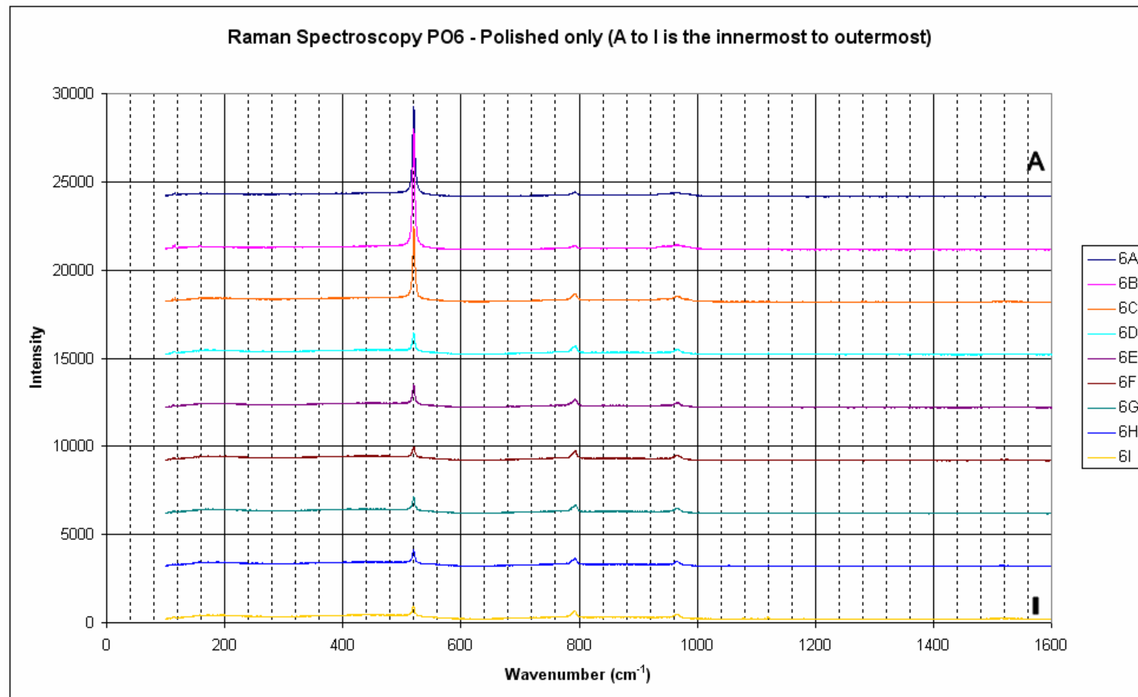

Figure 5.14 – Raman spectra of the SiC coating of PO6 polished coated particle. A is the innermost and I is the outermost spot along the SiC cross-section. The crystalline silicon increases from analysis A to B before progressively declining up to analysis I. The silicon to SiC ratio of some peaks is particularly high relative to that of other samples. There is no evidence of graphite.

The unetched polished sample, (figure 5.14), has peak positioning which is almost identical to that of the etched sample. Crystalline silicon peaks are also significantly high especially closer to the IPyC layer (analysis A-C). The 3C SiC is characterized by the peaks at 794 and 965 cm^{-1}, as seen in figure 5.15. The peaks occurring at 787 and 771 cm^{-1} confirm the presence of the 2/6 and 6/6 6H peaks. It is possible that the peak centered at 771 cm-1 could represent the 4/5 15R peak. This would however be surprising since the most intense TO 15R peak is the 2/5 peak expected at 785cm^{-1}. The split of the LO peak resulting in the peak occurring at 939 cm^{-1} is thought to be due to the 2/5 15R polytype. The 3C SiC polytype is further seen at 1520 cm^{-1}. No graphite is observed.

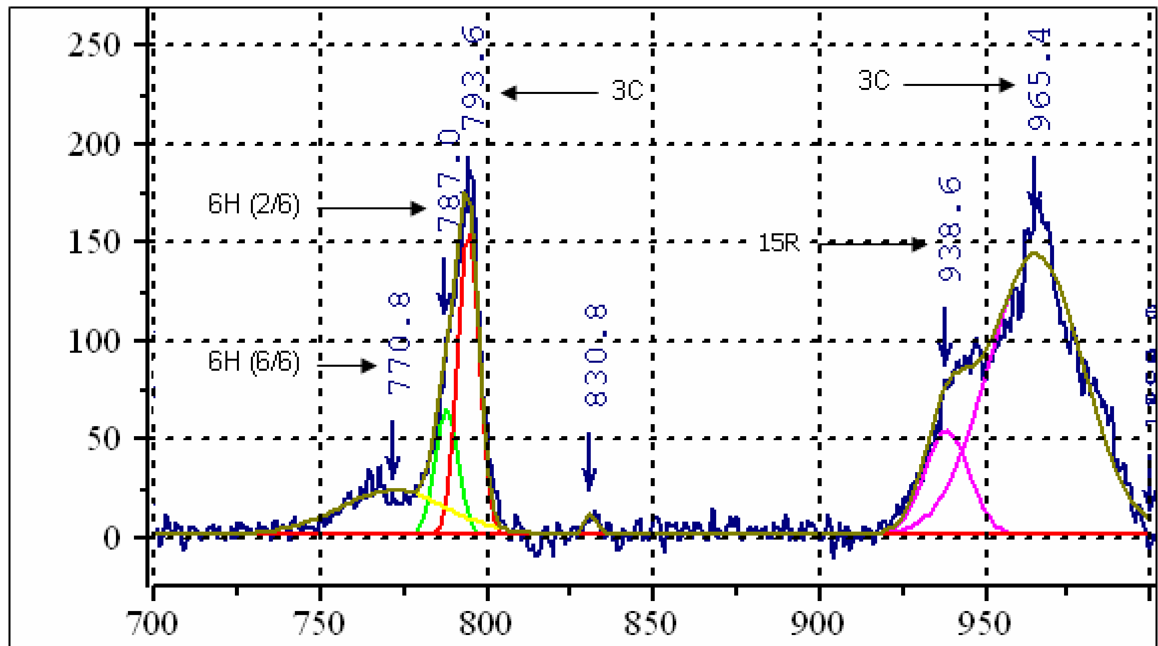

Figure 5.15 – Raman spectra of the TO SiC peaks after deconvolution for analysis 6A (polished). It was assumed that there were two components making up the main peak. The peaks indicate the presence of the 3C and 6H polytypes.

5.1.2. Silicon to Silicon Carbide ratios of PO samples

The silicon to silicon carbide peak intensity ratios (in terms of the area under the peaks) were measured, to get an idea of the relative quantities of the respective products. The values are averaged across the cross-section of the SiC layer. Figure 5.16 shows the mean values of the ratios of the crystalline silicon peak to the dominant TO mode SiC peak for all the samples (PO1 to PO10). The results reveal that a decrease of silicon content occurs with etching (with the exception of sample PO3). Samples PO1 and PO5 contain no crystalline silicon peaks, while sample PO7 has no SiC layer. Samples PO6 and PO8 seem to have very high free silicon contents. The use of different lasers is known to affect Raman spectra and in particular, the relative peak intensities[36]. As is stated in the experimental procedure, the Ar^+ (514.5 nm) and Kr^+ (647.1 nm) excitation lasers were used in collecting qualitative Raman data. However, samples PO3, PO5, PO6 and PO9 were used as independent measures of how the Raman spectra varied with excitation lasers. It was found that there was no general difference except for slight peak intensity

variations, which will slightly reduce the accuracy of the silicon quantification procedure. All quantitative data were collecting using only the Ar^{+} (514.5 nm) excitation laser.

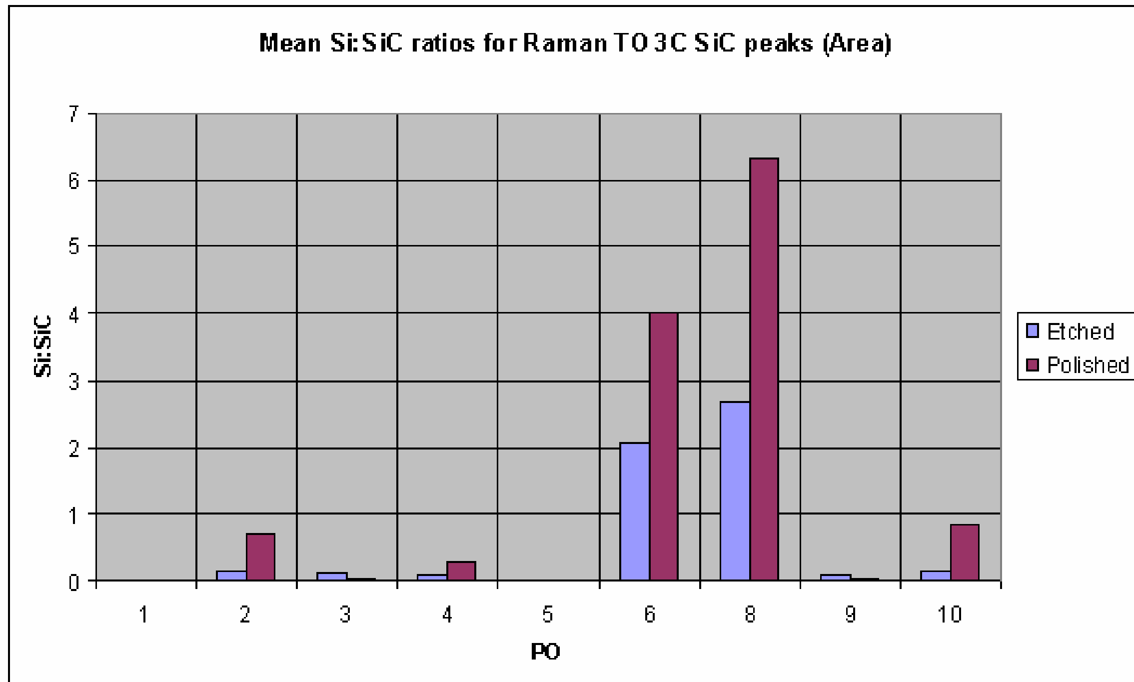

Figure 5.16 – Mean values of the ratio of the crystalline silicon peak to the dominant transverse optic mode SiC peak for both etched and unetched samples. Samples PO6 and PO8 clearly have high free silicon contents in the SiC layer.

5.1.3. Silicon Carbide Peak Width Half Maximum measurements

Figures 5.17 and 5.18 show the mean and standard deviation of the peak width half maximum (PWHM) values in terms of wavenumbers (cm^{-1}). From figure 5.17 the polished samples are generally broader than the etched samples, which suggest that etching has the effect of narrowing the peaks. There is significant difference in the peak width values. The biggest difference of 6 cm^{-1} is between PO3 and PO5. However, the high peak width value of PO3 is attributed to the presence of three peaks constituting the main peak (as is seen with figures 5.13 and 5.15), rather than disordering. Analysis of figure 5.18 reveals that the greatest scatter is from sample PO9. This is an indication that sample PO9 shows the greatest disorder (because of the broad peak). The trend seen from figure 5.18 is less general in this case.

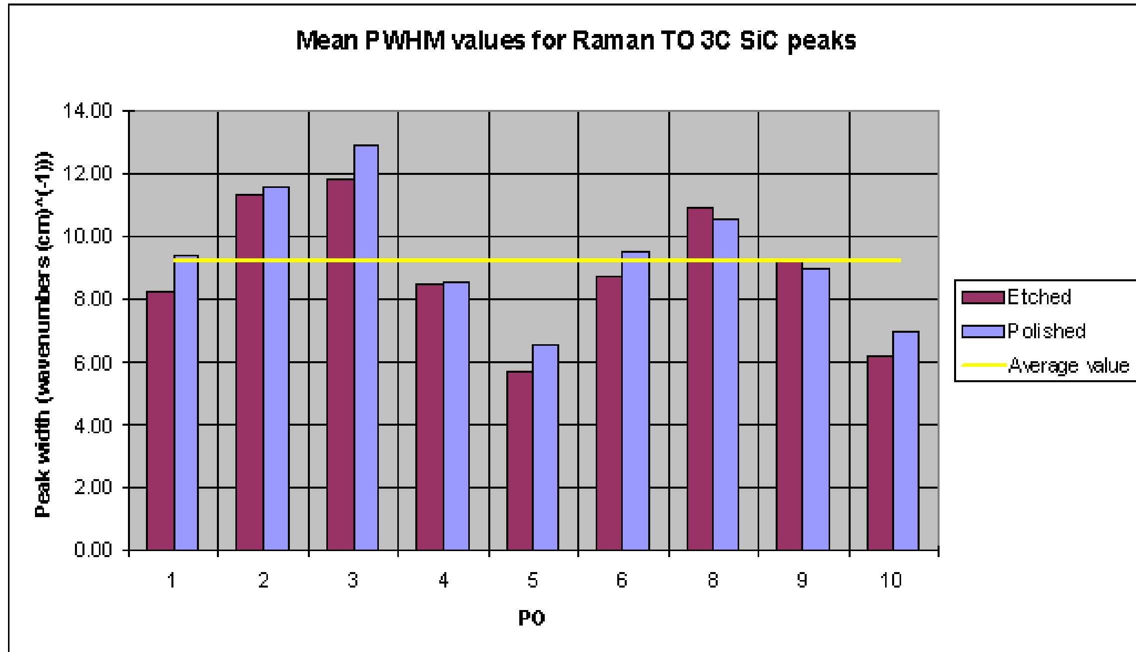

Figure 5.17 – Mean values of the Peak Width Half Maximum of the transverse optic mode SiC peak. There is significant difference in the peak width values, with the biggest being sample PO3 and PO5.

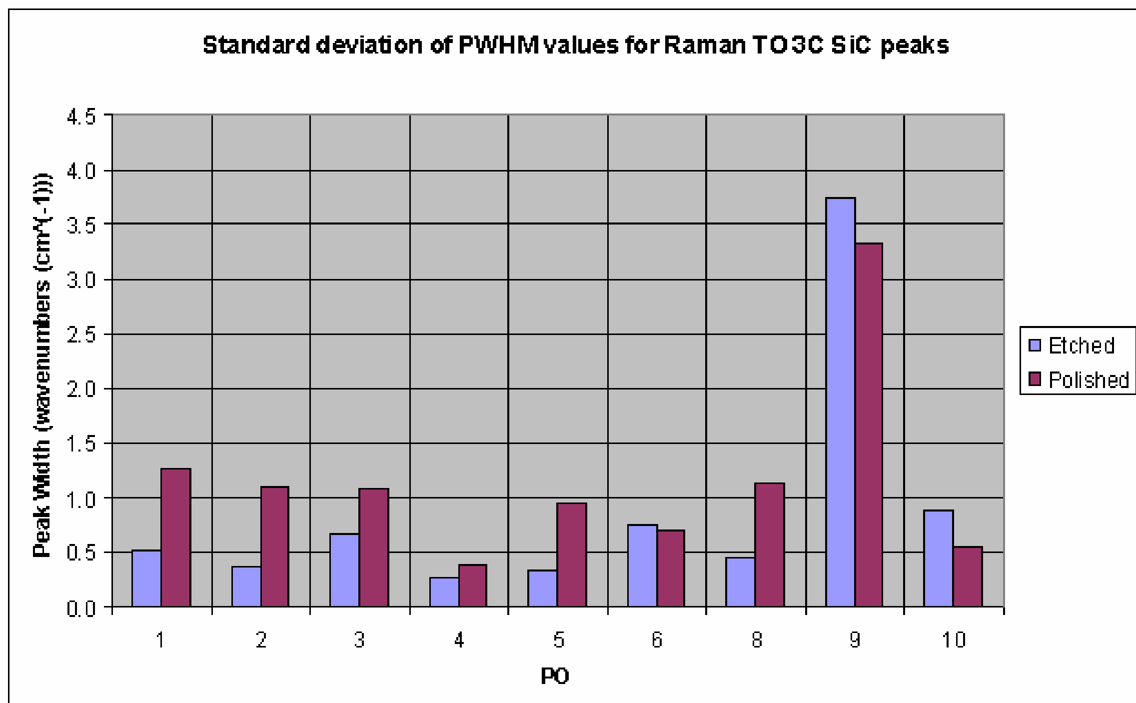

Figure 5.18 – Standard deviation values of the Peak Width Half Maximum of the transverse optic mode SiC peak

5.1.4. The Silicon to Silicon carbide ratio along the SiC layer cross-section

The Si:SiC ratio was plotted along the cross-section of the SiC layer. Point A represents the point closest to the IPyC layer (innermost), while the last point for each sample represents the point closest to the OPyC layer (outermost).

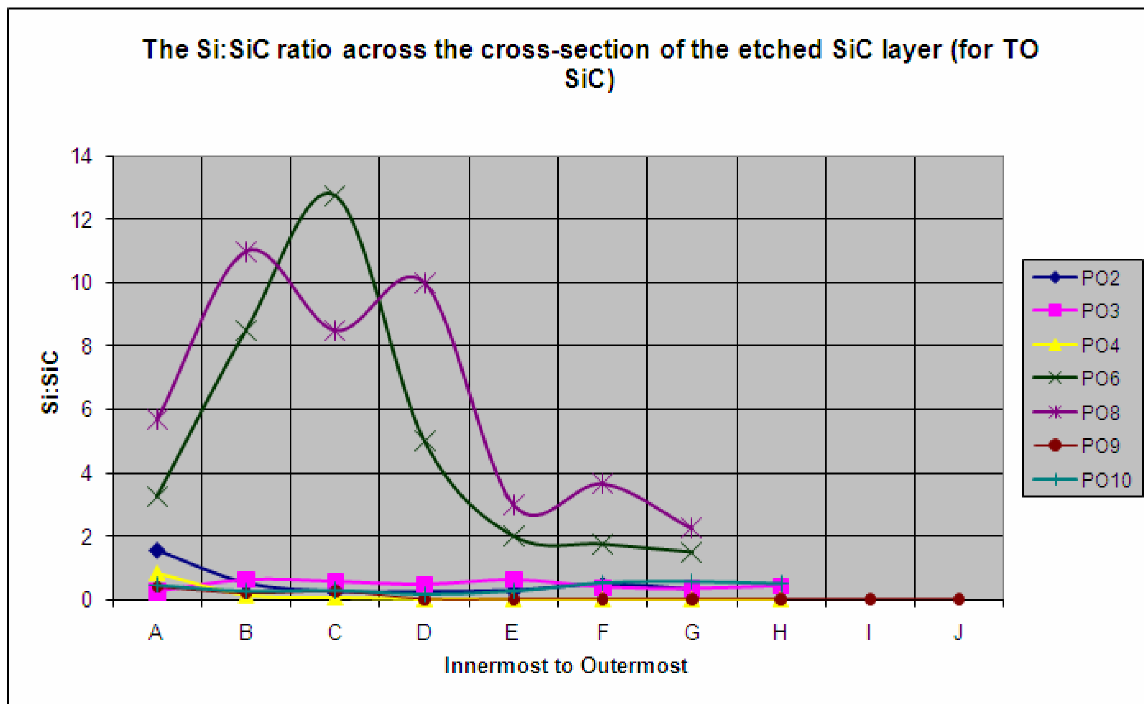

Figure 5.19 – The silicon to SiC ratio along the cross-section of the etched TO SiC layer, where A denotes the innermost part of the SiC and J the outermost. Samples PO6 and PO8 possibly have unacceptably high free silicon contents in the SiC layer. The general trend is that the silicon is mainly concentrated along the inner parts of the SiC layers.

Figures 5.19 is a plot of the silicon to SiC ratio along the cross-section of the etched TO SiC layer. As can be seen the most silicon is generally concentrated close to the innermost part of the SiC layer. Samples PO3 and PO10 seem to be exceptions to this rule, as the Si to SiC ratio does not decrease as a general rule. Sample PO2 shows a similar trend even though it is to a lesser extent. The highest ratios are for samples PO6

and PO8, reaching maximum values of about 13 and 11 respectively, indicating either the presence of unacceptably high free silicon in the SiC layer or an intrinsic silicon value that is much higher than that of the corresponding SiC. All other samples have maximum ratios of less than 2. In the cases where the Si to SiC ratio is zero, no crystalline silicon is present.

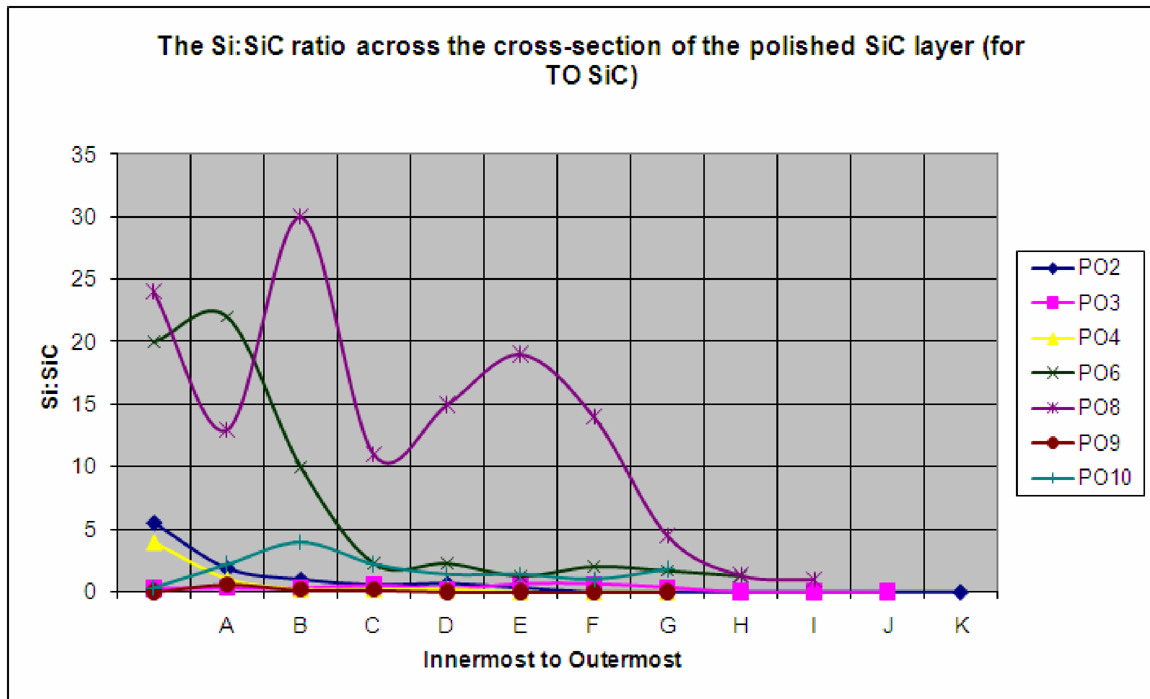

Figure 5.20 – The silicon to SiC ratio along the cross-section of the (unetched) polished TO SiC layer, where A denotes the innermost part of the SiC and K the outermost. Once more, samples PO6 and PO8 have unacceptably high free silicon contents in the SiC layer. The general trend is that the silicon is mainly concentrated along the inner parts of the SiC layers.

Figures 5.20 is a plot of the silicon to SiC ratio along the cross-section of the polished TO SiC layer. In general it is seen once again that there is decrease of the Si to SiC ratio from the innermost to the outermost part of the SiC. Sample PO8 fluctuates before declining. A similar trend is seen with sample PO6 though to a lesser extent. Only the sample PO10 increases towards the outermost part of the SiC layer. As was the case with the etched samples, the Si to SiC ratios of samples PO6 and PO8 are very high, reaching maximum

values of 22 and 30 respectively. However, since the analysis positions of points A to I do not correspond exactly, the curves of figures 5.19 and 5.20 have differing shapes.

5.2. Quantitative Raman spectroscopy

A variety of binary mixtures of silicon and SiC powders were prepared with the purpose of estimating the percentage of silicon in the TRISO layer by means of a calibration curve. The stacked spectra (without modification) used for the calibration curve are included in Appendix A.

5.2.1. Calibration curves

The calibration curves were constructed by using equation 5.1, derived using a similar equation by Kim et al. [100]. In the case of the silicon, only the crystalline peak at 520 cm^{-1} was used. The peak area considered for integration was from wavenumber 482.27 to 540.30 cm^{-1}. In each case, the main SiC peak of that polytype was used. In general the peak area chosen was from wavenumber 761.48 to 802.27 cm^{-1}.

$$x_{si} = f\left(\frac{I_{Si}}{I_{Si} + I_{SiC}}\right) \tag{5.1}$$

Where : I_{Si} represents the integrated peak intensity of the silicon peak

: I_{SiC} is the integrated peak intensity of the SiC main peak

The y-axis values used for the trend curves are average values of the intensity ratios

The calibration curve of silicon, relative to 3C SiC is given by figure 5.21. As mentioned in the experimental procedure, the 3C sample contained less than 80% 3C SiC. This has been corrected in the plot, resulting in values along the x-axis having higher values than those that we weighed-off. The y-axis values used for the trend curves are average values of the intensity ratios.

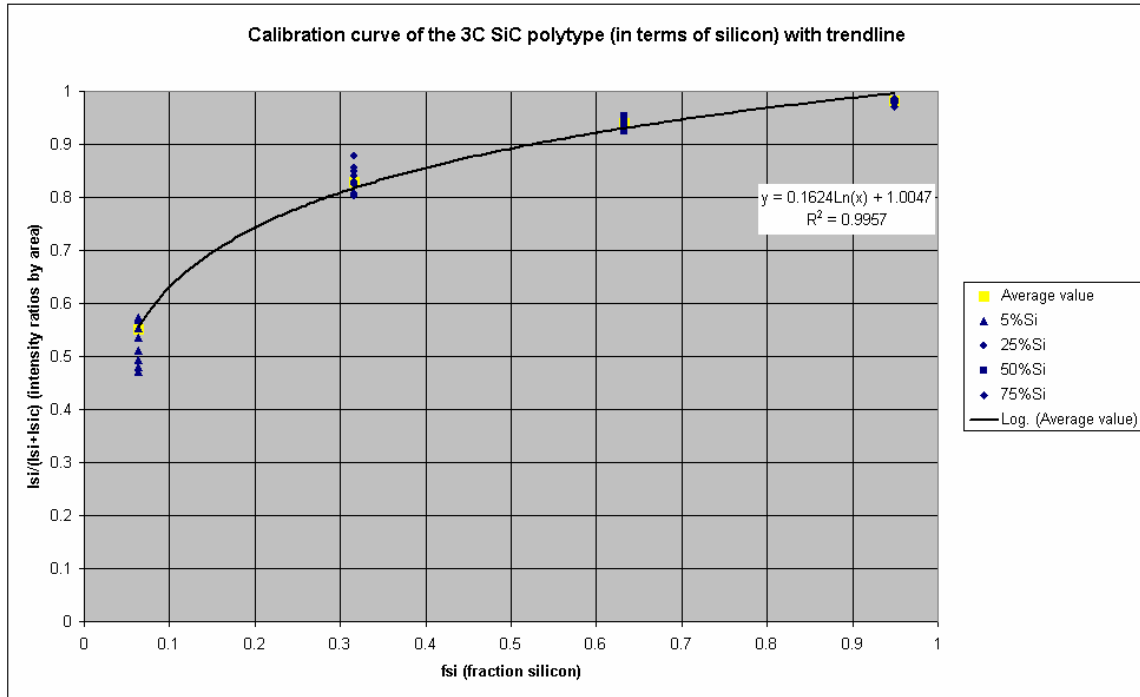

Figure 5.21 – Raman calibration curve of the 3C polytype

As can be seen, a logarithmic relationship exists between the intensity ratios and the fraction of silicon present governed by equation 5.2:

$$y = 0.1624\ln(x) + 1.0047 \tag{5.2}$$

The R^2 fit is 0.9957. Examination of the spectrum reveals that relatively small amount of silicon is reflected as a peak with significant area. For instance at about 7% Si, the relative peak area is 55%. At 50% Si, the peak area is about 88%, almost 9 times that of SiC.

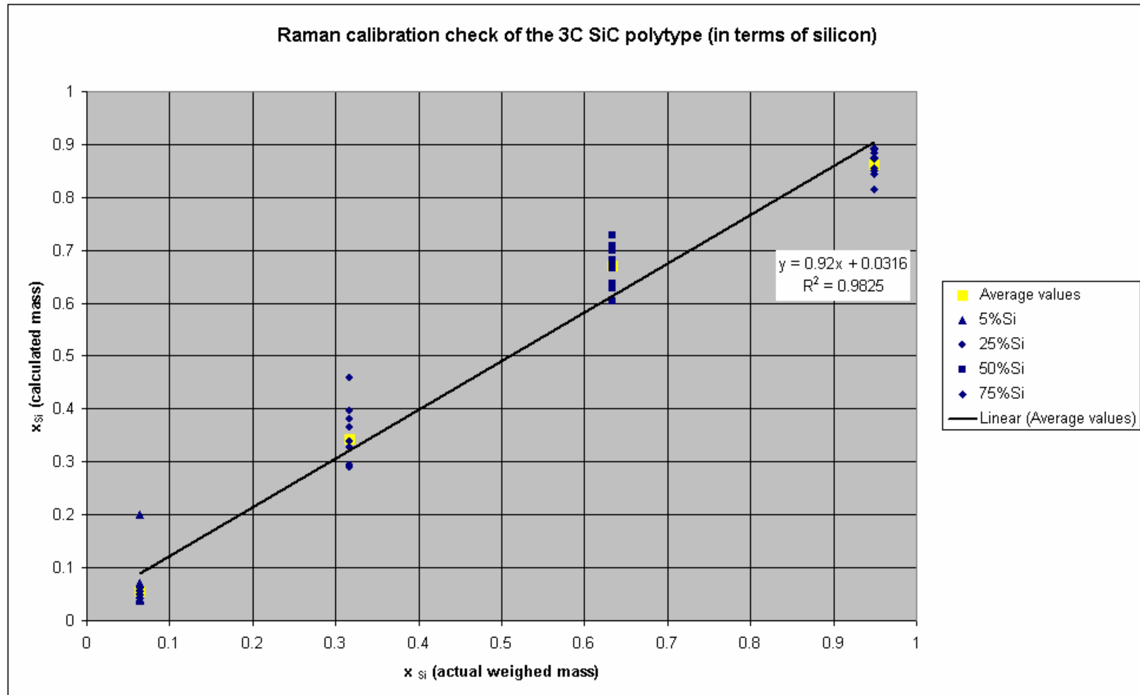

Figure 5.22 – Calibration check of the 3C polytype

The check for the accuracy of calibration was tested by plotting the calculated mass versus the weighed-off mass as is in figure 5.22. The ten points at each weighed mass were averaged to obtain a plot. Ideally, a straight line should be obtained, with the slope equal to one and the plot intercepting the y-axis at zero. This calibration is given by equation 5.3. The R^2 is 0.9825.

$$y = 0.92x + 0.0316 \quad (5.3)$$

It is evident that some points (about one point in ten) are significantly far from the average value. As such a single analysis is not enough to obtain statistically relevant data. The extent of segregation between the silicon and SiC phases is shown by scatter of points. The degree of fine grinding was found to have a dramatic influence on the scatter. In addition using the smallest objective lens spreads out the laser beam and analyzes a greater area.

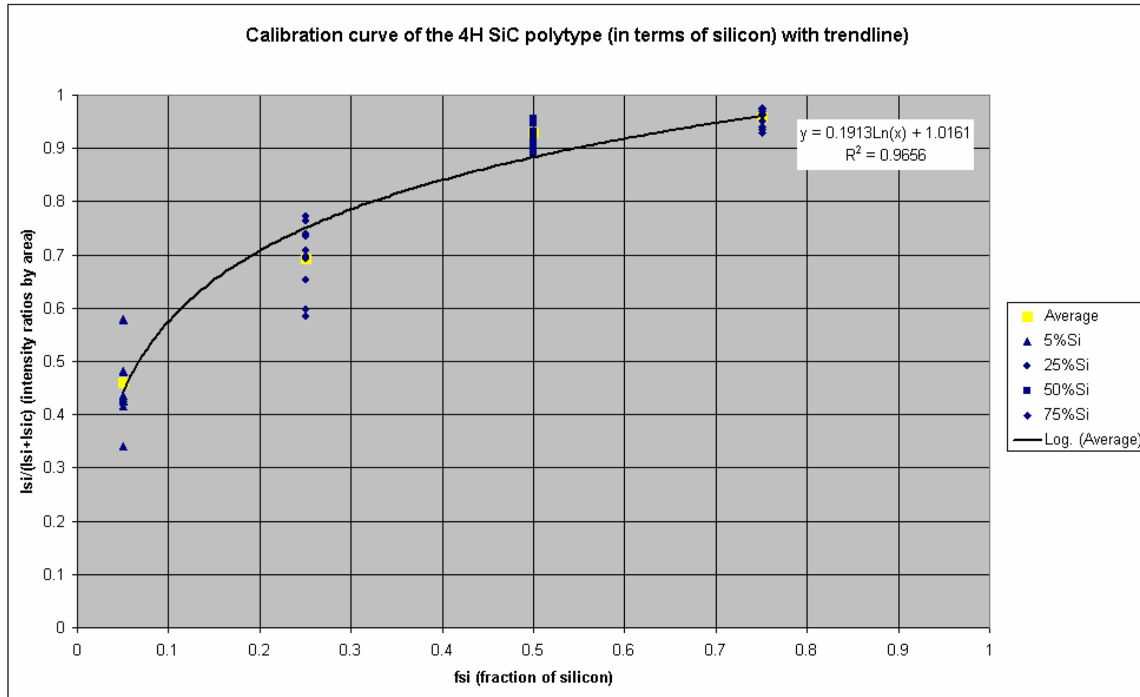

Figure 5.23 – Raman calibration curve of the 4H polytype

The calibration curve of silicon, relative to 4H SiC is given by figure 5.23. A similar trend in seen as with the 3C sample, since a logarithmic relationship exists between the intensity ratios and the fraction of silicon present as is shown by equation 5.4:

$$y = 0.1913\ln(x) + 1.0161 \quad (5.4)$$

The R^2 fit is 0.9656.

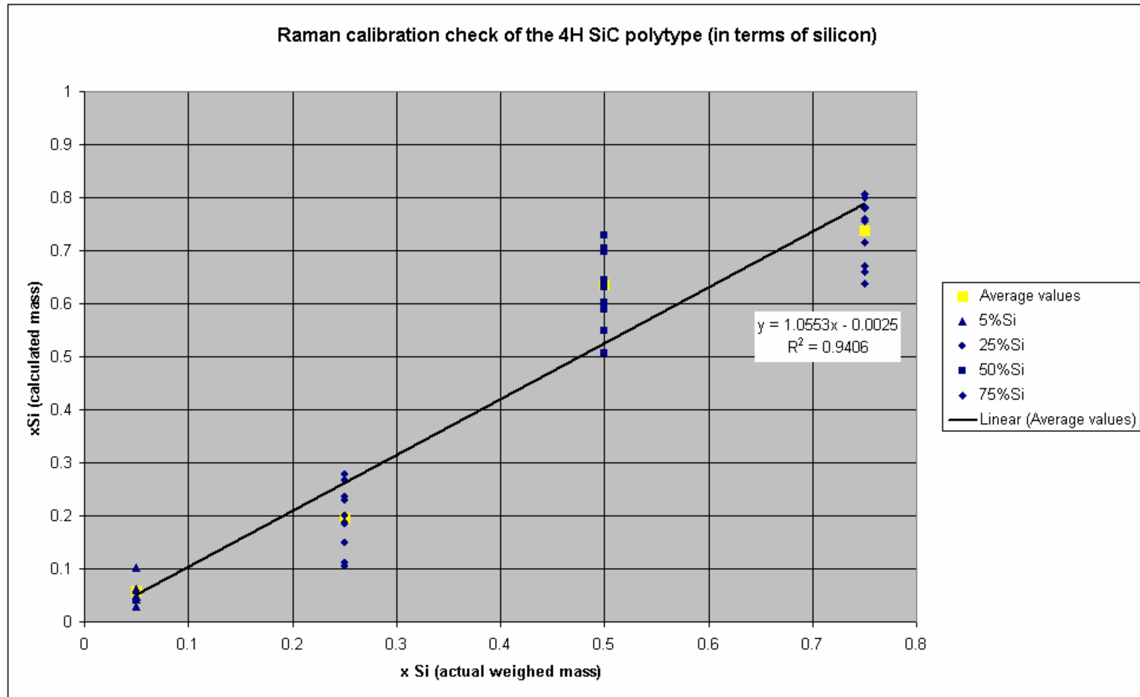

Figure 5.24 – Calibration check of the 4H polytype

Figure 5.24 shows the calibration curve check of the 4H polytype. The calibration check is given by equation 5.5. The R^2 is 0.9406.

$$y = 1.0553x + 0.0025 \tag{5.5}$$

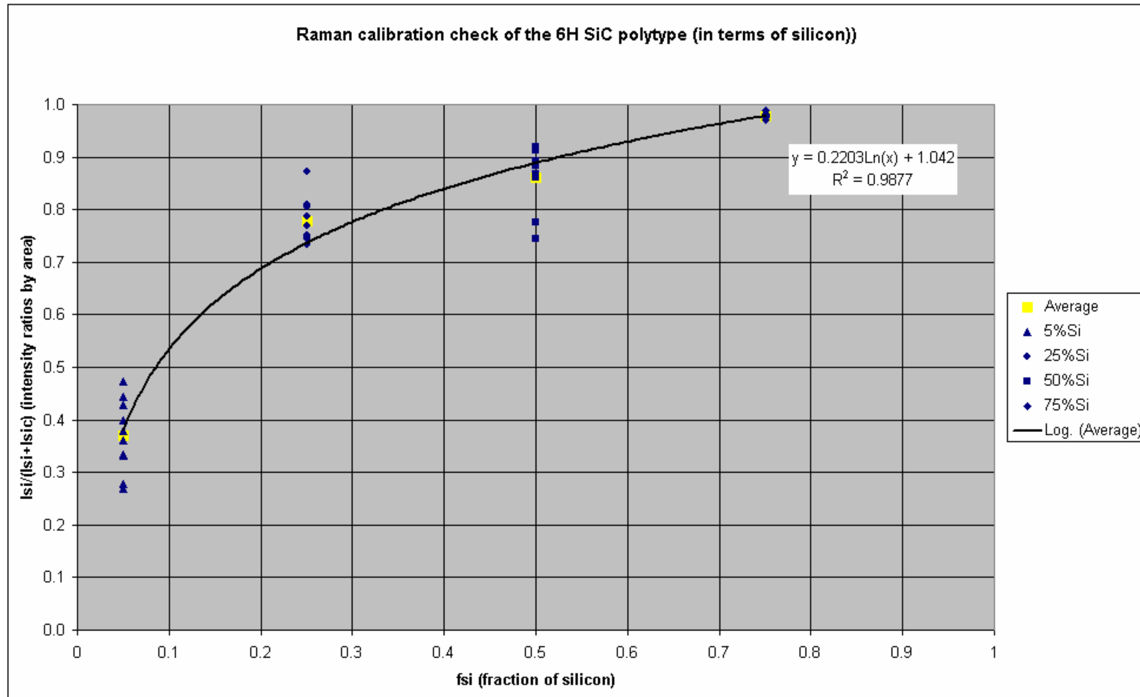

Figure 5.25 – Raman calibration curve of the 6H polytype

The calibration curve of silicon, relative to 6H SiC is given by figure 5.25. The calibration curve shows a similar trend as with the 3C and 4H samples. A logarithmic relationship exists between the intensity ratios and the fraction of silicon present as is shown by equation 5.6:

$$y = 0.2203\ln(x) + 1.042 \quad (5.6)$$

The R^2 fit is 0.9877.

Figure 5.26 shows the calibration curve check of the 6H polytype. The calibration check is given by equation 5.7. The R^2 is 0.9813.

$$y = 0.9528x + 0.02 \quad (5.7)$$

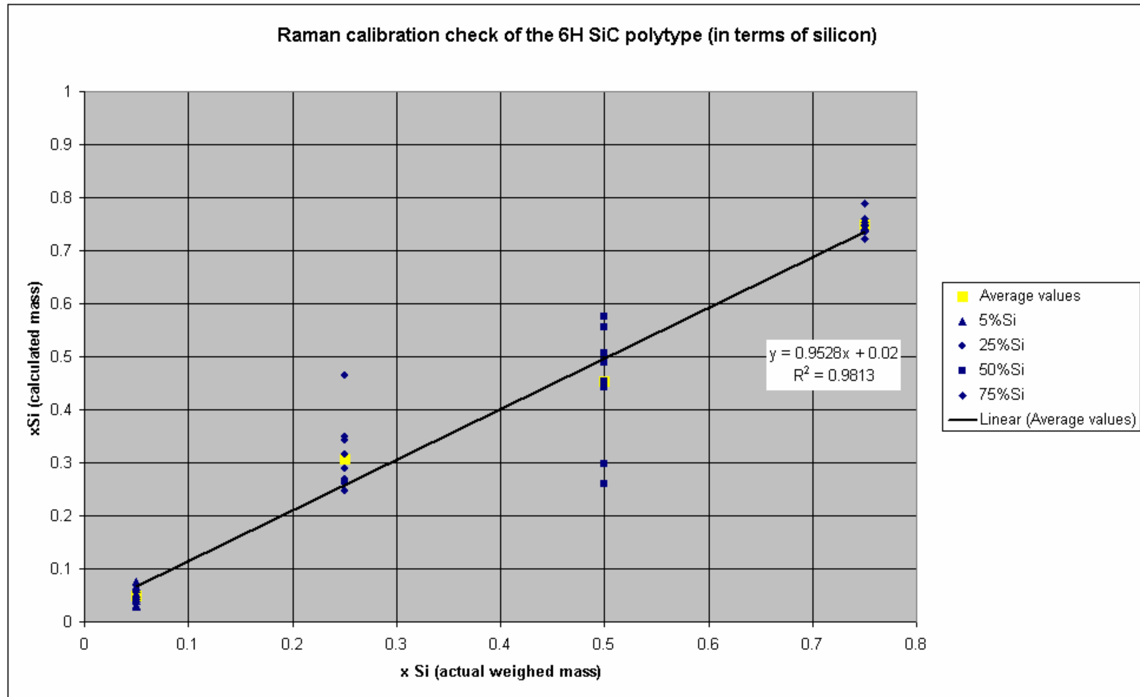

Figure 5.26 – Calibration check of the 6H polytype

Figure 5.27 illustrates the level of accuracy and repeatability that could be attained using the chosen sample preparation method with Raman spectroscopy.

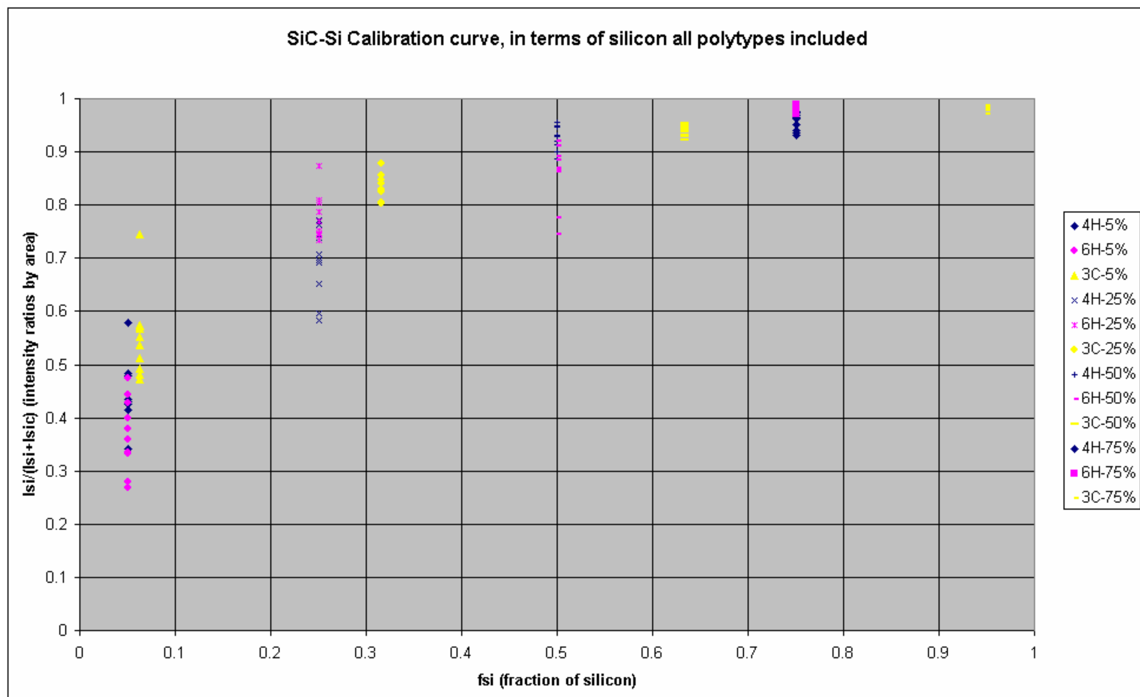

Figure 5.27 – Plot of the individual points of the calibration curve, illustrating the scatter.

5.2.2. Quantitative silicon distribution

The calibration curve of the 3C polytype was used to project the fraction of silicon that is present in the radial direction of the SiC layer. The qualitative results from Raman spectroscopy were used in conjunction with the calibration curve to obtain the quantitative line profile as is shown in figure 5.28. The reason the 3C calibration curve was chosen is because this is the most abundant polytype in each sample. Across the x-axis, point A represents the part of the SiC closest to the IPyC layer. It is evident that samples PO6 and PO8 have the most silicon. However, it is possible that this may simply be due to the silicon of these samples having high intrinsic scattering properties (Such a sample produces a high peak as a result of its intrinsic properties). The worst points in each case have silicon accounting for 60% of what is supposed to be SiC. As has been stated before, the silicon is concentrated mainly close to the IPyC layer. Sample PO8 is an obvious exception to this trend since silicon is abundant in the middle part of the SiC analysis. To a more limited extent, sample PO10 also has silicon concentrated throughout the SiC layer cross-section.

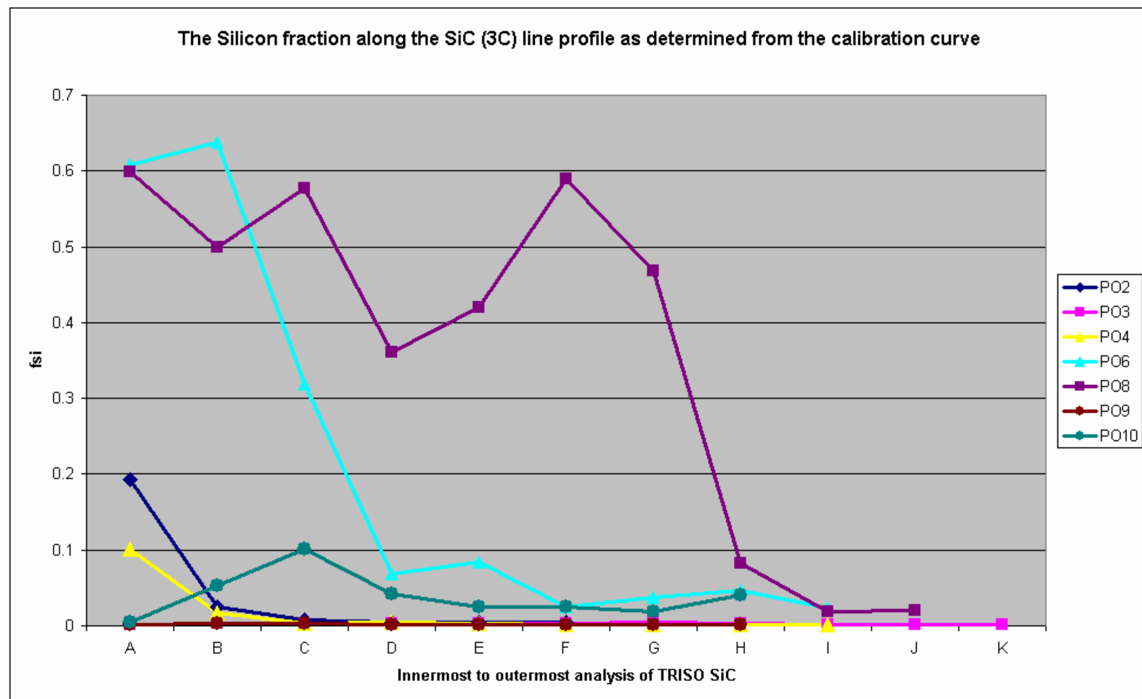

Figure 5.28 – Quantitative line profile of the fraction of silicon along the SiC cross-section

5.2.3. Error Analysis

In order to determine the sample error, five samples were split from the same batch. The samples of 50% silicon and 50% 3C SiC were prepared the same way and 10 random analyses from their surfaces were collected, as is illustrated in figure 5.29. The average relative intensity value is 0.931, with a standard deviation of 0.014. The upper and lower limits based on the σ-error are 0.945 and 0.918 respectively.

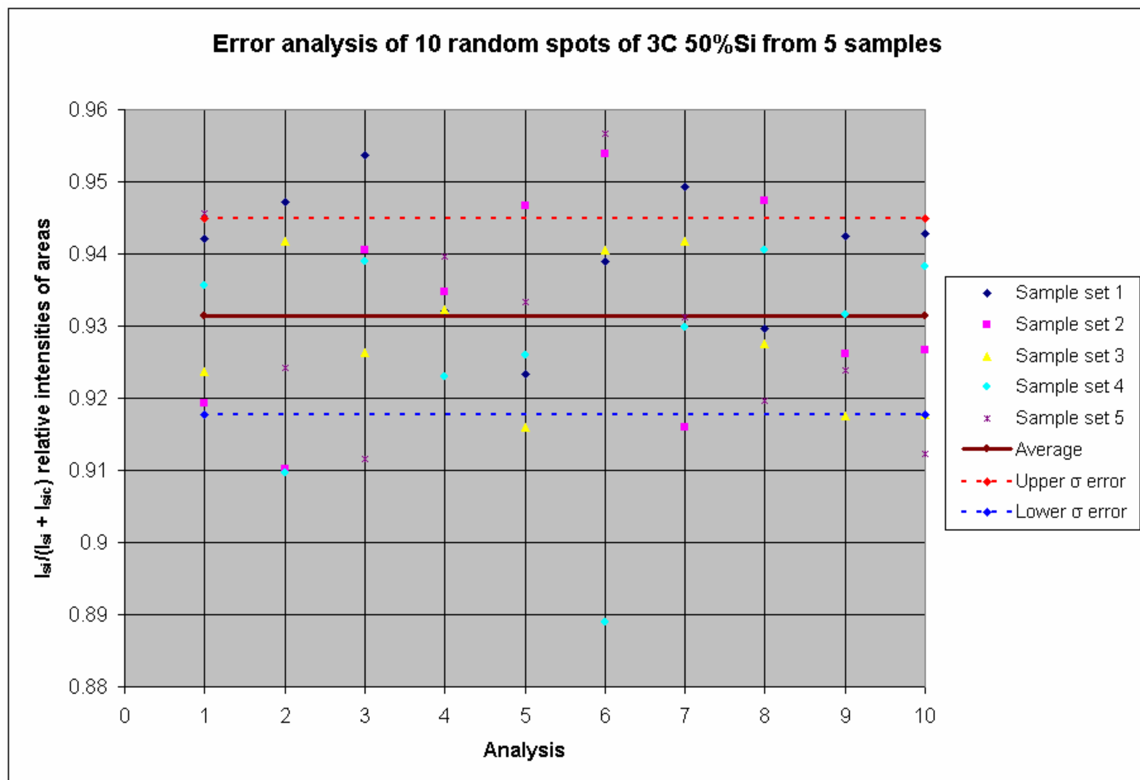

Figure 5.29 – Plot of relative Raman spectroscopy intensities from the five 50%Si-50%3C SiC mixtures.

5.2.4. Scanning electron microscopy analysis

It was decided to check the morphology of the 3C (50%Si) and 4H (50%Si) quantitative samples by the electron backscattering mode of the SEM. The aim is to verify particle size, the degree of homogeneity and segregation in a typical sample. The same sample procedure used for preparation of quantitative Raman spectroscopy was used to test if the

pressing process produces biased powder mixtures on the surface. These images are shown in figure 5.33. The three main phases present (from lightest to darkest) are α-iron, silicon and SiC. From the samples that have been examined, there does not seem to be segregation and the homogeneity seems reasonable. The reason for this conclusion is that the resolution with Raman spectroscopy, using the 5x objective is expected to be in excess of 60µm. The image on the left had large particle sizes and necessitated longer grinding times. The size of the grains resulting from the grinding process is a further factor that contributes to homogeneity. In figure 5.33, the image on the left (3C SiC- 50% silicon) has large particles because the grinding process was only 2 minutes long whereas the one on the right (4H SiC- 50% silicon) was ground for 30 minutes (and α-Fe has been removed).

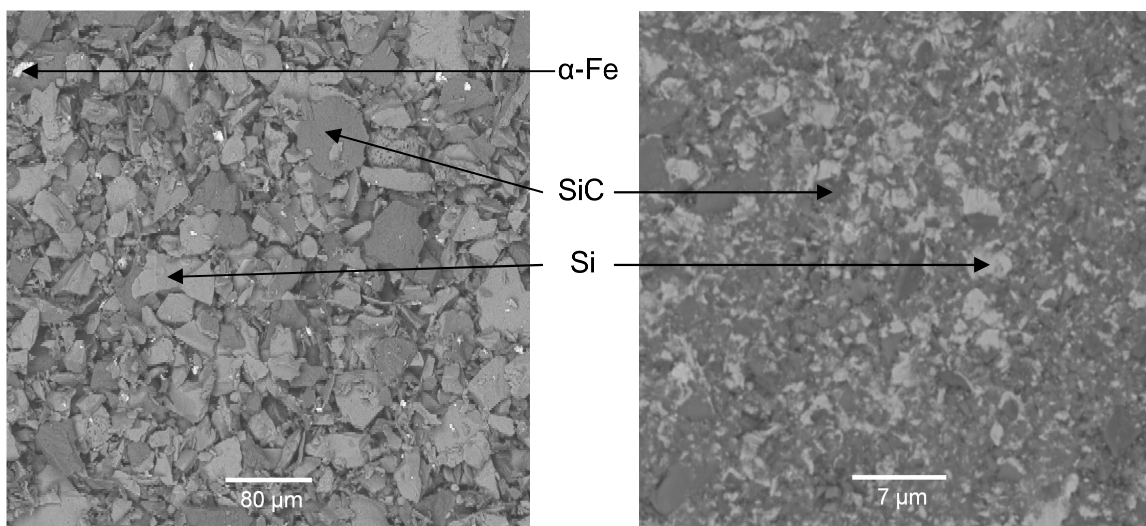

Figure 5.30 – Backscattered SEM images of mixture of two Raman spectroscopy quantitative samples. The sample on the left (3C SiC- 50% silicon) contains α-Fe after grinding, while the α-Fe of the sample on the right has been dissolved (4H SiC- 50% silicon).

With regard to the PO samples, PO6, PO8 and PO10 were analyzed with the SEM and high resolution SEM in the backscattered electron mode. The purpose was to locate the crystalline silicon that was identified in section 5.1. However the silicon was not irrefutably located. Figure 5.34 from left to right represents the cross-section of a particle from the outer to the inner SiC layer. Close to the inner PyC layer (right), there are bright

dispersed particles which are thought to be crystalline silicon. However, this may be an effect due to topographical effects. In a scenario where the silicon is located along the SiC-IPyC interface (maybe as a result of polishing) the silicon would not be detected by the SEM.

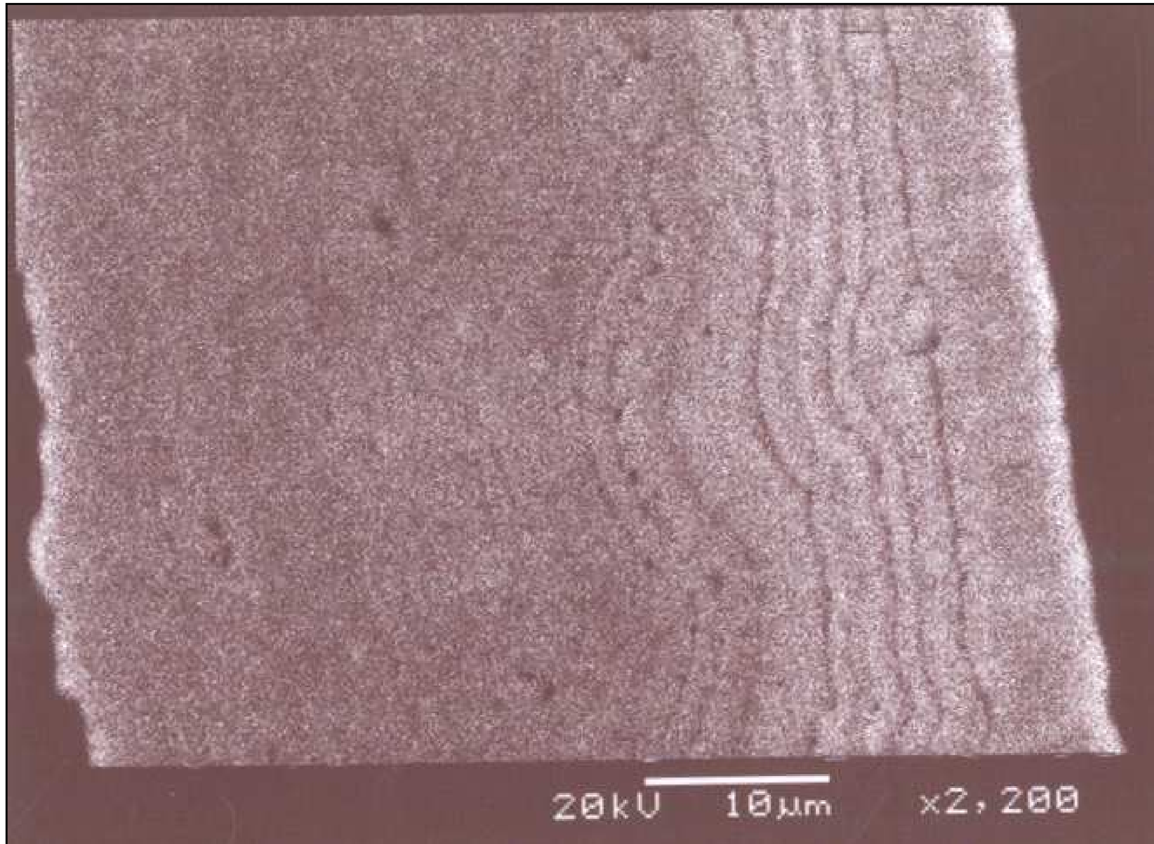

Figure 5.31 – Backscattered SEM image of the SiC layer of sample PO10

5.2.5. Particle size and distortion effects

It was decided to eliminate some of the variables that directly led to the scatter from the quantitative plots from the calibration curve. New samples were ordered because there was not enough NECSA SiC left. The silicon and SiC powders used were manufactured by American Elements. Since the XRD and TEM results revealed that the 3C SiC polytype is the most abundant in all samples, it was decided that focus be shifted specifically on improving the 3C SiC-silicon calibration curve. An α-SiC powder was

also ordered, which had a mixture of 4H, 6H, 8H and 15R polytypes. It was of importance to study the one component systems of silicon and SiC separately to better understand the binary mixtures.

<u>Particle size</u>

Particle size distribution

The particle size distribution of some of the powders was checked with the Malvern MU 2000 analyzer. The American Elements' silicon and SiC were ordered to specifically have a particle size range between 1 and 2 microns.

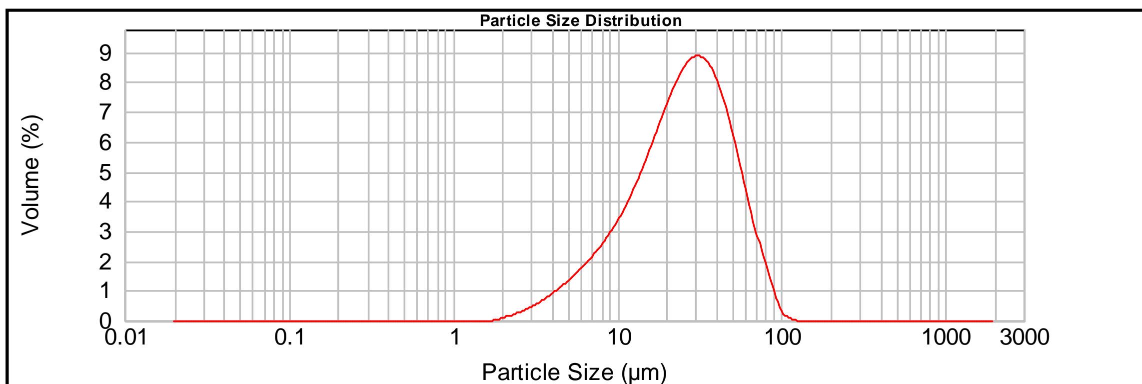

Figure 5.32 – The particle size distribution curve of American element' silicon powder

As can be seen from figures 5.32 and 5.33, there is an inherent problem associated with the silicon particle size in that the vast majority of the particles (>80%) are greater than 10 microns in diameter, significantly higher than the expected 1-2 microns range. The majority of particles (~37%) are around 30 microns in diameter. This discovery is particularly detrimental for quantitative micro Raman spectroscopy, where the spot size is at maximum several tens of microns in diameter.

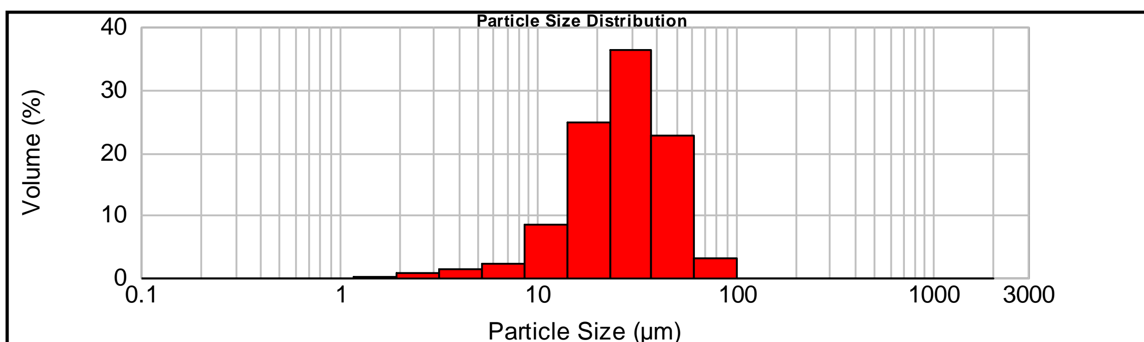

Figure 5.33 – The particle size distribution by size fraction bins, of American Elements' silicon powder.

Figures 5.34 and 5.35 are analyses of the particle size distribution of 3C SiC. It is observed that the majority of the particles (>40%) are less than 2 microns in diameter. What is of concern however are the secondary peaks from the 10-20 micron and 20-200 micron range which account for a large percentage of the remaining particles. The potential for analyzing a calibration curve accurately with such particle sizes is virtually nullified. This suggests that manufacturing SiC is not a trivial task, since a number of other samples were found to be out of specification, (especially in controlling which polytype is stable).

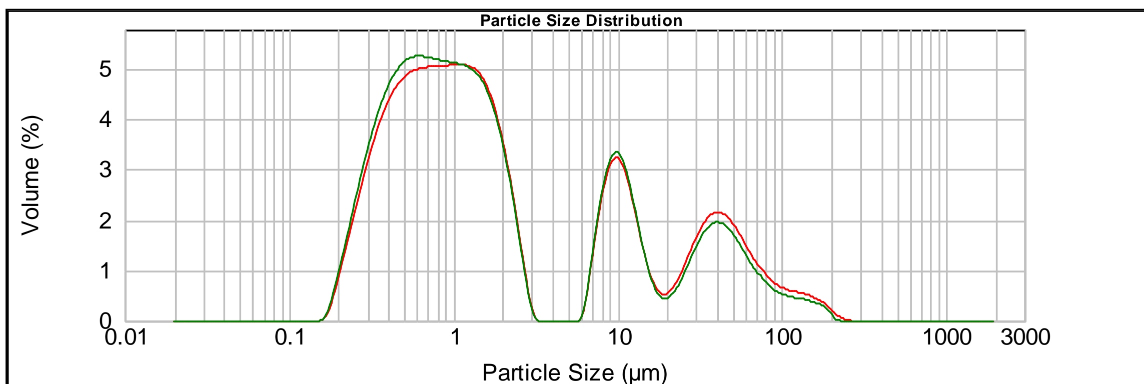

Figure 5.34 – The particle size distribution curve of American element' SiC powder

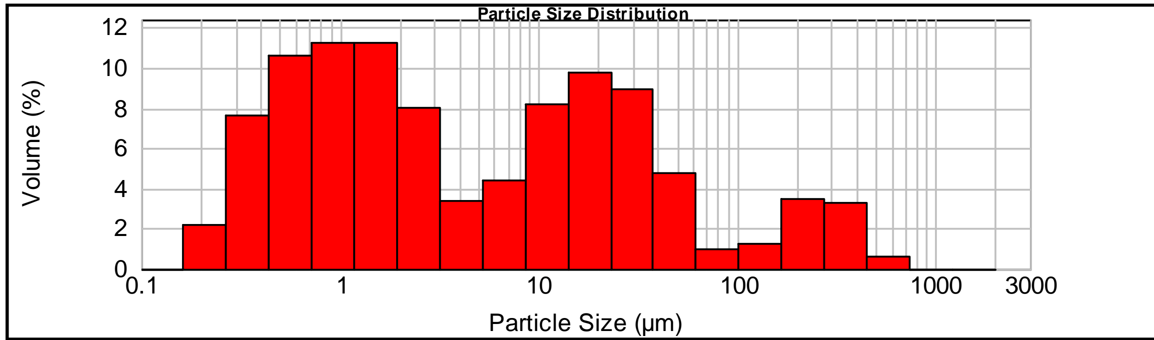

Figure 5.35 – The particle size distribution by size fraction bins, of American Elements' SiC powder.

Separation by particle size

It was therefore necessary to develop a method to separate the particles on the basis of particle sizes. The method that was used is separation based on settling rates according to Stokes' law as is seen in equation 5.8:

$$V_s = \frac{2}{9}\frac{\rho_p - \rho_f)}{\mu} gR^2 \tag{5.8}$$

Where V_s = particles' settling velocity (m/s), (vertically downwards if $\rho_p > \rho_f$, upwards if $\rho_p < \rho_f$); g = gravitational acceleration (m/s^2); ρ_p = mass density of the particles (kg/m^3); ρ_f = mass density of the fluid (kg/m^3), μ is the fluid's dynamic viscosity (Pa.s), R is the radius of the spherical object (m).

The settling time would in theory be determined by the particles' settling velocity and the level of the water in the measuring cylinder (assuming particles drop in a straight line). The level of water chosen was 20 cm. The particle sizes chosen are > 38 microns, 10-38 microns and < 10 microns. The setting times are summarized in table 5.2. For 38 microns particles, it takes 43 and 26 seconds for silicon and SiC particles to settle. On the other extreme end, a 1 micron particle takes 25.8 and 10.3 hours for silicon and SiC particles to settle.

φ (microns)	Time (minutes) Si	SiC
38	0.71	0.43
10	15.46	6.16
1	1546.43	615.77

Table 5.2 – Settling rates of silicon and SiC particles according to Stokes' law for 38, 10 and 1 micron particle sizes.

The validity of the method is subject to some error though. For instance, the effect of particle shape is not accounted for, which is known to significantly affect the settling patterns of particles. The basic assumption is then that the particles are spherically shaped.

Raman spectroscopy analyses of different silicon particle size fractions

The samples that were divided on the basis of size fractions were analyzed with the Raman. The laser beam was moved around the surface of the samples to get different measurements. Peak area values are summarized in table 5.3.

	>38 µm	>10<38 µn	<10 µm
1	13090	14240.9	24962.7
2	16233.1	9800.7	18863.6
3	5577.2	15456.6	14217.7
4	10115.8	15558.7	10482.1
5	10309.9	9216.7	9698.8
6	19141.6	13077.9	8686.1
7	22672.5	17111.7	21721.4
8	7393.1	12028.2	8702.6
Avg.	13066.65	13311.43	14666.88
Std. dev.	5901.483	2822.137	6404.473
Error %	45.16447	21.20086	43.66624

Table 5.3 – The individual peak area values showing variations for >38 microns, 10-38 microns and <10 microns silicon particle sizes.

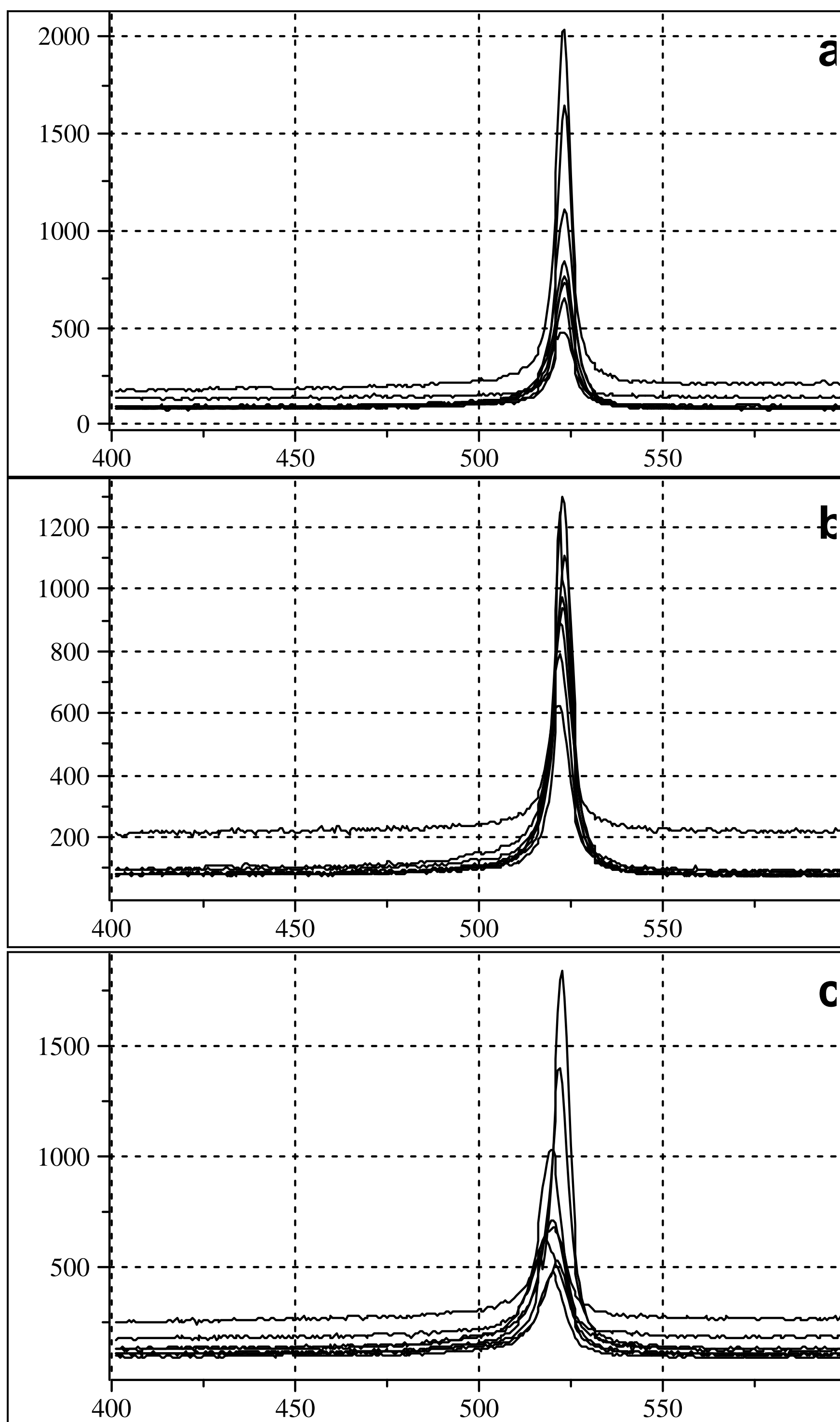

Figure 5.36 – Raman spectroscopy analysis of silicon particles sizes: (a) >38 microns, (b) 10-38 microns and (c) <10 microns. The y-axis is the intensity in arbitrary units, while the x-axis is the wavenumber in cm^{-1}.

The individual silicon plots for > 38 micron, 10-38 micron and <10 micron particles are shown in figure 5.36. The crystalline silicon peaks are centered at 520 cm^{-1}. There is significant variation in the intensities (and areas) of the peaks, which is verified by the error values. It is not clear why the σ-error value of the 10-38 micron size fraction (21.2%) is less than half that of the other two size fractions (45.2% and 43.7%) for silicon. None of the plots were offset on the vertical scale

Raman spectroscopy analyses of different SiC particle size fractions

Peak area values are summarized in table 5.4.

	>38 µm	>10<38 µn	<10 µm
1	7612.3	6276.3	5056.7
2	7699.3	6127.8	7417.3
3	5682.8	5676.8	5545.1
4	11180.7	3257.6	12559.1
5	9277	7529.9	9984.5
6	5042.6	5817.8	5619.2
7	10289.9	9581.7	12736.5
8	12644.9	9601.8	7894.5
Avg.	8678.688	6733.713	8351.613
Std. dev.	2652.162	2124.233	3090.942
Error %	30.55948	31.54623	37.01012

Table 5.4 – The individual peak area values showing variations for >38 microns, 10-38 microns and <10 microns SiC particle sizes.

SiC analysis was done following a similar particle size procedure as that of silicon. The individual SiC plots for > 38 micron, 10-38 micron and <10 micron particles are shown in figure 5.37. The crystalline SiC peaks are centered at 790 cm^{-1}. There is significant variation in the intensities (and areas) of the peaks, which is verified by the error values. Percentage values of the σ-errors range from 31% to 37%, and show no significant difference. None of the plots were offset on the vertical scale

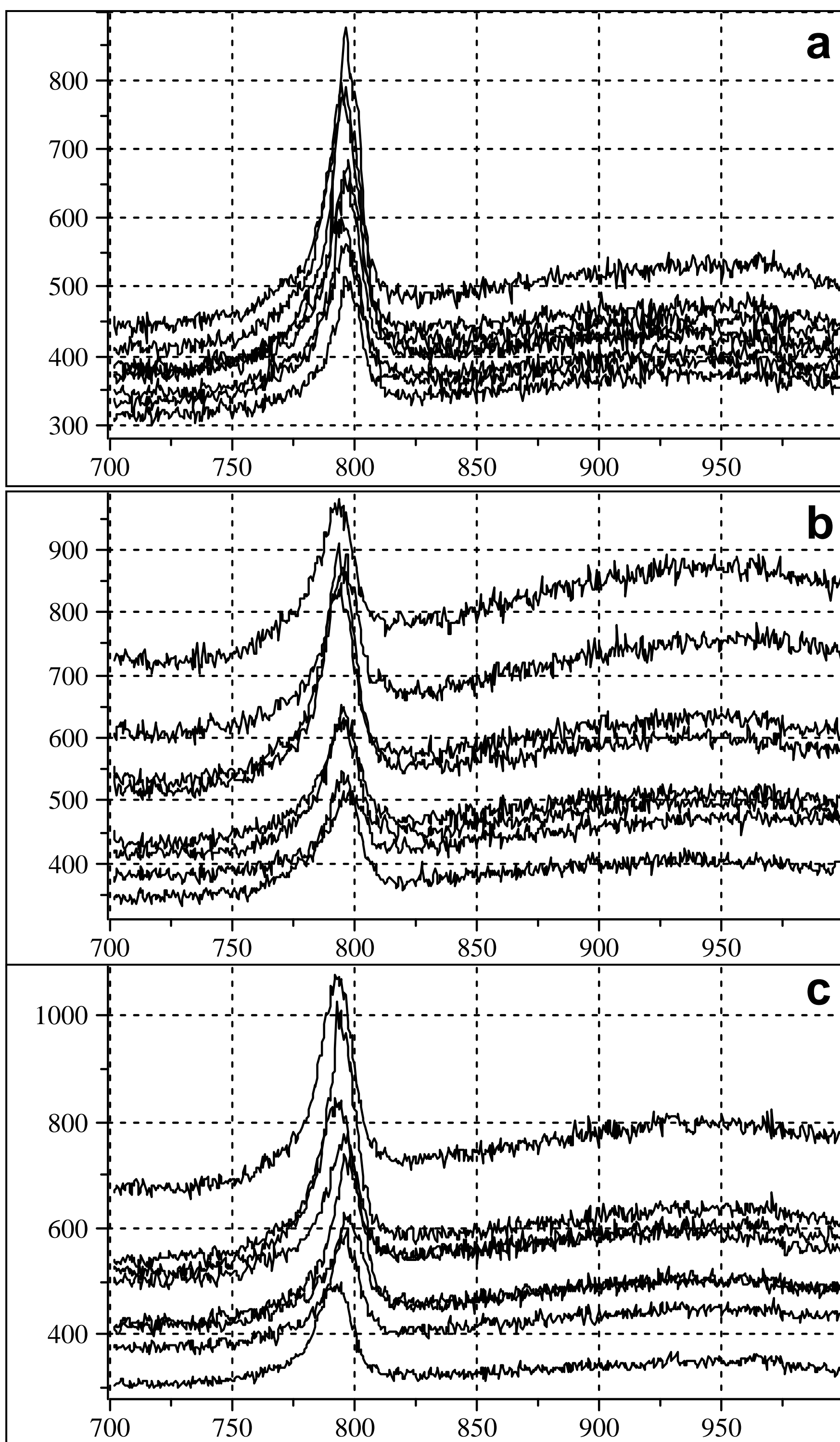

Figure 5.37 – Raman spectroscopy analysis of SiC particles sizes: (a) >38 microns, (b) 10-38 microns and (c) <10 microns. The y-axis is the intensity in arbitrary units, while the x-axis is the wavenumber in cm^{-1}.

The fact that the one component systems of silicon and SiC yield such significant errors, illustrates the complexity of using Raman spectroscopy to calibrate and predict a two component system of solid powders. Unlike with liquids or single crystals, the particles of powders are oriented in a range of directions leading to varying intensities when the sample is slightly rotated (or the laser focuses on another spot). In particular, as has been stated in the literature, particle size plays a major role in quantitative Raman analysis[32,36]. It is known that disorder and distortion alter the shape and intensities of the peaks.

Annealing

Disorder is known to exist in all of the samples analyzed, to varying degrees because of the shape of the peaks in comparison to the analyses of single crystals. Powders generally yield peaks that are significantly broader and less intense than those of single crystals (for both silicon and SiC). Peak broadening as an indication of disorder is also a feature x-ray powder diffraction. It was therefore expected that the shape of the peaks and the rough background would be improved by annealing.

Raman spectroscopy analysis of silicon after annealing

Peak area values are summarized in table 5.5.

	2 hrs	4 hrs	8 hrs
1	21955	31370.8	46648
2	54055.3	18872.6	37716.3
3	37921.6	29777.2	32139
4	28839.8	19141.6	35110.2
5	32217.6	51800.4	49324.8
6	37366.7	36552.1	62461.9
7	29066.7	29738.5	44281.5
8	40628.4	20025.3	24322.9
Avg.	35256.39	29659.81	41500.58
Std. dev.	9706.113	11087.17	11787.97
Error %	27.53008	37.38112	28.40436

Table 5.5 – The individual peak area values showing variations for 2 hours, 4 hours and 8 hours annealing of silicon.

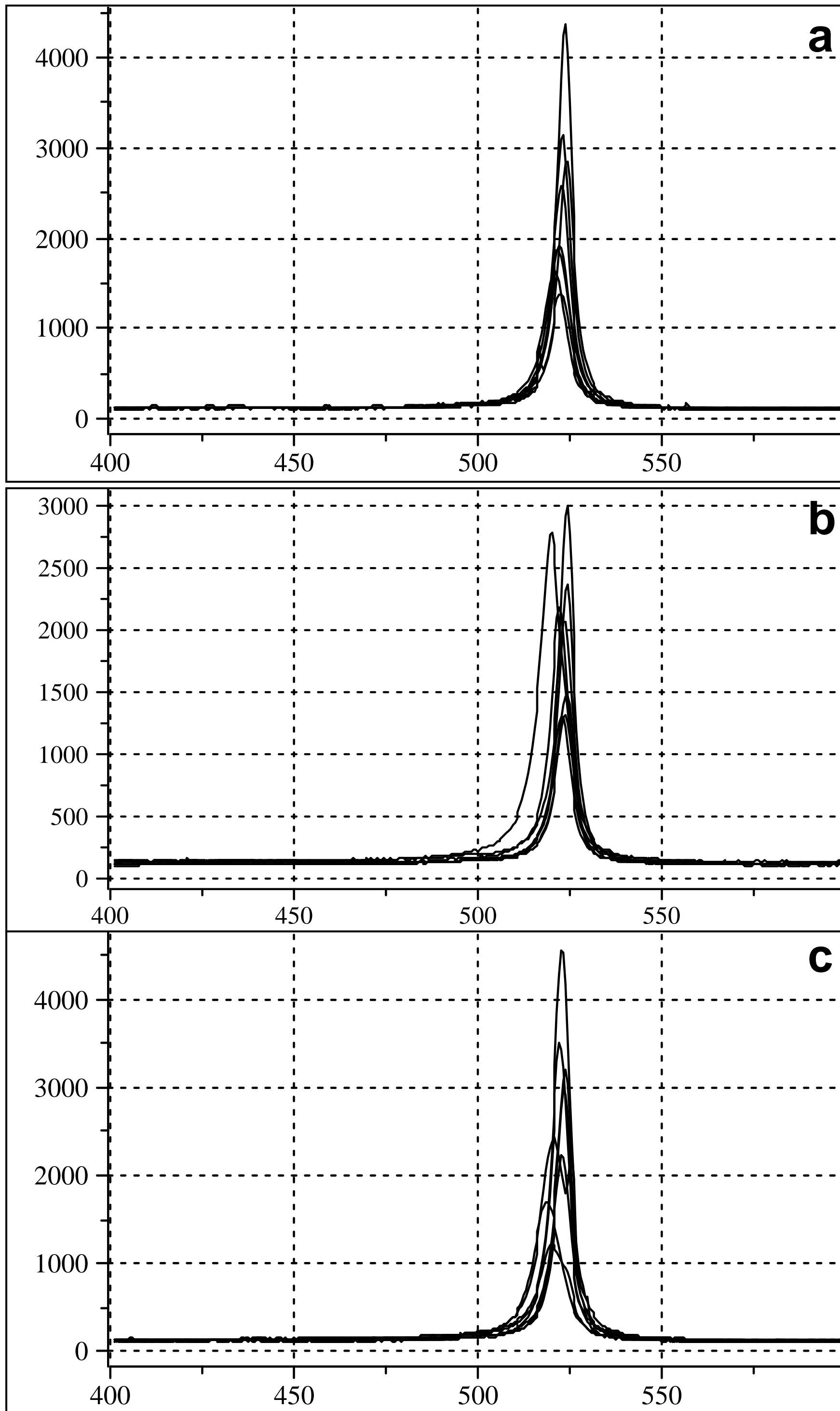

Figure 5.38 – Raman spectroscopy analysis of silicon particles annealed for: (a) 2 hours, (b) 4 hours and (c) 8 hours. The y-axis is the intensity in arbitrary units, while the x-axis is the wavenumber in cm^{-1}.

The individual silicon samples plots for 2 hour, 4 hour and 8 hour annealing times, are shown in figure 5.38. The crystalline silicon peaks are centered at 520 cm^{-1}. There is somewhat reduced variation of the intensities (and areas) of the peaks, with σ-error values ranging from 28 to 37%.

Annealing SiC Raman spectroscopy analysis

Peak area values are summarized in table 5.6.

	2 hrs	4 hrs	8 hrs
1	44633	62182.9	70292
2	63346.1	64708.7	60570.6
3	55534.6	78114.3	75138
4	59801.6	63939.9	60162.7
5	60492.3	74574.9	81865.1
6	64786.9		
7	46595.2		
Avg.	56455.67	68704.14	69605.68
Std. dev	7981.539	7145.016	9383.143
Error %	14.13771	10.39969	13.48043

Table 5.6 – The individual peak area values showing variations for 2 hours, 4 hours and 8 hours annealing of silicon.

The individual SiC samples plots for 2 hour, 4 hour and 8 hour annealing times are shown in figure 5.39. The crystalline SiC peaks are centered at 800 cm^{-1}.

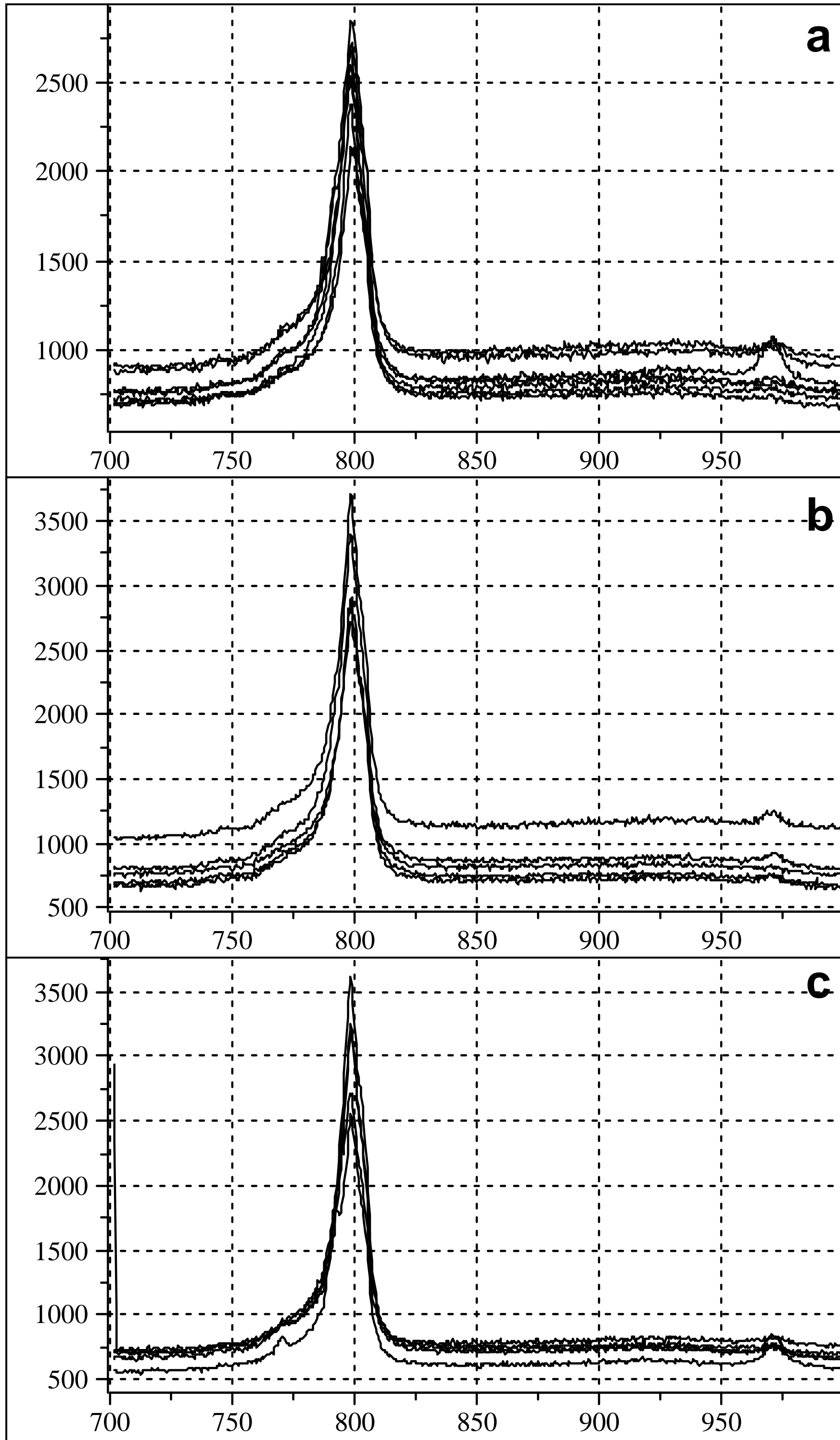

Figure 5.39 – Raman spectroscopy analysis of SiC particles annealed for: (a) 2 hours (b) 4 hours and (c) 8 hours. The y-axis is the intensity in arbitrary units, while the x-axis is the wavenumber in cm^{-1}.

The variation of the peak intensities (and areas) is significantly lower, with σ-error values ranging from 10 to 16%. Annealing temperature is known to be the most important variable affecting the annealing behaviour. This probably suggests that the 1100°C annealing temperature is fine for SiC but the 1000°C of silicon may not be an appropriate annealing temperature.

5.2.6. Quantitative Raman Spectroscopy discussion

In general the applicability of quantitative Raman spectroscopy is limited by the difficulties surrounding getting accurate and precise peaks mainly because of a large number of variables that have to be accounted for. The biggest obstacle is the size of the laser beam (which can at most be several tens of microns with micro-Raman spectroscopy), relative to the particle sizes. A technique such as Fourier Transform Raman spectroscopy samples several millimeters diameter to get a spectrum. The obvious limitation is that this cannot be applied to TRISO particles, where the entire SiC layer is several tens of microns at most. Another factor when analyzing solids with Raman spectroscopy is that the particles are oriented in an array of different angles. Depending on how the irradiated particles are oriented, there will be a varying influence on the peak intensity and area[36].

However, with regard to the results obtained, it is obvious that some of the calibration curve points vary significantly for the same particle size fraction of silicon. An average from repetitions of 10 analyses however is expected to yield more accurate results.

When dealing with quantitative Raman spectroscopy, it should always be remembered that technique counts the number of photons resulting when the laser interacts with the sample. The role of heterogeneity is therefore a very relevant issue. For instance if a mixture is weighed off as 50% silicon and 50% SiC, chances are this is not what will be reflected by the analysis, because only a few particles are measured with each analysis (even when the laser beam is 60 microns in diameter). Therefore even though the 10

points are plotted on the same 50% silicon x-axis point this is not necessarily what the Raman laser spot samples. As is discussed in more detail in section 2.4.3, 2.4.4 and the conclusions and recommendations section, the most immediate challenge with quantitative Raman spectroscopy is the large number of variables that have an effect on the intensity signal. Even though particle size and peak shapes and backgrounds were optimized by sample preparation, it is difficult to say what role the rest of the variables were playing when analyses were made.

Since Raman spectroscopy counts the number of photons subjected to the laser beam and the more particles are sampled, the more accurate the photometric results will be. With micro Raman spectroscopy, the inherent disadvantage is that the laser beam is several tens of microns in diameter at best. This can be achieved by using the smallest available magnification (5X objective) and defocusing the beam (a feature of more modern Raman spectroscopy machines). These factors disperse the beam diameter at the expense of peak intensity, meaning that a relatively strong signal is required. If the laser beam is too intense, the sample contents may burn or the signal to noise ratio may significantly be worsened because of fluorescence contributing to the background. If the signal is weak not only is the intensity further reduced, but the spot size becomes smaller as well. The beam size becomes problematic when powder samples are out of specification. The American Elements' samples were supposed to be about 1-2 micron particles. However, analysis with the Malvern particle size analyzer revealed particles several tens of microns in size, with a few that were in the hundreds of microns range. This observation was further confirmed by SEM analyses. This is problematic not only because of the relatively small laser beam, but also because of particle segregation (heterogeneity) introduced by mixing two components together (SiC and silicon). Manufacturing particle sizes of SiC that are around 1 micron is particularly challenging especially when the goal is to avoid contamination with the grinding medium. SiC has a Moh's hardness of 9.3 (more than corundum = 9 and less than diamond = 10) making its grinding particularly challenging. A recommended way of getting around this particle size issue is to have a fixed stage which spins the sample around while the analysis data are being collected. It

not recommended that particle sizes in the nanometer range be used because a whole lot of other factors come into play as is highlighted in section 2.4.3.

5.3. Quantitative X-ray Diffraction Characterization

The unequivocal identification of the 6H, 8H and 15R SiC polytypes is restricted by peak overlapping and the small quantities relative to the 3C polytype. The crystallite sizes of these minor phases were constrained to values similar to those of the 3C polytype, using the Rietveld method via the AUTOQUAN software package. This is done in order to avoid the broadening of the minor phase thereby merging with the background and reflecting unrealistically high percentages of the minor values. One of the assumptions made when analyzing with x-ray powder diffraction is a powder mix that is randomly mixed. This has implications for analysis of TRISO particles (especially for quantitative analyses), where the layers are firmly attached to each other. Appendix B contains the high temperature XRD data used.

5.3.1. As-received (normal) samples

When all the layers are fully intact, the graphite phase is in all the samples by far the most abundant phase, ranging from 57% to 90%, as shown by figure 5.40. This is expected since the buffer layer, IPyC and OPyC layer are all carbon phases. Owing to the fact that the x-rays penetrate through the entire TRISO particles and therefore yields a bulk analysis, it is not possible to analyze the SiC layer in isolation in comparison to Raman spectroscopy. There is also a small amount of quartz in each sample. The predominant SiC polytype is the 3C. There are in addition significant quantities of the 6H, 8H and 15R polytypes. Even though the 2H and 4H polytypes were also considered in the refinement, their contribution was in most cases either zero or minimal, hence for the sake of better refinement these small contributions are not included. Sample PO7 contains no SiC layer. The varying quantities of the components from one sample to the next are the result of differences in the layer thicknesses.

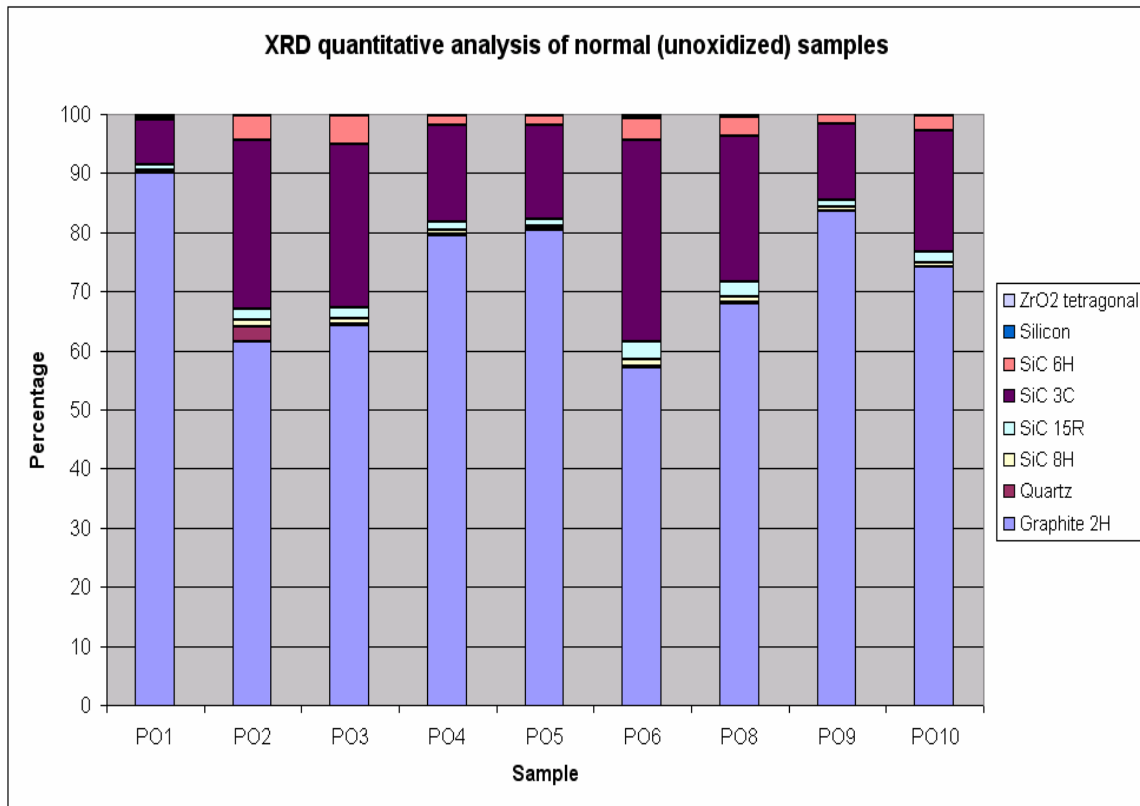

Figure 5.40 – Quantitative analysis of PO samples by x-ray diffraction with all layers intact. Graphite is by far the most abundant phase.

Figure 5.41 is derived from figure 5.40, where the amounts of SiC polytypes and silicon are isolated and normalized to 100%. The general trend is that the 3C polytype is predominant (with values ranging from 78-83% of the normalized total), followed by 6H, 15R and 8H respectively. An exception to this trend is seen with sample PO1, where the 15R polytype is the second most abundant polytype.

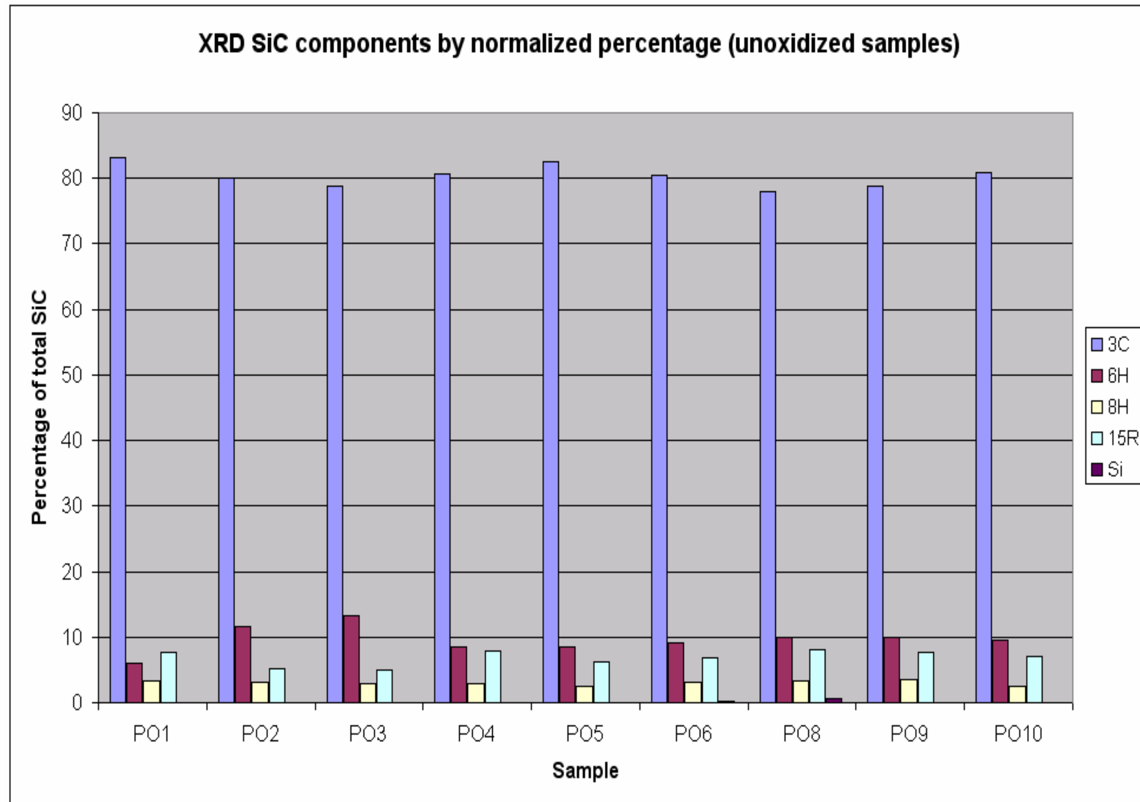

Figure 5.41 – Quantitative analysis of PO samples in the normal (as received) condition considering only the SiC polytypes, normalized to 100%. The 3C polytype is by far the most abundant ranging from 78% to 83%.

5.3.2. Oxidized samples

The samples were oxidized in order to remove the OPyC layers of the TRISO particles, thereby reducing the intensity of the poorly crystalline carbon peaks. For this reason, it was expected that the accuracy of the SiC quantification would improve.

The samples shown in figure 5.42 were oxidized in an attempt to remove the OPyC layer. In most samples, the graphite is still the most abundant phase indicating that the buffer layer and the IPyC layer alone contribute significantly to the overall graphite content. The graphite phase quantities range from 28% to 83%.

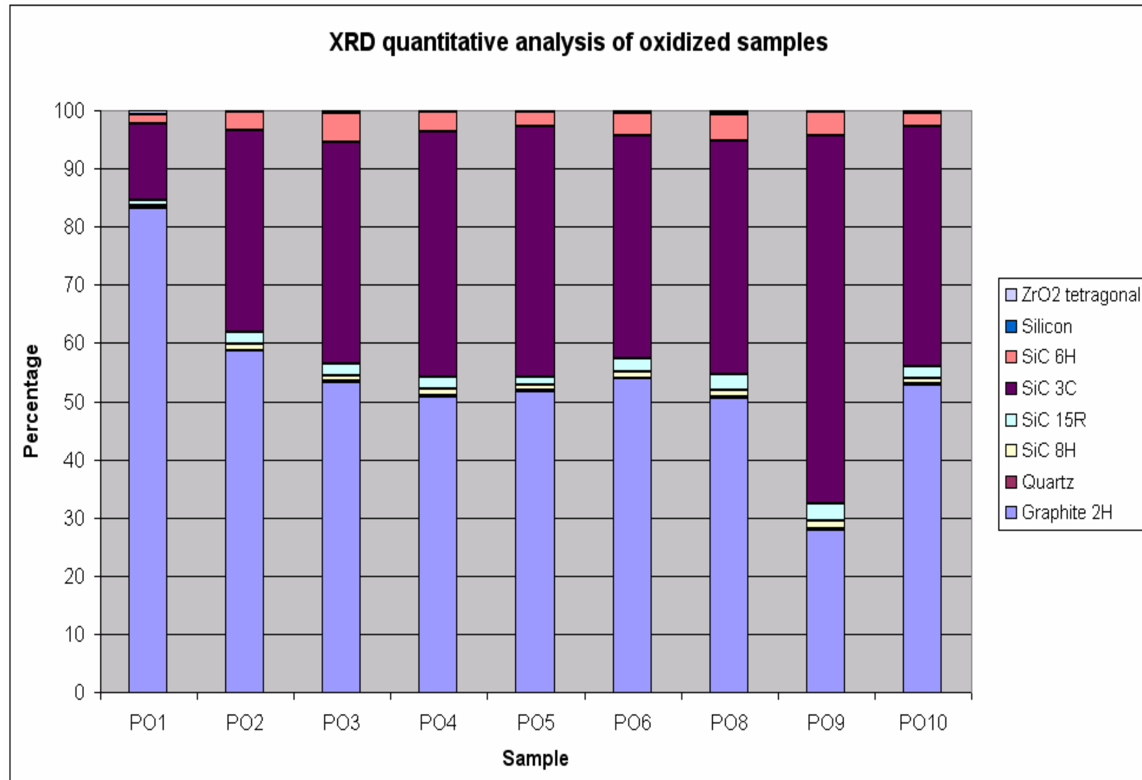

Figure 5.42 – Quantitative analysis of PO samples by x-ray diffraction, with the samples oxidized at 850°C. Even after oxidizing the OPyC layer, graphite is still the most abundant phase.

Figure 5.43 is a derivation of figure 5.42, with only the SiC polytypes and silicon contributions considered and normalized to 100%. A similar trend is seen as in figure 5.41, where the 3C polytype is most abundant (82%- 90% of the normalized total), followed by the 6H, 15R and 8H respectively. Unlike with figure 5.41, sample PO1 also follows this trend.

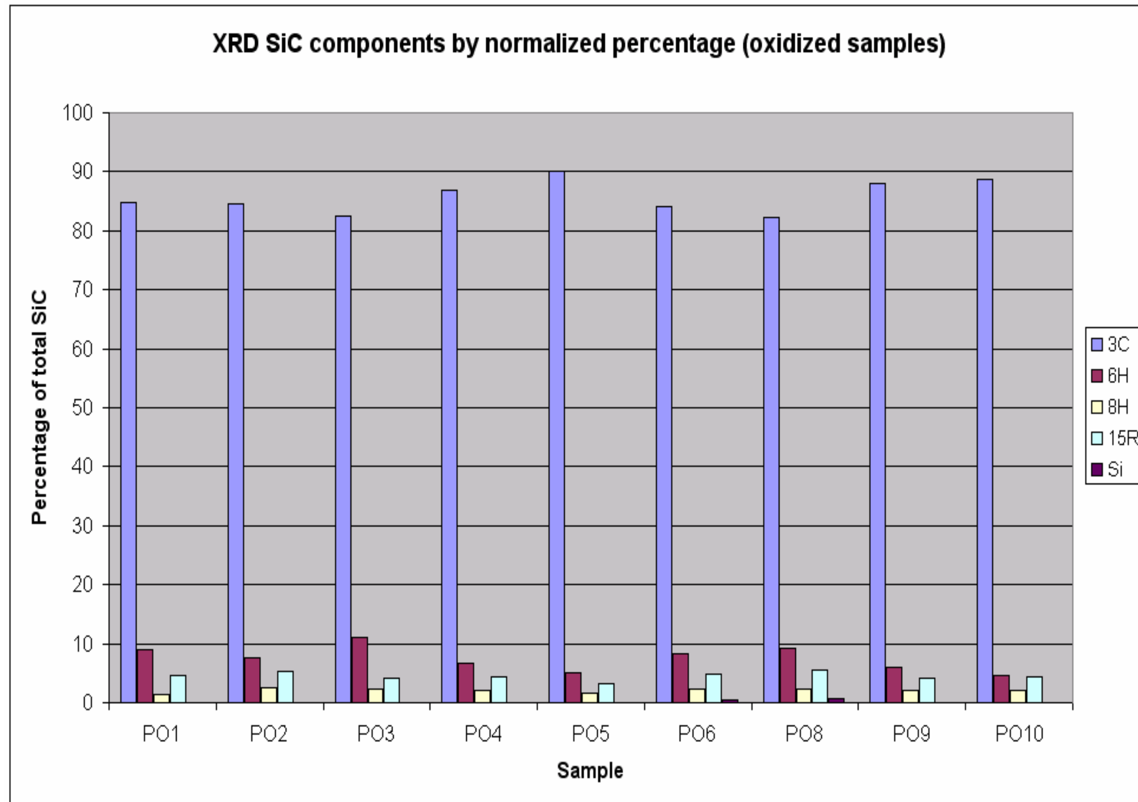

Figure 5.43 – Quantitative analysis of PO samples in the oxidized condition considering only the SiC polytypes, normalized to 100%. The 3C polytype is by far the most abundant ranging from 82% to 90%.

The actual values comparing the SiC polytype percentages of the normal and the oxidized samples are summarized by table 5.7. The included R_{wp} values are a measure of the accuracy for the least squares refinement, with smaller values signifying a better refinement[101]. It can be seen that the oxidized values yield refinements that are worse than the normal samples. The lower R_{wp} values of the unoxidized samples are attributed to the graphite's dominance of the refinements (graphite has only a few peaks to fit) and not better refinements.

Sample	SiC 3C	SiC 6H	SiC 8H	SiC 15R	Silicon	R_{wp}%
PO1	83.2	6.0	3.2	7.6	0.0	4.19
$PO1_{oxidized}$	84.9	9.0	1.4	4.7	0.0	8.20
PO2	80.0	11.6	3.1	5.3	0.0	4.12
$PO2_{oxidized}$	84.6	7.7	2.4	5.2	0.0	8.81
PO3	78.8	13.3	3.0	4.9	0.0	4.19
$PO3_{oxidized}$	82.5	11.1	2.2	4.2	0.0	9.32
PO4	80.7	8.6	2.9	7.8	0.0	4.00
$PO4_{oxidized}$	86.8	6.6	2.1	4.5	0.0	9.44
PO5	82.6	8.6	2.6	6.3	0.0	4.18
$PO5_{oxidized}$	90.0	5.1	1.7	3.2	0.0	9.00
PO6	80.5	9.1	3.2	6.9	0.3	4.25
$PO6_{oxidized}$	84.1	8.3	2.4	4.9	0.4	8.79
PO8	78.1	10.1	3.3	8.0	0.6	4.12
$PO8_{oxidized}$	82.2	9.3	2.4	5.6	0.6	8.75
PO9	78.9	9.9	3.6	7.6	0.0	4.45
$PO9_{oxidized}$	87.9	5.9	2.0	4.1	0.0	10.53
PO10	80.8	9.5	2.6	7.1	0.0	4.16
$PO10_{oxidized}$	88.7	4.7	2.2	4.3	0.1	10.54

Table 5.7 – A summary of the AUTOQUAN refinements, comparing the original and oxidized samples. The 3C polytype is the significantly the most abundant SiC polytype. Sample PO7 contains no SiC layer and has for this reason been excluded.

5.3.3. Calibration curve

Figure 5.44 is the x-ray diffraction calibration curve from the same initial quantitative mixtures of silicon and SiC as was used in the Raman spectroscopy analysis. The graph correlates the mass fraction calculated from AUTOQUAN versus the initial weighed-off mass fraction. The linear regression R^2 value is 0.984 for the 4H polytype, 0.978 for the 6H polytype and 0.991 for the 3C polytype. It is evident that the measured mass fraction values for the 3C polytype do not correspond with those of the other polytypes. The reason for this is that the sample is about 79% pure and this is corrected for the plot. In general however, there is good fit from refinement with AUTOQUAN.

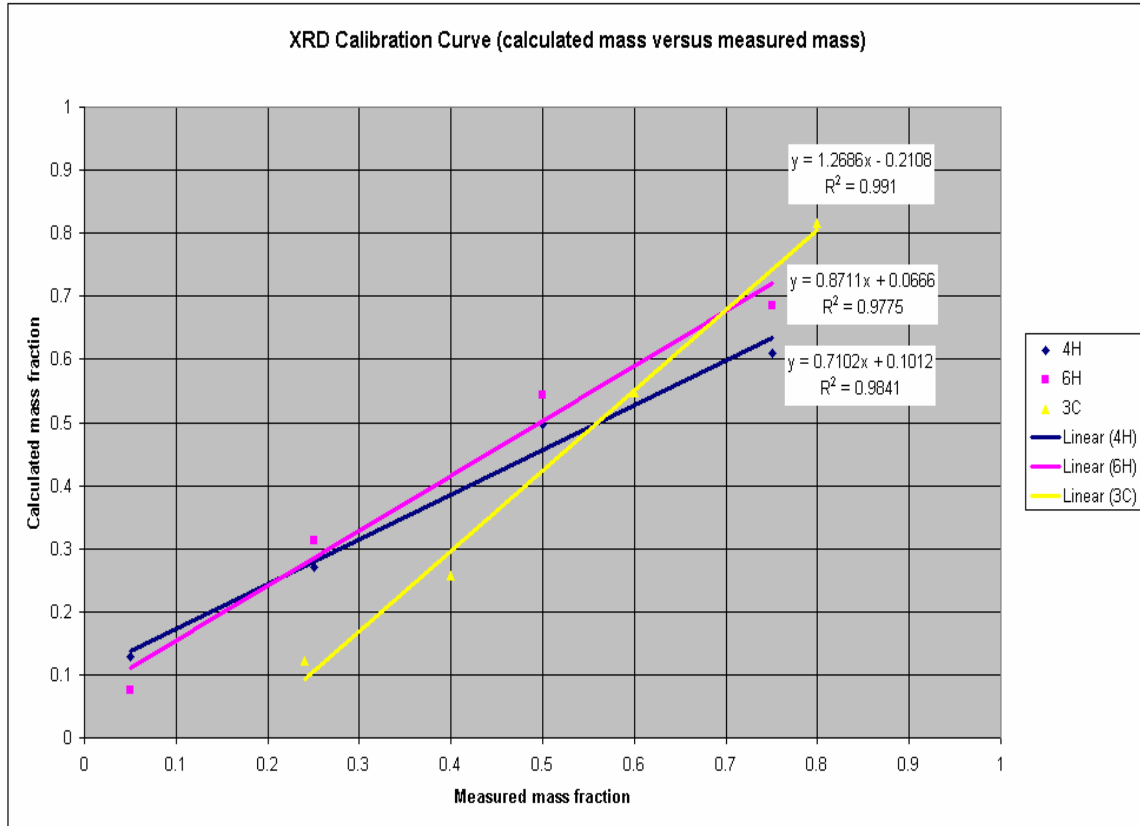

Figure 5.44 – The XRD calibration curve relating the mass fraction of silicon determined by AUTOQUAN versus the weighed off mass fraction of silicon. The binary mixtures are of silicon and the 3C, 4H and 6H polytypes of SiC.

5.4. High temperature XRD thermal expansion of SiC and graphite

The high temperature XRD results were collected to evaluate the thermal expansion properties of the SiC and graphite layers for three TRISO samples. Samples PO4, PO9 and G102 were chosen. The effect of layer thickness on the thermal expansion coefficients is of interest. Sample PO9 has a SiC layer that is more than double that of PO4 (51 and 25 microns respectively). Furthermore, it is of interest to check if an inflection point does indeed exist along the profile of the thermal expansion of SiC, which would suggest change of the stable SiC phase (i.e. polytypic change). The high temperature refinements were done using the TOPAS software package.

5.4.1. Experimental results

Al_2O_3

The analysis of Al_2O_3 is important because it provides an internal standard for correcting the thermal expansion values, and to what extent the experimental values differ from the theoretical values. The a-axis and c-axis measurements of Al_2O_3 therefore provide an independent measure for calibrating the a-axis of SiC and the c-axis of graphite. Sample displacement due to higher temperatures was accounted for in the TOPAS refinements. Figure 5.45 shows the plots of a-axis lattice parameter values against temperature of the Al_2O_3 internal standard for G102, PO4 and PO9. The theoretical Al_2O_3 curve was calculated using equation 5.9.

$$a(T) = 4.75814(1 + 6.55\times10^{-6}T + 1.82\times10^{-9}T^2) \quad (5.9)$$

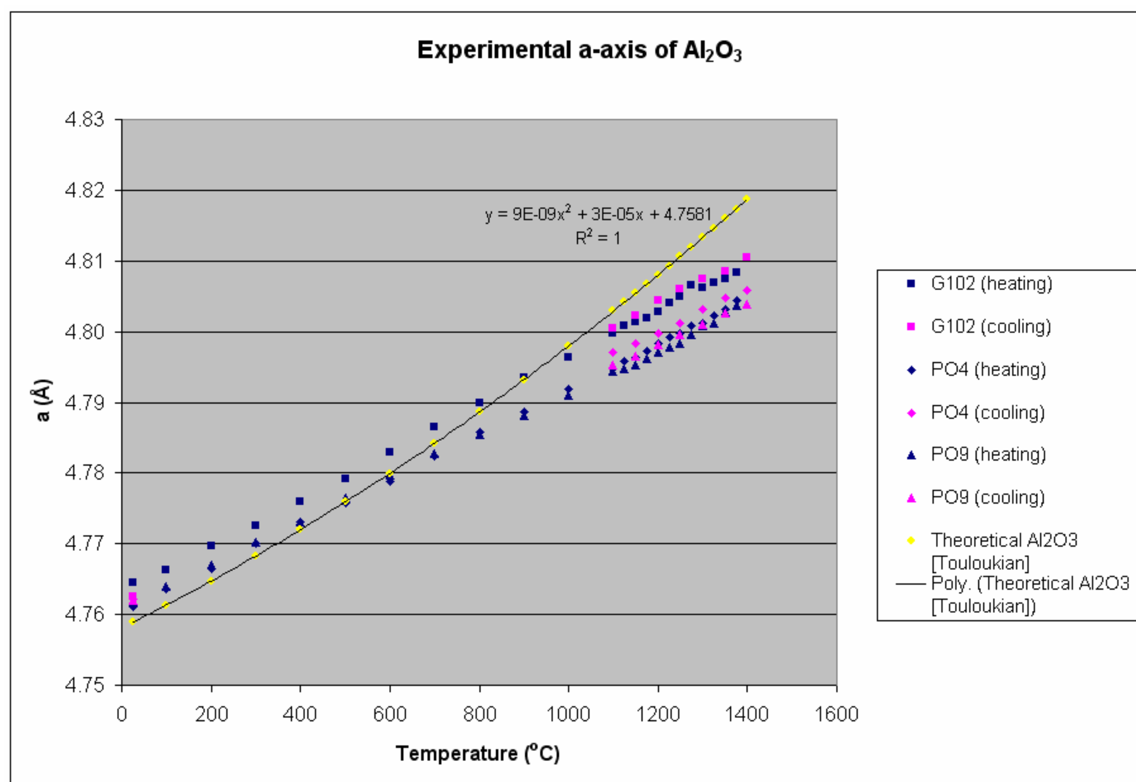

Figure 5.45 – Plots of the uncorrected experimental a-axes lattice parameters versus temperature of Al_2O_3 for G102, PO4 and PO9, compared with the theoretical Al_2O_3 a-

axis lattice parameter. A molybdenum heating strip was used for G102 whereas PO4 and PO9 were analyzed using a graphite heating strip.

It is clear from figure 5.45 that the a-lattice parameter values of Al_2O_3 in G102 have the poorest correspondence with the literature values at lower temperatures and the best at higher temperatures. PO4 and PO9 display similar behaviour when compared to each other. Collectively, the best correlations are at lower temperatures, with rather significant deviations at higher temperatures.

Figure 5.46 shows the plots of c-axis lattice parameter values against temperature of the Al_2O_3 internal standard for G102, PO4 and PO9. These are compared with the theoretical c-axis values of Al_2O_3 using equation 5.10.

$$c(T) = 12.99113(1 + 6.54 \times 10^{-6} T + 2.60 \times 10^{-9} T^2) \qquad (5.10)$$

A similar trend is observed as with the thermal expansion along the a-axis. The deviation of the G102 sample is greatest at lower temperatures and the least at higher temperatures, when compared with the theoretical values. PO4 and PO9 almost coincide and this is attributed to the use of heating strips (leading to differing temperature profiles), as opposed to sample variables. Differences in the lattice parameters when heating up and cooling down are not perfectly reversible along the c-axis.

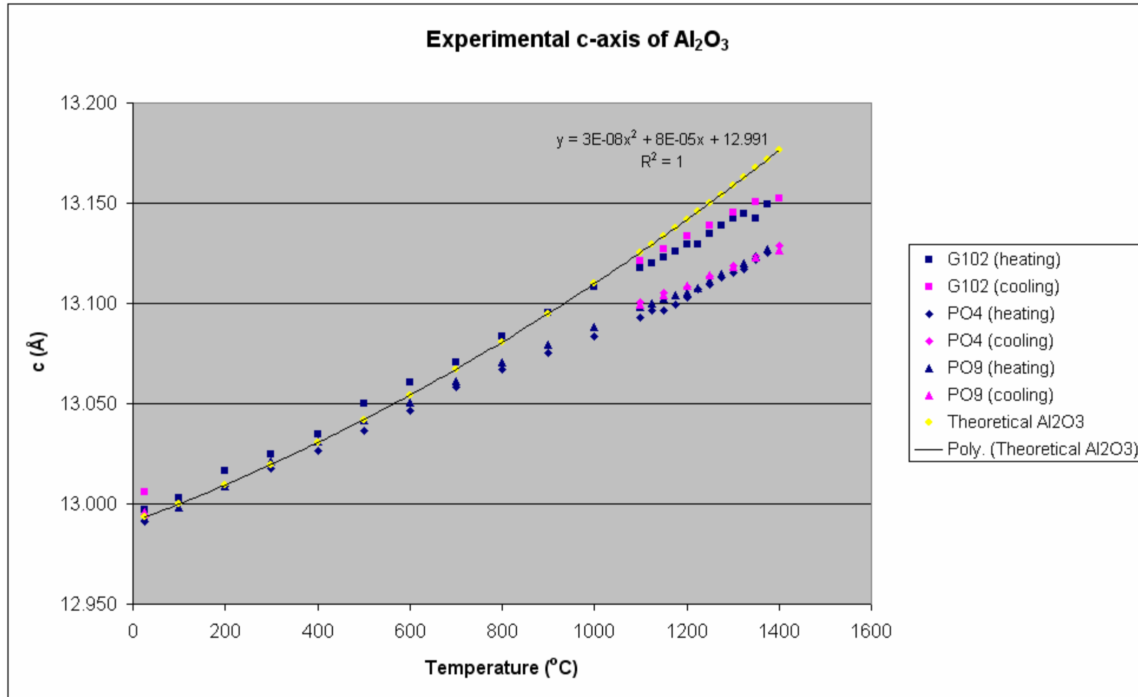

Figure 5.46 – Plots of the experimental a-axes lattice parameters versus temperature of Al_2O_3 for G102, PO4 and PO9, compared with the theoretical Al_2O_3 c-axis lattice parameter. A molybdenum heating strip was used for G102 and a graphite strip for PO4 and PO9.

SiC

The a-axis lattice parameter of the SiC was analyzed with the purpose of monitoring the thermal expansion properties of the TRISO particle samples. The Al_2O_3 data served as a means of correcting the SiC values thereby monitoring how close to theoretical values the SiC experimental results are. Figure 5.47 shows the plots of a-axis lattice parameter values against temperature of SiC for G102, PO4 and PO9. As is the case with the Al_2O_3 plots, the G102 results are higher than those of PO4 and PO9. The heating and cooling results are closer to each other than is the case with the Al_2O_3 plots.

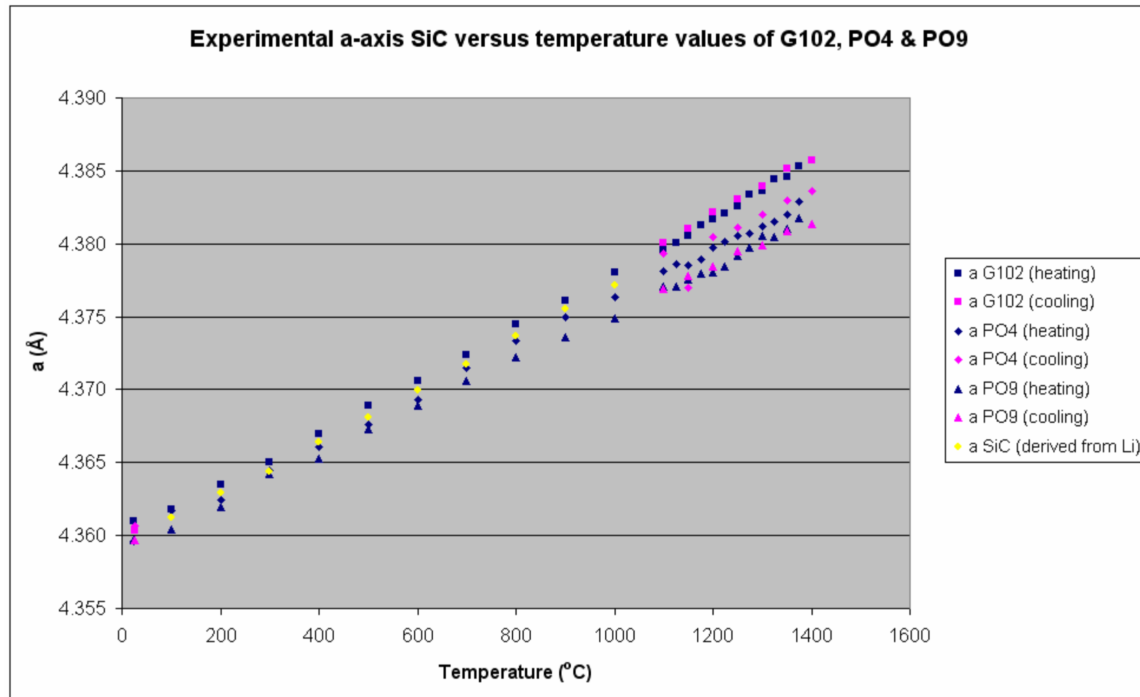

Figure 5.47 – Plot of experimental the a-axis lattice parameter for SiC

5.4.2. Corrected Curves

The temperature values of the a-axis of SiC and the c-axis of graphite were recalculated on the basis of the theoretical Al_2O_3 a-axis and c-axis values. The thermocouple measured a single spot on the heating strip. It is however expected that there is a temperature profile along the heating strip. As a result, the actual temperature tends to vary significantly from the one detected by the thermocouple.

Al_2O_3

Figure 5.48 shows temperature corrected values using the a-axis of Al_2O_3. The values of G102, PO4 and PO9 superimpose those of the theoretical Al_2O_3 after correction. The temperature error was calculated based on the differences in a-axes values of the experimental uncorrected Al_2O_3 (for G102, PO4 and PO9) and the theoretical curve values. In order to obtain accurate curves, temperature was plotted as the dependant variable against the a-axis values. The resulting relationship was fitted as a binomial with

six decimal places for increased accuracy. The new (corrected) temperature values were then used as a basis for plotting the corrected Al_2O_3 plots.

For instance, the G102 temperature versus lattice parameter curve, based on the a-axis of Al_2O_3 is summarized by equation 5.11. Based on this equation, it is possible to calculate what the temperature should have been to yield the resultant lattice parameter. In this way a corrected temperature profile is obtained for each lattice parameter.

$$T = -101233.8 \times a_{Al_2O_3}{}^2 + 992297.1 \times a_{Al_2O_3} - 2429553 \tag{5.11}$$

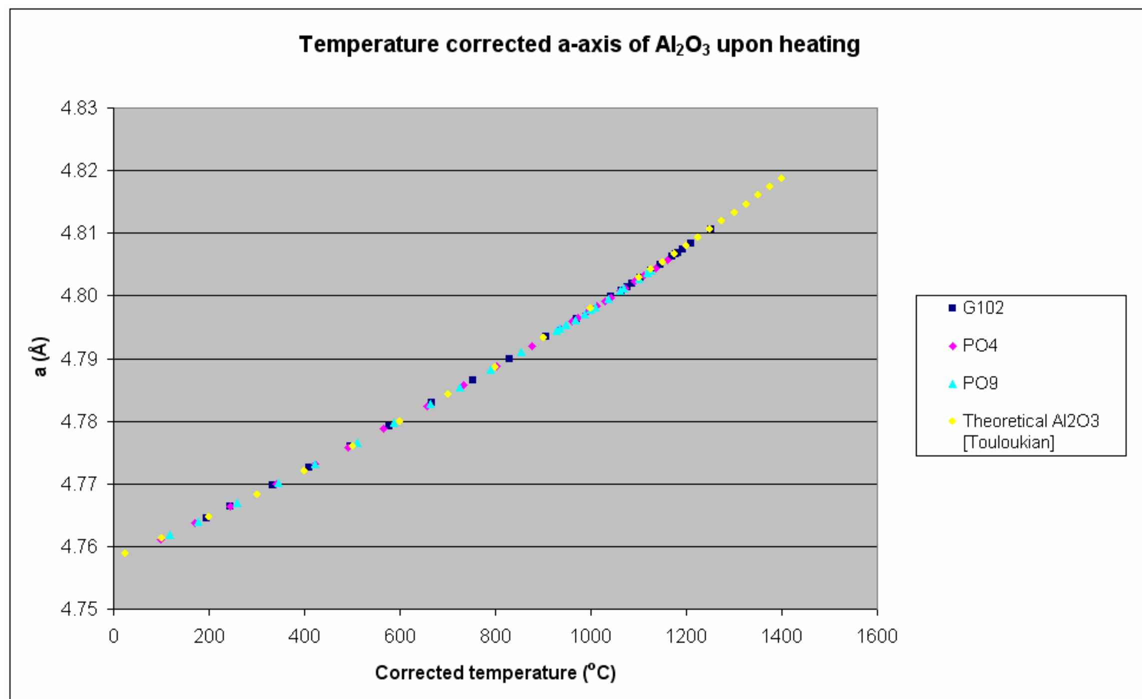

Figure 5.48 – Plot of the experimental a-axis lattice parameter at corrected temperatures for Al_2O_3, superimposed on the theoretical curve.

Figure 5.49 shows temperature corrected values along the c-axis of Al_2O_3. The values of G102, PO4 and PO9 superimpose on those of the theoretical Al_2O_3. The temperature correction of the c-axis was done exactly the same way as that of the a-axis. Once more, the corrected values superimpose on those of the theoretical curve.

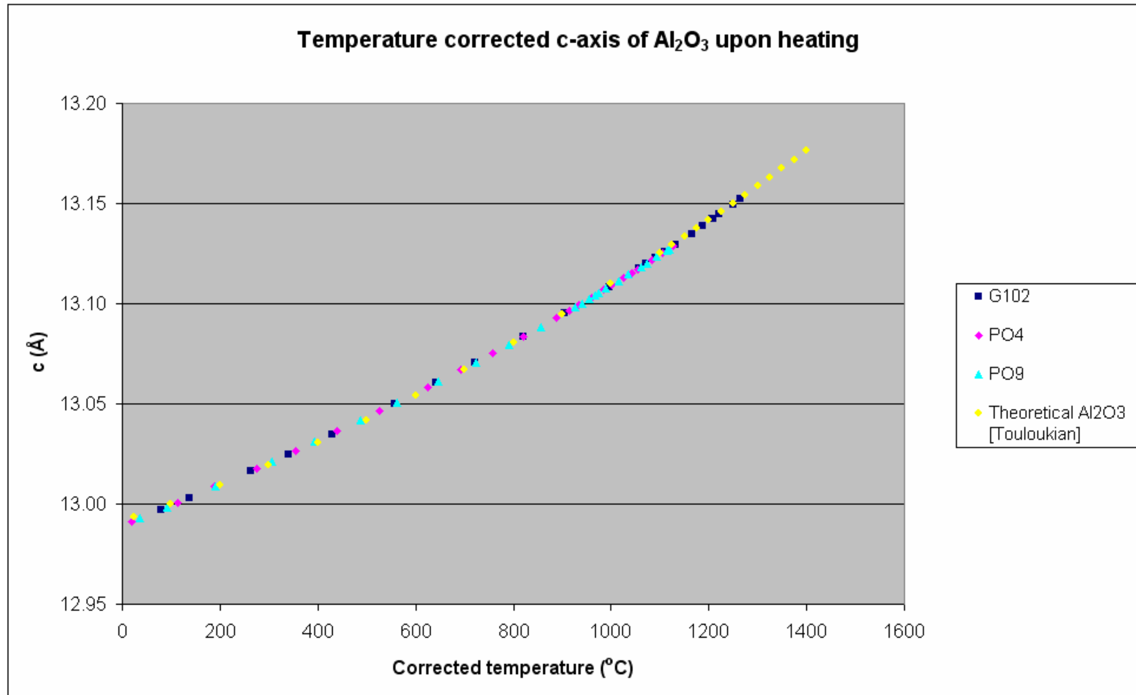

Figure 5.49 – Plot of the corrected c-axis lattice parameter at corrected temperatures for Al_2O_3.

Silicon Carbide

The temperature corrections of the experimental SiC are based on the temperature correction of the a-axis and c-axis of Al_2O_3. A high number of decimals are used (as is seen in the figures) to yield accurate thermal expansion coefficient values.

Figure 5.50 illustrates the plots of the a-axes values of G102, PO4 and PO9 SiC against temperature corrected values when heating up and cooling down, where the temperature correction values are based on the a-axis of Al_2O_3. The G102 profile is fitted by a binomial (equation 5.12), with an R^2 value of 0.9988.

$$a_{G102}(T) = 4.3580(1 + 3.34\times10^{-6}T + 1.42\times10^{-9}T^2) \qquad (5.12)$$

The PO4 profile is fitted by a second order polynomial (equation 5.13), with an R^2 value of 0.9993.

$$a_{PO4}(T) = 4.3579(1 + 4.27\times10^{-6}T + 6.65\times10^{-10}T^2) \qquad (5.13)$$

The PO9 profile is fitted by a second order polynomial (equation 5.14), with an R^2 value of 0.9991.

$$a_{PO9}(T) = 4.3573(1 + 4.10\times10^{-6}T + 8.05\times10^{-10}T^2) \qquad (5.14)$$

The heating up and cooling down curves are reasonably similar suggesting that cyclic effects are minimal. The corrected curves are all similar in shape and almost superimpose.

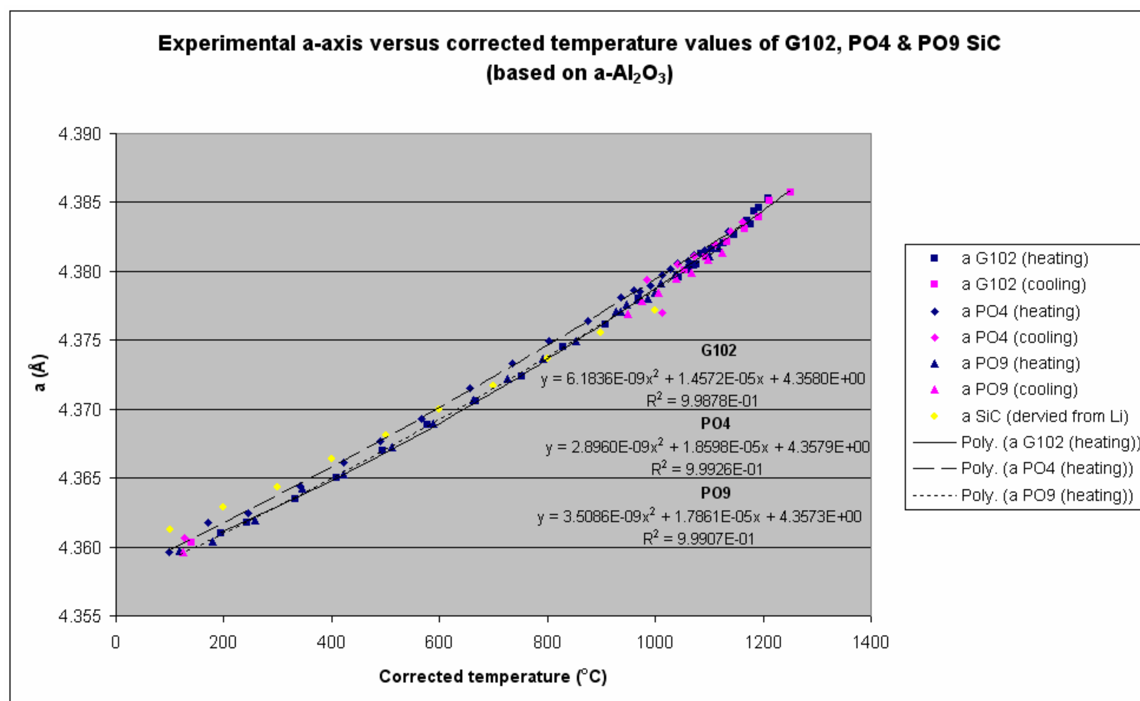

Figure 5.50 – Plot of experimental the a-axis lattice parameter for G102, PO4 and PO9 SiC, upon heating up and cooling down (the correction is based on a-axis values of Al_2O_3). There is very good correspondence with the data by Li et al. [72].

Figure 5.51 is a plot of a-axis of G102, PO4 and PO9 SiC against temperature corrected values when heating up and cooling down, where the temperature correction values are

based on the c-axis of Al_2O_3. The G102, PO4 and PO9 (equations 5.15, 5.16 and 5.17) SiC binomial curves are fitted with R^2 values of 0.9989, 0.9990 and 0.9996 respectively. The corrections are further apart relative to the correction made on the basis of the a-axis of Al_2O_3. For each of the curves, the heating up and cooling down values have only slight deviation therefore no cyclic effects are evident.

$$a(T)_{G102} = 4.3601(1 + 2.81\times10^{-6}T + 1.42\times10^{-9}T^2) \quad (5.15)$$

$$a(T)_{PO4} = 4.3592(1 + 4.24\times10^{-6}T + 6.30\times10^{-10}T^2) \quad (5.16)$$

$$a(T)_{PO9} = 4.3591(1 + 3.24\times10^{-6}T + 1.24\times10^{-9}T^2) \quad (5.17)$$

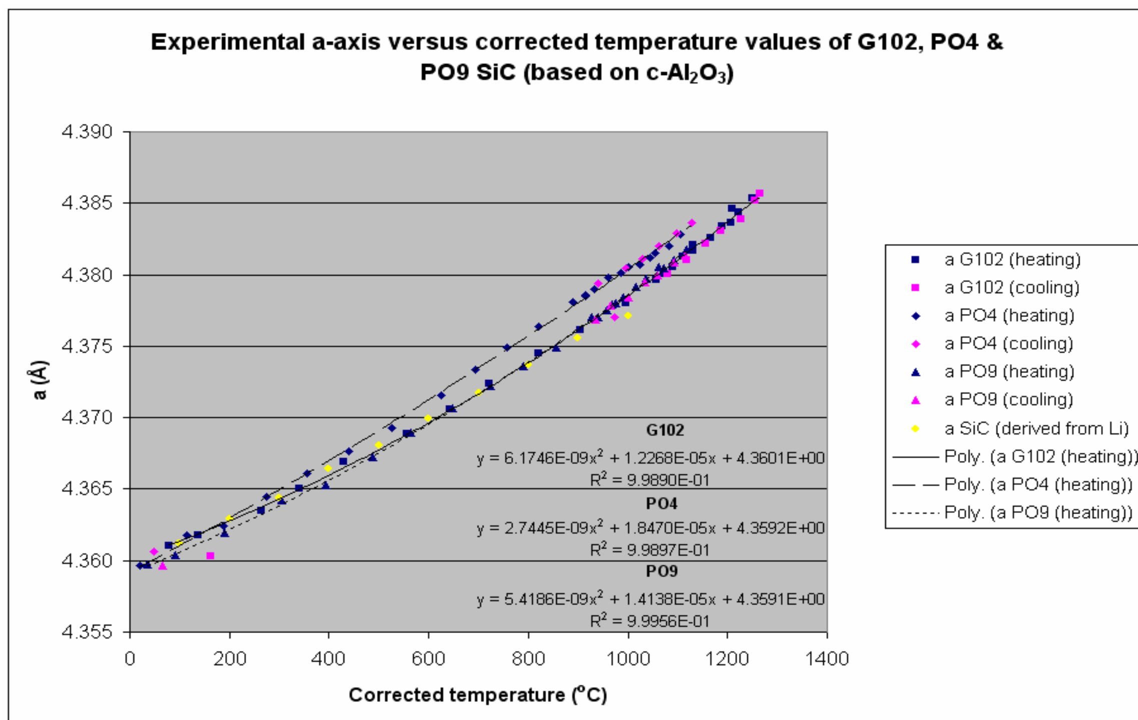

Figure 5.51 – Plot of experimental the a-axis lattice parameter for G102, PO4 and PO9 SiC, upon heating up and cooling down (the correction is based on c-axis values of Al_2O_3).

There is no evidence to suggest a change of SiC slope for the correction based on the a-axis or the c-axis. There is therefore no change in the mechanism governing the lattice parameters. The process was also checked for the case where the temperature correction applied was that of the c-axis of Al_2O_3.

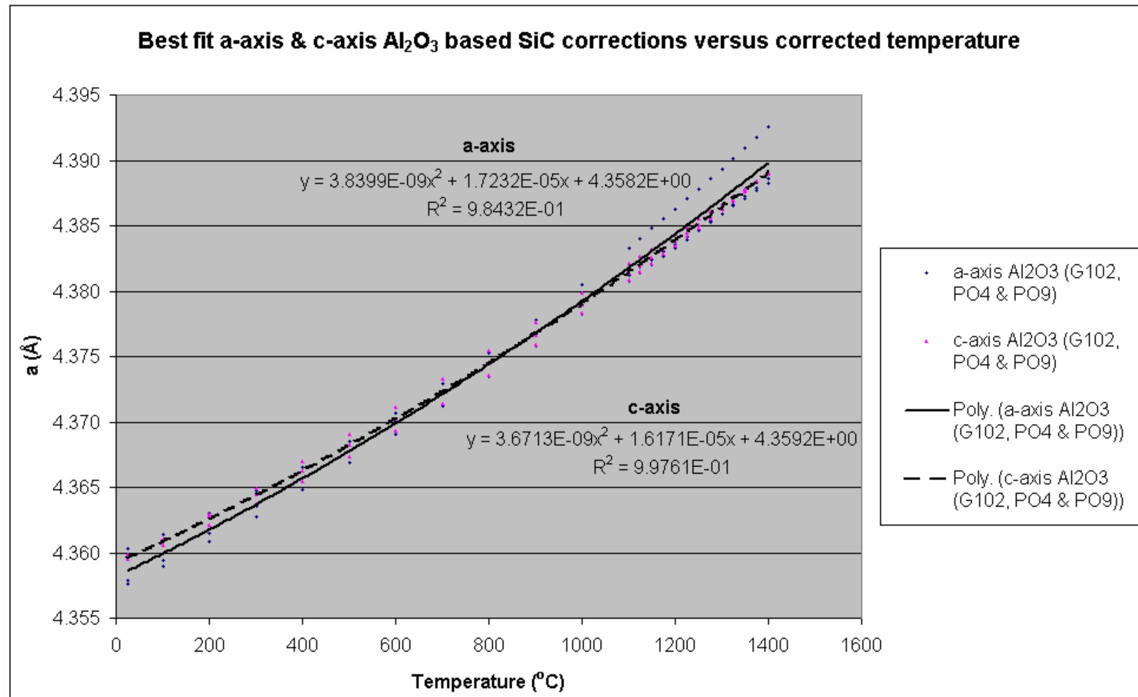

Figure 5.52 – The best fit a-axis SiC lattice parameter fits for G102, PO4 and PO9 based on the a-axis and c-axis temperature corrected values. There is generally a good correlation between the a-axis and c-axis based correction data.

The best fit a-axis lattice parameters of G102, PO4 and PO9 SiC are shown in figure 5.52. The temperature corrected values based on the a-axis and c-axis of Al_2O_3 are compared. Even though there is some scatter with individual plots, there is good correlation of the fitted curves, which combine the individual G102, PO4 and PO9 data. There is a slight deviation at lower temperatures from room temperature up to 500°C. From 1200 to 1400°C, there is a much smaller deviation as well. The relationships between the lattice parameters and temperature are given by equations 5.18 and 5.19.

$$a(T)_{a-axis} = 4.3582(1 + 3.95\times10^{-6}T + 8.81\times10^{-10}T^2) \quad (5.18)$$

$$a(T)_{c-axis} = 4.3592(1 + 3.71\times10^{-6}T + 8.42\times10^{-10}T^2) \quad (5.19)$$

Graphite

The temperature corrections of graphite are based on the temperature correction of the a-axis and c-axis of Al_2O_3.

Figure 5.53 illustrates the c-axis plot of G102, PO4 and PO9 graphite against temperature when heating up and cooling down, based on the a-axis Al_2O_3 temperature correction.

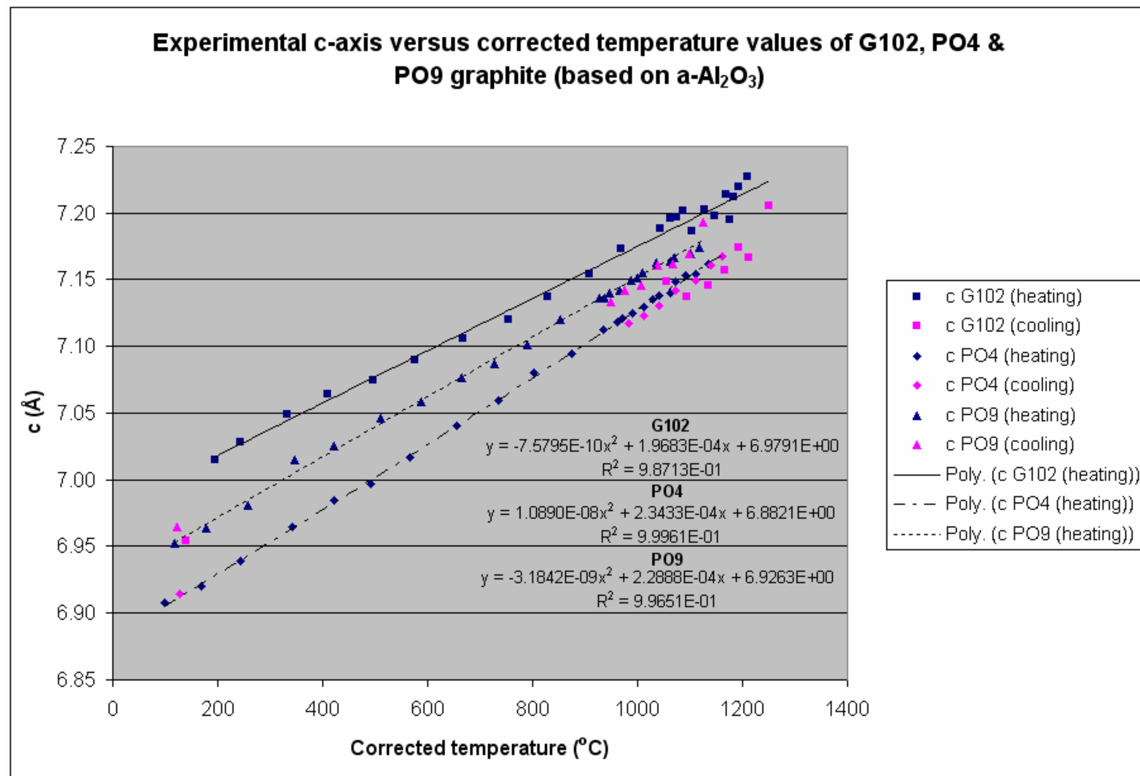

Figure 5.53 – Plot of experimental the c-axis lattice parameter for G102, PO4 and PO9 graphite upon heating up and cooling down (the correction is based on a-axis values of Al_2O_3).

The resulting profiles (for G102, PO4 and PO9) are fitted as binomials with R^2 values of 0.9871, 0.9996 and 0.9965 (equations 5.20, 5.21 and 5.22). The c-axis errors for graphite are several orders of magnitude larger than the Al_2O_3 and SiC errors.

$$c_{G102}(T) = 6.9791(1 + 2.82 \times 10^{-5} T + 1.09 \times 10^{-10} T^2) \quad (5.20)$$

$$c_{PO4}(T) = 6.8821(1 + 3.40 \times 10^{-5} T + 1.58 \times 10^{-9} T^2) \quad (5.21)$$

$$c_{PO9}(T) = 6.9263(1 + 3.31 \times 10^{-5} T - 4.59 \times 10^{-10} T^2) \quad (5.22)$$

At lower temperatures the graphite c-axis values differ significantly, with the difference gradually narrowing as temperature increases. Above 1100°C, there is significant scatter for the G102. Since sample displacement at high temperature is accounted for, the reason is likely to be the broad graphite peak. The centre for broader peaks tends to vary in TOPAS. There is also a possibility of a contribution to the graphite peak from the graphite heating element. This would be from a different height than the sample.

Figure 5.54 illustrates the c-axis plot of G102, PO4 and PO9 graphite against temperature when heating up and cooling down, based on the c-axis Al_2O_3 temperature correction. The plots and their relationships are very similar to those of figure 5.53. It is not clear why the G102 cooling values are so different from the heating up values. The profiles (for G102, PO4 and PO9) are fitted as binomials with R^2 values of 0.9891, 0.9984 and 0.9962 respectively (equations 5.23, 5.24 and 5.25).

$$c_{G102}(T) = 7.0051(1 + 2.21 \times 10^{-5} T + 1.89 \times 10^{-9} T^2) \quad (5.23)$$

$$c_{PO4}(T) = 6.8983(1 + 3.30 \times 10^{-5} T + 1.66 \times 10^{-9} T^2) \quad (5.24)$$

$$c_{PO9}(T) = 6.9479(1 + 2.66 \times 10^{-5} T + 2.69 \times 10^{-9} T^2) \quad (5.25)$$

From figure 5.53 and 5.54, it is clear that there is significant scatter associated with the thermal expansion of the c-axis of graphite. This is attributed to the broad amorphous graphite peak, which is fitted at varying 2θ positions. Analyses of PO4 and PO9 are further complicated by the use of the graphite heating strip, which yielded sharp crystalline graphite peaks of its own in addition to those from the TRISO particles. As a result these curves are not expected to be very reliable and the thermal expansion coefficient curve is not plotted.

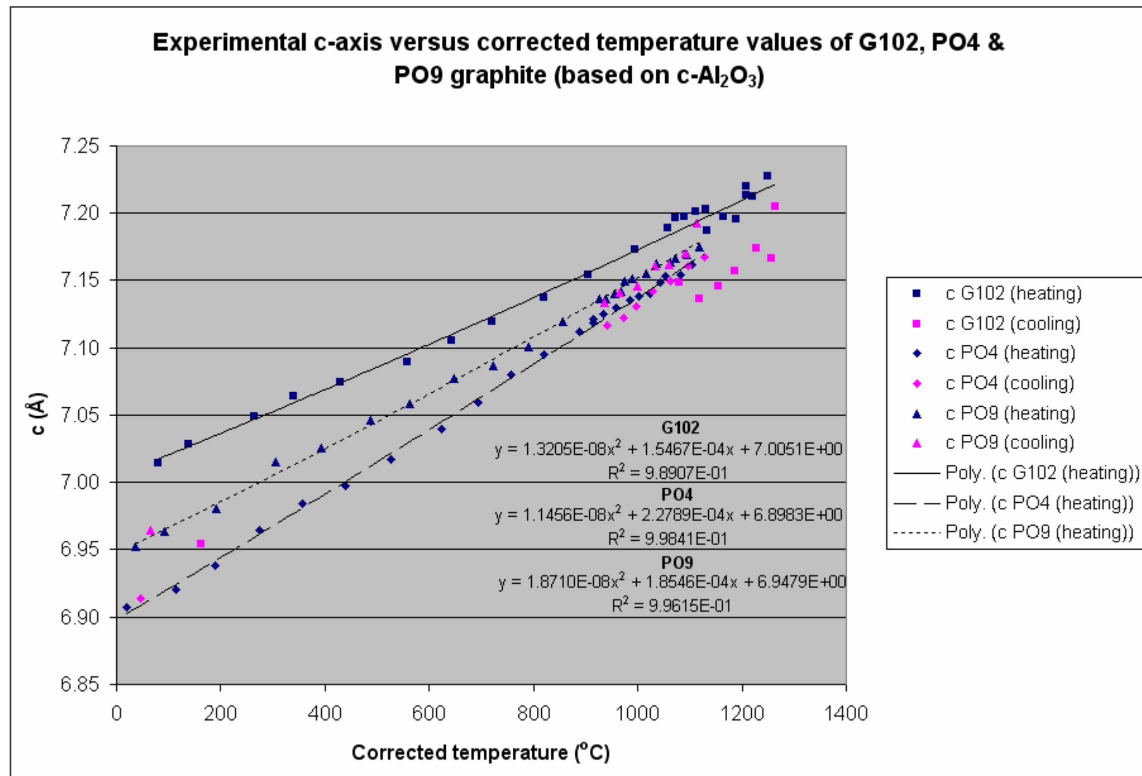

Figure 5.54 – Plot of experimental the c-axis lattice parameter for G102, PO4 and PO9 graphite upon heating up and cooling down (the correction is based on c-axis values of Al_2O_3).

5.4.3. Thermal expansion coefficients of SiC

The corrected a-axis SiC values were recalculated based on the temperature corrected curve for each sample. The temperature range used is chosen to be the same as the

original experimental increments (i.e. 25°C to 1400°C). These values were then used to calculate the linear thermal expansion coefficients of graphite and SiC according to equation 5.26 below, assuming one-dimensional length change with temperature. The thermal expansion coefficient was calculated using the derivatives of figures 5.50 and 5.51.

$$\alpha_L = \frac{d(\ln L)}{dT} \approx \frac{1}{L_0} . \frac{dL}{dT} \qquad (5.26)$$

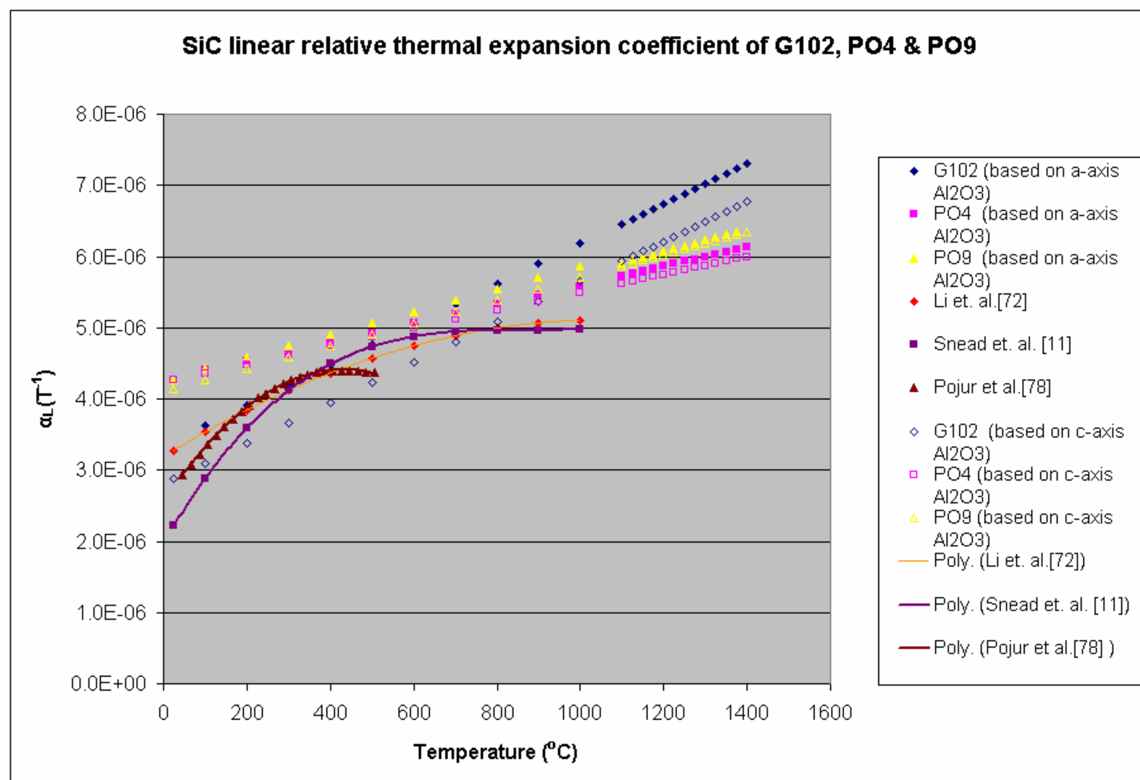

Figure 5.55 – Plot of the a-axis SiC thermal expansion coefficients of the TRISO samples.

The thermal expansion coefficient results of G102, PO4 and PO9 SiC are shown in figure 5.55. The values chosen to construct the thermal expansion coefficient curves are lattice parameter, temperature-corrected curves based on the a-axis and c-axis of Al_2O_3. There are general similarities between G102 and the results by Li[79], Snead[11] (CVD SiC) and Pojur[82] (TRISO particles), up to about 800°C. Thereafter the experimental data show

significantly greater thermal expansivity. It should be noted that the TRISO samples by Pojur[82] were hollow hemispherical SiC shells, prepared by the fluidized bed method. Sample PO4 and PO9 data becomes accurate from about 500°C. It is worth noting that the data by Li[79] is accurate only up to 1000°C. It is not conclusive why the results for PO4 and PO9 deviate from room temperature. The best fit plot, which combines G102, PO4 and PO9 data is shown in figure 5.56. As is seen, there is deviation from literature data at room temperature. At higher temperatures, the thermal expansion coefficient curve does not level off (as is the case with literature data) resulting in higher expansivity.

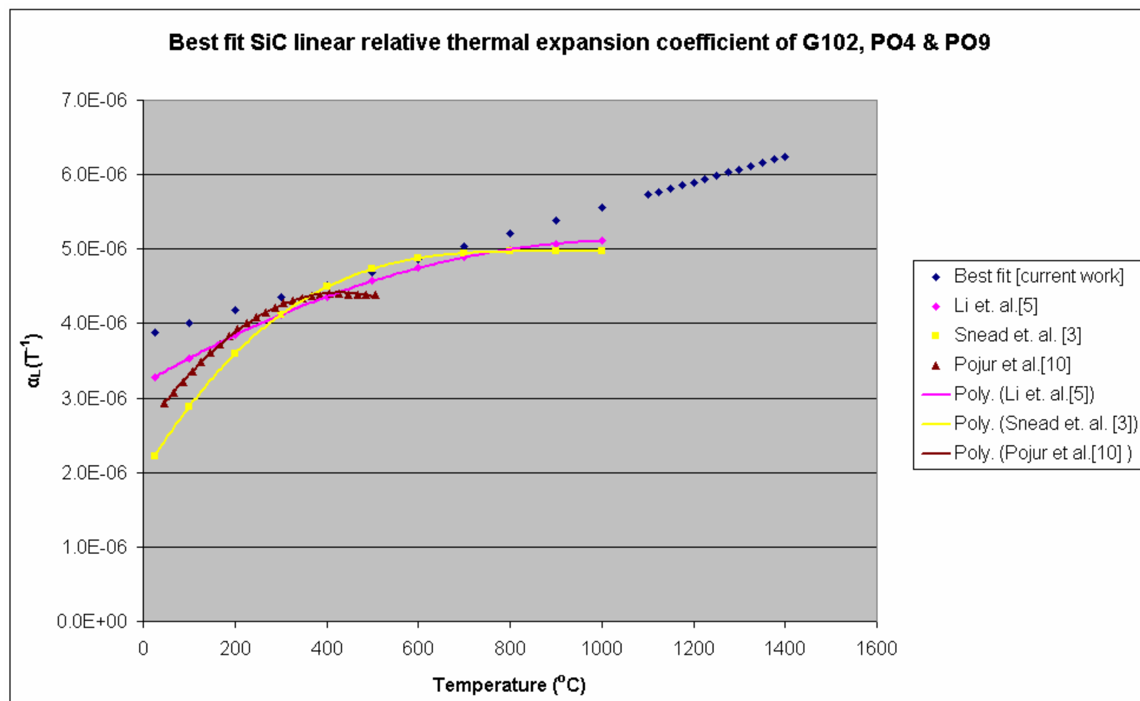

Figure 5.56 – Best fit plot of the a-axis SiC thermal expansion coefficients of the TRISO samples.

It is however known that the thermal expansion of SiC is significantly dependent on its crystal structure. This is not likely to be the cause since the 3C polytype has been shown to be dominant and differences are in any case minimal. Some studies have claimed that the presence of impurities such as free carbon or silicon could reduce the TRISO SiC thermal expansivity. Micropores have also been known to have an effect on the thermal expansion behaviour[11]. Furthermore, it is not known what effect the surrounding layers

(of pyrolytic and porous carbon and the ZrO_2 kernel) have on the thermal expansion of each TRISO particle.

5.5. Transmission electron microscopy

From the total of 10 samples, PO5, 6 and 9 were selected for analysis with the TEM. The indisputable characterization of the SiC polytypes is possible by interpretation of the diffraction patterns of the associated crystallites. Streaking was identified from some of diffraction patterns and the bright field and dark field images.

5.5.1. Polytype characterization

PO 5

Image #	Diffraction	Polytype	Zone axis
1	1	3C	[100]
	2	3C	[211]
	3	3C	[122]
2	1	3C	[111]
	2	6H	[001]
3	1	3C	[211]
4	1	3C	[111]
5	1	3C	[111]
	2	3C	[100]
6	1	6H	[001]
7	1	3C	[110]
8	1	3C	[111]

Table 5.8 – Summary of the interpreted diffraction patterns of PO5 included in the appendix section, showing that the 3C polytype is the most commonly occurring.

The interpretation of all the crystals analyzed is summarized in table 5.8. Some of the images have more than one diffraction pattern resulting in repetition of the crystal number. In cases where two zone axes are listed for the same diffraction pattern, multiple overlapping crystals yield more than one diffraction pattern. Only the 3C and the 6H SiC polytypes were identified. The 3C polytype is the most commonly occurring. The PO5 images, diffraction patterns and calculated patterns are listed in appendix C.

From figure 5.57, the two diffraction patterns represent the 3C [100] and 3C [111] zone axes. The diffraction pattern of figure 5.58 represents the 3C [111] zone axis. The two diffraction patterns of figure 5.57 come from different parts of the same twinned crystal.

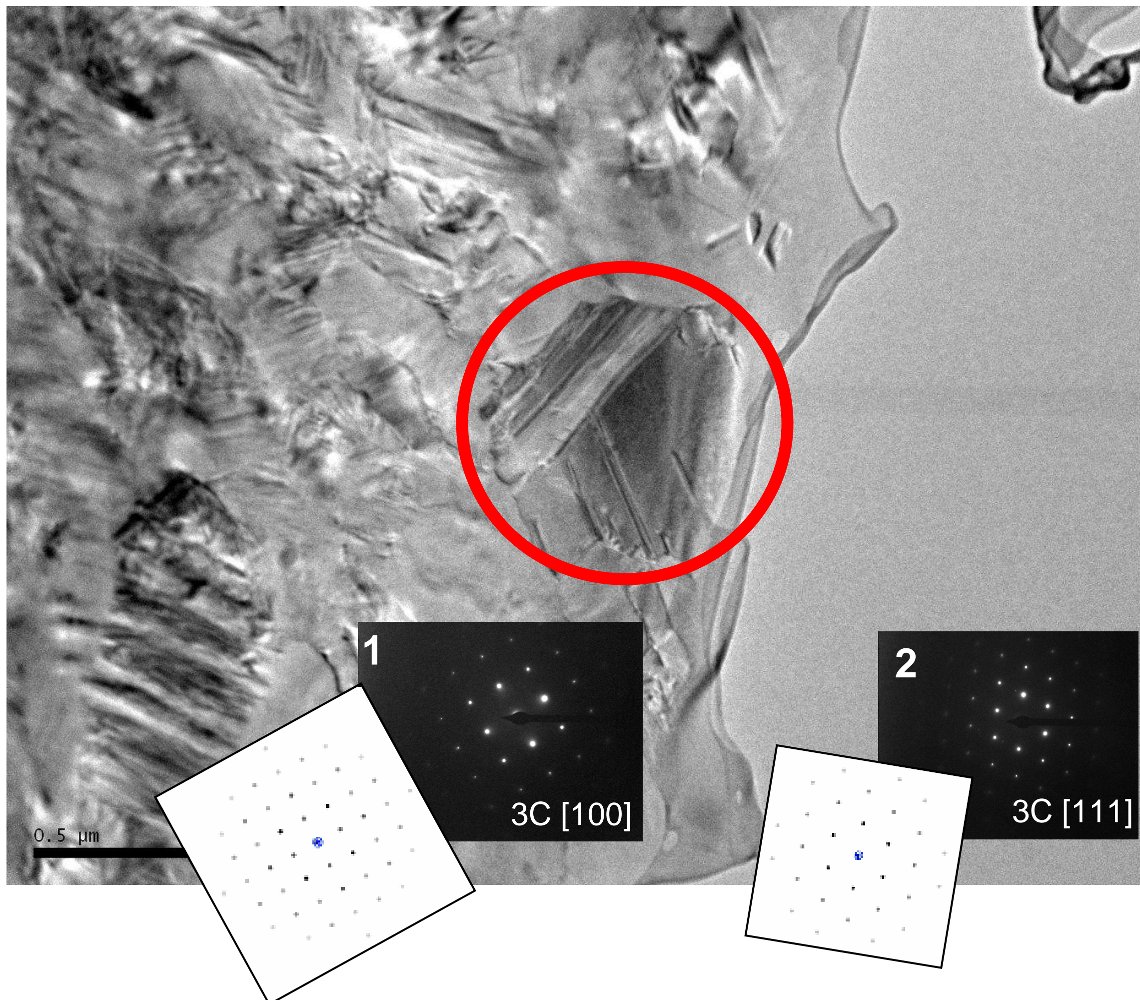

Figure 5.57 – Bright field image of PO5 image 5 (from the appendix C), along with its diffraction patterns. The two ordered diffraction patterns represent the 3C [100] and 3C [111] zone axes of the same twinned crystal. The central direct beam diffraction spot is blanked out on the experimental diffraction patterns.

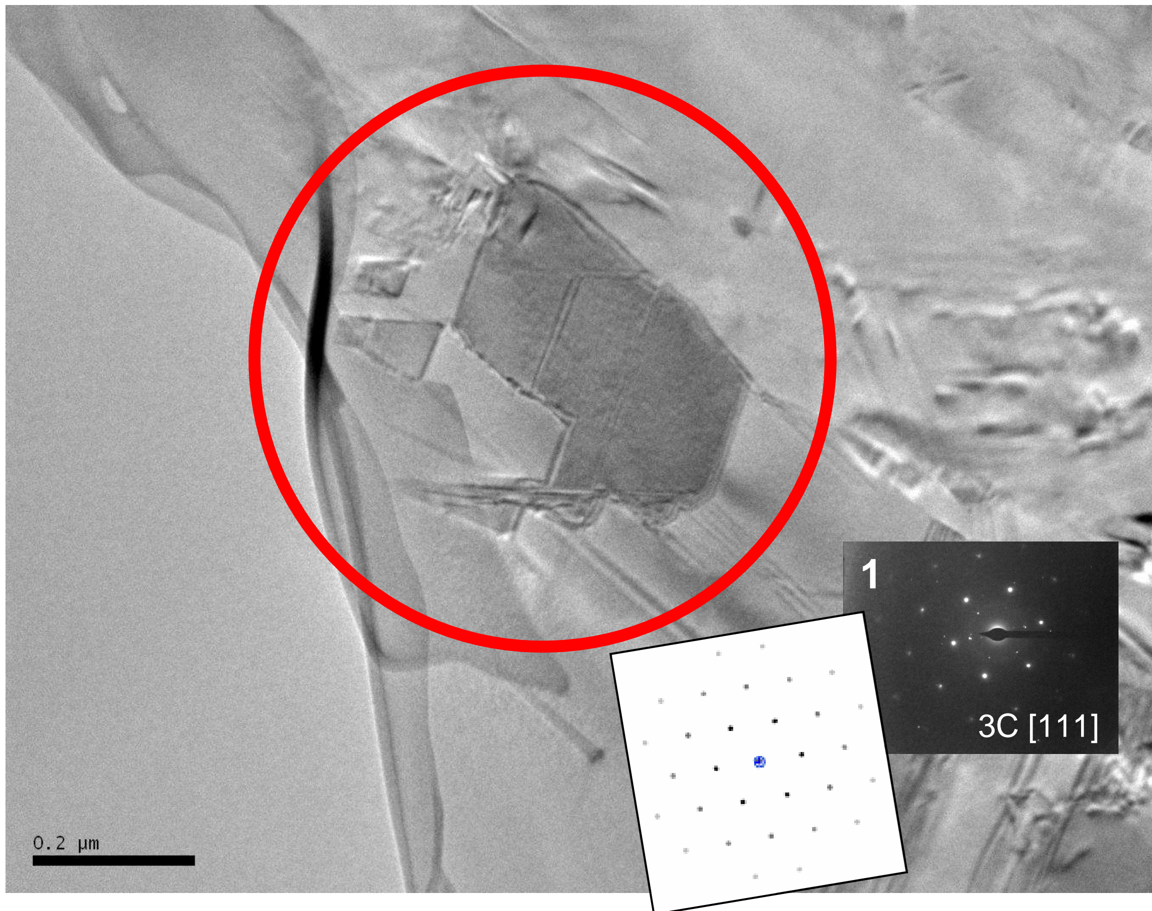

Figure 5.58 – Bright field image of PO5 image 4 (from the appendix C) along with its diffraction pattern. The diffraction pattern represents the 3C [111] zone axis. The central direct beam diffraction spot is blanked out on the experimental diffraction pattern.

PO 6

From XRD results it is clear that of the SiC polytypes, the 3C is most abundant followed by the 6H, 8H and 15R respectively. Table 5.9 summarizes the interpretation of the PO6 diffraction patterns. The 3C SiC polytype is the most commonly occurring. The 6H polytype is the only other SiC polytype detected. All the PO6 images, diffraction patterns and calculated patterns are listed in appendix C.

Image #	Diffraction	Polytype	Zone axis
1	1	3C	[111]&[100]
2	1	3C	[211]
	2	3C	[111]&[110]
	3	3C	[111]
3	1	6H	[001]
4	1	3C	[111]
5	1	3C	[111]
6	1	3C	[111]
7	1	3C	[111]
8	1	3C	[110]&[211]

Table 5.9 – Summary of the interpreted diffraction patterns of PO6 included in the appendix section. The 3C polytype is the most commonly occurring polytype of SiC.

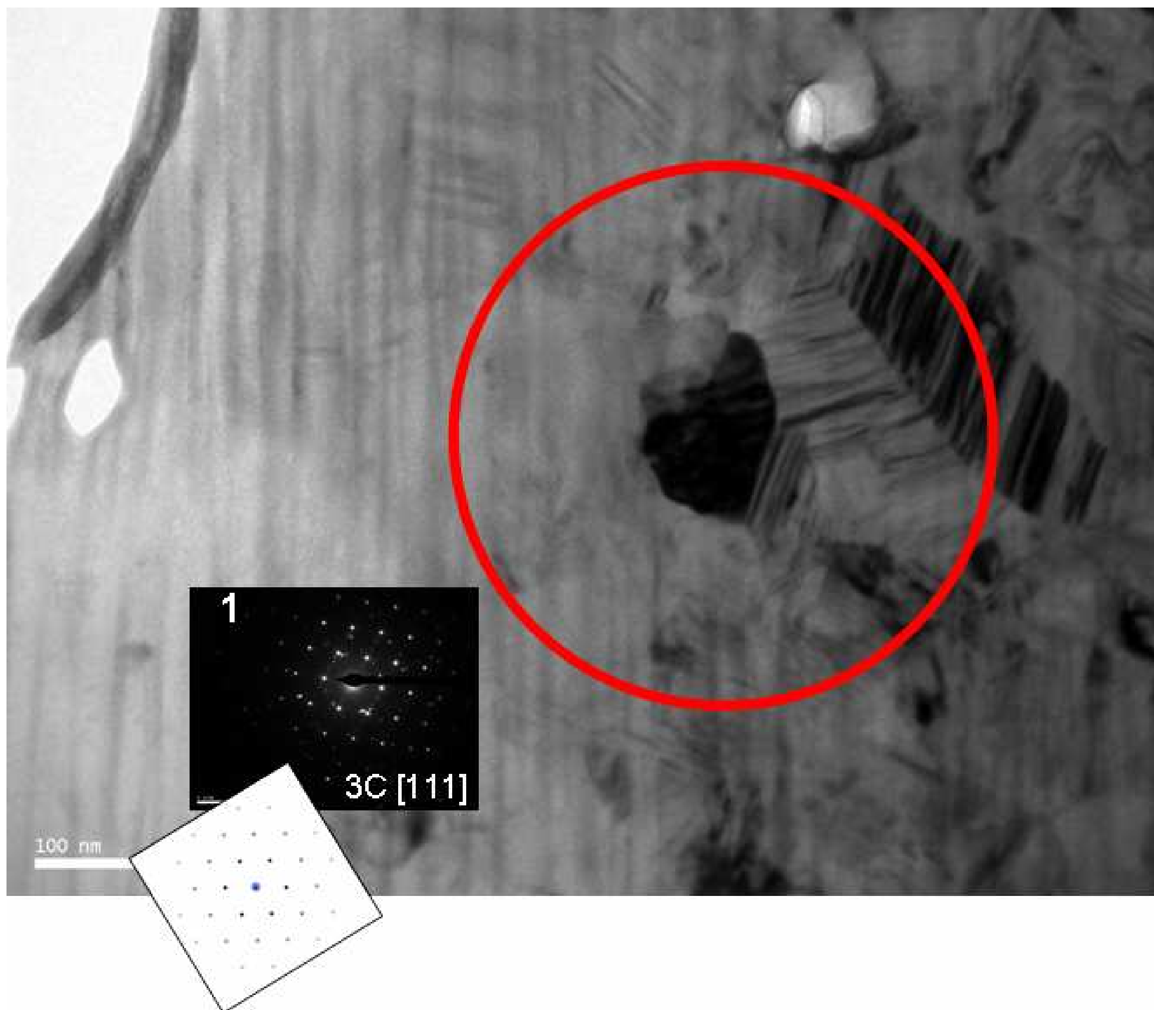

Figure 5.59 – Bright field image of PO6 image 7 (from the appendix C) along with its diffraction pattern. The disordered diffraction patterns represents the 3C [111] zone axis.

The central direct beam diffraction spot is blanked out on the experimental diffraction patterns.

Analysis of figure 5.59 reveals weaker spots surrounding the 3C [111] zone axis, which indicates that the crystals tend to overlap. The diffraction pattern of figure 5.60 is characterized by two separate diffraction patterns (from more than a single crystal), interpreted to be the 3C [211] and 3C [110] zone axes.

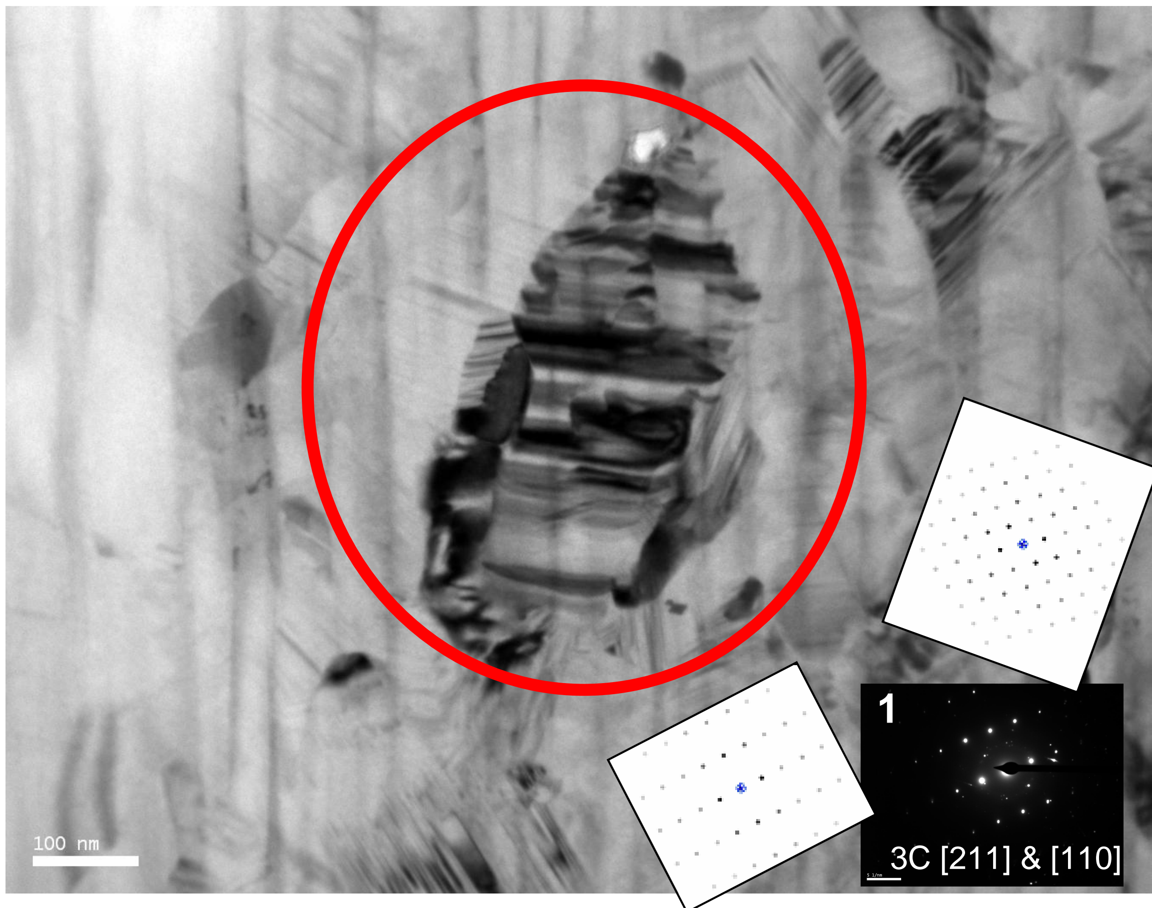

Figure 5.60 – Bright field image of PO6 image 8 (from the appendix C) along with its diffraction pattern. The two ordered diffraction patterns represent the 3C [211] and 3C [110] zone axes of the same crystal. The central direct beam diffraction spot is blanked out on the experimental diffraction patterns.

PO 9

Table 5.10 summarizes the interpretation of PO9 crystals. It is evident that the 3C is once again the most abundant. There are also several diffraction patterns interpreted to be the 6H polytype. The PO9 images, diffraction patterns and calculated patterns are listed in appendix C.

Image #	Diffraction	Polytype	Zone axis
1	1	6H	[100]/[110]
2	1	3C	[110]&[111]
	2	3C	[111]
3	1	3C	[111]
4	1	3C	[111]
5	1	3C	[111]
6	1	6H	[001]
7	1	3C	[111]&[110]
8	1	3C	[211]
9	1	3C	[111]
10	1	3C	[111]&[110]
11	1	3C	[211]
12	1	6H	[001]
13	1	6H	[100]/[110]
14	1	3C	[111]
15	1	6H	[100]/[110]
16	1	3C	[100]

Table 5.10 – Summary of the interpreted diffraction patterns of PO9 included in the appendix section. The 3C polytype is once more dominant, and 6H is the only other polytype that was detected.

Figures 5.61 and 5.62 represent the 3C [100] and 6H [100 or 110] zone axes respectively. Sample PO9 has the most complex crystals and subsequent diffraction patterns of the three samples studied.

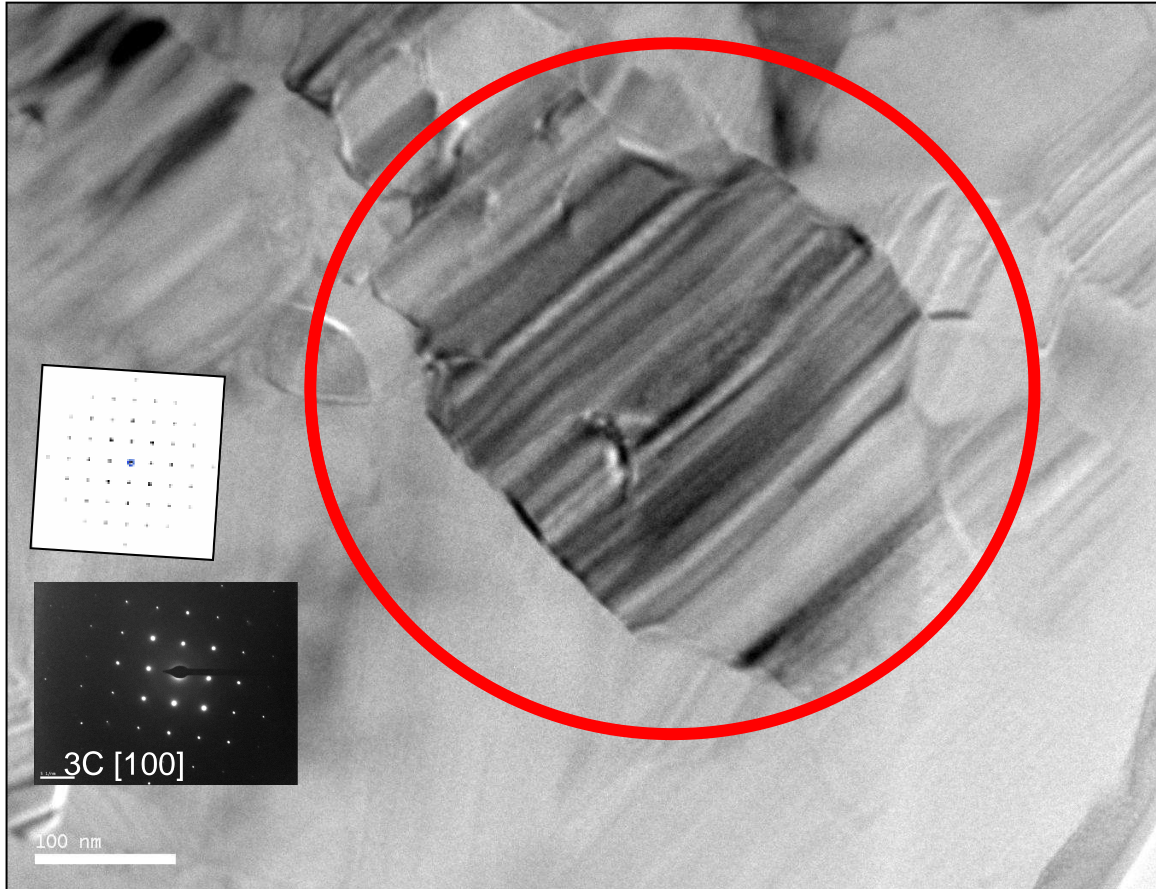

Figure 5.61 – Bright field image of PO 9 crystal 16 (from the appendix C) along with its diffraction pattern. The diffraction pattern represents the 3C [100] zone axis. The central direct beam diffraction spot is blanked out on the experimental diffraction pattern.

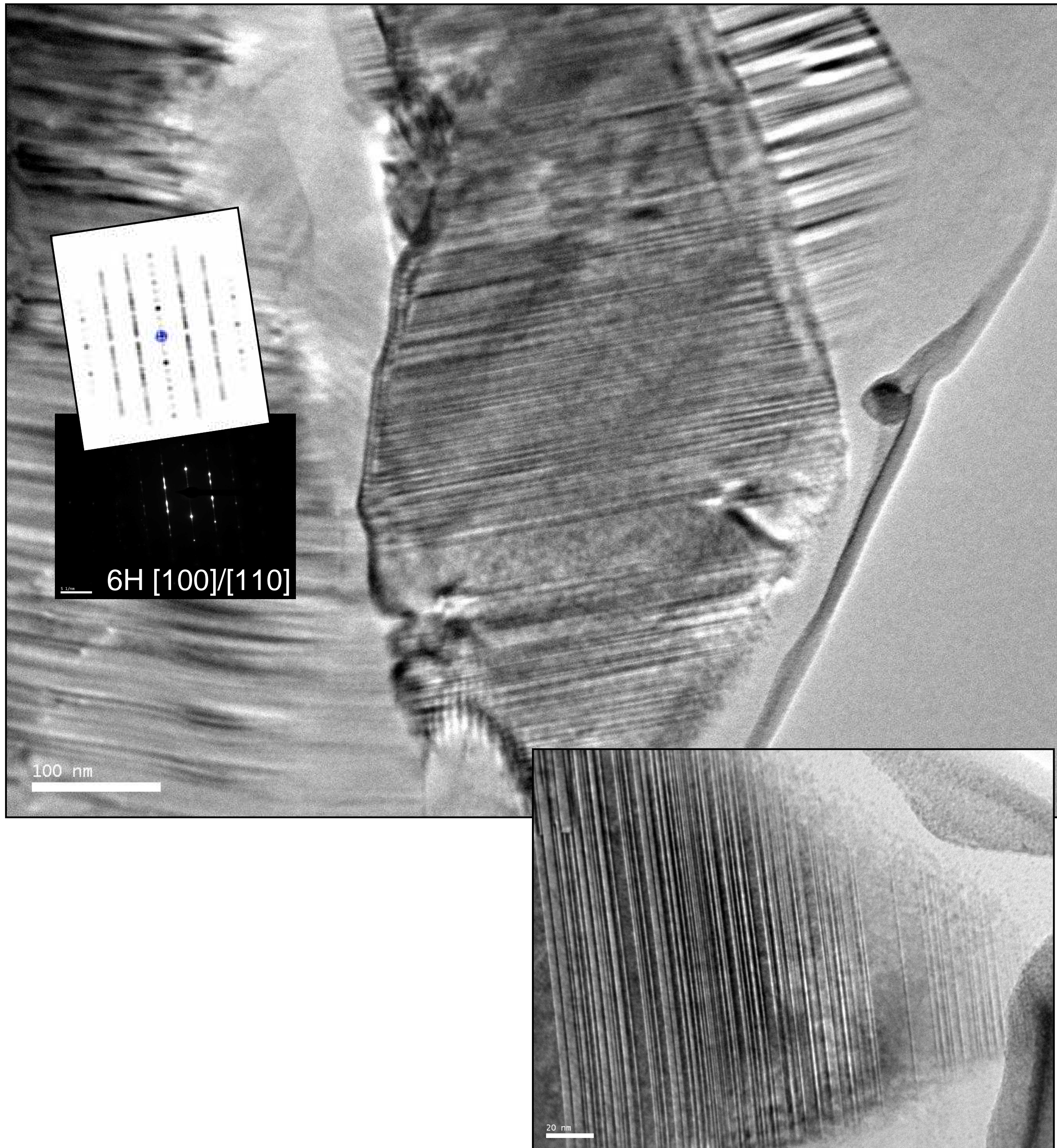

Figure 5.62 – Bright field image of PO 9 image 15 (from the appendix C) along with its diffraction pattern. The diffraction pattern represents the 6H [100] or [110] zone axis. The magnified image shows the varying periodicity of the stacking disorder. The central direct beam diffraction spot is blanked out on the experimental diffraction pattern. The scale bar of the lower image is 20 nm long.

5.5.2. Disorder and twinning

PO 5

The analysis of PO5 from Raman spectroscopy and X-ray powder diffraction revealed that it consisted predominantly of 3C-SiC with minimal 6H, 8H and 15R) and virtually no amorphous silicon.

Of the three samples chosen from the 10 (i.e. PO5, PO6 and PO9), it is clear from the images and diffraction patterns that sample PO5 is the least disordered. The crystals are well-ordered, with a few disordered crystallites and streaking due to stacking disorder, as is seen in figures 5.57 and 5.58. There is no stacking disorder streaking evident from all the diffraction patterns that have been analyzed. Some overlapping diffraction spots were identified resulting in more than one diffraction pattern (as is seen in figure 5.58). There is also evidence of some twinning from both figures 5.57 and 5.58. The rest of the images taken and their interpreted diffraction patterns are included in appendix C.

PO 6

Sample PO6 had a narrow region of SiC and therefore a limited number of crystals could be analyzed. Raman spectroscopy analysis of PO6 revealed high crystalline silicon peaks.

Analysis of TEM images reveals that the crystals are generally well-ordered. However, sample PO6 has significantly more disordered crystals than PO5. The image of figure 5.59 was analyzed in bright field mode. The striking contrast of light and dark lines is evidence of denser streaking due to stacking disorder, as is seen in figure 5.63. The stacking disorder streaking is also observed from the diffraction patterns, along the [111] direction for the 3C polytype and the [001] direction for the 6H polytype. In some of the crystals, there is evidence of overlapping resulting in two diffraction patterns as is seen in both figure 5.59 and figure 5.60. There is also evidence of twinning. All of this is evident by examination of figures 5.59 and 5.60.

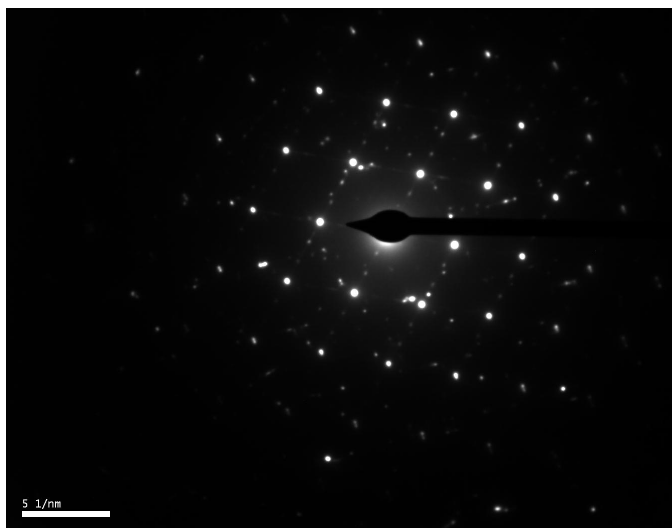

Figure 5.63 – A magnified image of the diffraction pattern of figure 5.59, depicting streaking due to stacking disorder evident between the diffraction spots. Overlapping crystals yield additional, weaker diffraction spots.

PO 9

Sample PO9 had a very broad region of SiC and a lot of other crystals could have been analyzed. In comparison to samples PO5 and PO6, sample PO9 is the most disordered. There are generally well-defined crystals. Some of the images were analyzed in dark field mode. The streak lines are generally denser than those of sample PO6. The streaking occurs along the [111] direction for the cubic polytype and the [001] direction for the hexagonal polytypes. In addition there is evidence of twinning and complex twinning. Some of these features are seen in figures 5.61 and 5.62.

The magnified image of figure 5.62 reveals planar defects revealed by extensive streaking due to stacking disorder. It is clear that there is a lack of consistency in terms of the periodicity. This suggests that on the scale of tens of angstrom units, there are a variety of SiC polytypes that are stable. The broad bands that are in between the periods are thought to be interpreted by the macroscopic techniques of Raman spectroscopy and XRD as mainly the 3C polytype.

All the PO samples studied had 3C SiC as the predominant polytype. A few 6H SiC crystals were detected from all samples. Sample PO5 is the least disordered. Crystals are well-ordered, with a few disordered crystallites and streaking due to stacking disorder. Some twinning is observed. Sample PO6 is more disordered than PO5, evidenced by heavier streaking due to stacking disorder. There are several diffraction patterns resulting from a composite of two patterns. Twinning is also evident. Sample PO9 is the most disordered of the three analyzed. There are generally well-ordered crystals, characterized by dense streaking due to stacking disorder and twinning.

7. REFERENCES

[1] PBMR website; http://www.pbmr.co.za/download/Operation.pdf; (2006/08/18).

[2] Minato K, Fukuda K, Ishikawa A, Mita N; Advanced coatings for HTGR fuel particles against corrosion of SiC layer; Journal of Nuclear Materials **246;** (1997); pp 215-217.

[3] PBMR website; http://www.pbmr.co.za/download/FuelSystem.pdf); (2006/08/18).

[4] Fissel A; Artificially layered heteropolytypic structures based on SiC polytypes: molecular beam epitaxy, characterization and properties; Physics reports **379**; (2003); pp 152-154, 162-166, 180-181, 187.

[5] Nakashima S, Higashihira M, Maeda K; Raman scattering characterization of polytype in silicon carbide ceramics: comparison with x-ray diffraction, Journal of the American ceramic society **86**; (2003), pp 823-824.

[6] Ortiz A.L, Sanchez-Bajo F, Padture N.P, Cumbrera F.L, Guiberteau F, Quantitative polytype-composition analyses of SiC using X-ray diffraction: a critical comparison between the polymorphic and Rietveld method; Journal of the European ceramic society **21**, (2001), pp 1237-1246.

[7] Peters R; Personal communication; PBMR (Pty) Ltd.; (2006/06/29).

[8] Minato K, Ogawa T, Fukuda K, Tayama Y, Shimizu M, Tayama Y, Takahashi I; Fission product behavior in Triso-coated UO_2 fuel particles; Journal of Nuclear Materials **208** (1994); pp 266,270, 273-281.

[9] Helary D, Bourrat X, Dugne O, Maveyraud G, Perez M, Guillermier P; Microstructure of silicon carbide and pyrocarbons coatings for fuel particles for high temperature

reactors, in: Proceedings of the 2nd international topic meeting on high temperature reactor technology, Beijing, September (2004); #Paper B 07 pp 1-3, 5-7.

[10] PBMR, http://www.pbmr.co.za/contenthtml/pictureFX/imgcache/20051117FuelElemDesCom.jpg, (2006/08/18).

[11] Snead L, Nozawa T, Katoh Y, Byun T, Kondo S, Petti D; Handbook of SiC properties for fuel performance modeling; Journal of Nuclear Materials **371**; (2007); pp 329-377.

[12] Minato K, Kikuchi H, Fukuda K, Suzuki N, Tomimoto H, Kitamura N; Failure mechanisms of fuel particle coating for High-Temperature Gas-Cooled reactors during the coating processes; Nuclear technology **111**; (1995) pp 260-261.

[13] Hofmann D.H, Müller M.H; Prospects of the use of liquid phase techniques for the growth of bulk silicon carbide crystals; Materials Science and Engineering B61–62; 1999; pp 30.

[14] Knippenberg W.F; Growth phenomena in silicon carbide; Philips Research Report **18**; 1963; pp 161-274.

[15] Scace R.I, Slack G.A; Solubility of carbon in silicon and germanium; Journal of Chemical Physics **30**; 1959; pp 1551-1556.

[16] Dolloff R.T; Research study to determine the phase equilibrium relations of selected metal carbides at high temperatures; WADD Technical Report **60**; (1960); pp 143

[17] Verma A.R, Krishna P; Polymorphism and polytypism in crystals; John Wiley & sons Inc; New York; (1966).

[18] Minato K, Fukuda K; SiC coating of small particles in a fluidized bed reactor; Advanced Materials & Manufacturing Processes; 3(4); (1988) pp 617, 637.

[19] Einspruch N.G, Claiborne L.T; Elastic constants of SiC; Journal of the Acoustical Society of America **35**; (1963); pp 925-926.

[20] Hongchao L, Changlin K; Quantitative analysis of SiC polytype distributions by the Rietveld method; Journal of Nuclear Materials **32**; (1997); pp 2661-2664.

[21] Bechstedt F, Käckell P, Zywietz A, Karch K, Adolph B, Tenelsen K, Furthmüller; Polytypism and properties of silicon carbide; Physica Status Solidi B **202**; (1997); pp 35-42.

[22] Thibault N. W; Morphological and structural crystallography and optical properties of silicon carbide; American Mineralogist **29;** (1944); pp 249–278.

[23] Daulton T.L, Bernatowicz T. J, Lewis R.S, Messenger S, Stadermann F.J, Amari S; Polytype distribution of circumstellar silicon carbide: Microstructural characterization by transmission electron microscopy; Geochimica et Cosmochimica Acta, vol. 67; no. 24; (2003); pp 4746-4748.

[24] Tairov Y.M, Tsvetkov V.F.; Process in controlling the growth of polytypic crystals; Progress in crystal growth and characterization (ed. P. Krishna); Oxford, New York, Pergamon Press; (1982); pp 111-162.

[25] Ramsdell L. S; Studies on silicon carbide; American Mineralogist **32**; (1947); pp 64–82.

[26] Zhdanov G. S; The numerical symbol of close packing of spheres and its application in the theory of close packings; Comptes. Rendus de l'Académir des Sciences. USSR. **48**; (1945); pp 39–42.

[27] Harris D.C, Bertolucci, M.D; Symmetry and Spectroscopy: An Introduction to Vibrational and Electronic Spectroscopy; Dover Publications; New York; (1989)

[28]Grasselli J.G, Bulkin B. J, Snavely M. K, Chemical applications of Raman spectroscopy, New York, John Wiley & sons, inc., (1981), pp 2-6.

[29] Smith E, Dent G; Modern Raman spectroscopy; John Wiley & sons Ltd, Chichester; (2005) pp 2-5

[30] McCreery R L; Raman spectroscopy for chemical analysis, Volume 157 in Chemical analysis (series editor: Wineforder J D); (2000); pp 15-24, 103-106, 295-300

[31] Schrader B; General survey of vibrational spectroscopy in infrared and Raman spectroscopy - methods and applications; ed. Schrader B; VCH; Wieinheim; (1995); pp 7-61

[32] Everall N.J; Raman Spectroscopy of the Condensed phase, in 'Handbook of Vibrational Spectroscopy'; eds. Chalmers J. M. and Griffiths P. R; Wiley, Chichester; (2002); pp 141 -149.

[33] Stander B; Tools for Infrared and Raman Spectroscopy in 'Infrared and Raman spectroscopy: Methods and Applications', ed. Stander B; VCH, Weinheim; (1995); pp 138-143

[34] Turrel G; Raman sampling, in 'Practical Raman Spectroscopy', eds. Gardiner D.J and Graves P.R; Springer-Verlag; Berlin; (1989); pp 31-37

[35] Everall N, Lumsdon J; Journal of Materials Science **26**; (1991); pp 5269

[36] McCreery R.L; Raman Spectroscopy for chemical analysis; Wiley Chemical Analysis Series, ed. Winefordner J; Wiley & Sons; New York; (2000)

[37] Fryling M, Frank C.J, McCreery R.L; Applied Spectroscopy **47**; (1993); pp 1965

[38] Feldman D.W, Parker J.H, Jr., Choyke W.J, Patrick L; Phonon dispersion curves by Raman scattering in SiC polytypes 3C, 4H, 6H, 15R and 21R; Physics Review **173** [3]]; (1968); pp 787-793

[39] Nakashima S, Katahama H, Nakakura Y, Mitsuishi A; Physics Review B **33**(8); (1986); pp 5721.

[40] Loudon R; Advances in Physics **13**; (1964); pp 423

[41] Chollon G; Structural and textural analyses of SiC-based and carbon CVD coatings by Raman Microspectroscopy; Thin Solid Films **516**; (2007); pp 388-396

[42] Khanna, R.K. (1957). Evidence of ion-pairing in the polarized Raman spectra of a Ba^{2+}CrO doped KI single crystal. John Wiley & Sons, Ltd.

[43] Ward Y, Young R.J, Shatwell R.A; A microstructural study of silicon carbide fibres through the use of Raman microscopy; Journal of materials science **36**; 2001; pp 55, 57-58.

[44] Nakashima S, Ohta H, Hangyo M, Palosz B; Detection of defects in SiC crystalline films by Raman scattering; Philosophical Magazine **B70**; (1994); pp 971.

[45] Gouadec G, Comlomban P; Non-destructive mechanical characterization of SiC fibres by is Raman spectroscopy; Journal of the European ceramic society **21**; (2001); pp 1251, 1255, 1257.

[46] Nakashima S, Kisoda K, Niizuma H, Harima H; Raman scattering of disordered SiC; Physica **B219&220** (1996) pp 371-373.

[47] Fisher G.R, Barnes P; Towards a unified view of polytypism in silicon carbide; Philosophical Magazine **B61**; (1990); pp 217

[48] Barnes P, Kelly J.F, Fisher G.R; Observation of fine one-dimensionally disordered layers in silicon carbide; Philosophical Magazine Letters **64** (1991); pp 21.

[49] Lu Y.M, Leu I.C; Quantitative study of beta silicon carbide residual stress by Raman spectroscopy; Thin solid films **377-378**; (2000); pp 389-393.

[50] Olega D, Cardona M; Pressure dependence of Raman phonons of Ge and 3*C*-SiC; Physical Review **B25**; (1982); pp 1151.

[51] Krautwasser P, Begun G.M, Angelini P; Raman spectral characterization of silicon carbide nuclear fuel coatings; Journal of the American Ceramic Society **66** [6]; (1983); pp 425.

[52] Veprek S, Iqbal Z, Oswald H.R, Webb; Properties of polycrystalline silicon prepared by chemical transport in hydrogen plasma at temperatures temperatures between 80 and 400°C; Journal of Physics C **14** [3]; (1981); pp 295-308.

[53] Smith J.W Jr, Brodsky M.H, Crowder B.L, Nathan M.I; Raman scattering in amorphous Si, Ge and III-IV semiconductors; Journal of Non-Crystalline Solids **8-10**; (1972); pp 179-184.

[54] Tuinstra F, Koenig J.L; Raman spectra of graphite; Journal of Chemical Physics **53** [3]; (1970); pp 1126-30.

[55] Elman B.S, Dresselhaus M.S, Dresselhaus G, Maby E.W, Mazurek H; Raman scattering from ion-implanted graphite; Physics Review B **24** [2]; (1981); pp 1027-1034.

[56] Nathan M.I, Smith J.E, Tu K.N; Raman spectra of glassy carbon; Journal of Applied Physics **45** [5]; (1974); pp 2370.

[57] Perez-Rodriguez A, Cornet A, Morante J.R, Physical techniques for silicon layer analysis, Microelectronic engineering **80**, 1998; pp 228-232.

[58] Hongchao L, Changlin K; Quantitative analysis of SiC polytype distributions by the Rietveld method; Journal of Materials Science **32**, 1997; pp 2661-2664.

[59] Young R.A; The Rietveld method; International Union of Crystallography Monographs on Crystallography; Oxford science publications; (1996).

[60] Werner P.E, Salomé S, Malmros G, Thomas O.J; Quantitative analysis of multicomponent powders by full-profile refinement of Guinier-Hägg X-ray film data; Journal of Applied Crystallography **12**; (1979); pp 107-109.

[61] Hill R.J, Howard C.J; Quantitative phase analysis from neutron powder diffraction data using the Rietveld method; Journal of Applied Crystallography **20**; (1987); pp 467-474.

[62] Bish D.L, Howard S.A; Quantitative phase analysis using the Rietveld method; Journal of Applied Crystallography **21**; (1988); pp 86-91.

[63] O'Connor B.H, Raven M.D; Applications of the Rietveld refinement procedure in assaying powdered mixtures; Powder Diffraction **3**; (1988); pp 2-6.

[64] Hill R.J; Expanded use of the Rietveld method in studies of phase abundance in multiphase mixtures; Powder Diffraction **6**; (1991); pp 74 -77.

[65] Klug H.P, Alexander L.E; X-ray diffraction procedures for polycrystalline and amorphous materials; Wiley-Interscience. New York; (1974).

[66] Bridley G.W; The effect of grain or particle size on X-ray reflexions from mixed powders and alloy considered in relation to the quantitative determination of crystalline substances by X-ray methods; Philosophical Magazine. **36**; (1945); pp 347-369.

[67] Hermann H, Ermrich M; Microabsorption correction of x-ray intensities diffracted by multiphase powder specimens; Powder Diffraction **4**; (1989); pp 189-195.

[68] Will G, Parrish W, Huang T.C; Crystal-structure refinement by profile fitting and least-squares analysis of powder diffractometer data; Journal of Applied Crystallography **16**; (1983); pp 611-622

[69] Hill R.J, Howard C.J; Quantitative phase analysis from neutron powder diffraction data using the Rietveld method; Journal of Applied Crystallography. **20**; (1987); pp 467-74

[70] Ortiz A.L, Sanchez-Bajo F, Padture N.P, Cumbrera F.L, Guiberteau F, Quantitative polytype-composition analyses of SiC using X-ray diffraction: a critical comparison between the polymorphic and Rietveld methods, Journal of the European ceramic society **21**, 2001, pp 1237-1238,1241, 1246

[71] Beck M, Mittemeijer E.J; Simultaneous determination of specimen temperature and specimen displacement in high-temperature X-ray diffractometry applying Bragg-Brentano geometry; Journal of Applied Crystallography **35**; (2002); pp 103-107.

[72] Pecharsky V, Zavilij P; Fundamentals of Powder Diffraction and Structural Characterization of Materials; Dordrecht: Kluwer; (2003).

[73] Touloukian Y.S, Kirby R.K, Taylor R.E, Lee T.Y.R; Thermal Expansion of Nonmetallic Solids; Thermophysical Properties of Matter **13**; (1977); pp 176-185.

[74] Taylor D; Thermal expansion data: 1 Binary oxides with the sodium chloride and wurtzite structures, MO; British Ceramic Transactions Journal **83**; (1984); pp 92-98.

[75] Stinton G.W, Evans J.S.O; Parametric Rietveld refinement; Journal of Applied Crystallography **40**; (2007); pp 88-92.

[76] Li Z, Bradt R.C; Thermal expansion of the Cubic (3C) Polytype of SiC; Journal of Materials Science **21** [12]; (1986); pp 4366-4368

[77] Li Z, Bradt R.C; Thermal expansion of the Hexagonal (4H) Polytype of SiC; Journal of Applied Physics **60** [2]; (1986); pp 612-614

[78] Li Z, Bradt R.C; Thermal expansion of the Hexagonal (6H) Polytype of SiC; Journal of the American Ceramic Society **69** [12]; (1986); pp 863-866

[79] Li Z, Bradt R.C; Thermal expansion and thermal expansion anisotropy of SiC polytypes; Journal of the American Ceramic Society **70** [7]; (1987); pp 445-448

[80] Megaw H.D; Crystal Structures and Thermal Expansion; Materials Research Bulletin **8**; (1971); pp 1007-1018

[81] Hazen R.M, Finger L.M; Comparative Crystal Chemistry; Wiley-Interscience, New York; (1984); pp 115

[82] Pojur A.F, Yates B, Kelly B.T; Thermal expansion at elevated temperatures III, A hemispherical laminar composite of pyrolytic graphite, silicon carbide and its constituents between 300 and 800K; Journal of Physics D: Applied Physics Vol. **5**; (1972) pp 1321-1329

[83] Kern E.L, Hamill D.W, Deem H.W, Sheets H.D; Thermal properties of β-Silicon Carbide from 20 to 2000°C; Thermal Properties **4** [SiC issue]; (1968); pp 25-32

[84] Riley D.P; The thermal expansion of graphite part II: Theoretical; Proceedings of the Physical Society, London **57**; (1945); pp 486-495

[85] Morgan W.C; Thermal expansion coefficients of graphite crystal; BNWL-SA-3838; (1971)

[86] Kellet E.A, Richards B.P; The thermal expansion of graphite within the layer planes; Journal of Nuclear Materials **12**; (1964); pp 184-192

[87] Steward E.G, Look B.P, Kellet E.A; Dependence on temperature of the interlayer spacing in carbons of different graphite perfection; Nature **187**; (1960); pp 1015-1016

[88] Tsang D.K.L, Marsden B.J, Fok S.L, Hall G; Graphite thermal expansion relationship for different temperature ranges; Carbon **43**; (2005); pp 2902-2906

[89] Nelson J.B, Riley D.P; Thermal expansion of graphite from 15°C to 800°C, Part I. Experimental; Proceedings of the Physical Society, London **57**; (1945); pp 477-486

[90] Yates B, Pirgon Q, Kelly B.T; Proceedings of the 4th international carbon and graphite conference, London: Society of Chemical Industry; (1974)

[91] Harrison J.W; Absolute measurements of the coefficients of thermal expansion of pyrolytic graphite from room temperature to 1200 K and a comparison with current theory. High Temp-High Pressure **9**; (1977); pp 211-229

[92] Reimer L; Transmission electron microscopy, physics of image formation and microanalysis, 3rd edition; Springer-Verlag, Berlin Heidelberg; (1993); pp 6-10, 115, 272

[93] Williams D.B, Carter B.C; Transmission Electron Microscopy: A Textbook for Materials Science; Springer; (1996); pp 9-11

[94] Edington J.W; Practical electron microscopy in materials science, Monograph two, Electron Diffraction in the electron microscope; Phillips publishing, Eindhoven; (1975); pp 4-7

[95] Labspec version 404; Jobin Yvon Horiba, Labspec spectral software

[96] AUTOQUAN Version 2.70; GE Inspection Technologies GmbH; (2005)

[97] TOPAS Version 3.0; GmbH; Karlsruhe, West Germany; (2003-2005)

[98] Stadelmann P; JEMS software for MS Windows; (2005)

[99] O'Grady A, Dennis A.C, Denvir D, McGarvey J.J, Bell S.E.J; Quantitative Raman Spectroscopy of Highly Fluorescent Samples Using Pseudosecond Derivatives and Multivariate Analysis; Analytical Chemistry **73** (9); (2001); pp 2058-2065

[100] Kim B, Hahn J, Han K; Quantitative phase analysis in tetragonal-rich tetragonal/ monolithic two phase zirconia by Raman spectroscopy; Journal of Materials Science letters **16**; (1997); pp 669-671

[101] Pecharsky V.K, Zavalij P.Y; Fundamentals of powder diffraction and structural characterization of materials; Springer; (2005); p 713

APPENDIX A1
Qualitative Raman Spectra

Sample PO1

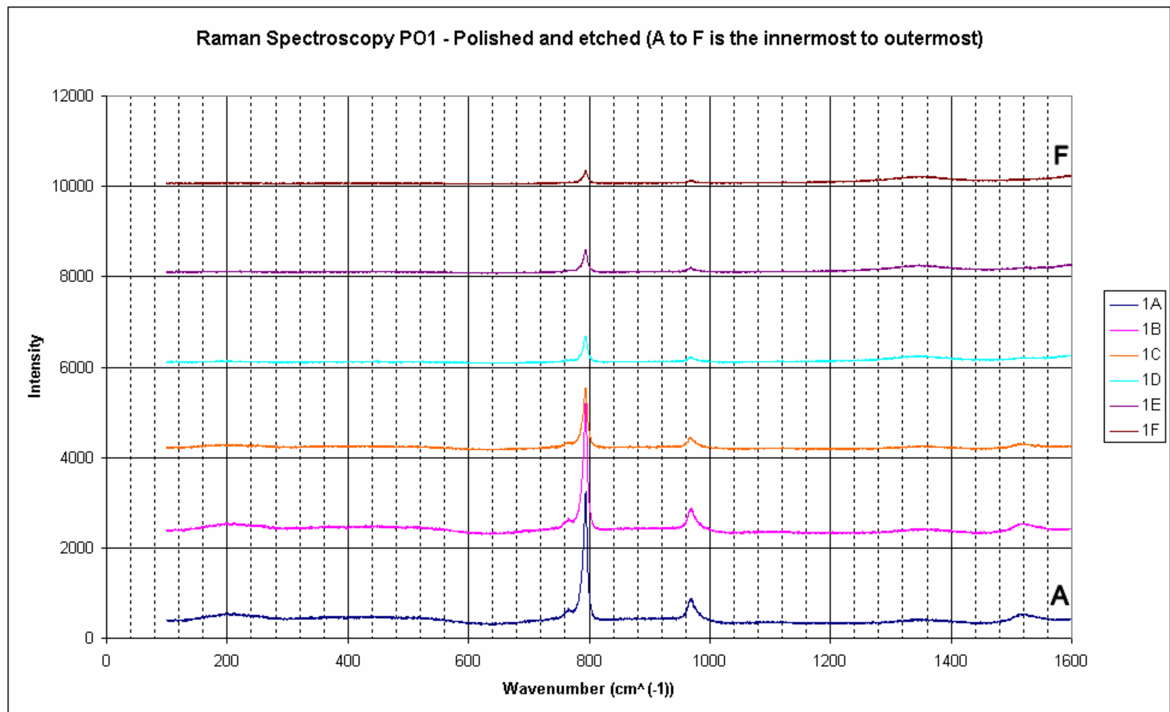

Raman spectra of the SiC coating of PO1 polished and etched coated particle. A is the innermost and F is the outermost spot along the SiC cross-section. There is no polycrystalline silicon. There is peak splitting evident across the inner part of the SiC and therefore 6H SiC. The SiC peaks progressively get smaller from analysis A to F. This is thought to be as a result of a variation of crystallinity and absorption, with point A having the most crystalline SiC crystals.

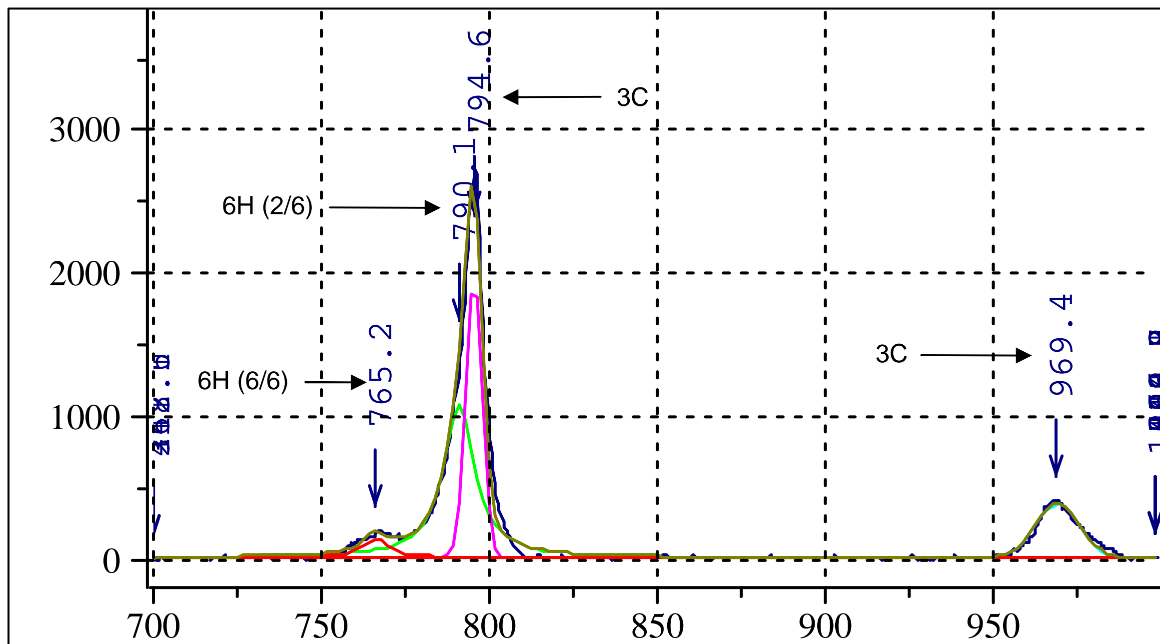

Raman spectra of the TO SiC peaks after deconvolution for analysis 1A (etched). It was assumed that there were two components making up the main peak. The peaks indicate the presence of the 3C and 6H polytypes.

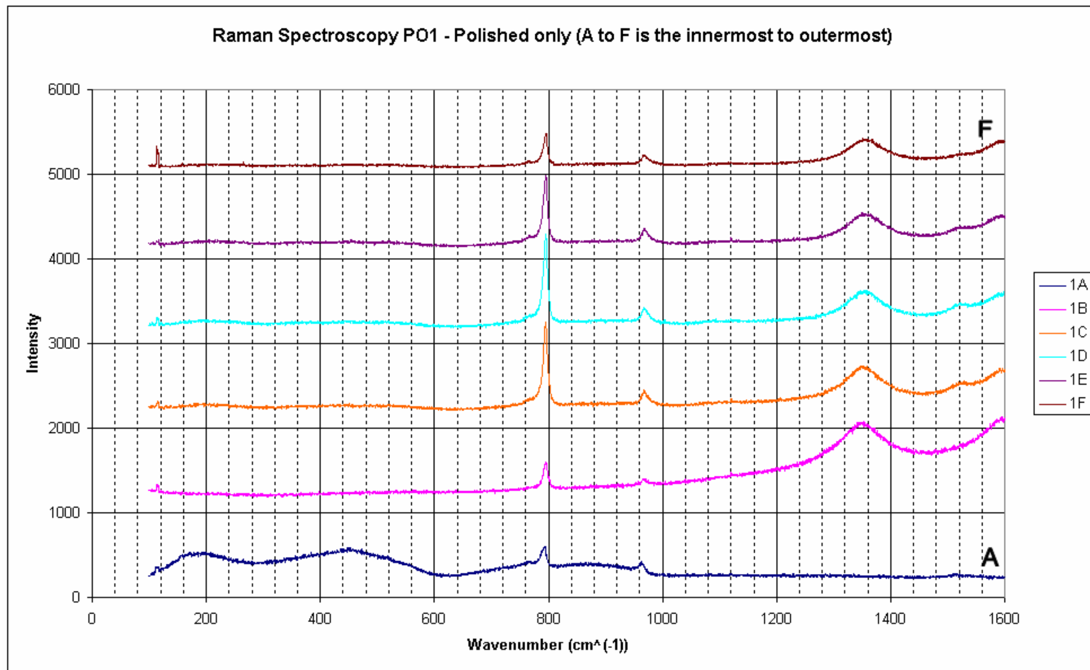

Raman spectra of the SiC coating of PO1 polished coated particle. A is the innermost and F is the outermost spot along the SiC cross-section. There is no polycrystalline silicon. There is peak splitting evident for some of the SiC profiles, confirming the presence of 6H SiC. There is evidence of free carbon from analysis B to F. The most intense SiC peaks are towards the outer part of the SiC layer. This is thought to be as a result of a variation of crystallinity and absorption of the crystals.

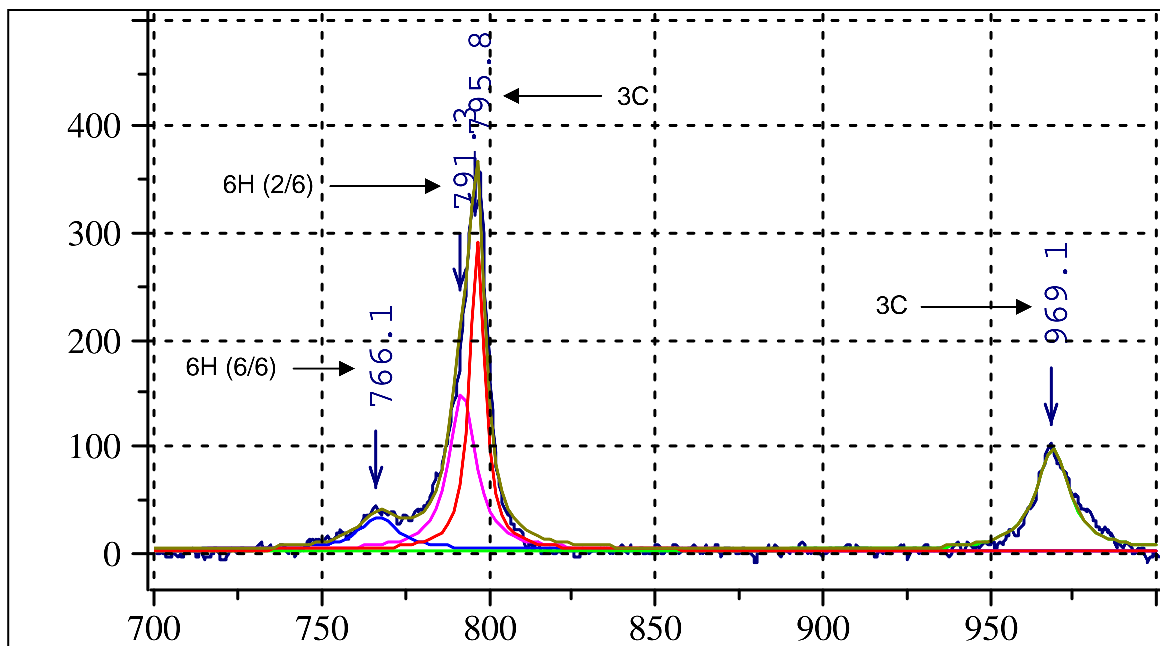

Raman spectra of the TO SiC peaks after deconvolution for analysis 1A (polished). It was assumed that there were two components making up the main peak. The peaks indicate the presence of the 3C and 6H polytypes.

Sample PO2

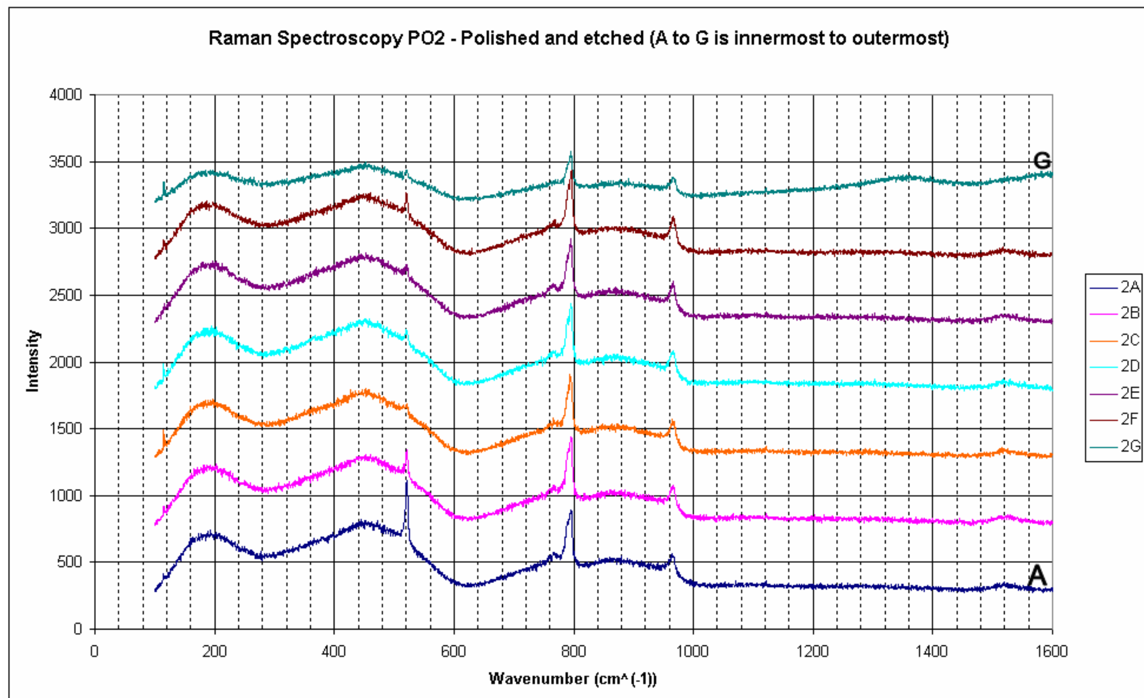

Raman spectra of the SiC layer of PO2 polished and etched coated particle. A is the innermost and G is the outermost spot along the SiC cross-section. The polycrystalline silicon peak is evident throughout the analyses, with the most intense peaks found across the inner parts of the SiC layer (analysis A and B). There is evidence of amorphous silicon throughout the analyses. There is peak splitting evident across the inner part of the SiC and therefore 6H SiC across the profile. The presence of graphite is only seen at analysis G.

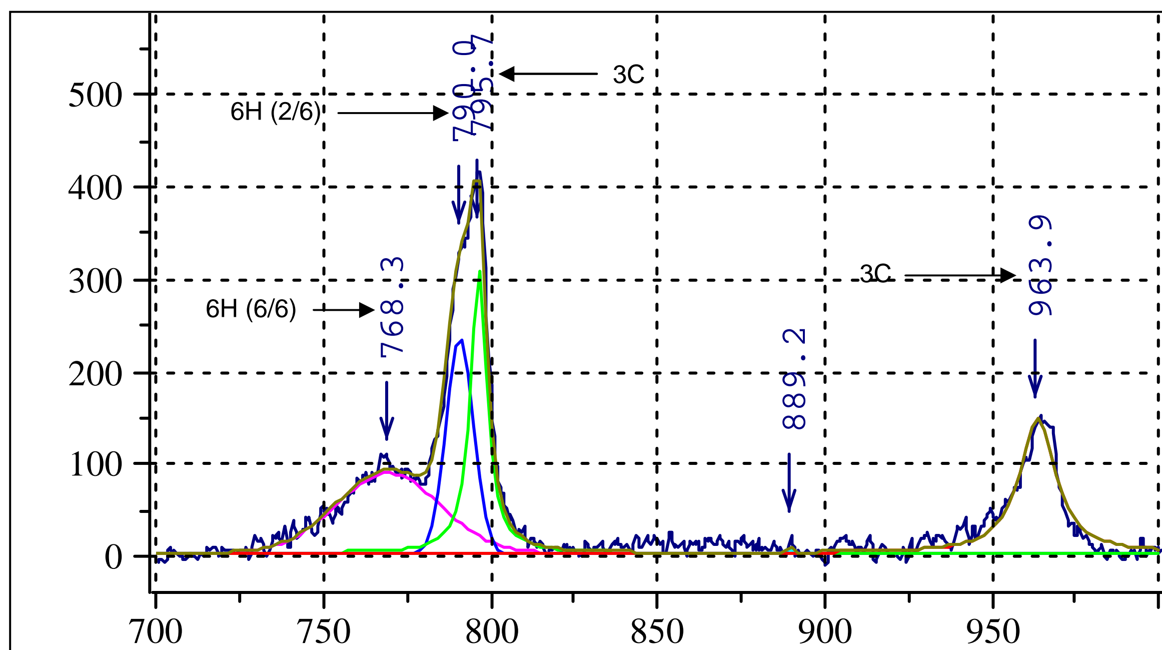

Raman spectra of the TO SiC peaks after deconvolution for analysis 2A (etched). It was assumed that there were two components making up the main peak. The peaks indicate the presence of the 3C and 6H polytypes.

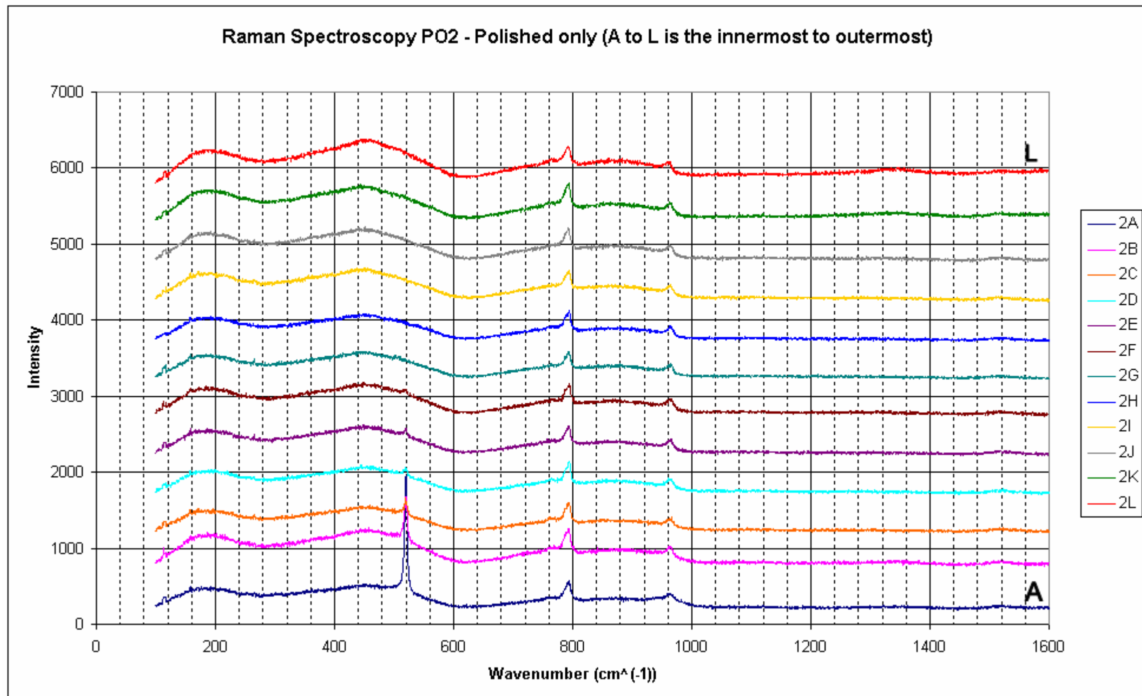

Raman spectra of the SiC coating of PO2 polished coated particle. A is the innermost and L is the outermost spot along the SiC cross-section. The polycrystalline silicon peak is evident throughout analyses A to F, with the most intense peaks found across the inner part of the SiC layer (analysis A). Amorphous silicon seems more evident closer to the OPyC layer. There is peak splitting evident across the inner part of the SiC and therefore 6H SiC across the profile. This is clearly evident from peak deconvolution. There is no evidence of graphite.

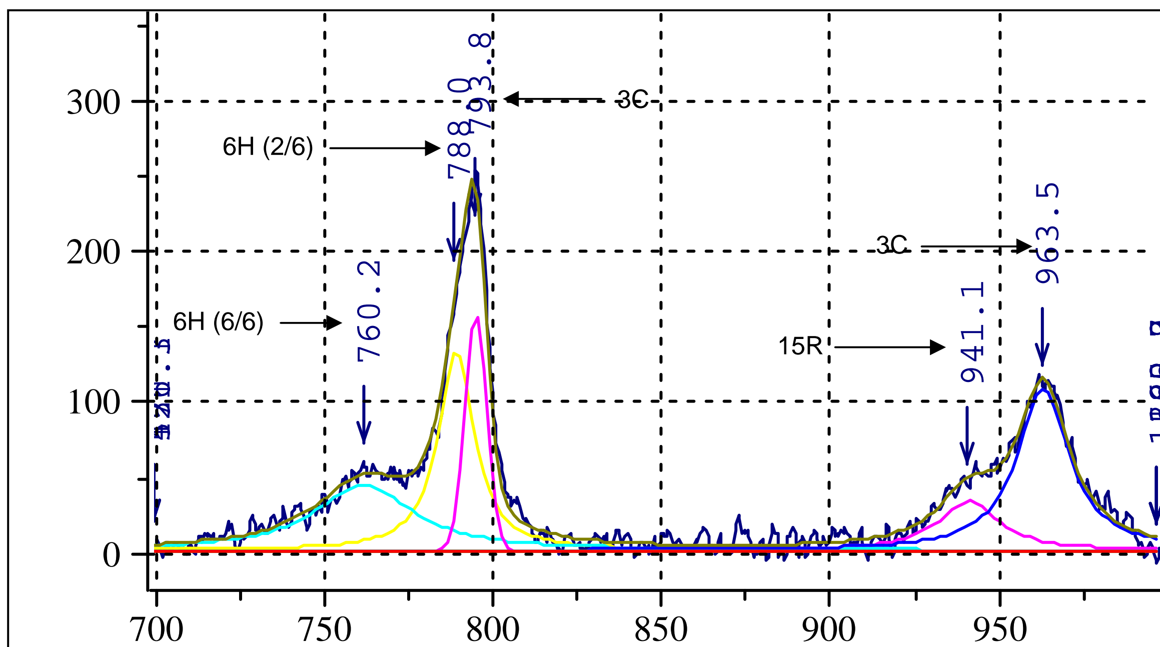

Raman spectra of the TO SiC peaks after deconvolution for analysis 2A (polished). It was assumed that there were two components making up the main peak. The peaks indicate the presence of the 3C and 6H polytypes.

Sample PO3

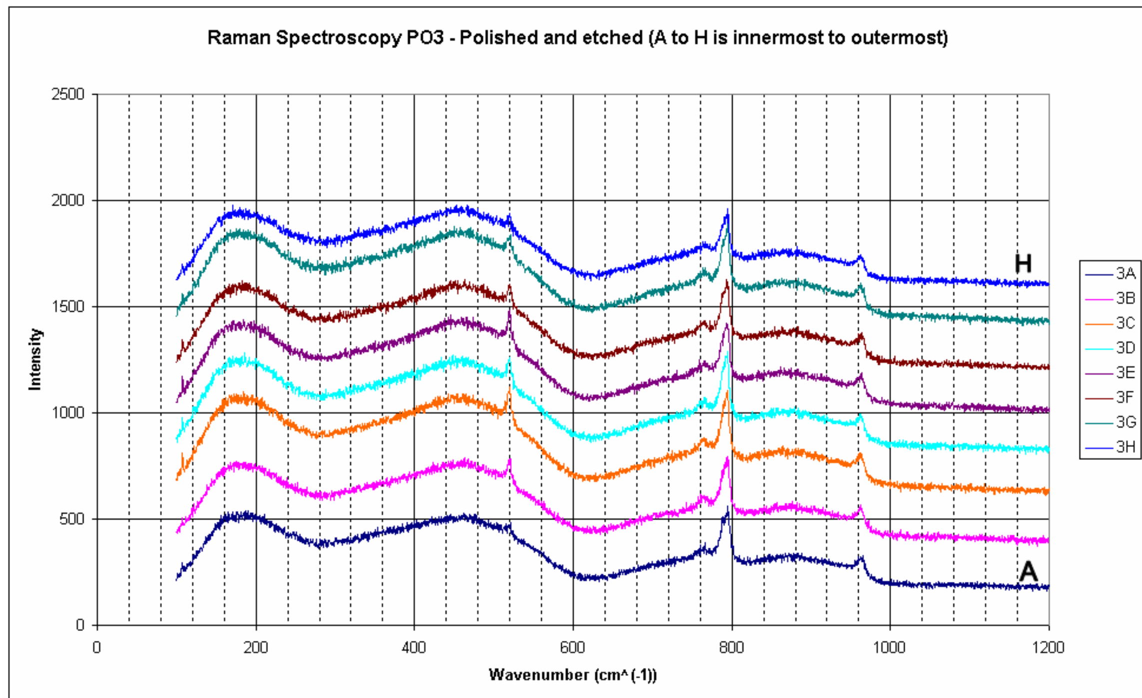

Raman spectra of the SiC layer of PO3 etched and polished coated particle. A is the innermost and H is the outermost spot along the SiC cross-section. There seems to be a mixture of amorphous and crystalline silicon throughout the analyses. The most intense crystalline silicon peaks occur in the middle of the SiC layer (analysis C to E) Peak splitting is clearly evident, indicating that the 3C polytype is not the only one that is stable.

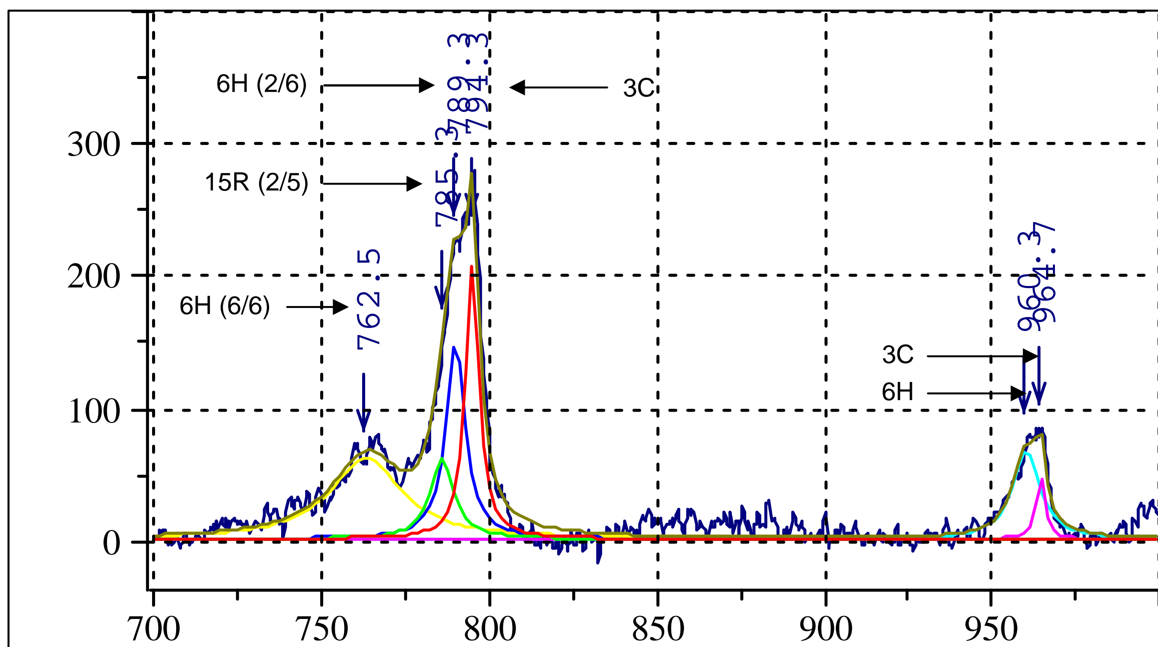

Raman spectra of the TO SiC peaks after deconvolution for analysis 3A (etched). It was assumed that there were three components making up the main peak. The peaks indicate the presence of the 3C, 6H and 15R polytypes.

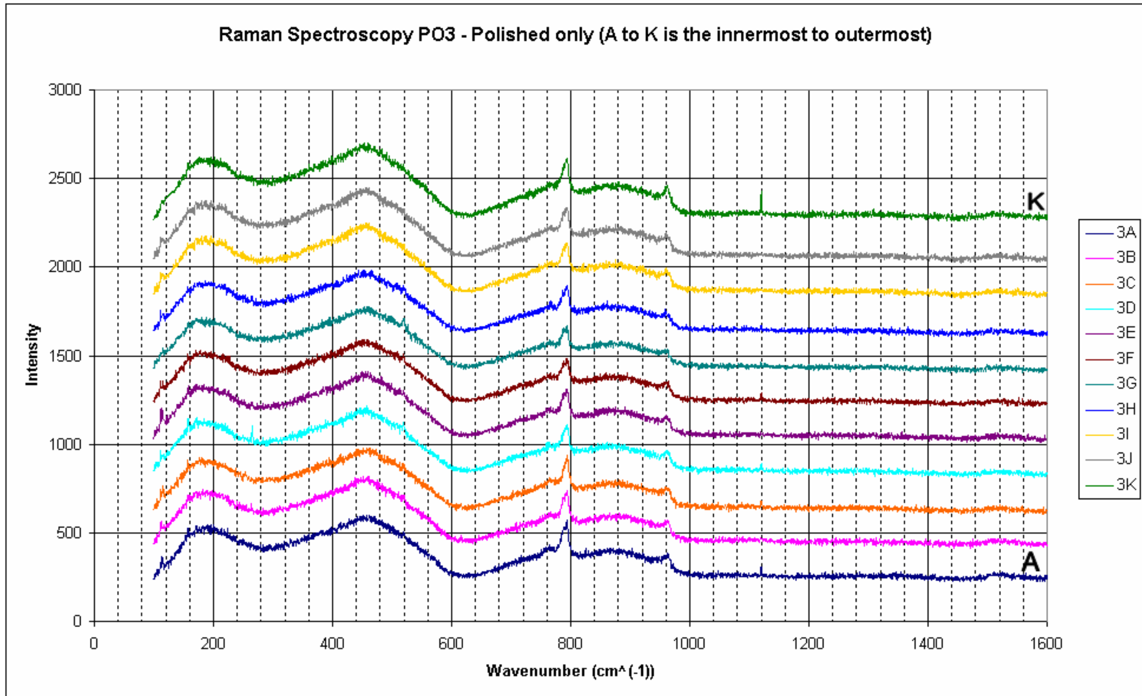

Raman spectra of the SiC coating of PO3 polished coated particle. A is the innermost and K is the outermost spot along the SiC cross-section. There seems to be predominantly amorphous, with small silicon peaks evident for some analyses. Peak splitting is clearly evident, indicating that the 3C polytype is not the only one that is stable. There is no evidence of graphite.

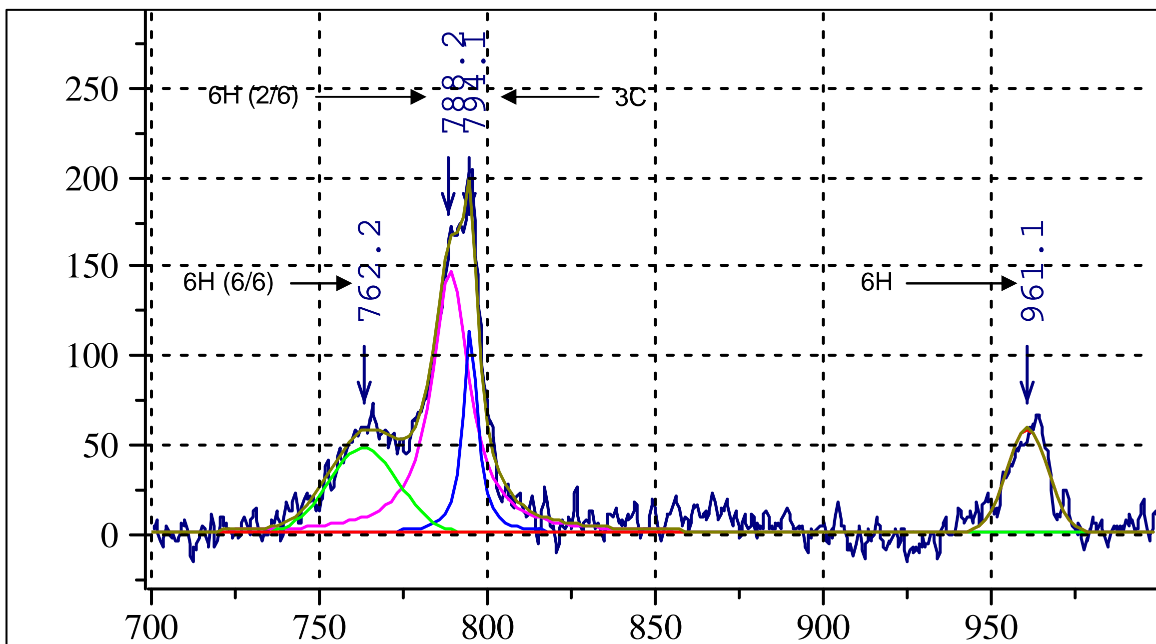

Raman spectra of the TO SiC peaks after deconvolution for analysis 3A (polished). It was assumed that there were three components making up the main peak. The peaks indicate the presence of the 3C, 6H and 15R polytypes.

Sample PO4

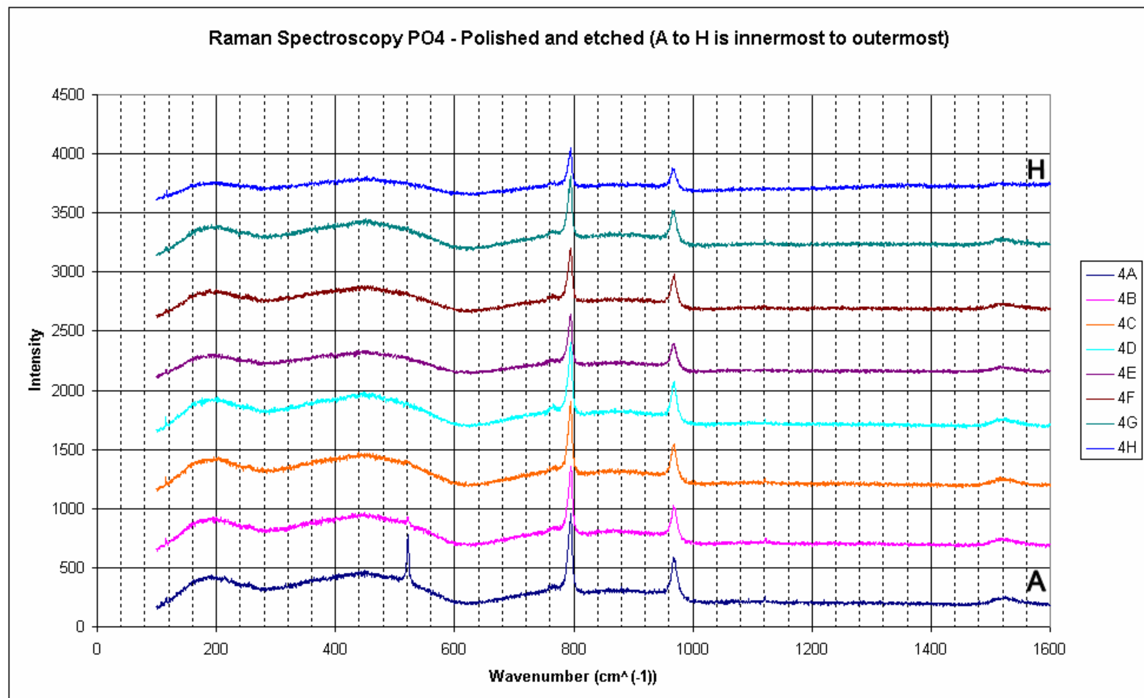

Raman spectra of the SiC coating of PO4 etched and polished coated particle. A is the innermost and K is the outermost spot along the SiC cross-section. There seems to be a mixture of amorphous and crystalline silicon towards the inner part of the SiC layer (analysis A-C). Analysis A has by far the most intense silicon peak. Peak splitting is clearly evident and is confirmed by the peak deconvolution. There is no evidence of graphite.

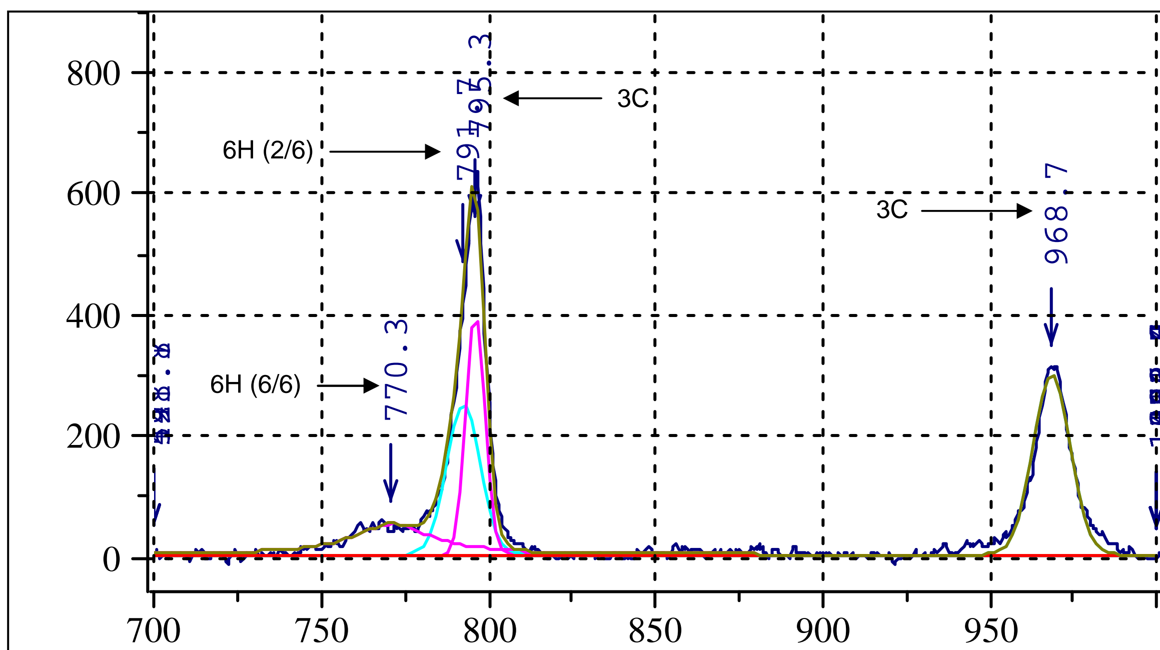

Raman spectra of the TO SiC peaks after deconvolution for analysis 4A (etched). It was assumed that there were two components making up the main peak. The peaks indicate the presence of the 3C and 6H polytypes.

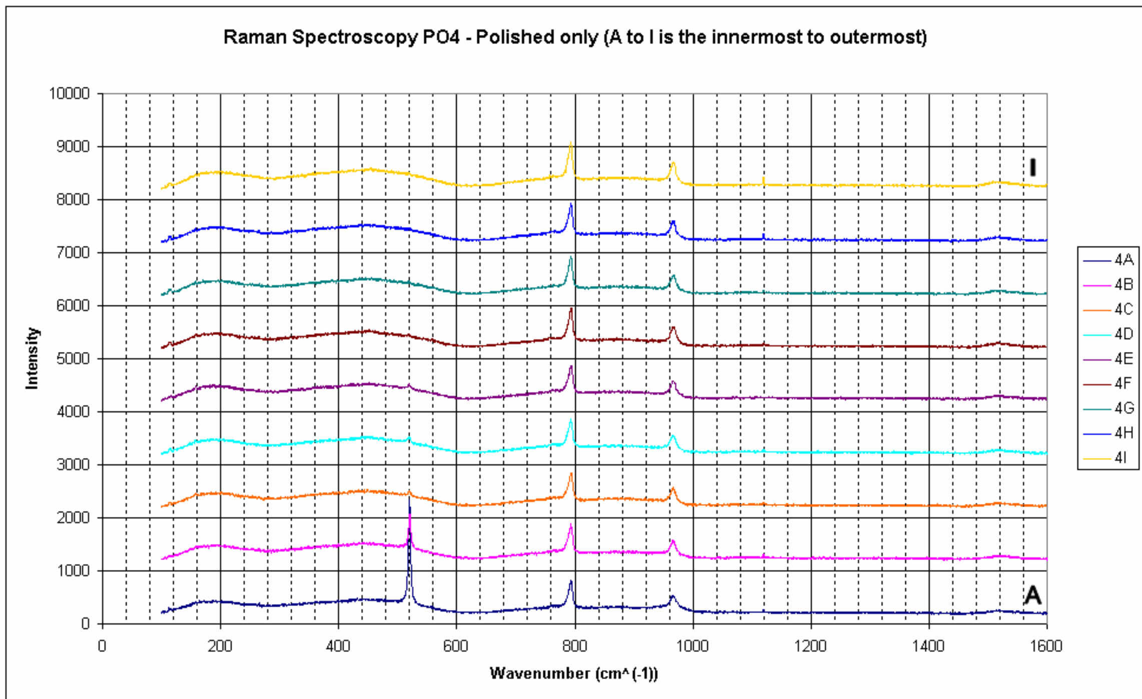

Raman spectra of the SiC coating of PO4 polished coated particle. A is the innermost and I is the outermost spot along the SiC cross-section. There seems to be a mixture of amorphous and crystalline silicon towards the inner part of the SiC layer (analysis B-E). Analysis A has by far the most intense silicon peak. Peak splitting is not clearly evident but is confirmed by the peak deconvolution. There is no evidence of graphite.

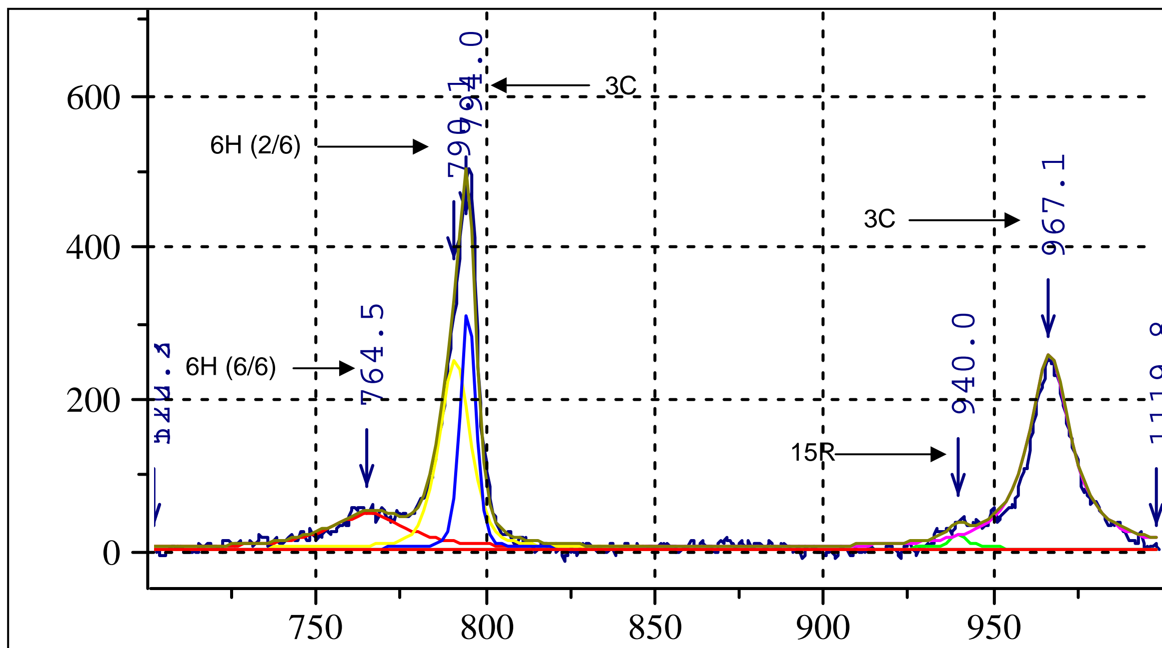

Raman spectra of the TO SiC peaks after deconvolution for analysis 4A (polished). It was assumed that there were two components making up the main peak. The peaks indicate the presence of the 3C and 6H polytypes.

Sample PO5

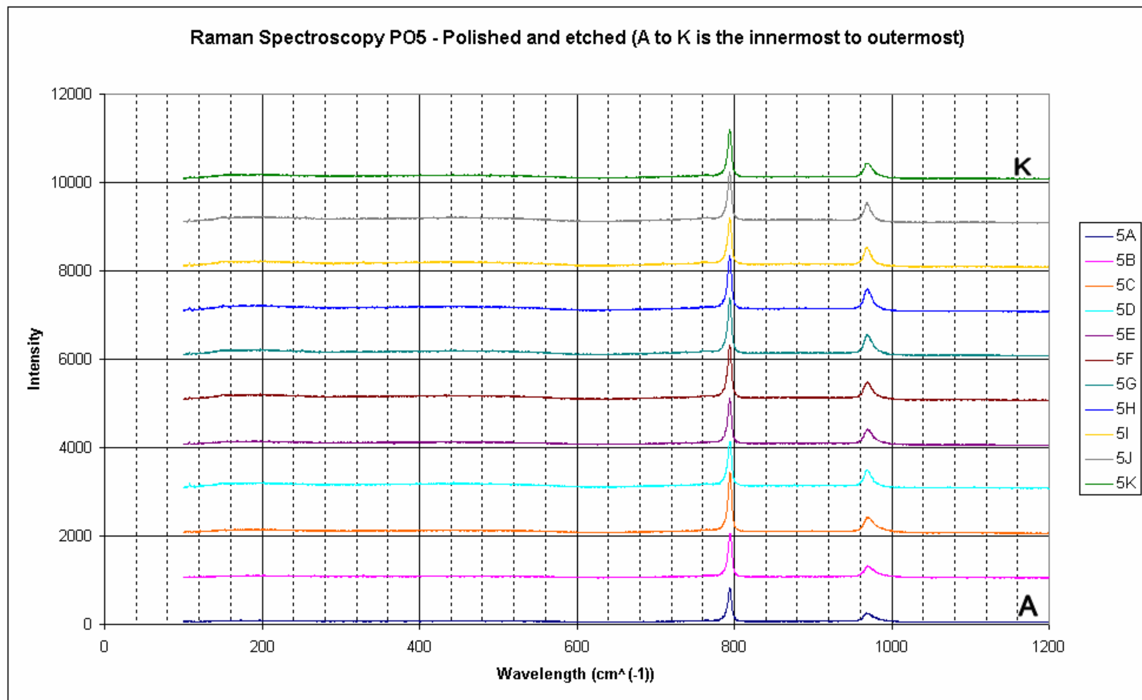

Raman spectra of the SiC coating of PO5 etched and polished coated particle. A is the innermost and K is the outermost spot along the SiC cross-section. Neither the amorphous nor crystalline silicon is seen throughout the SiC layer. The SiC peaks do not split, however peak deconvolution indicates the presence of a relatively small 6H peak.

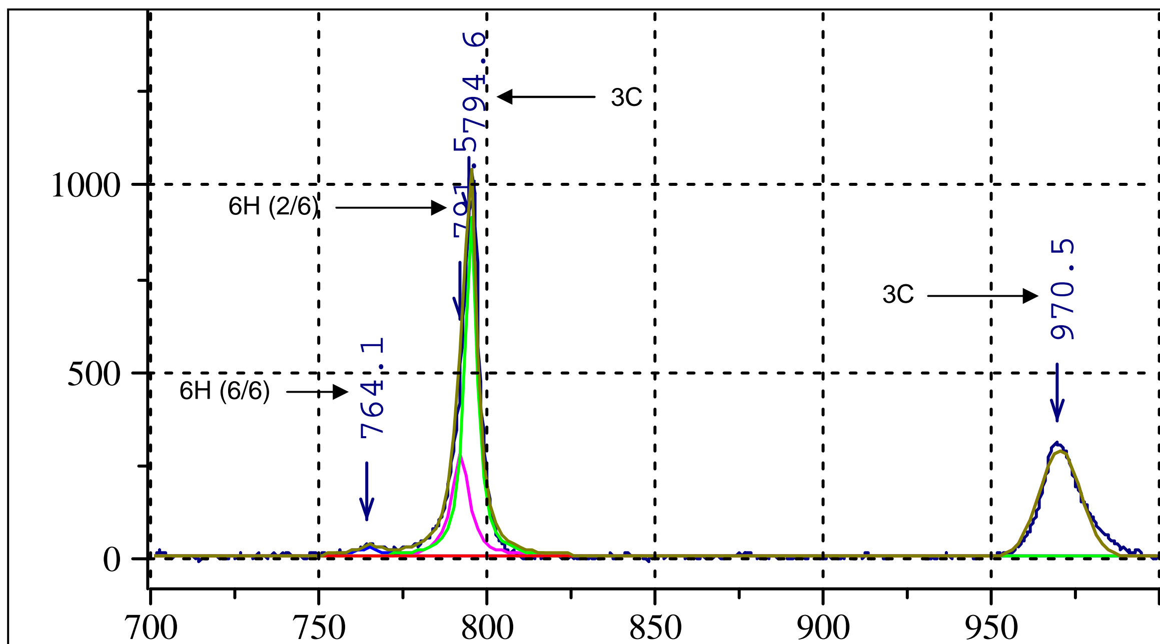

Raman spectra of the TO SiC peaks after deconvolution for analysis 5A (etched). It was assumed that there were two components making up the main peak. The peaks indicate the presence of the 3C and 6H polytypes.

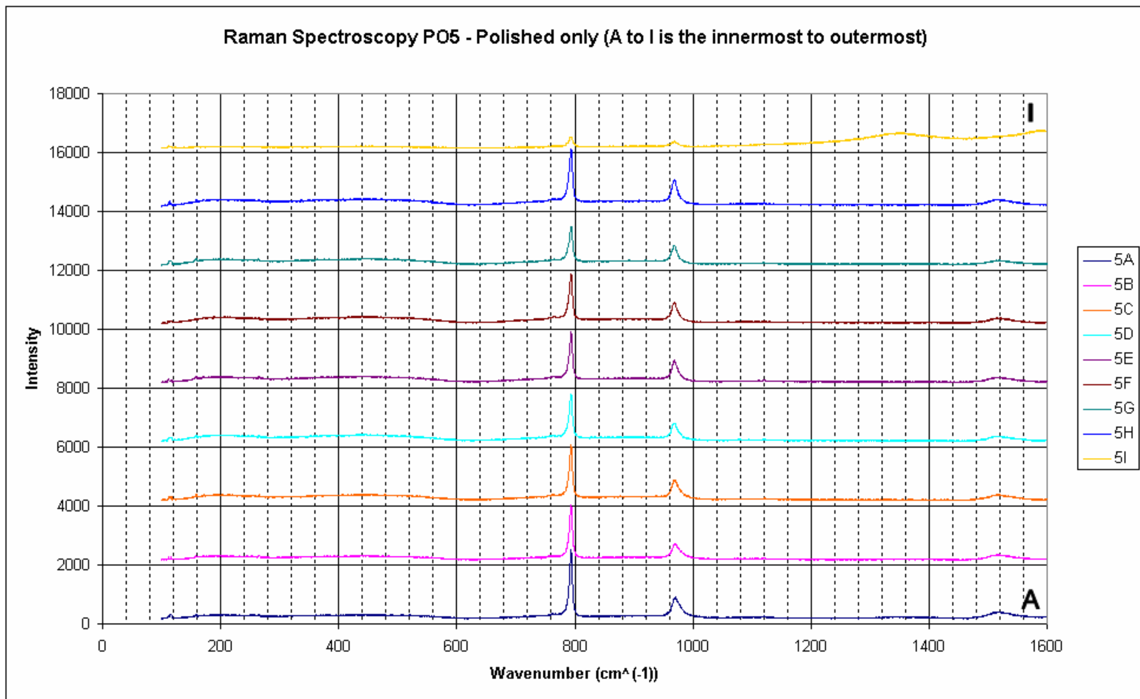

Raman spectra of the SiC coating of PO5 polished coated particle. A is the innermost and I is the outermost spot along the SiC cross-section. Neither the amorphous nor crystalline silicon is seen throughout the SiC layer. The SiC peaks do not split, however peak deconvolution indicates the presence of a relatively small 6H peak. Graphite is only seen at analysis I.

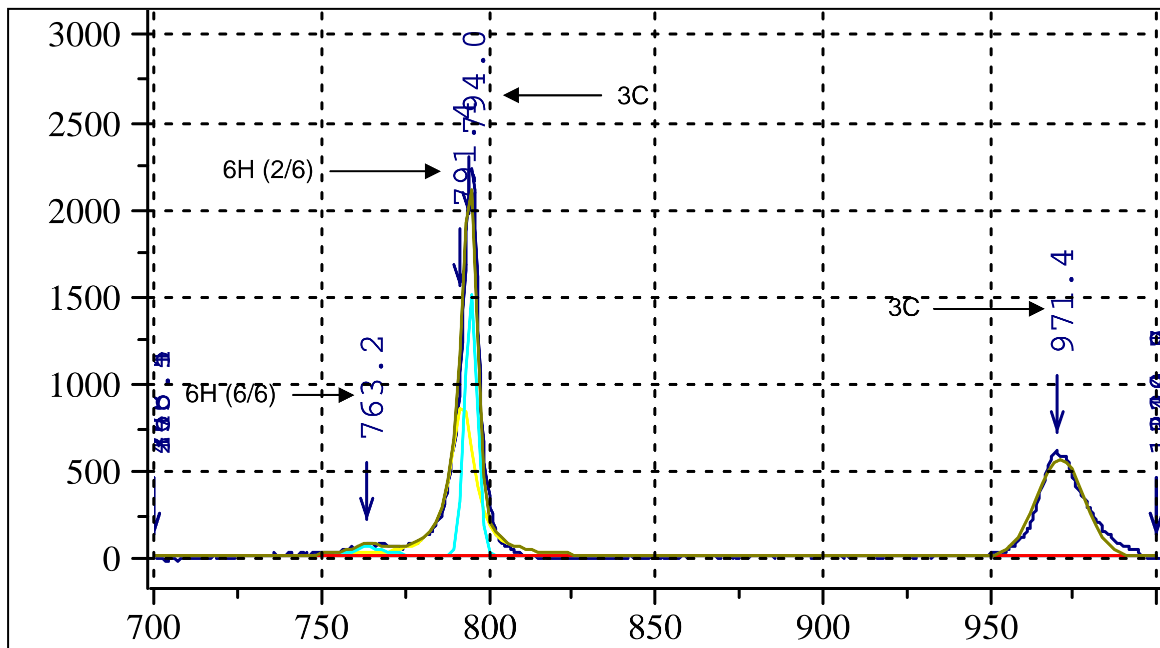

Raman spectra of the TO SiC peaks after deconvolution for analysis 5A (polished). It was assumed that there were two components making up the main peak. The peaks indicate the presence of the 3C and 6H polytypes.

Sample PO6

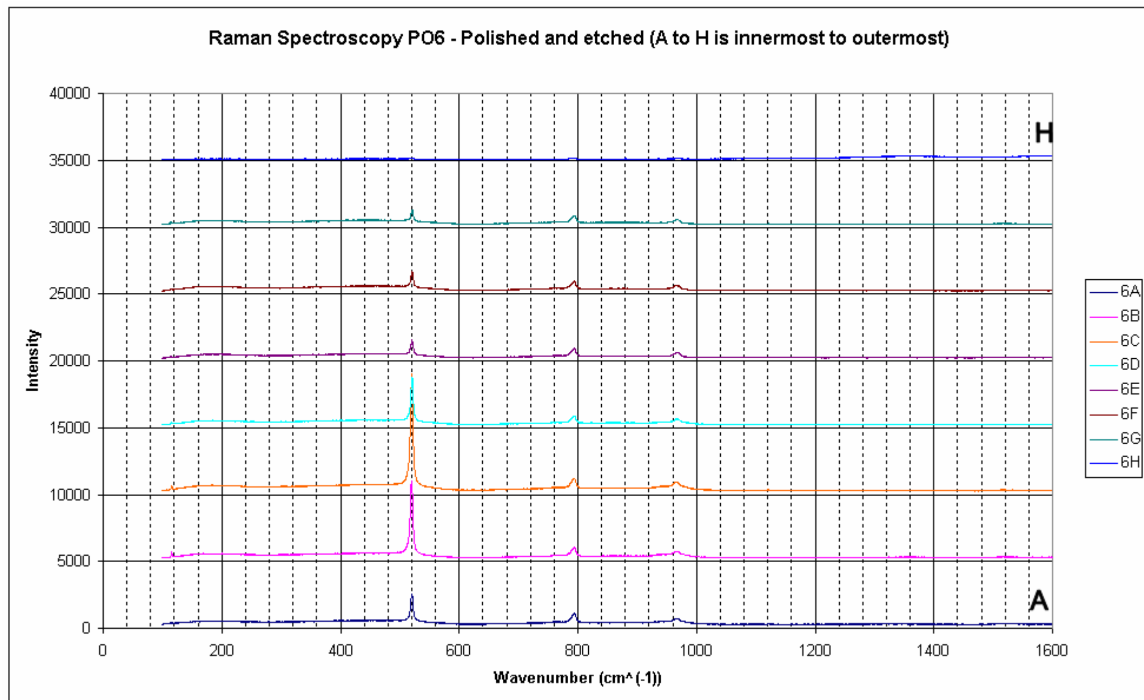

Raman spectra of the SiC coating of PO6 etched and polished coated particle. A is the innermost and H is the outermost spot along the SiC cross-section. The crystalline silicon progressively increases from analysis A to C before declining again. The silicon to SiC ratio of peaks is particularly high relative to that of other samples. Consequently, there is very little that can be said about the SiC peaks. There is a hint of graphite detected from the slight change of slope from analysis B.

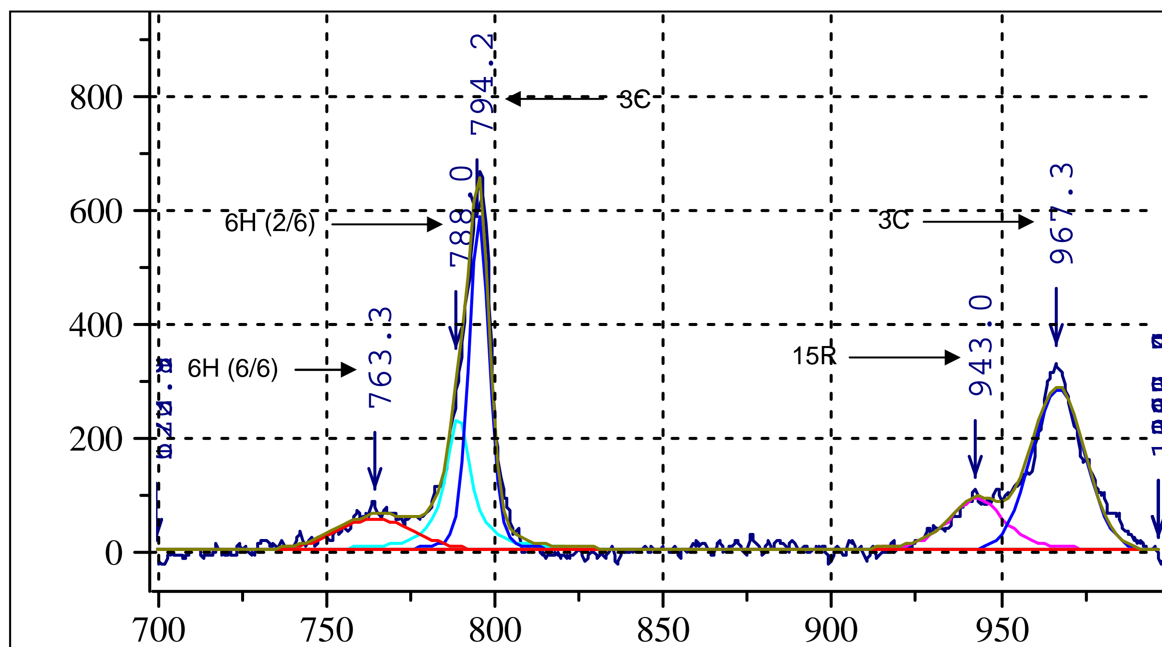

Raman spectra of the TO SiC peaks after deconvolution for analysis 6A (etched). It was assumed that there were two components making up the main peak. The peaks indicate the presence of the 3C and 6H polytypes.

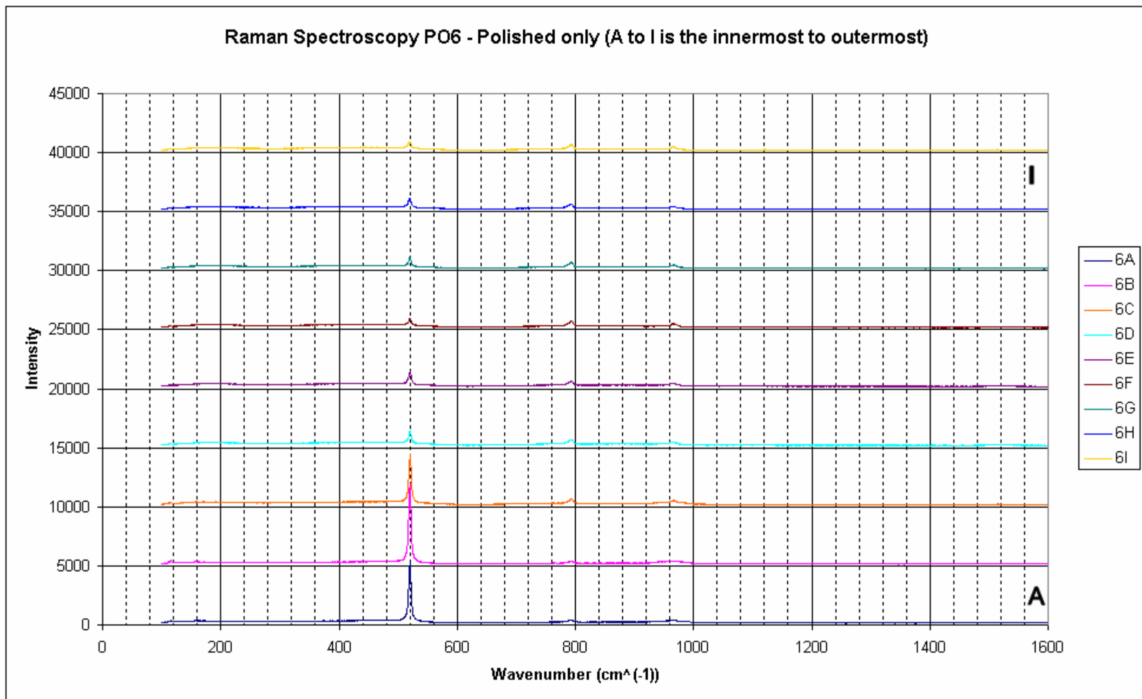

Raman spectra of the SiC coating of PO6 polished coated particle. A is the innermost and I is the outermost spot along the SiC cross-section. The crystalline silicon increases from analysis A to B before progressively declining up to analysis I. The silicon to SiC ratio of some peaks is particularly high relative to that of other samples. There is no evidence of graphite.

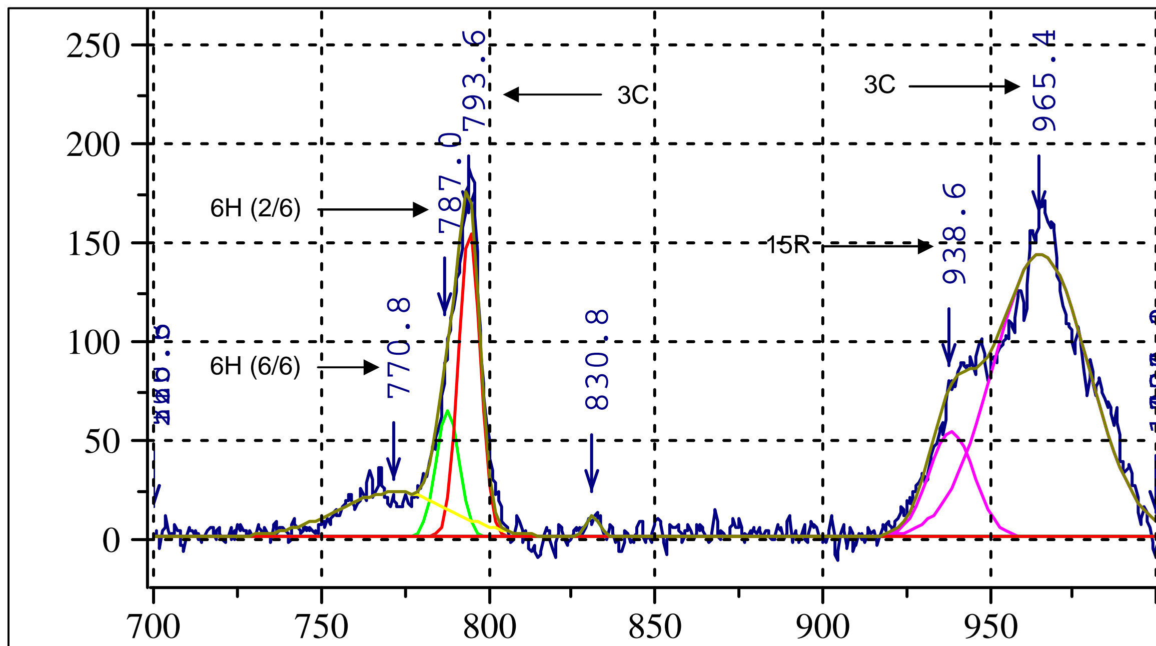

Raman spectra of the TO SiC peaks after deconvolution for analysis 6A (polished). It was assumed that there were two components making up the main peak. The peaks indicate the presence of the 3C and 6H polytypes.

Sample PO8

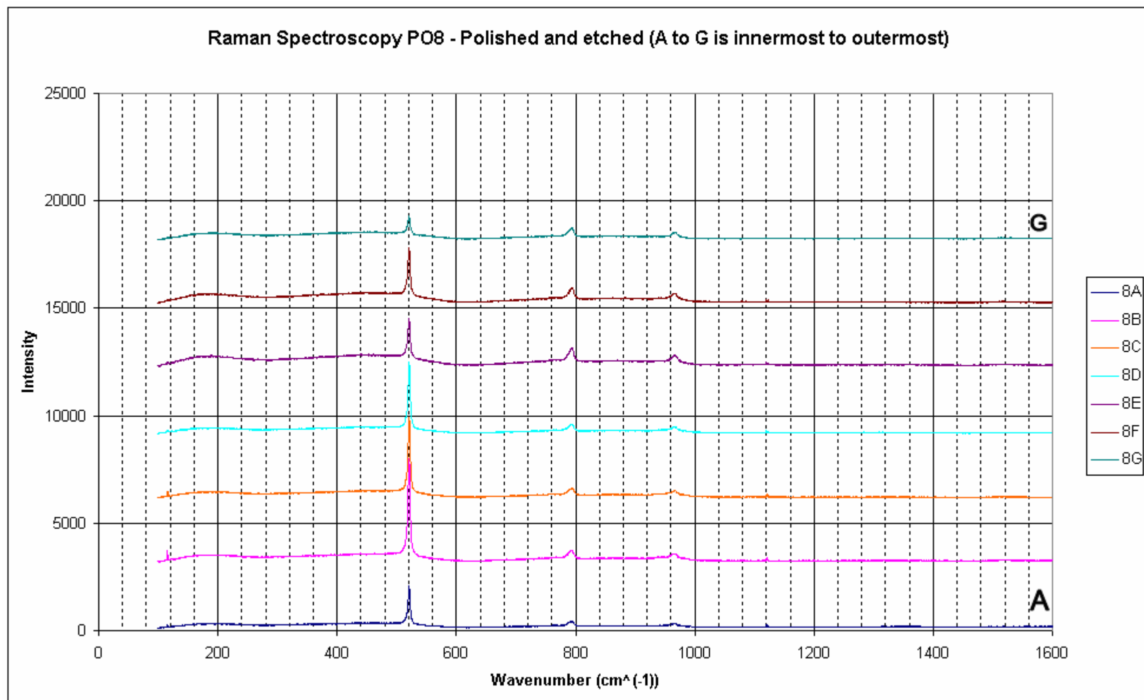

Raman spectra of the SiC coating of PO8 etched and polished coated particle. A is the innermost and G is the outermost spot along the SiC cross-section. The crystalline silicon increases from analysis A to C before progressively declining up to analysis G. The silicon to SiC ratio of peaks is particularly high relative to that of other samples, with the exception of sample PO6. There is little detail that can be extracted from the SiC peaks. There is no evidence of graphite being present.

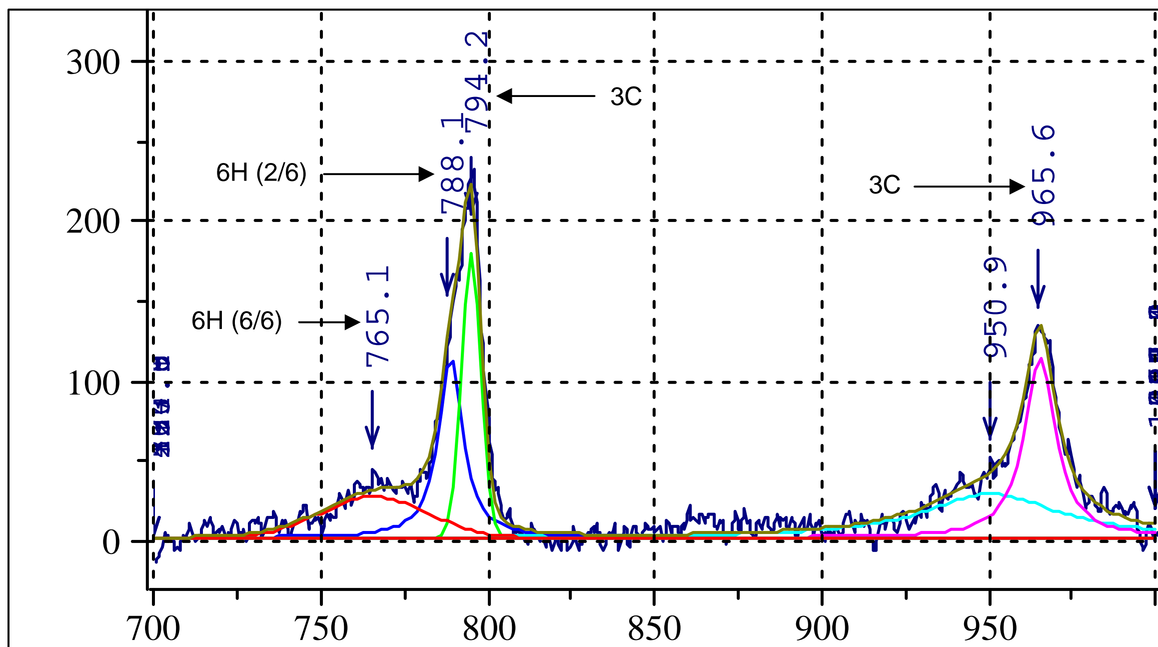

Raman spectra of the TO SiC peaks after deconvolution for analysis 8A (etched). It was assumed that there were two components making up the main peak. The peaks indicate the presence of the 3C and 6H polytypes.

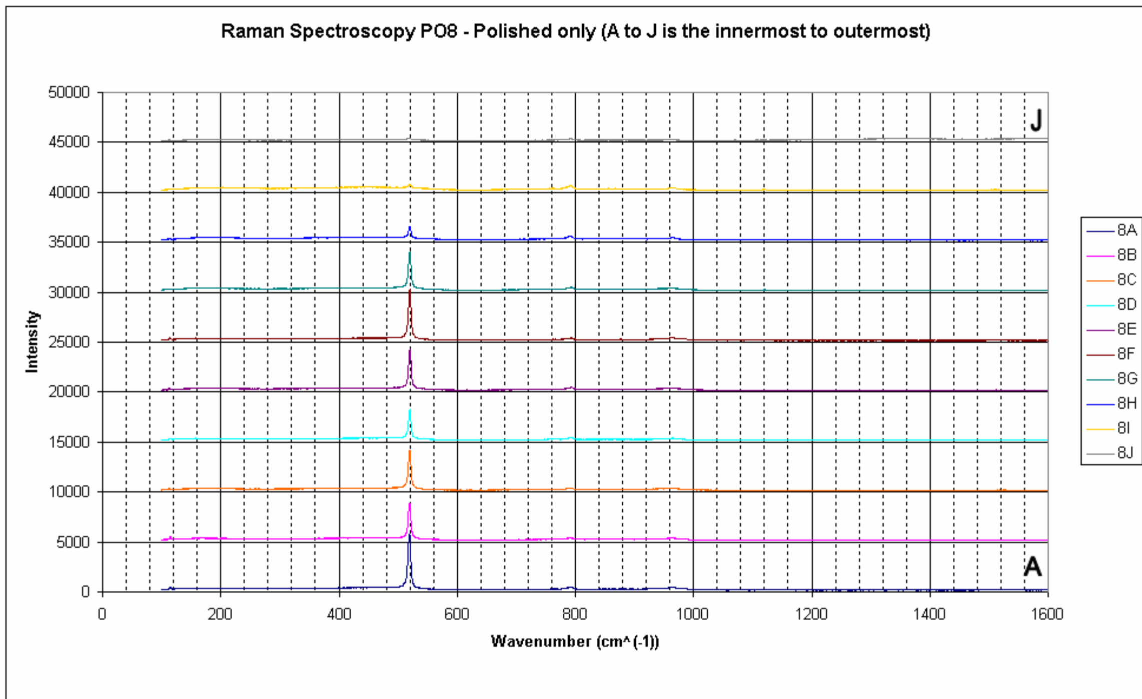

Raman spectra of the SiC coating of PO8 polished coated particle. A is the innermost and J is the outermost spot along the SiC cross-section. The crystalline silicon progressively increases from analysis A to G, before declining up to analysis J. As with the etched sample, the silicon to SiC ratio of peaks is particularly high relative to that of other samples, with the exception of sample PO6. There is little that can be concluded regarding the SiC peaks. There is no evidence of graphite being present.

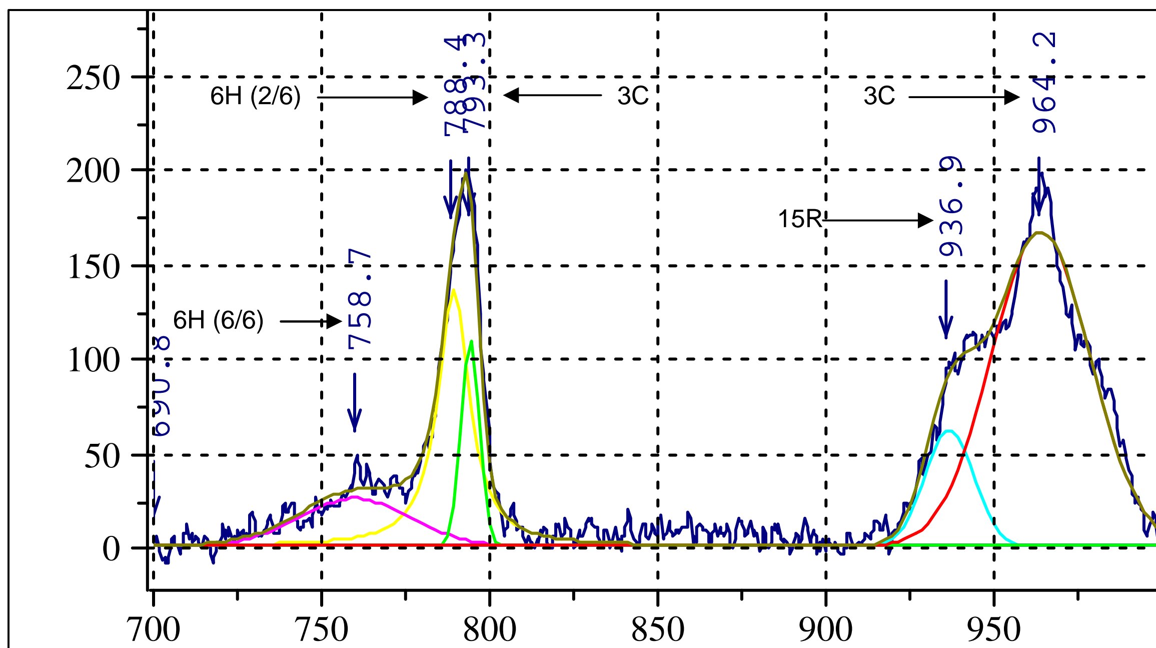

Raman spectra of the TO SiC peaks after deconvolution for analysis 8A (polished). It was assumed that there were two components making up the main peak. The peaks indicate the presence of the 3C and 6H polytypes.

Sample PO9

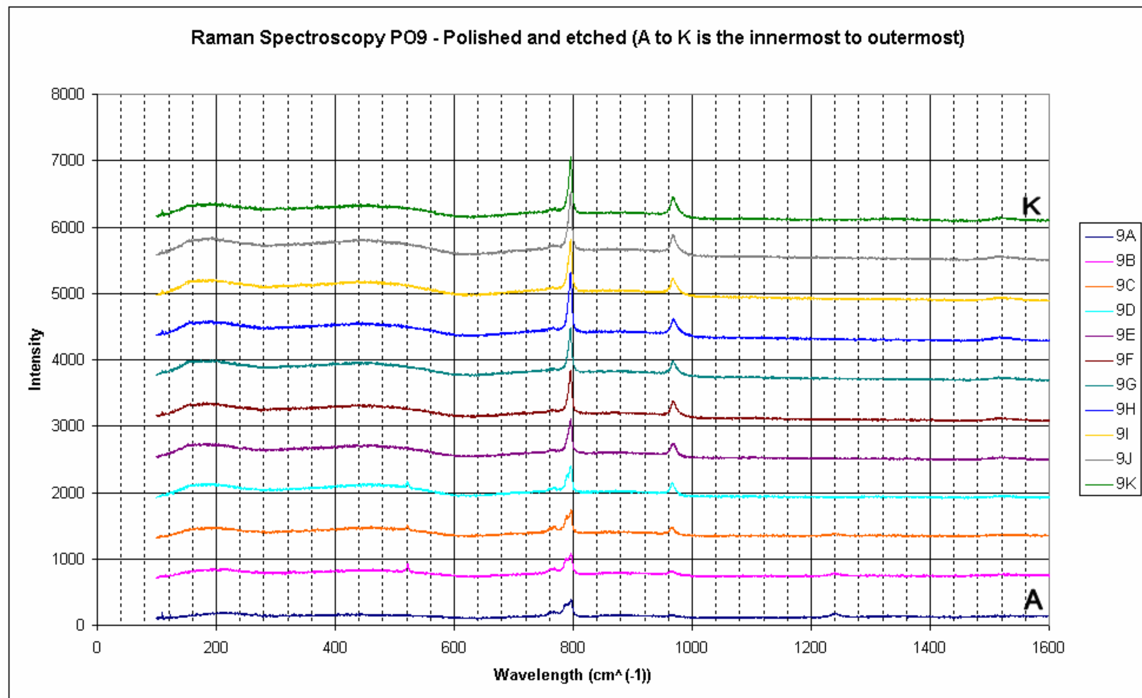

Raman spectra of the SiC coating of PO9 etched and polished coated particle. A is the innermost and K is the outermost spot along the SiC cross-section. Amorphous silicon is generally found throughout the analyses. Small peaks of crystalline silicon are also found along the inner parts of the SiC layer. Peak splitting is clearly more evident along the inner parts of the SiC layer. The SiC peak intensity also increases outwards reaching the maximum at analysis K. This is thought to be as a result of crystallinity and absorption. There is no evidence of graphite.

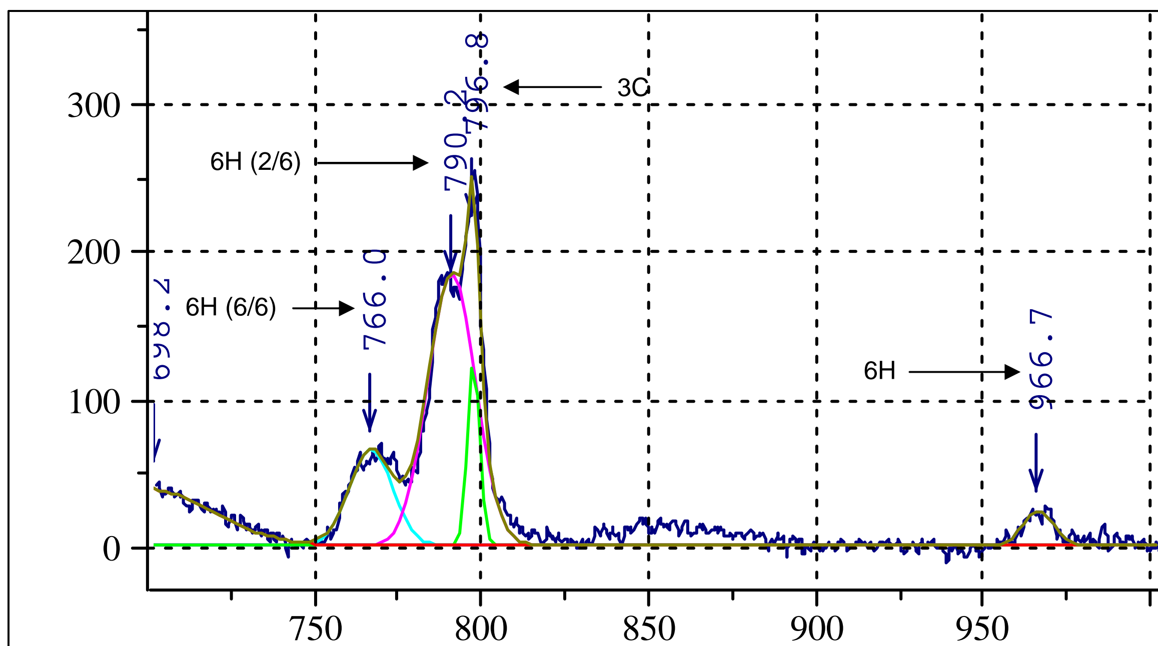

Raman spectra of the TO SiC peaks after deconvolution for analysis 9A (etched). It was assumed that there were two components making up the main peak. The peaks indicate the presence of the 3C and 6H polytypes.

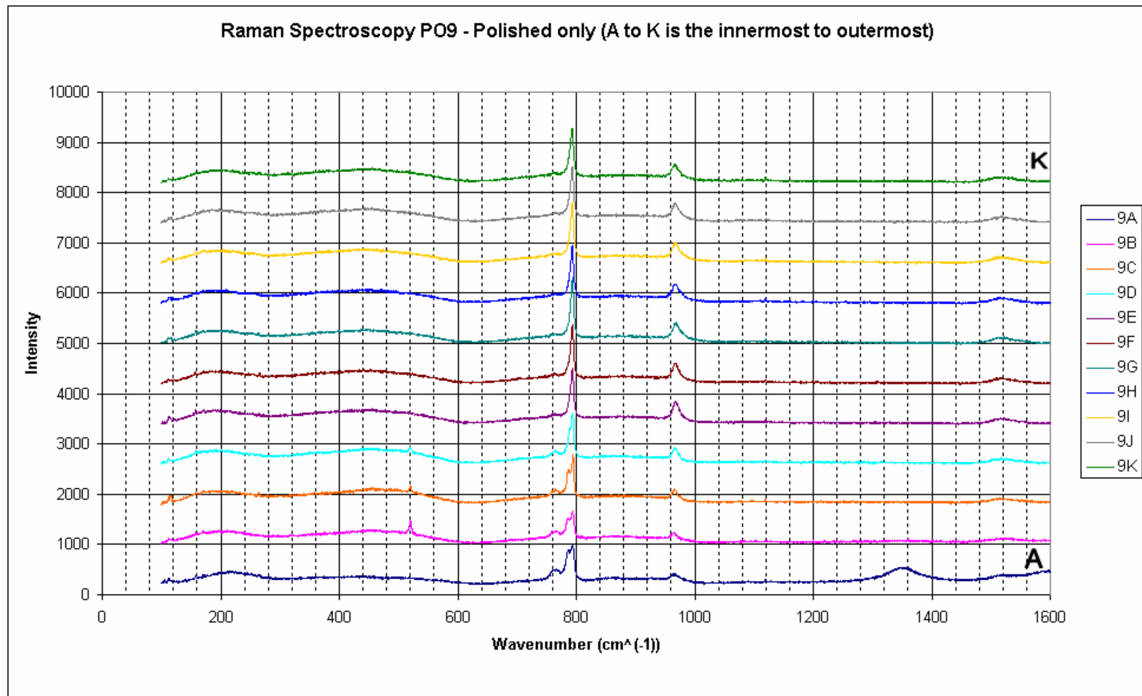

Raman spectra of the SiC coating of PO9 polished coated particle. A is the innermost and K is the outermost spot along the SiC cross-section. Amorphous silicon is generally found throughout the analyses. Small peaks of crystalline silicon are also found along the inner parts of the SiC layer. As with the etched sample, peak splitting is more evident along the inner parts of the SiC layer. Unlike with the etched sample, the SiC peak intensity remains rather consistent throughout the analyses. Graphite is only seen from analysis A.

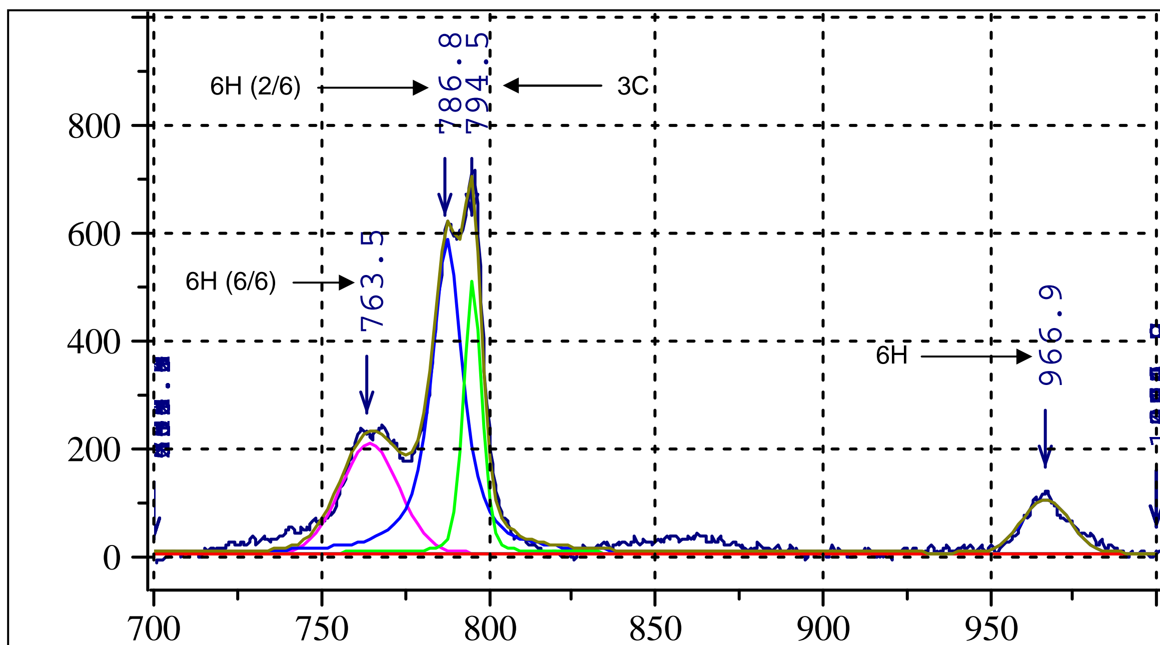

Raman spectra of the TO SiC peaks after deconvolution for analysis 9A (polished). It was assumed that there were two components making up the main peak. The peaks indicate the presence of the 3C and 6H polytypes.

Sample PO10

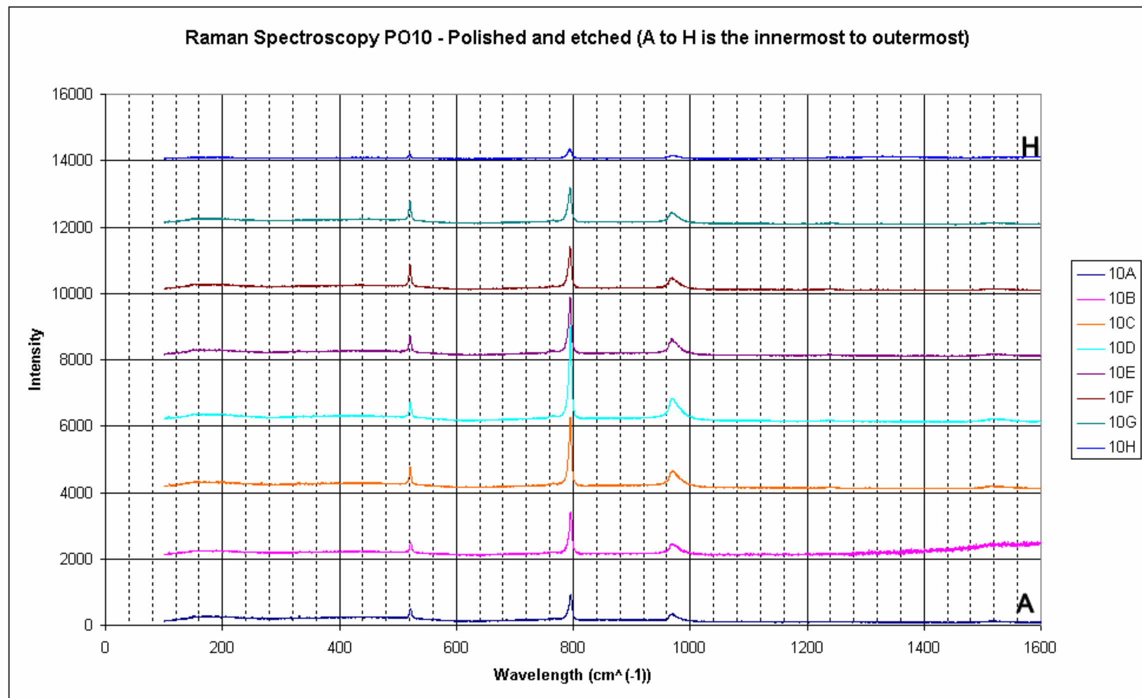

Raman spectra of the SiC coating of PO10 etched and polished coated particle. A is the innermost and H is the outermost spot along the SiC cross-section. Crystalline silicon peaks are evident throughout the analyses. Peak splitting is not evident but is confirmed by the deconvolution. The middle of the SiC layer has the most intense SiC peak as a result of improved crystallinity and absorption. There is no evidence of graphite.

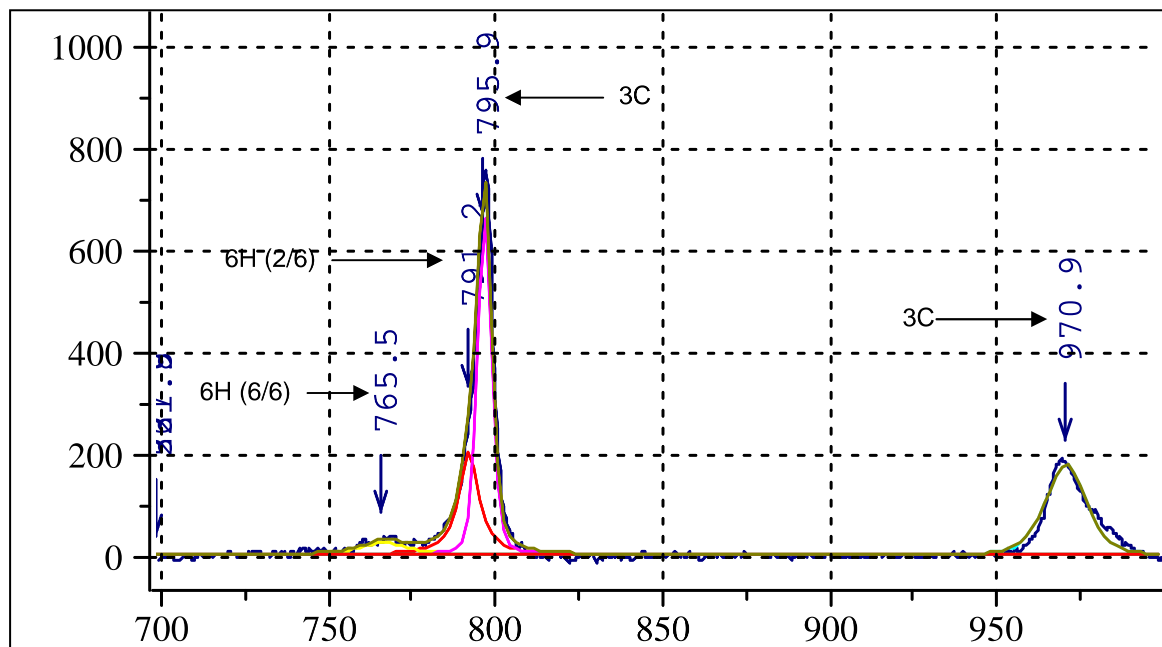

Raman spectra of the TO SiC peaks after deconvolution for analysis 10A (etched). It was assumed that there were two components making up the main peak. The peaks indicate the presence of the 3C and 6H polytypes.

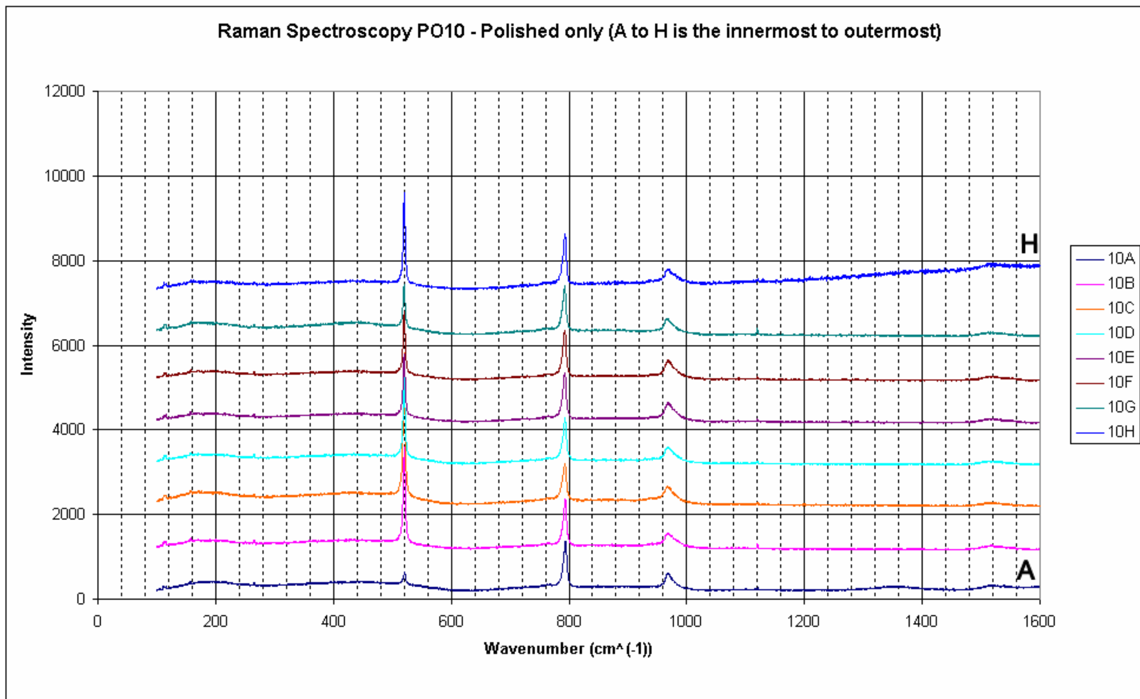

Raman spectra of the SiC coating of PO10 polished coated particle. A is the innermost and H is the outermost spot along the SiC cross-section. Crystalline silicon peaks are evident throughout the analyses. Unlike with the etched sample the silicon peaks vary significantly, with a maximum at analysis B. Peak splitting is not evident but is confirmed by the deconvolution. Also in contrast to the etched sample, the SiC intensities remain fairly consistent. There is no evidence of graphite.

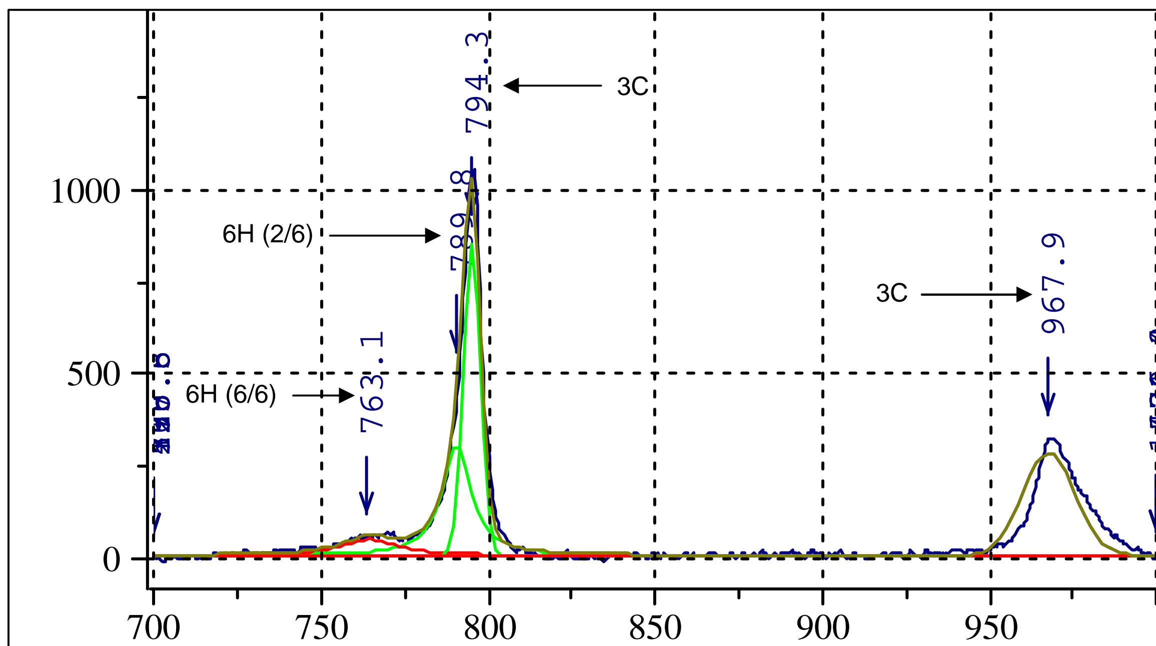

Raman spectra of the TO SiC peaks after deconvolution for analysis 10A (polished). It was assumed that there were two components making up the main peak. The peaks indicate the presence of the 3C and 6H polytypes.

APPENDIX B
XRD 3C NECSA sample & high temperature data

3C NECSA sample

- XRD quantitative analysis in AUTOQUAN

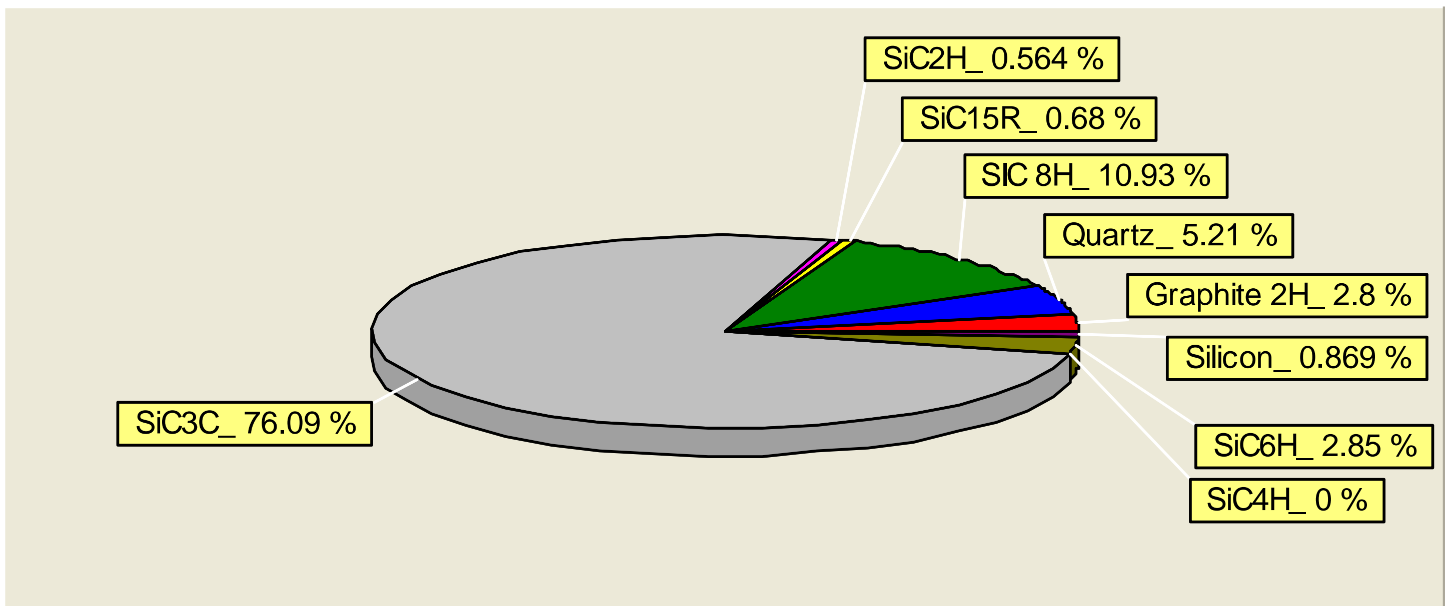

High temperature data

- G102
  - Lattice parameters (units in Å)

EXPERIMENTAL VALUES				
Temp	a - 3C-SiC	a - Al_2O_3	c - Al_2O_3	c - graphite
25	4.361	4.76456	12.99708	7.01469
100	4.36178	4.76635	13.00309	7.02852
200	4.36348	4.76969	13.01653	7.04916
300	4.36505	4.77258	13.02489	7.06377
400	4.36695	4.77593	13.03497	7.0744
500	4.36889	4.77918	13.05006	7.08981
600	4.37059	4.78293	13.06044	7.1058
700	4.37241	4.78657	13.07039	7.11968
800	4.37448	4.78987	13.08358	7.13734
900	4.37612	4.79342	13.0951	7.15452
1000	4.37801	4.79631	13.10834	7.1728
1100	4.3796	4.79984	13.11777	7.18882
1125	4.38005	4.80082	13.12004	7.19605
1150	4.38054	4.80143	13.12284	7.19713
1175	4.38123	4.80195	13.12613	7.20159
1200	4.38165	4.80285	13.12948	7.18689
1225	4.38206	4.804	13.12936	7.20292
1250	4.3826	4.80502	13.13498	7.19772
1275	4.38338	4.80659	13.13886	7.19527
1300	4.38363	4.80623	13.14206	7.21384
1325	4.38439	4.80691	13.1445	7.21233
1350	4.38461	4.80741	13.14245	7.21976
1375	4.38533	4.80837	13.14965	7.22768
1400	4.38569	4.81056	13.15212	7.2051
1400	4.38569	4.81056	13.15212	7.2051
1350	4.38515	4.80845	13.15067	7.16657
1300	4.38392	4.80744	13.14543	7.17392
1250	4.38308	4.80602	13.13871	7.15682
1200	4.38213	4.80438	13.1334	7.14617
1150	4.381	4.80233	13.12732	7.13675
1100	4.38007	4.80044	13.121	7.14869
26	4.36032	4.76259	13.00579	6.95403

High temperature data

- PO4
  - Lattice parameters (units in Å)

EXPERIMENTAL VALUES				
T	a - Al_2O_3	c - Al_2O_3	a-SiC	c-graphite
25	4.76112	12.991	4.35961	6.90744
100	4.76367	13.00066	4.36174	6.9206
200	4.76639	13.00855	4.36243	6.93873
300	4.76998	13.01769	4.36444	6.96462
400	4.77309	13.02669	4.3661	6.98457
500	4.77574	13.03619	4.36763	6.99705
600	4.77874	13.04637	4.36929	7.01692
700	4.78245	13.05822	4.37153	7.0401
800	4.78576	13.06687	4.37335	7.05911
900	4.78873	13.07505	4.37494	7.07995
1000	4.79196	13.08348	4.37637	7.095
1100	4.79474	13.09292	4.37808	7.11209
1125	4.79589	13.09663	4.3786	7.11849
1150	4.79643	13.09642	4.37853	7.12101
1175	4.79729	13.09927	4.37895	7.125
1200	4.79838	13.10301	4.37977	7.12981
1225	4.79914	13.10683	4.38014	7.13532
1250	4.79975	13.10927	4.38056	7.13836
1275	4.80077	13.11273	4.38072	7.14048
1300	4.80125	13.11557	4.38122	7.14847
1325	4.80226	13.11711	4.3815	7.15292
1350	4.80324	13.12162	4.38198	7.15384
1375	4.80443	13.12518	4.38286	7.1618
1400	4.80577	13.12877	4.38362	7.16708
1400	4.80577	13.12877	4.38362	7.16708
1350	4.80471	13.12379	4.38293	7.1608
1300	4.80318	13.11856	4.38199	7.14987
1250	4.80125	13.11328	4.38111	7.14228
1200	4.79971	13.10852	4.38046	7.13038
1150	4.79836	13.10514	4.377	7.1226
1100	4.79701	13.1003	4.37936	7.11683
26	4.76213	12.99382	4.36063	6.91399

APPENDIX C
TEM images and diffraction patterns

UNIVERSITEIT VAN PRETORIA
UNIVERSITY OF PRETORIA
YUNIBESITHI YA PRETORIA

PO 5 Image 1

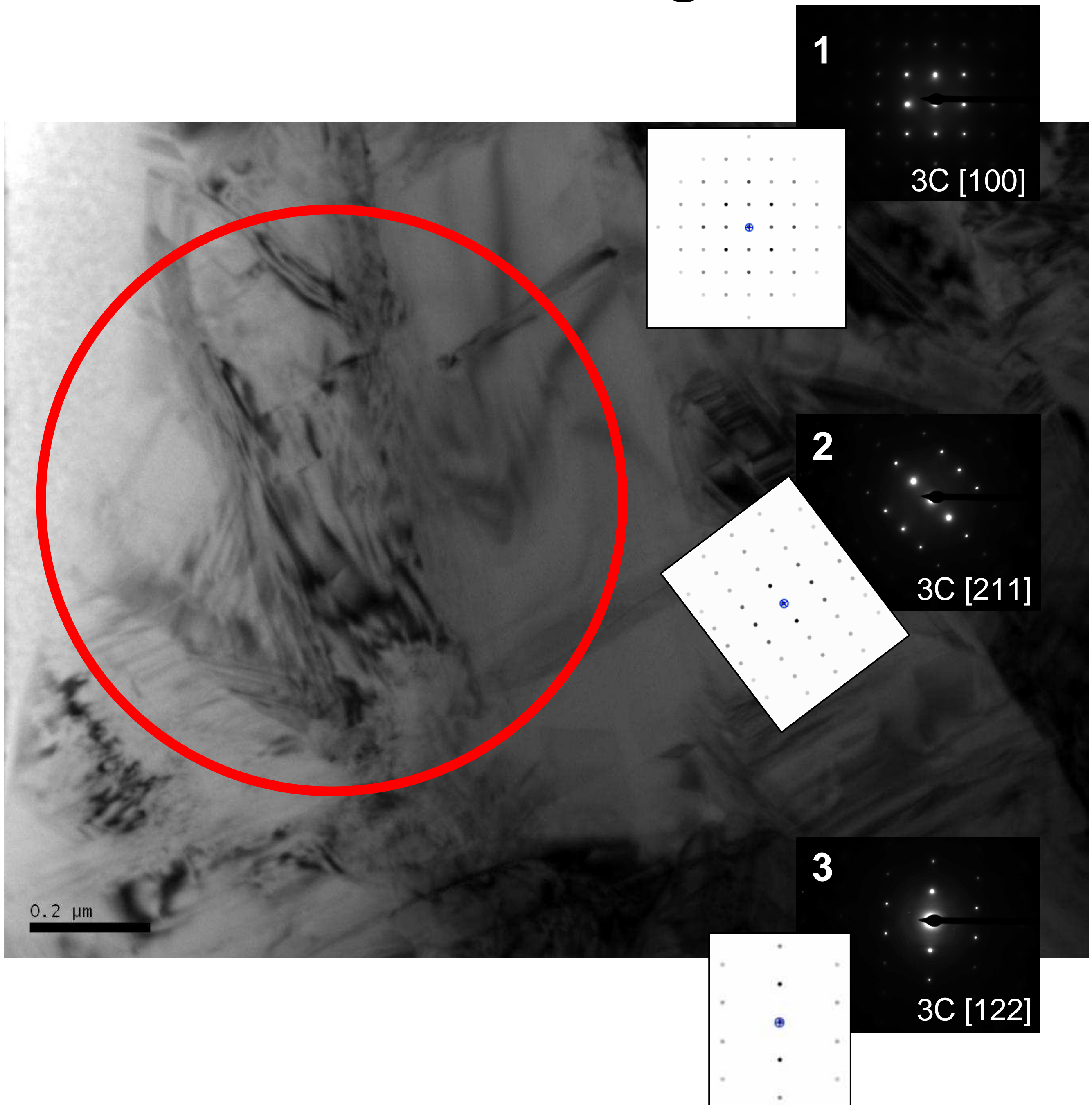

PO 5 image 2

0.2 µm

1

3C [111]

2

6H [001]

UNIVERSITEIT VAN PRETORIA
UNIVERSITY OF PRETORIA
YUNIBESITHI YA PRETORIA

PO5 image 3

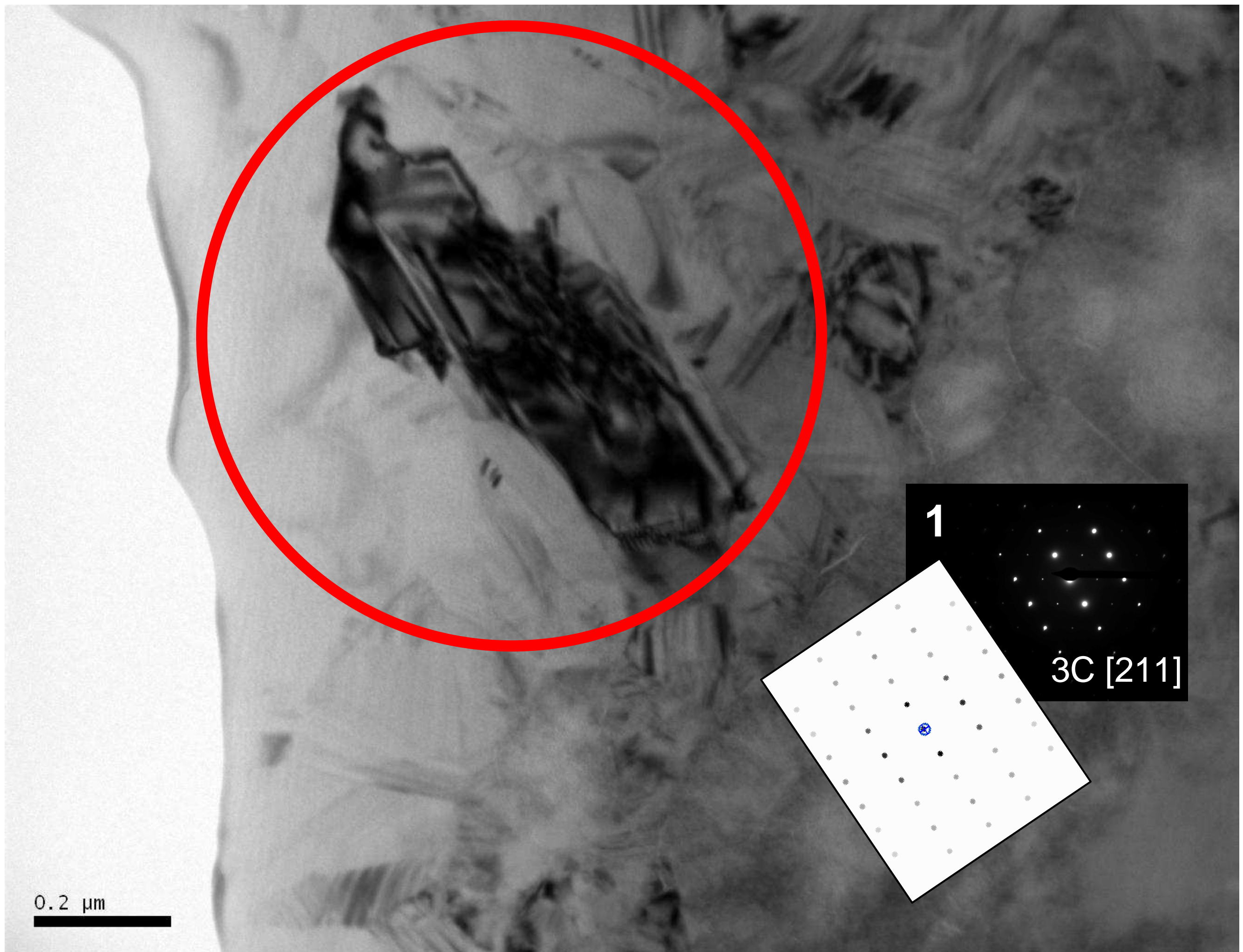

UNIVERSITEIT VAN PRETORIA
UNIVERSITY OF PRETORIA
YUNIBESITHI YA PRETORIA

PO5 Image 4

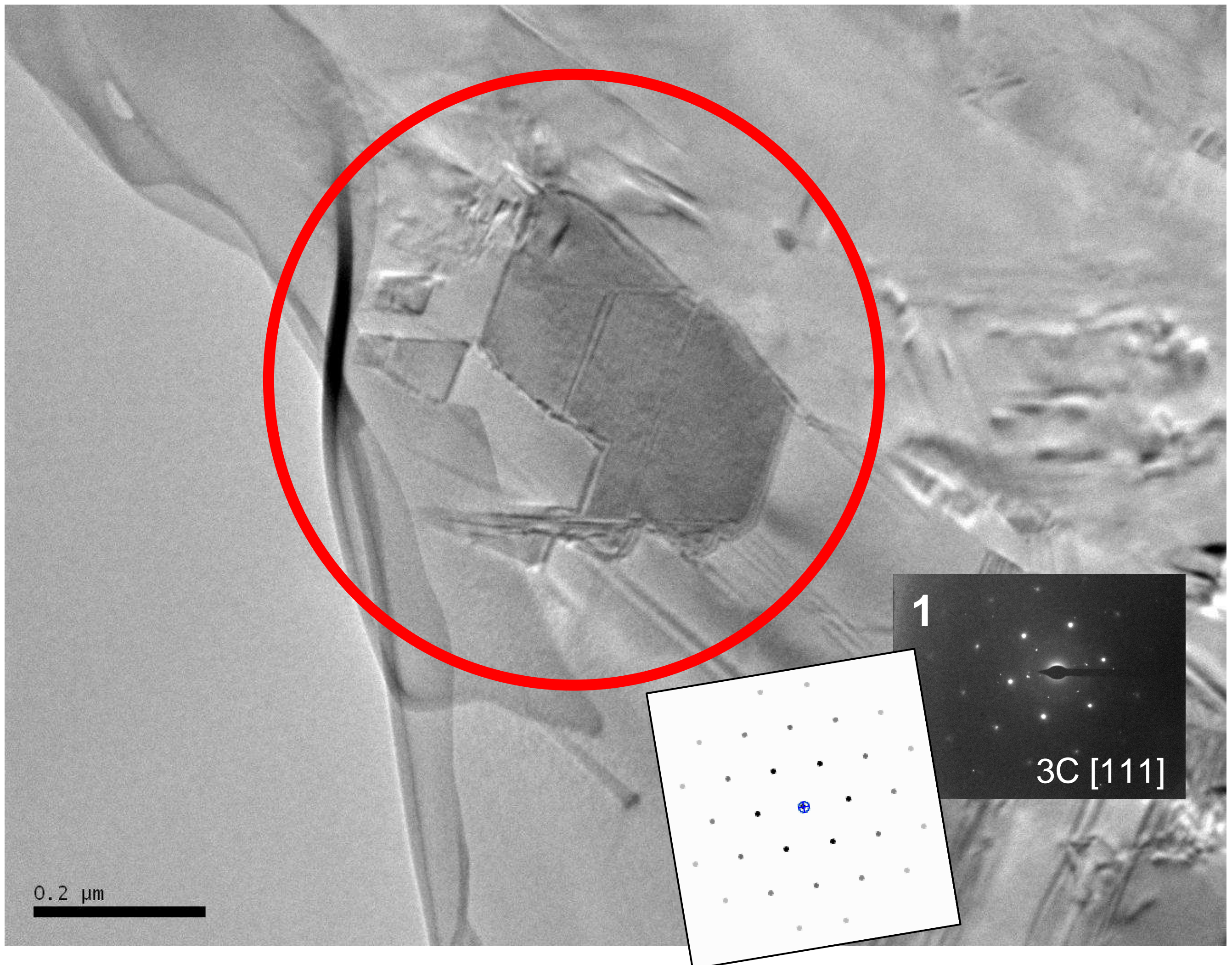

UNIVERSITEIT VAN PRETORIA
UNIVERSITY OF PRETORIA
YUNIBESITHI YA PRETORIA

PO5 Image 5

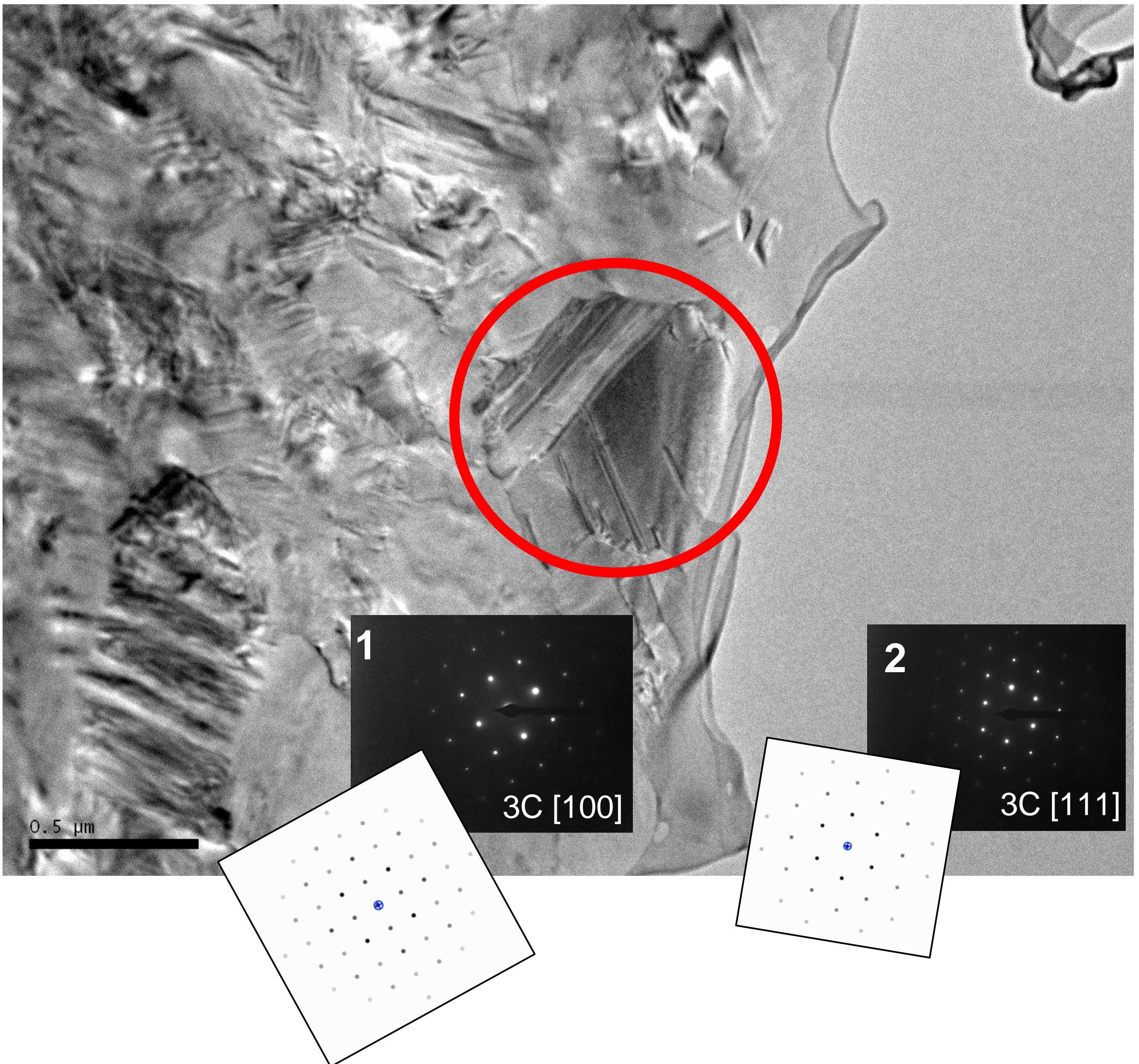

UNIVERSITEIT VAN PRETORIA
UNIVERSITY OF PRETORIA
YUNIBESITHI YA PRETORIA

PO5 Image 6

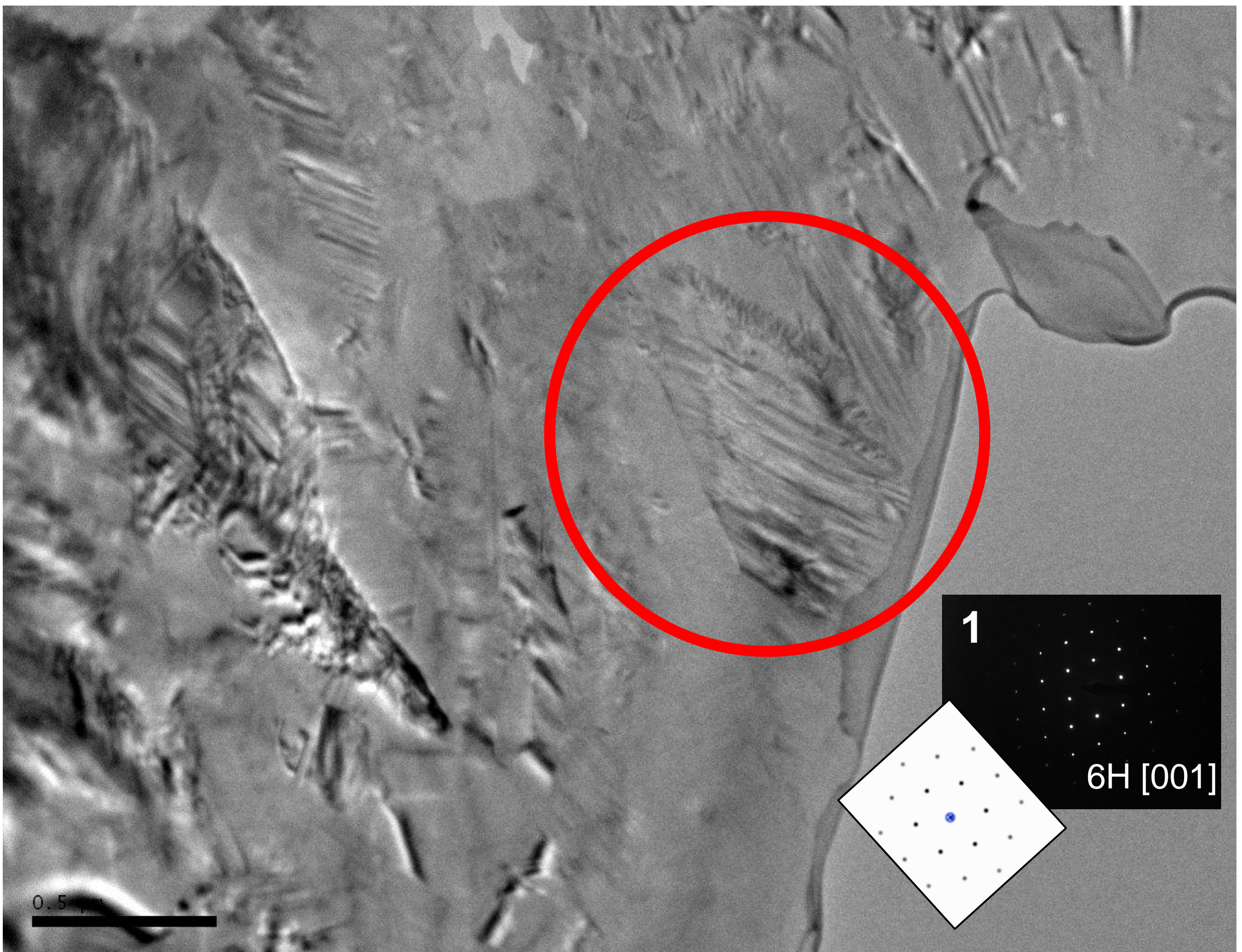

UNIVERSITEIT VAN PRETORIA
UNIVERSITY OF PRETORIA
YUNIBESITHI YA PRETORIA

PO5 Image 7

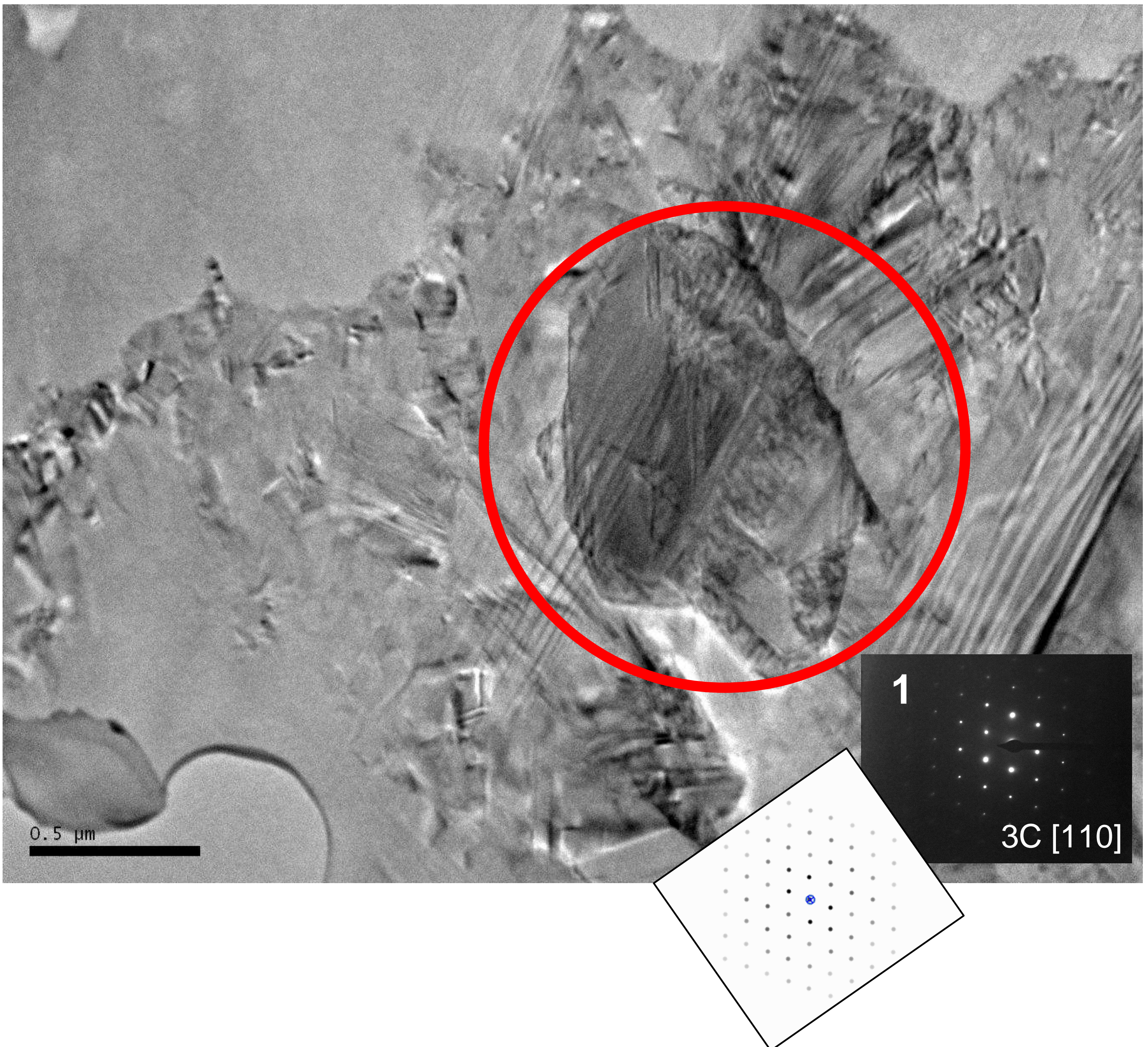

UNIVERSITEIT VAN PRETORIA
UNIVERSITY OF PRETORIA
YUNIBESITHI YA PRETORIA

PO5 Image 8

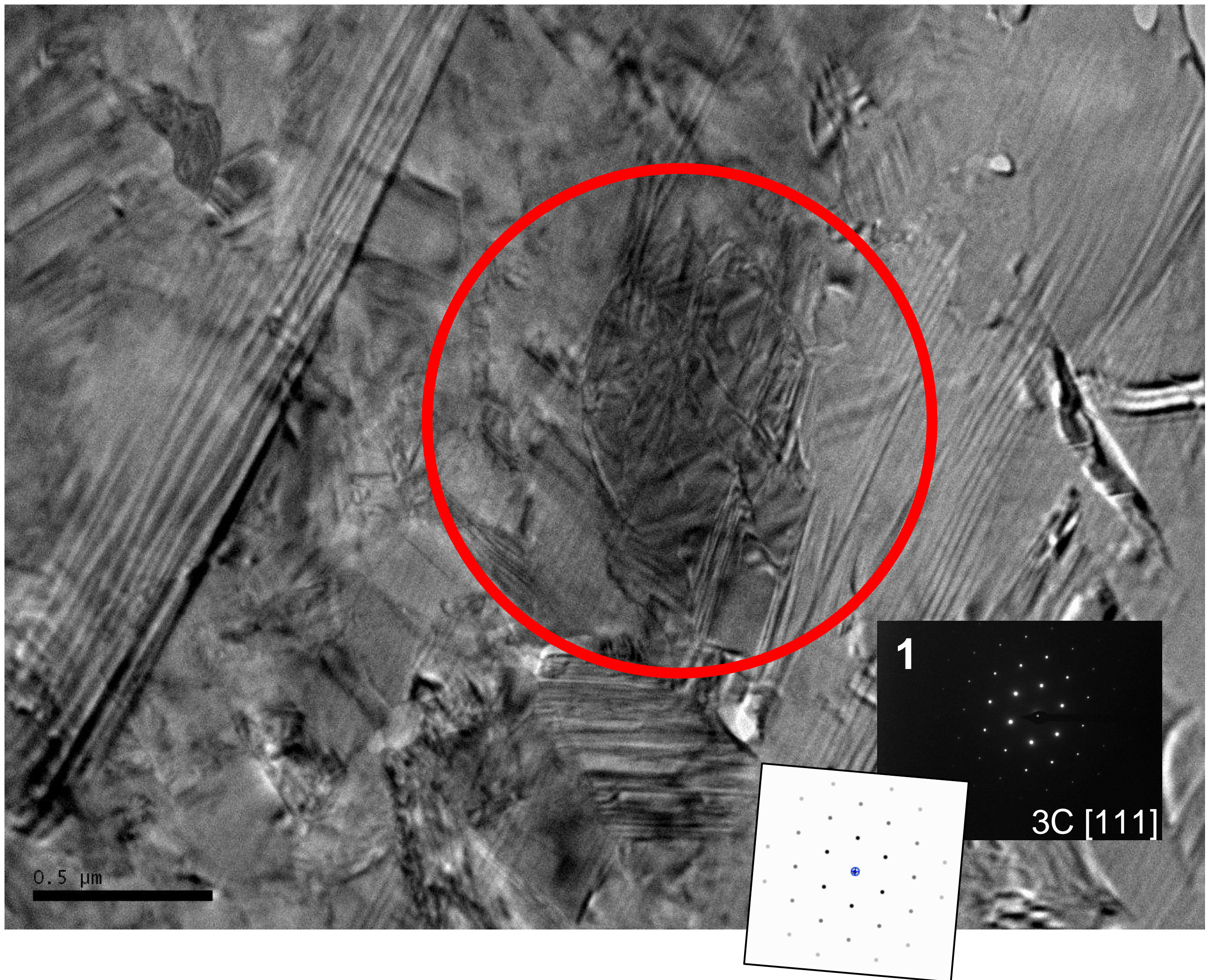

UNIVERSITEIT VAN PRETORIA
UNIVERSITY OF PRETORIA
YUNIBESITHI YA PRETORIA

PO6 Image 1

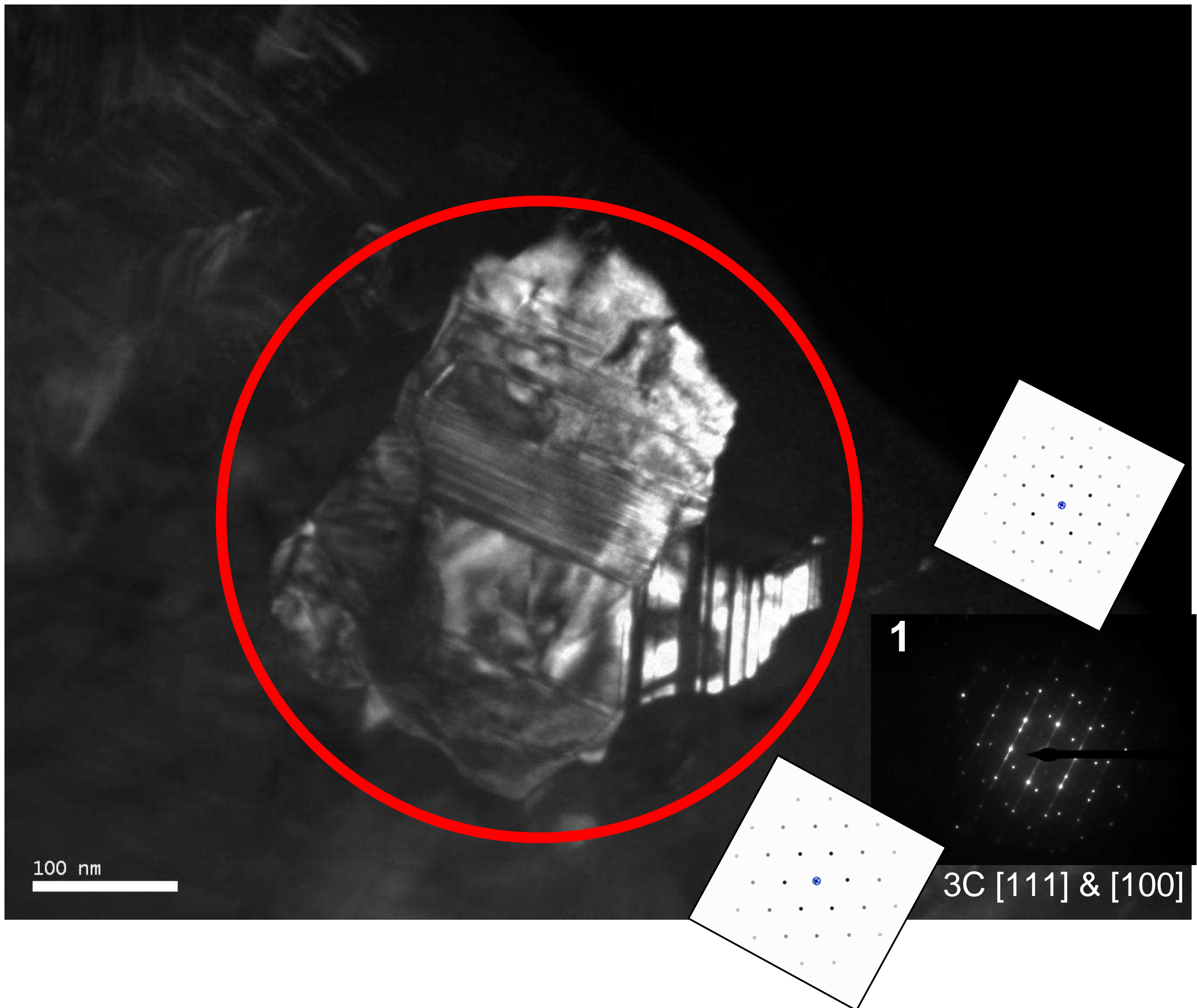

UNIVERSITEIT VAN PRETORIA
UNIVERSITY OF PRETORIA
YUNIBESITHI YA PRETORIA

PO6 Image 2

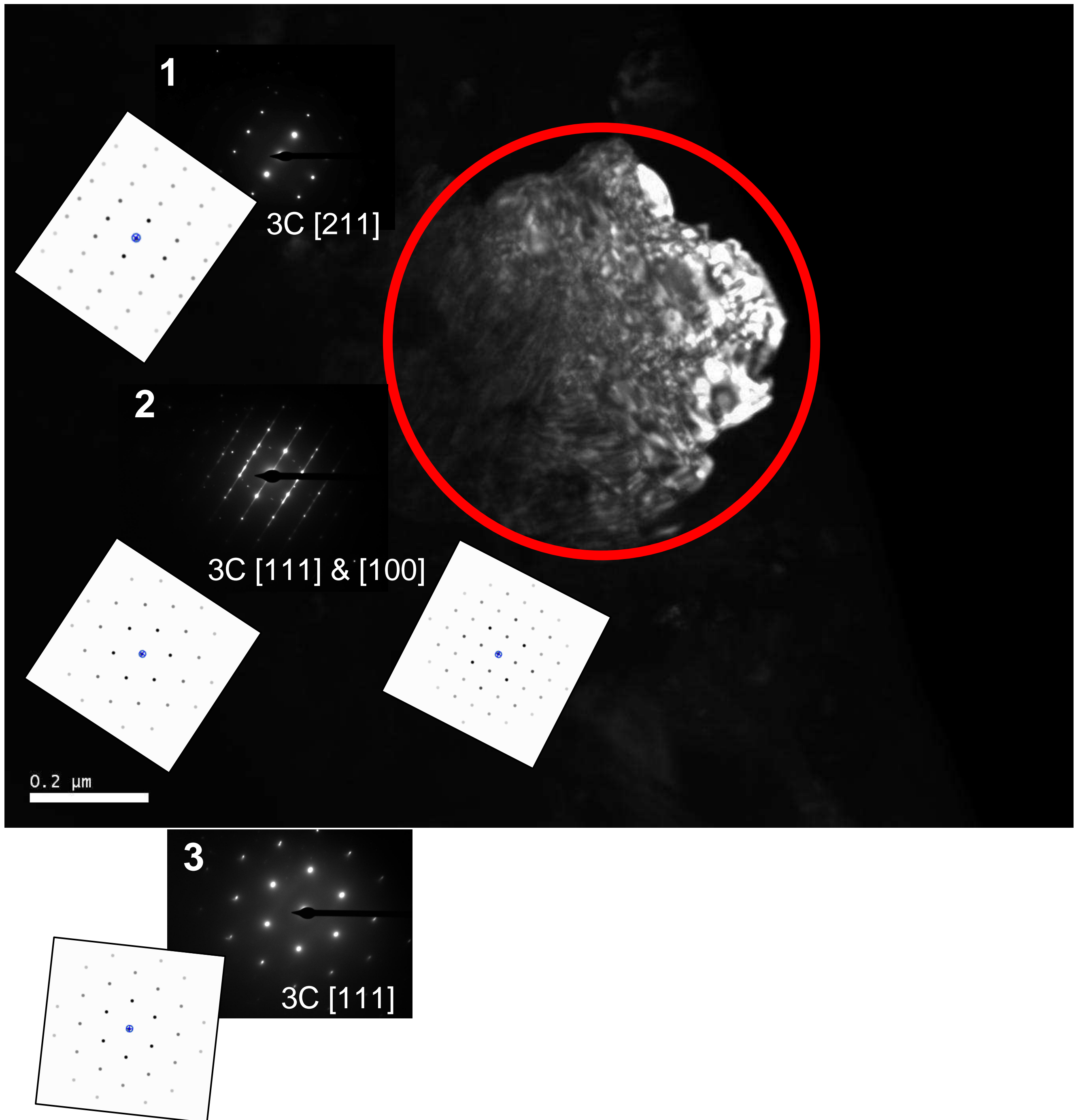

UNIVERSITEIT VAN PRETORIA
UNIVERSITY OF PRETORIA
YUNIBESITHI YA PRETORIA

PO6 Image 3

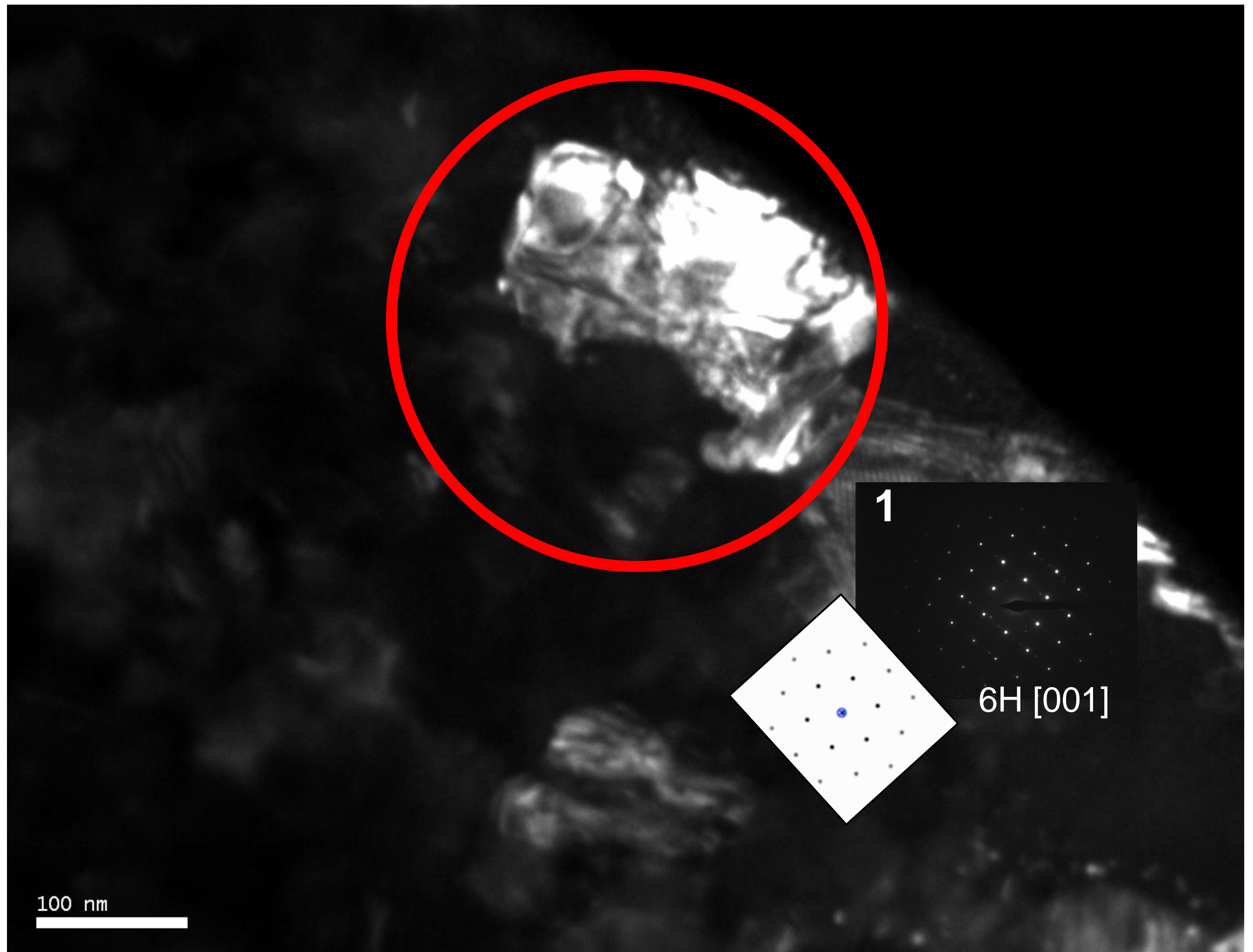

UNIVERSITEIT VAN PRETORIA
UNIVERSITY OF PRETORIA
YUNIBESITHI YA PRETORIA

PO6 Image 4

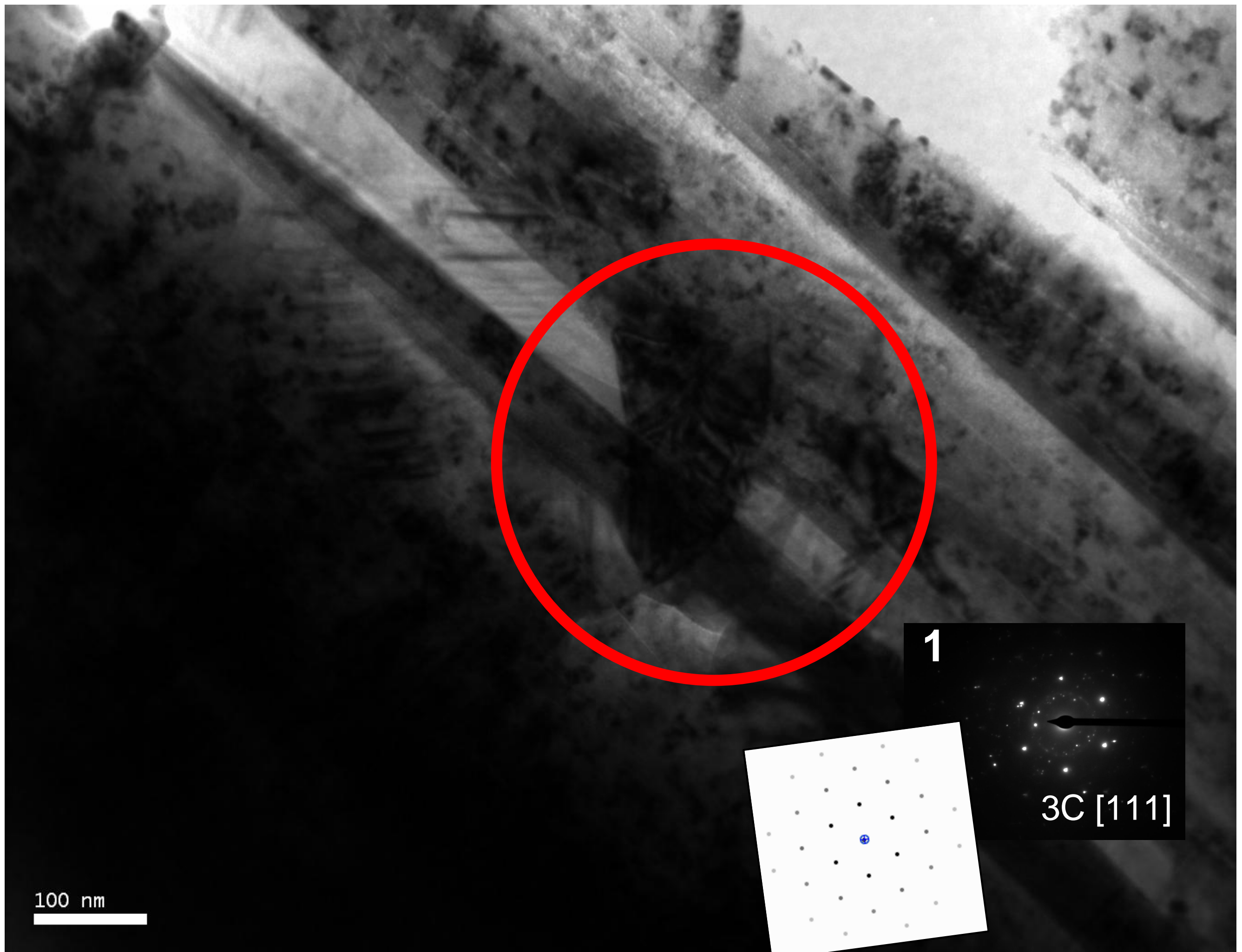

UNIVERSITEIT VAN PRETORIA
UNIVERSITY OF PRETORIA
YUNIBESITHI YA PRETORIA

PO6 Image 5

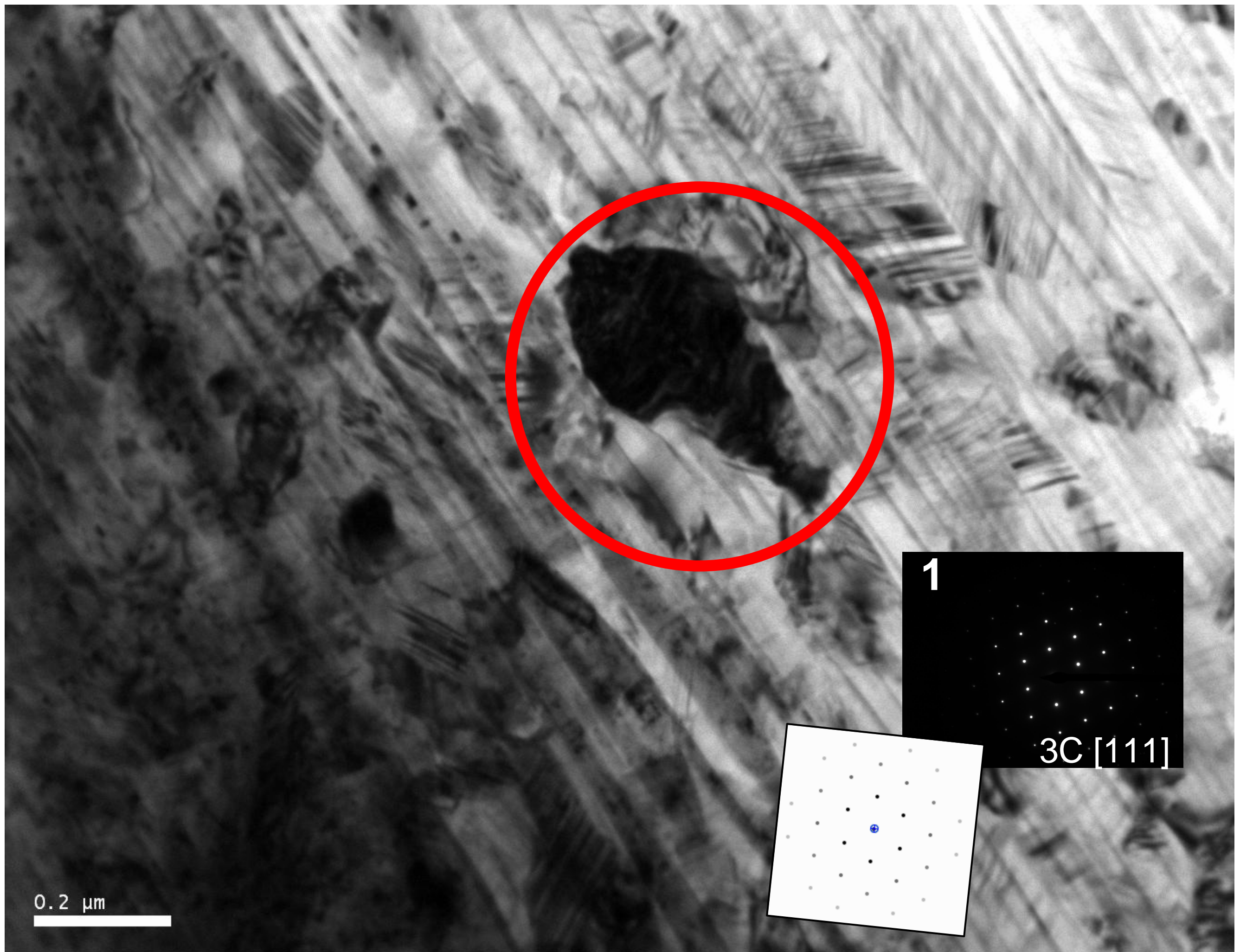

UNIVERSITEIT VAN PRETORIA
UNIVERSITY OF PRETORIA
YUNIBESITHI YA PRETORIA

PO6 Image 6

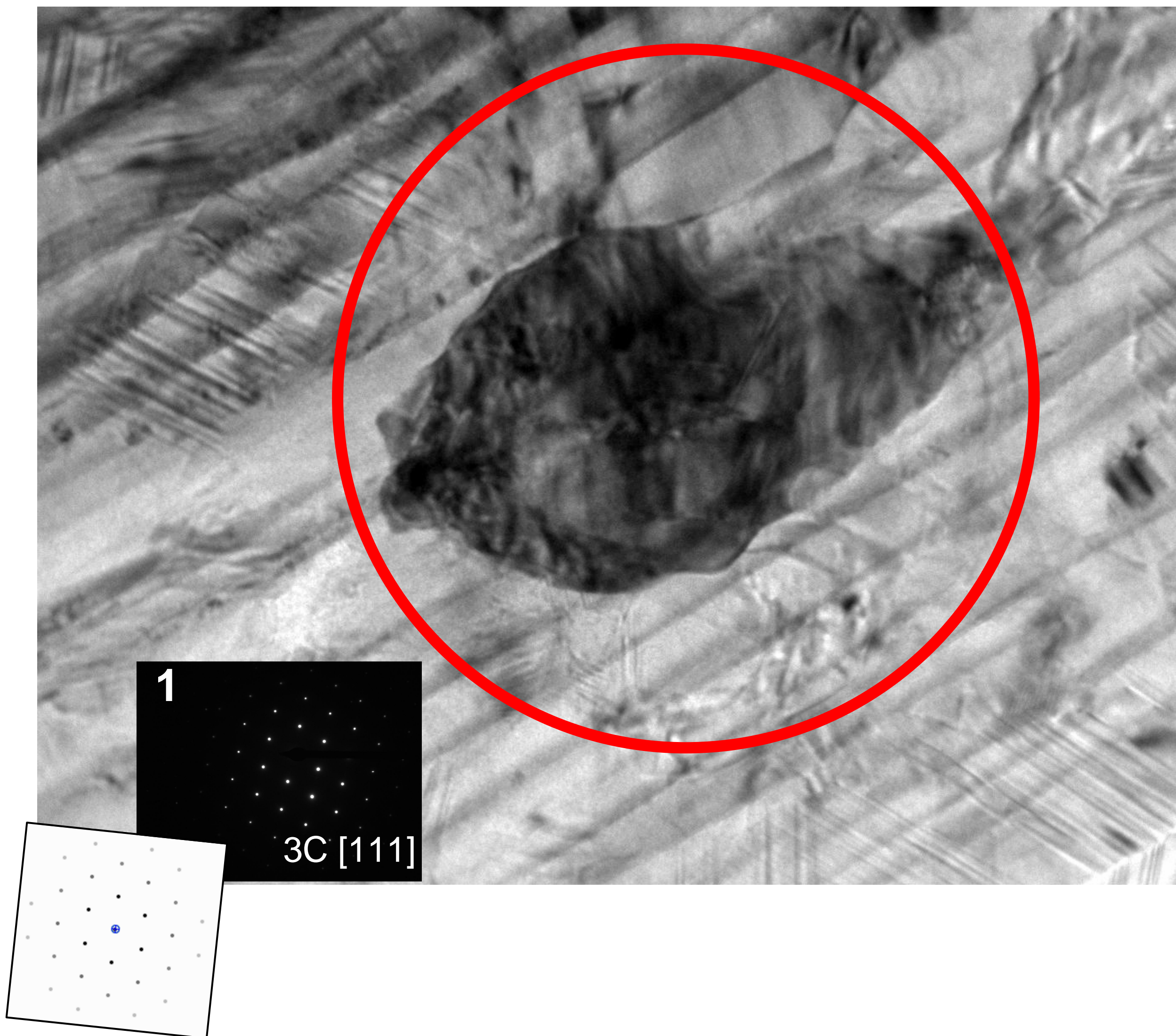

UNIVERSITEIT VAN PRETORIA
UNIVERSITY OF PRETORIA
YUNIBESITHI YA PRETORIA

PO6 Image 7

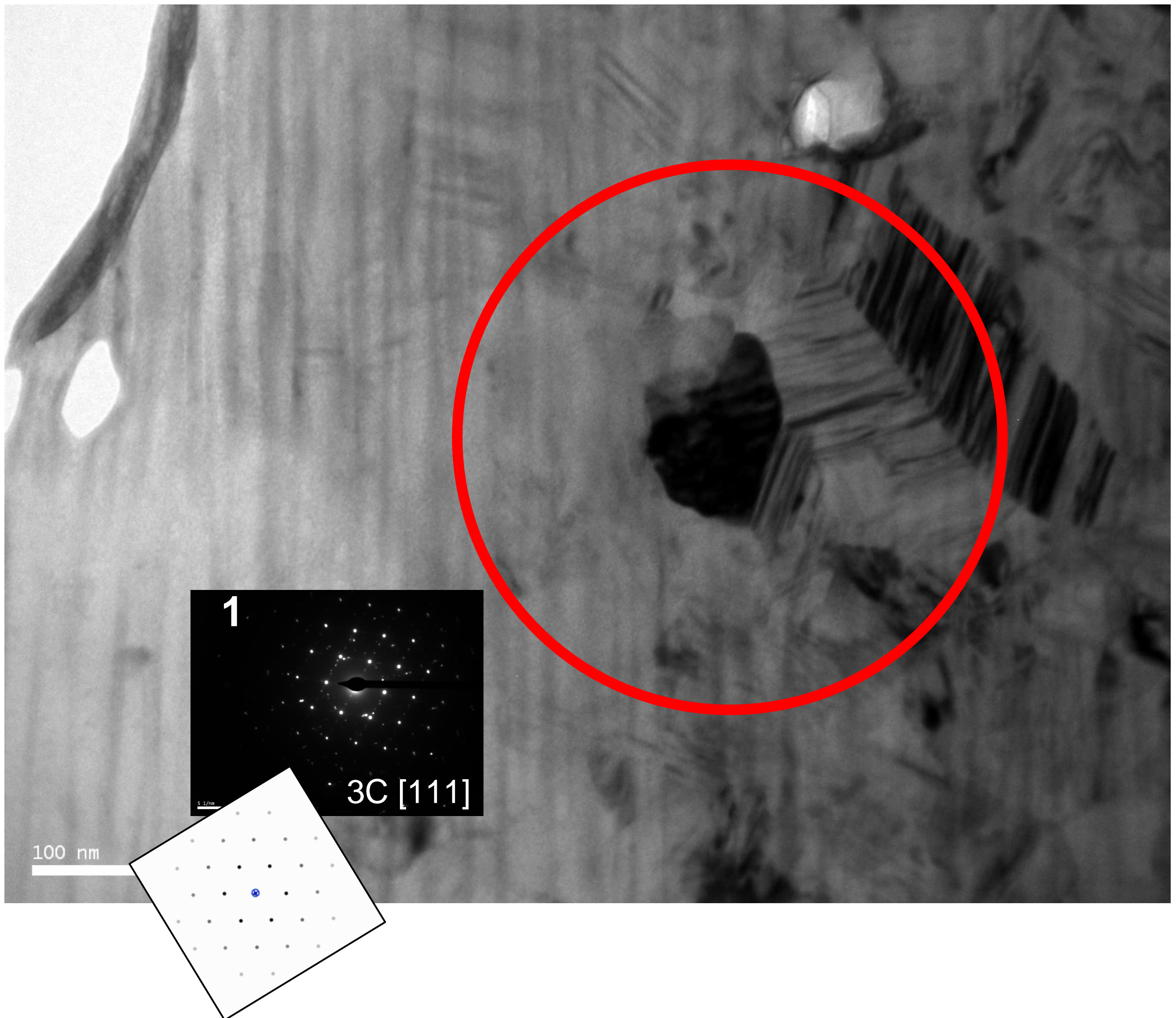

UNIVERSITEIT VAN PRETORIA
UNIVERSITY OF PRETORIA
YUNIBESITHI YA PRETORIA

PO6 Image 8

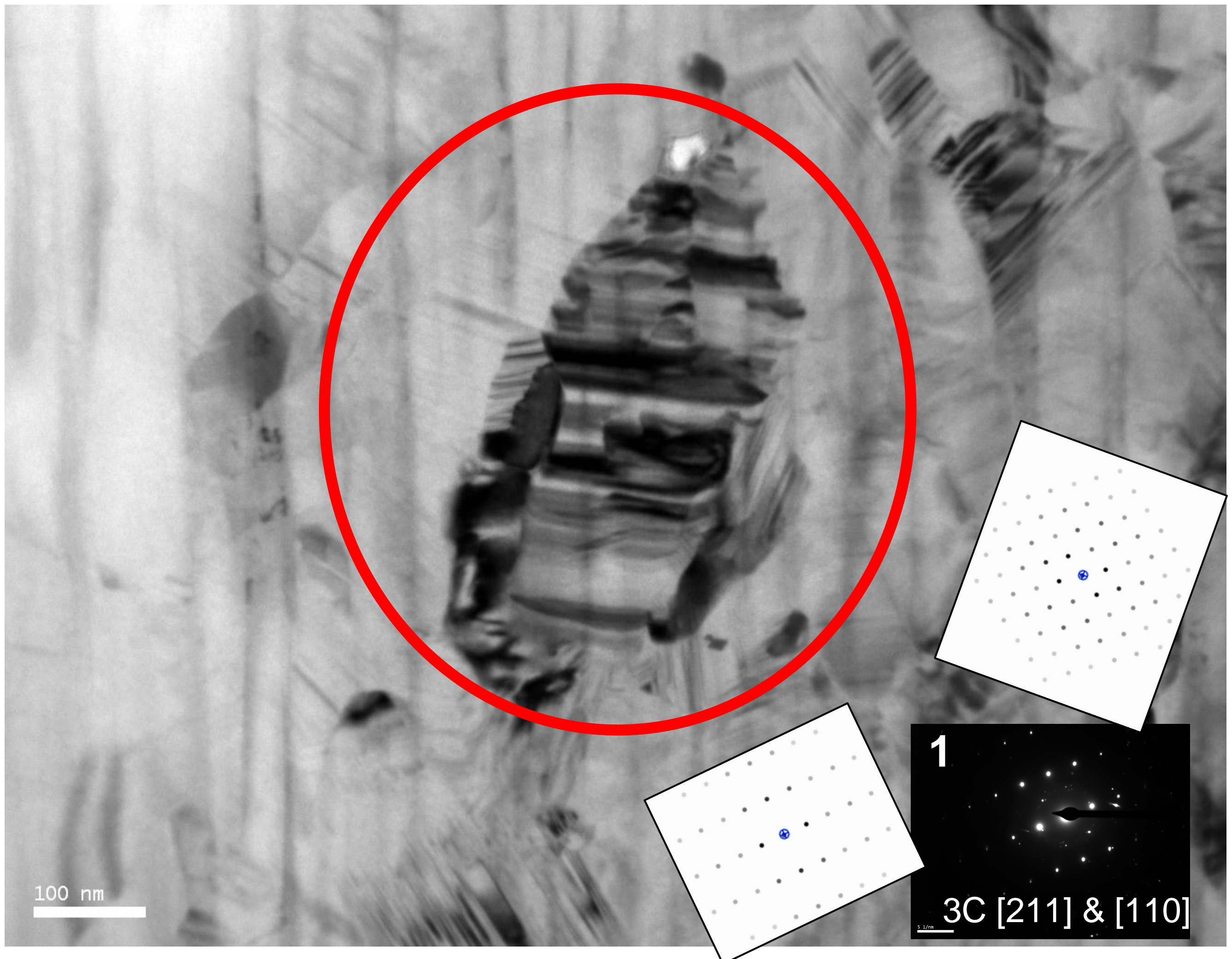

UNIVERSITEIT VAN PRETORIA
UNIVERSITY OF PRETORIA
YUNIBESITHI YA PRETORIA

PO9 Image 1

1

100 nm

6H [100]/[110]

UNIVERSITEIT VAN PRETORIA
UNIVERSITY OF PRETORIA
YUNIBESITHI YA PRETORIA

PO9 Image 2

1

3C [111] &[110]

2

3C [111]

0.2 µm

UNIVERSITEIT VAN PRETORIA
UNIVERSITY OF PRETORIA
YUNIBESITHI YA PRETORIA

PO9 Image 3

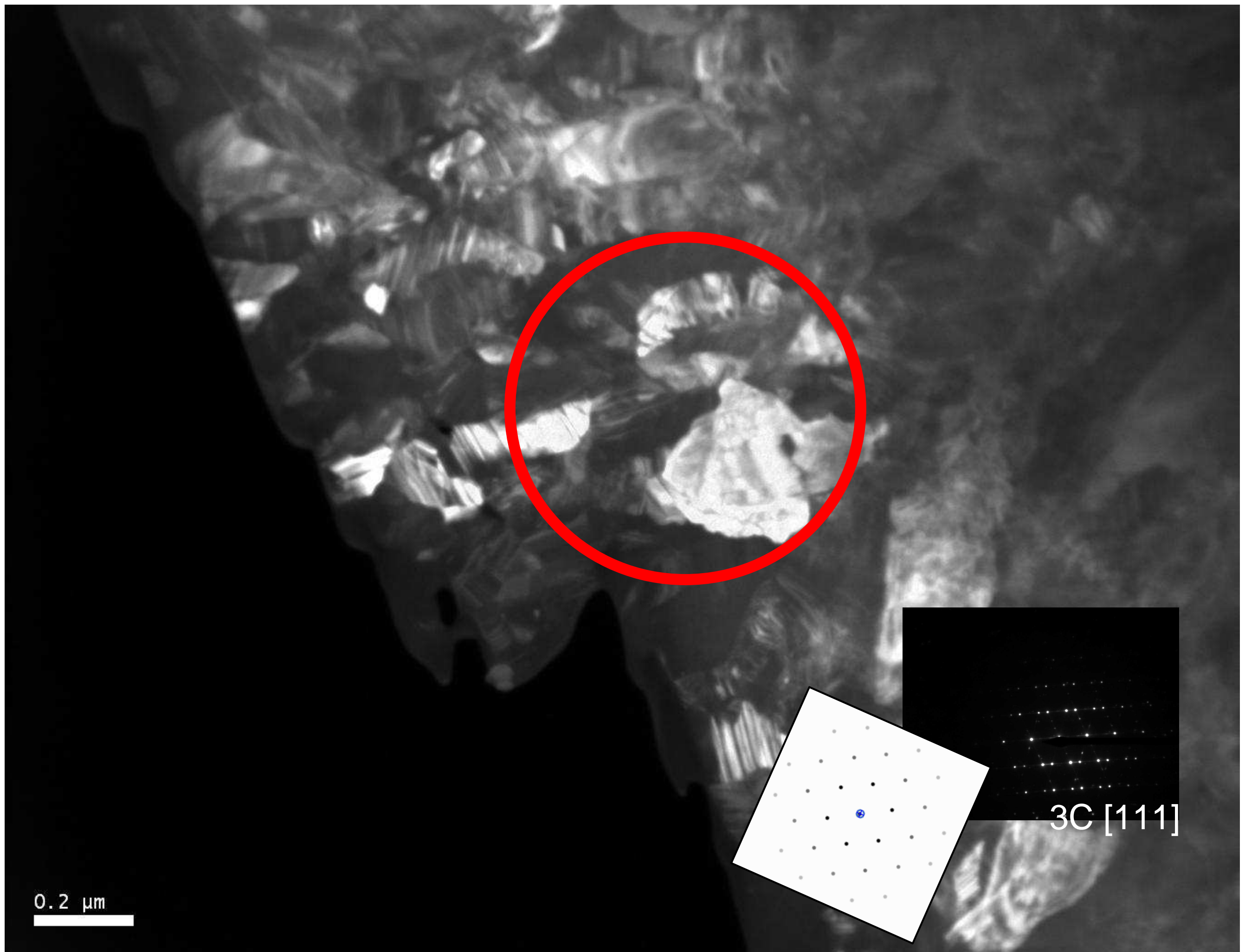

UNIVERSITEIT VAN PRETORIA
UNIVERSITY OF PRETORIA
YUNIBESITHI YA PRETORIA

PO9 Image 4

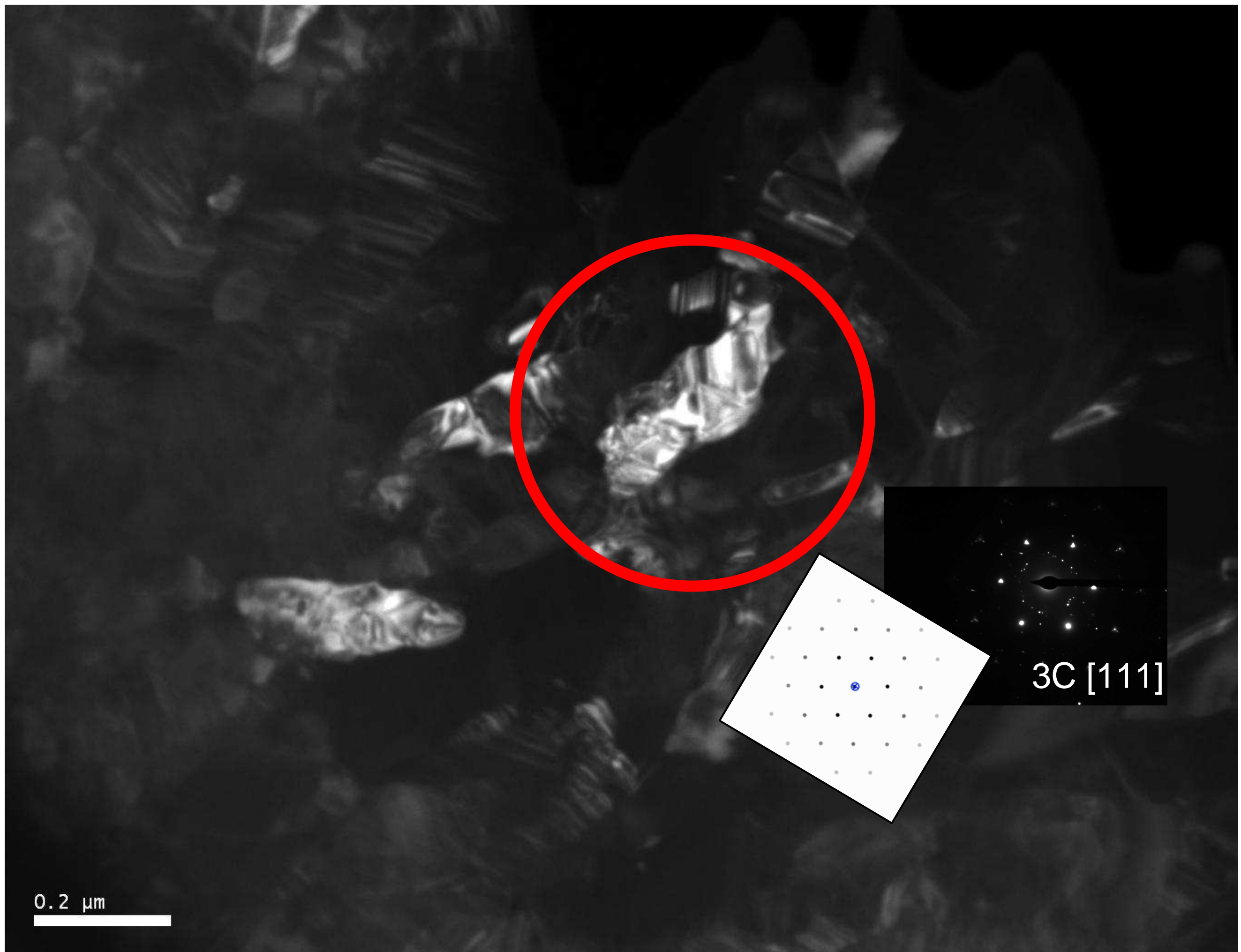

PO Image 5

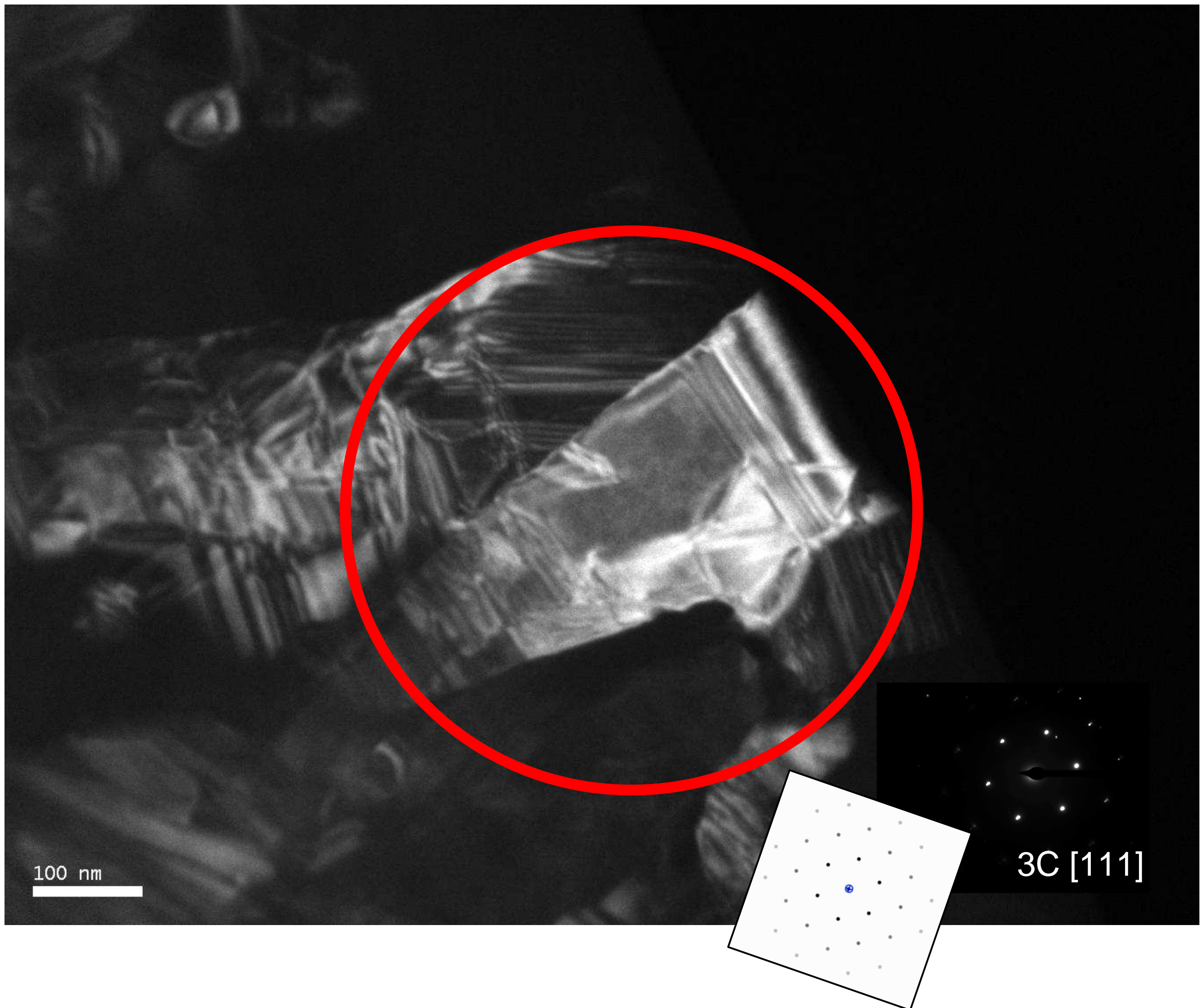

UNIVERSITEIT VAN PRETORIA
UNIVERSITY OF PRETORIA
YUNIBESITHI YA PRETORIA

PO9 Image 6

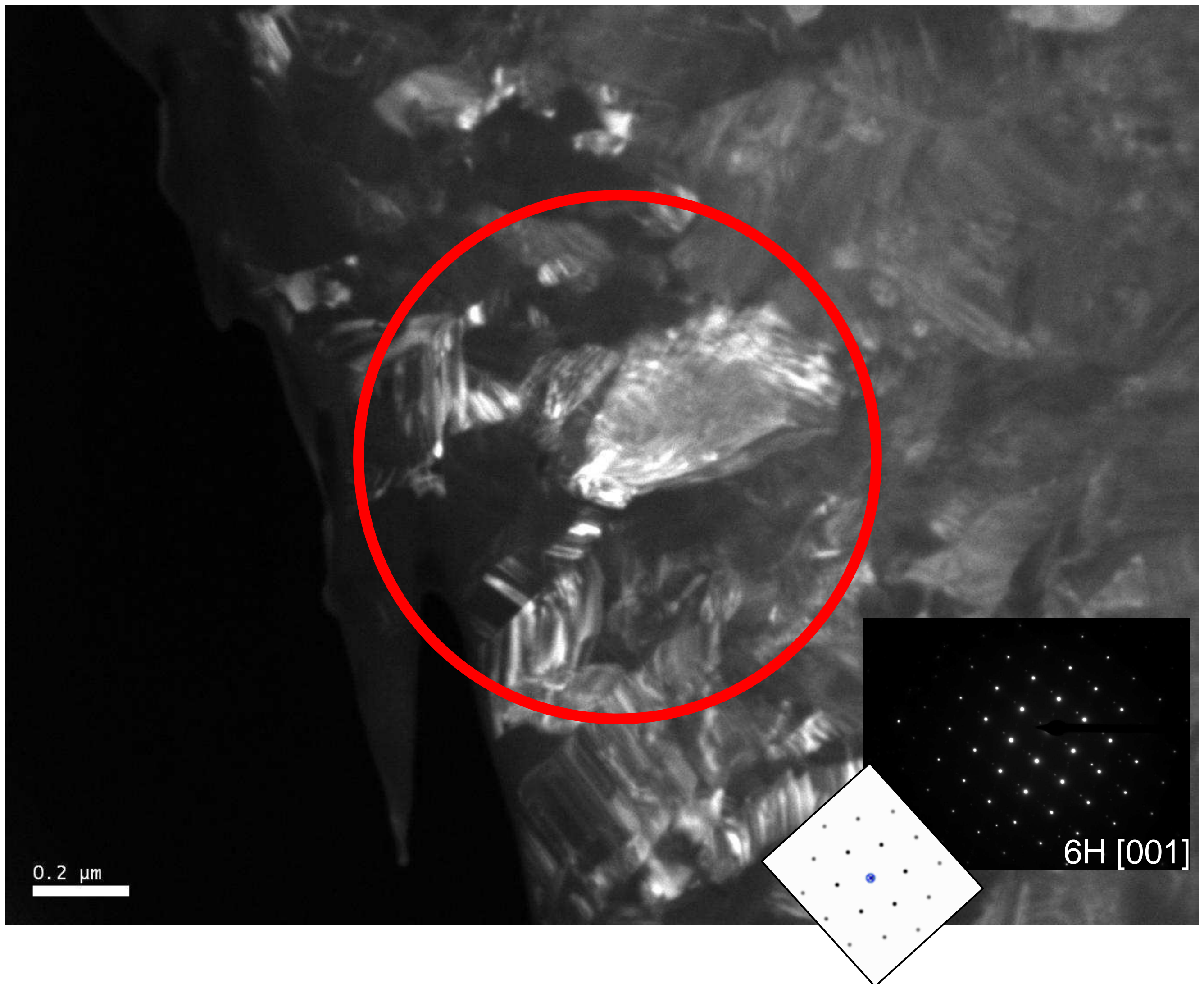

PO9 Image 7

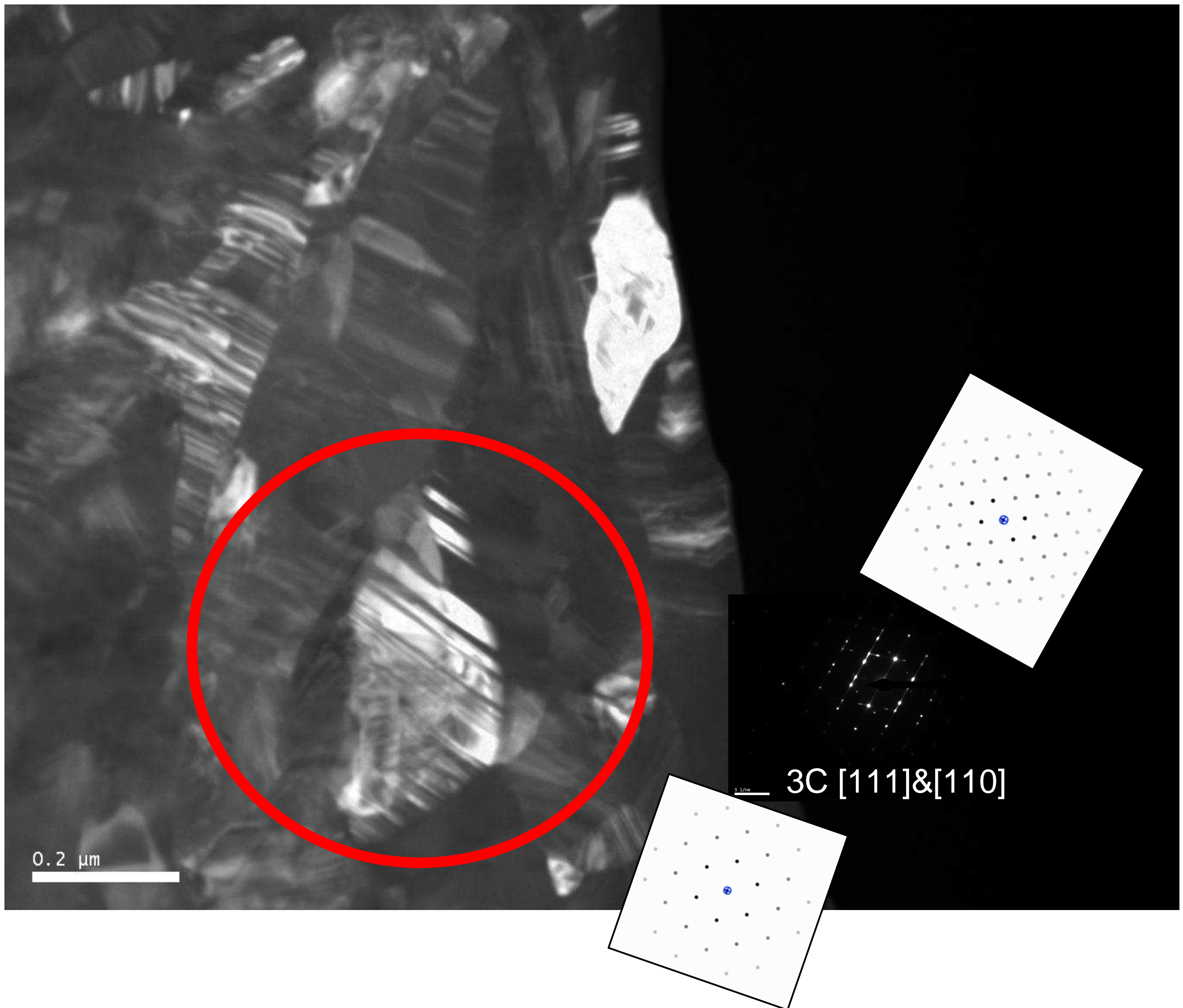

UNIVERSITEIT VAN PRETORIA
UNIVERSITY OF PRETORIA
YUNIBESITHI YA PRETORIA

PO9 Image 8

0.2 µm

3C [211]

UNIVERSITEIT VAN PRETORIA
UNIVERSITY OF PRETORIA
YUNIBESITHI YA PRETORIA

PO9 Image 9

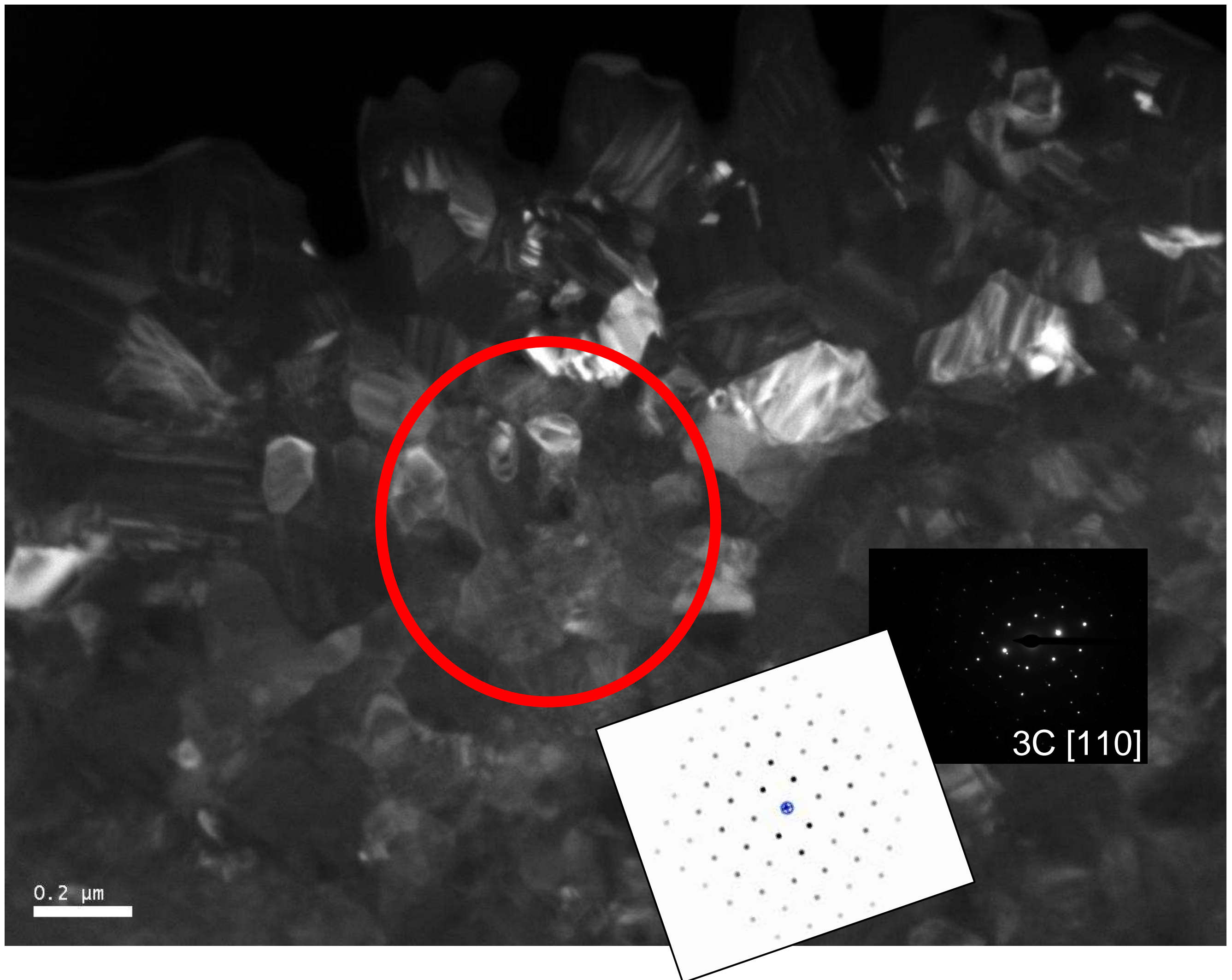

UNIVERSITEIT VAN PRETORIA
UNIVERSITY OF PRETORIA
YUNIBESITHI YA PRETORIA

PO9 Image 10

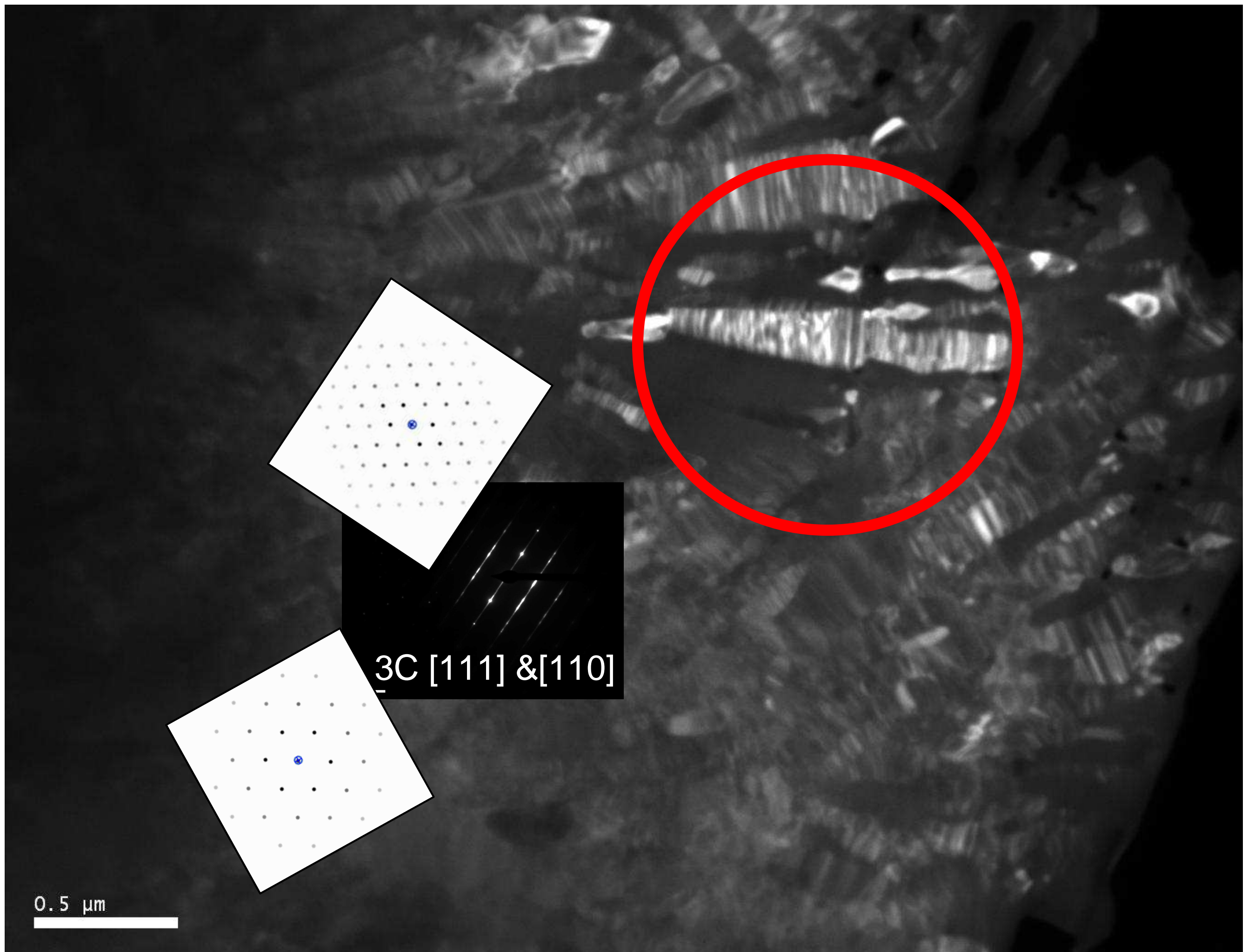

UNIVERSITEIT VAN PRETORIA
UNIVERSITY OF PRETORIA
YUNIBESITHI YA PRETORIA

PO9 Image 11

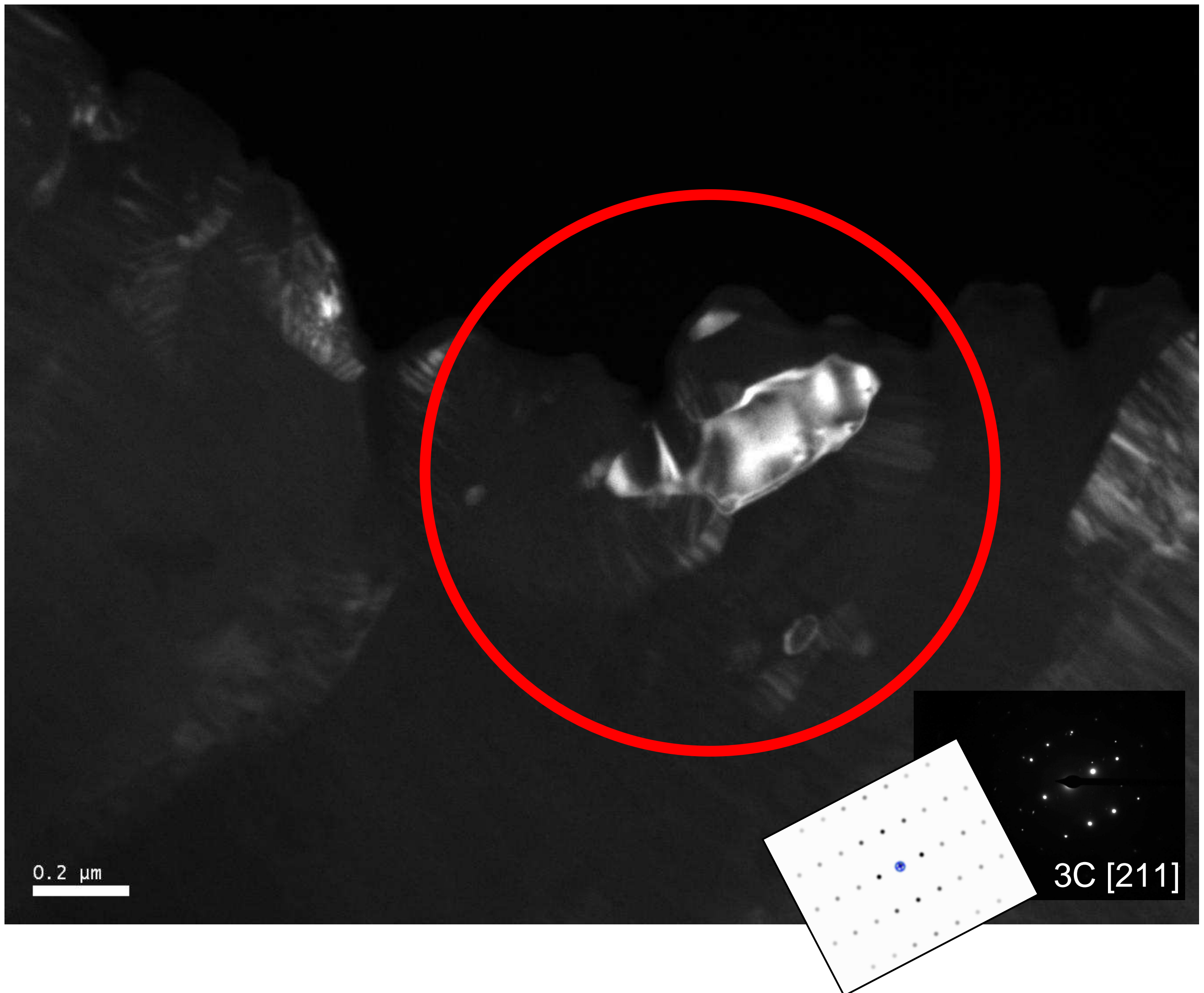

PO9 Image 12

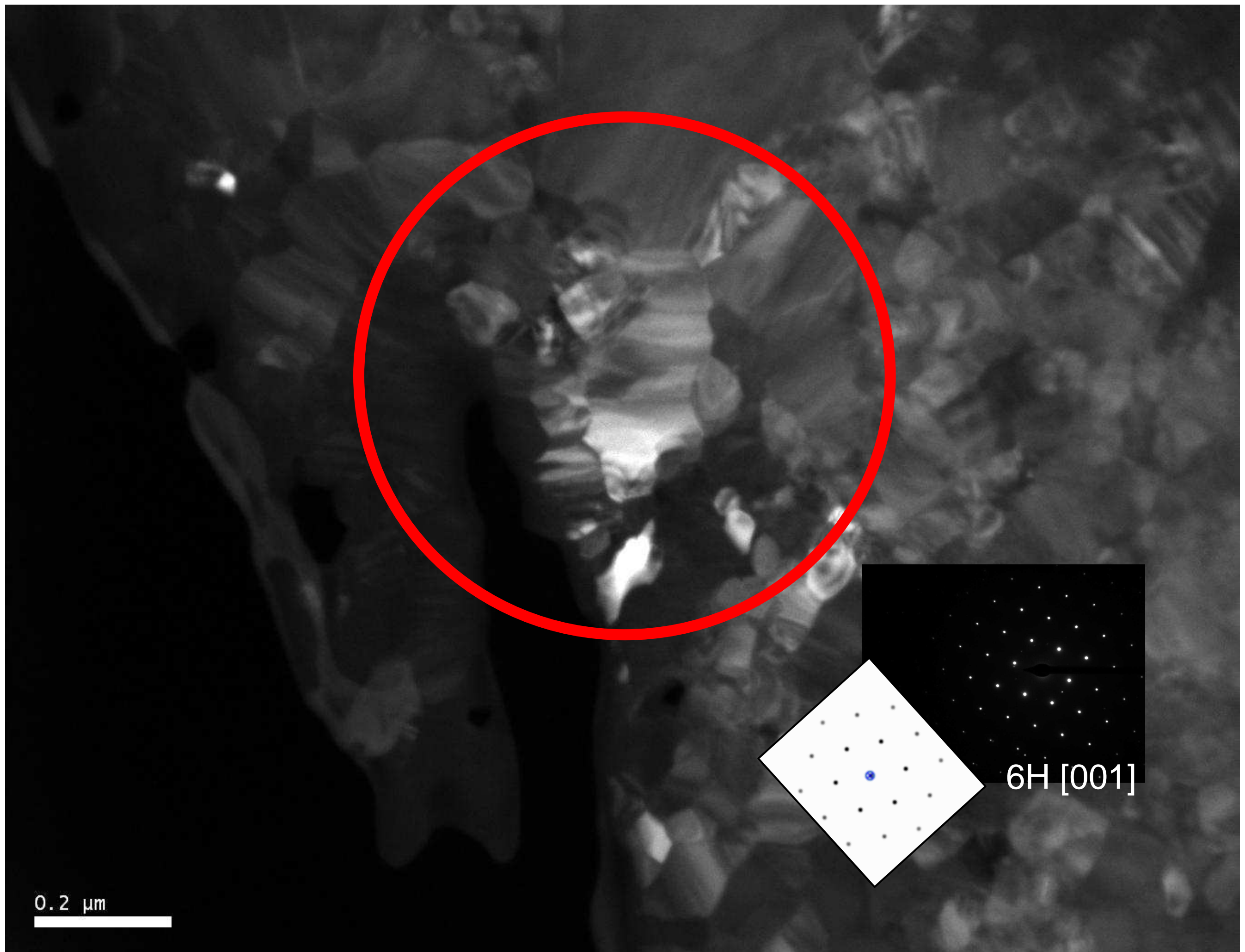

PO9 Image 13

UNIVERSITEIT VAN PRETORIA
UNIVERSITY OF PRETORIA
YUNIBESITHI YA PRETORIA

PO9 Image 14

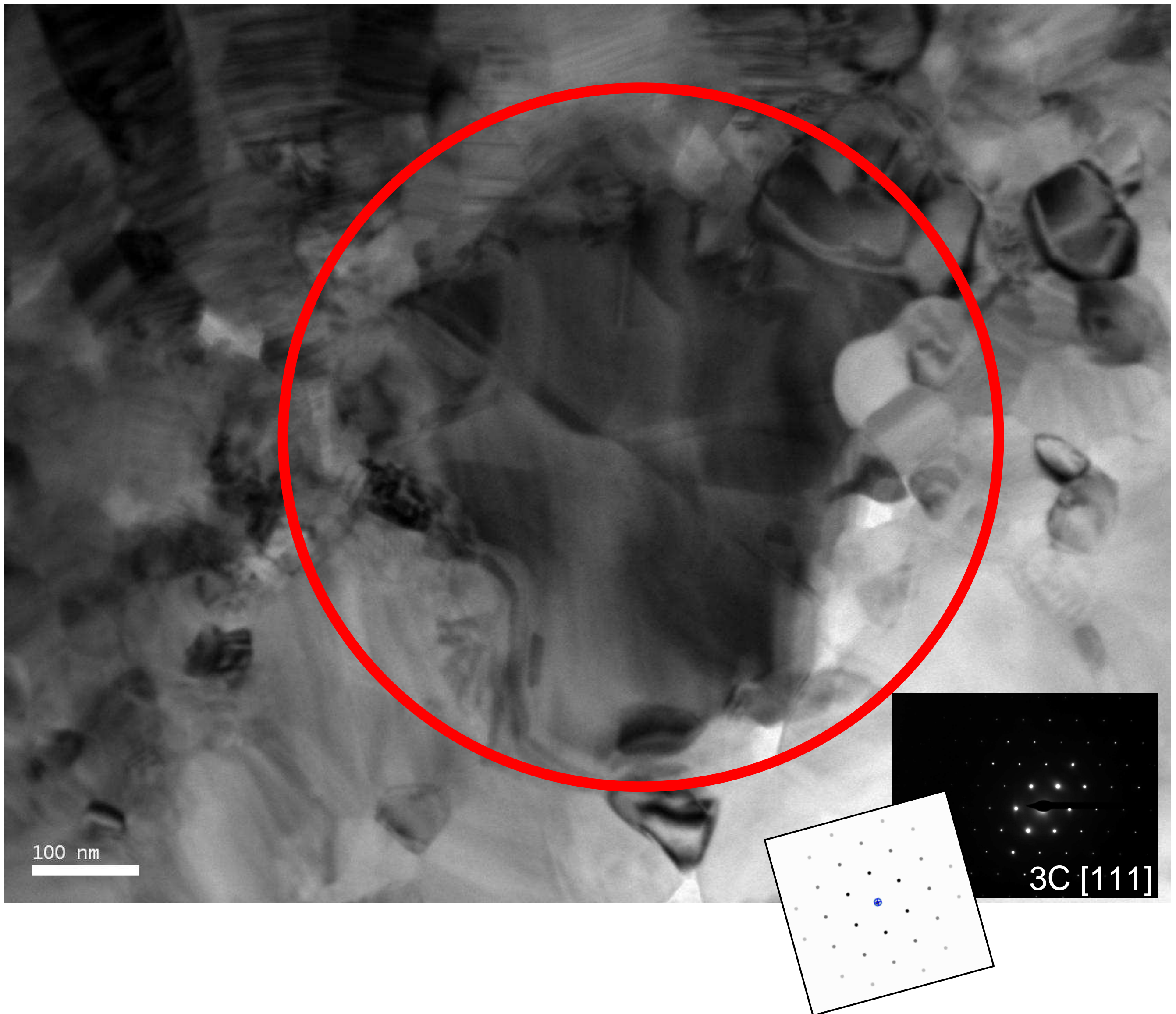

UNIVERSITEIT VAN PRETORIA
UNIVERSITY OF PRETORIA
YUNIBESITHI YA PRETORIA

PO9 Image 15

6H [100]/[110]

100 nm

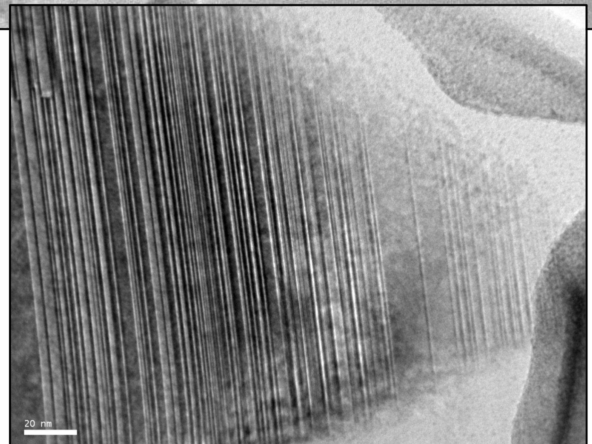

PO9 Image 16

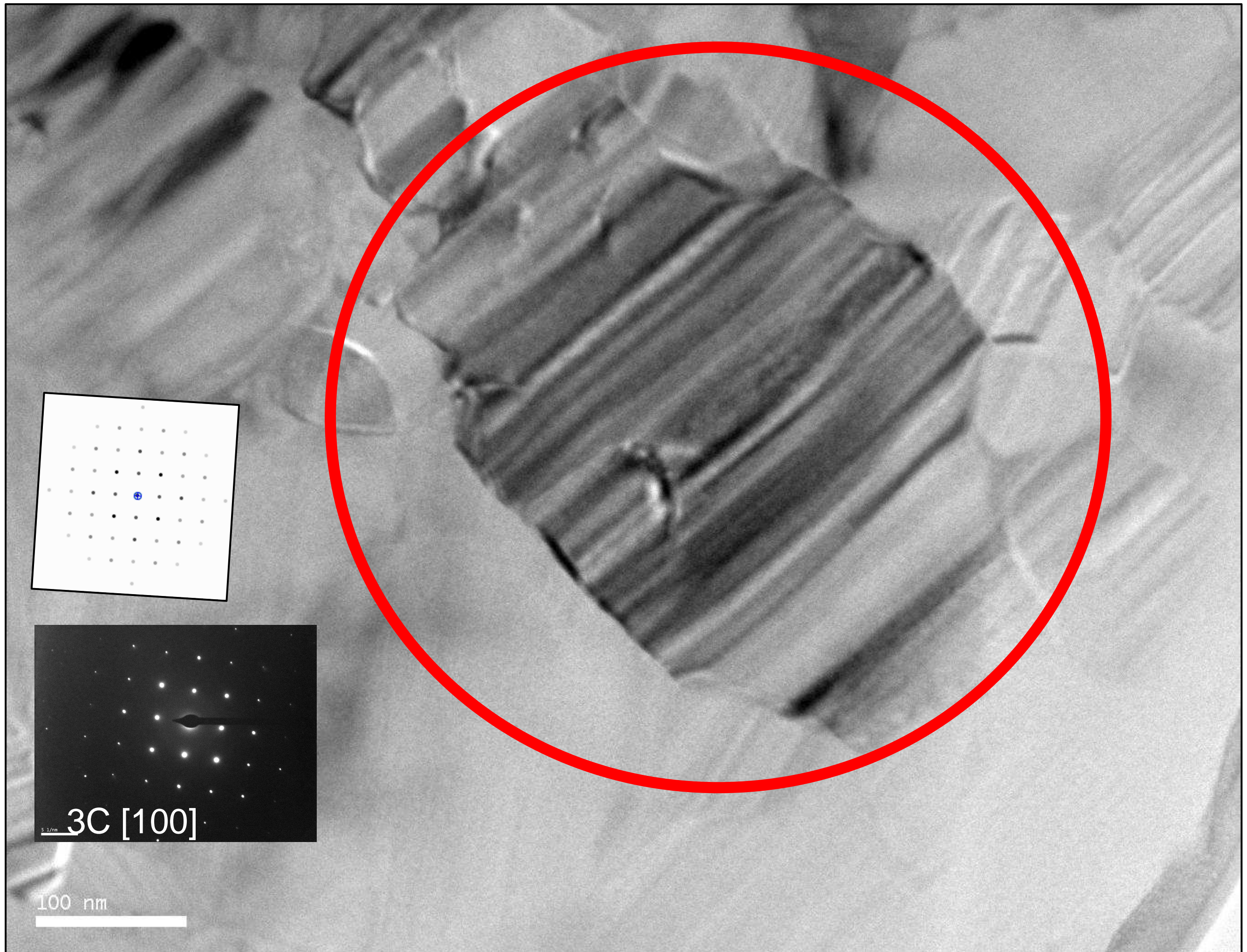

High temperature data

- PO9
  - Lattice parameters (units in Å)

EXPERIMENTAL VALUES				
T	a - Al_2O_3	c - Al_2O_3	c-graphite	a-SiC
25	4.76182	12.99269	6.95261	4.35972
100	4.76399	12.99832	6.96335	4.36038
200	4.76692	13.00881	6.98064	4.36192
300	4.77019	13.02118	7.0149	4.36421
400	4.77309	13.03091	7.02579	4.36526
500	4.77657	13.0417	7.04581	4.36726
600	4.77966	13.05079	7.05891	4.36894
700	4.78277	13.06108	7.077	4.37064
800	4.78542	13.07075	7.08706	4.37223
900	4.7882	13.07963	7.1011	4.37363
1000	4.79099	13.08833	7.11972	4.37491
1100	4.79435	13.09828	7.13628	4.37706
1125	4.79477	13.10019	7.13666	4.37706
1150	4.79531	13.10262	7.14042	4.37755
1175	4.7962	13.10427	7.14197	4.37794
1200	4.79714	13.10536	7.14978	4.37804
1225	4.79779	13.10757	7.15186	4.37843
1250	4.79824	13.11146	7.15506	4.37917
1275	4.79949	13.11442	7.16239	4.37974
1300	4.80077	13.11851	7.16351	4.38054
1325	4.80114	13.1201	7.16618	4.38048
1350	4.80272	13.12333	7.16964	4.38106
1375	4.80361	13.12732	7.17442	4.38174
1400	4.80394	13.12673	7.19272	4.38132
1400	4.80394	13.12673	7.19272	4.38132
1350	4.80256	13.12303	7.16977	4.38083
1300	4.80099	13.11813	7.16192	4.37993
1250	4.79963	13.11412	7.16058	4.37949
1200	4.79808	13.10907	7.14562	4.37843
1150	4.79658	13.10388	7.14152	4.37782
1100	4.79532	13.09964	7.13344	4.37689
26	4.76203	12.99573	6.9647	4.35966